The University of Nottingham

UNITED KINGDOM • CHINA • MALAYSIA

Bone: A study of machining-induced damage and the role of interstitial fluid

José Alberto Robles Linares Alvelais

Thesis submitted to the University of Nottingham in fulfilment of the requirements for the degree of Doctor of Philosophy

Faculty of Engineering

Department of Mechanical, Materials and Manufacturing Engineering

June 2022

"... I seem, then, in just this little thing to be wiser than this man at any rate, that what I do not know I do not think I know either."

Plato's Apology of Socrates

Para Nayara, el amor de mi vida y mi incondicional fuente de apoyo y motivación. Gracias por tanto.

Abstract

Bone cutting is a common process in orthopaedics, dentistry and neurosurgery. However, it comprises a challenging set of tasks when it comes to machining analysis and damage assessment due to its complex hierarchical and porous microstructure. Additionally, given its biological nature, bone is not only an engineering material, but also a tissue that holds living cells and interstitial fluid within.

During machining, temperature rise is inevitable, and if the temperature surpasses a certain threshold, it will cause cellular death (i.e. necrosis). Histological analysis has been the gold standard technique for assessing bone quality, as it enables a straightforward necrosis measurement. However, being mostly used in the medical field and having a biological nature aimed at cellular observation, this technique does not capture mechanical damage, which is essential for a full material assessment, especially considering that many times following bone machining, an implant might be put in close contact with the machined surface.

To understand and minimise the machining-induced tissue damage, many studies and models have been proposed regarding both conventional and non-conventional machining processes. However, most of these studies have been conducted in a laboratory scenario principally consisting of machining bone in a dry state or with external coolant supply. While all of these are valuable, they have typically neglected the in-vivo conditions of bone by not considering the interstitial fluid that is contained within the porosities of the bone's microstructure. However, it is believed that this internal irrigation condition of in-vivo bone will locally affect other properties that impact the cutting process, such as the friction coefficient or the shear strength.

This research aims to understand the machining-induced damage in cortical bone not only from a biological point of view, but also from a micromechanical perspective, by employing micromechanical testing (i.e. micropillar compression) post-machining to

assess thermomechanical damage. The machining techniques selected for damage assessment are conventional (i.e. drilling, fly cutting) and non-conventional (i.e. laser machining).

This research also presents a novel laboratory machining setup that allows to mimic the in-vivo conditions of cortical bone during a cutting process. The setup permits to fix the sample for machining while also enabling to pump fluid through the vascular porosities of the bone, thereby producing a more realistic method for bone cutting in a laboratory scenario.

This study shows that in conventional machining, micromechanical damage beneath the machined surface could be more significant than necrotic damage, even showing that a ductile-to-brittle failure mode transition can take place at the microscale in regions both inside and outside the necrotic zone. Also, the effect of internal irrigation during bone cutting, as enabled by the novel machining setup, produces a drastic difference in chip formation, cutting forces, surface morphology and thermal damage, as opposed to traditional dry cutting experiments. The results from this work are expected to contribute and promote in-depth research of bone machining towards improved tooling and tooling systems that could improve surgical procedures by minimising damage inducement and benefiting patient recovery.

Keywords: cortical bone; bone cutting; bone machining; necrosis; surface damage; histology; micromechanics; micropillar compression; bone failure mechanism; interstitial fluid; chip formation; internal irrigation.

Acknowledgements

This work could not have been completed without the help, support, advice and guidance from so many people. First, I would like to thank Nayara, my wife, for her always-increasing support. Even when I was passing through difficult times, she always cheered me to keep on going and managed to make herself present. Being these years apart was super difficult for both of us, but it was her transmitted strength and love that always kept me motivated. Thank you for everything! Our story is barely getting written.

My parents, José Luis and Verónica have been an incredible source of unconditional love and support not only these past 3 years, but my whole life. They have always motivated me to be better and have given me the best example of a loving family. I am thankful that you have always been there for me and have shown a great interest in my research, even when you did not understand it fully. However, I would also like to thank the rest of my family (Ani, Gody, José Raúl and Tetey) for always being there for me too, by giving me superb support.

I want to express my gratitude towards Prof. Dragos Axinte for his incredible support on my research project not only through the PhD, but since we met back in my master's degree when I was still in Mexico. Since then, he has been an incredible source of support and, as my leading supervisor and mentor, he has taught me about Academia and the proper pathway to do high quality research. Moreover, he made me feel excited about my research topic, even at times when some ideas or results were not what I was expecting. Thank you!

Zhirong and Andres, I thank you both for being excellent supervisors of my research too. Both of you gave me great guidance not only from a research or academic perspective, but you were always there to give me tips and advice about hands-on engineering and life in general.

Many others from my UTC (and extensions) family deserve a special mention for their support (both in my research and in my life), friendship, gossiping, beers at R&C and cake Mondays: Gon, Javi, Irati, Juan, Ángela, Josué, Cecy, Erik, Andrea, David Cha, Floriana, Luca, Kieran, Dima, Matteo, Moni, Artem, Thomas, Chris, Steve and Dan. You guys have made my time in the UTC simply amazing. I am humbled by being in such an incredible group.

I would like to acknowledge the support and guidance that I received from other members of the university. I am grateful with all the staff from the nmRC, but especially with Chris Parmenter and Martin Roe, for their incredible expertise on materials characterisation at the nano- and microscales and for teaching me how to use advanced equipment that I could have never imagined on using before starting this PhD. It has been an honour to learn from you. Additionally, I would like to thank Ian Ward and Denisse McLean from the School of Life Sciences for their guidance and training in the histology lab at QMC, where I learned about tissue processing and the challenges of doing histological analysis on such a hard tissue like bone.

Additionally, I want to thank the staff from the Rose & Crown (R&C) for making of that pub a homely place not only for me, but for all the UTC members by enabling us to wash down our PhD stress with a cold pint. On this note, I would like to thank Andrea for always keeping the ‘Wings Wednesday’ tradition alive.

Finally, I must thank the sponsors of this PhD: CONACYT, SEP and The University of Nottingham. Thanks to the funding received by these academic institutions, I was able to complete my PhD.

To everyone herein mentioned: a BIG thank you!

Table of contents

List of figures

List of tables

List of abbreviations

Abbreviation	Description
AD	Across direction relative to the longitudinal axis of the osteon
AM	Additive manufacturing
AMMDA	Alemnis Materials Mechanics Data Analyzer
ASA	Alemnis Standard Assembly
avg	Average
az	Affected zone
B	Bulk zone
B_{HT}	Bulk zone in the high temperature (HT) drilling bone sample
B_{LT}	Bulk zone in the low temperature (LT) drilling bone sample
CAP	Collagen-hydroxyapatite porosity
CNC	Computer numerical control
CT	Computed tomography
CW	Continuous wave laser
D	Dry condition
DE	Dry condition with external coolant delivery condition
DOC	Depth of cut
DPX	Distyrene, plasticiser and xyelene
FC	Fracture cutting mode
FEG	Field Emission Gun
FEM	Finite Element Method
FIB	Focused Ion Beam
FWHM	Full width at half maximum

H&E	Haematoxylin and eosin
HSS	High speed steel
HT	High temperature
HV	High vacuum
I	Internally irrigated condition
I_1	Intermediate location 1 in the HT drilling bone sample
I_2	Intermediate location 2 in the HT drilling bone sample
IE	Internally irrigated with external coolant delivery condition
IR	Infrared
JC	Johnson-Cook
LCP	Lacunar-canalicular porosity
LT	Low temperature
LV	Low vacuum
N	Necrotic zone
Nano	Nanosecond laser
N_{HT}	Necrotic zone in the high temperature (HT) drilling bone sample
N_{LT}	Necrotic zone in the low temperature (LT) drilling bone sample
PD	Parallel direction relative to the longitudinal axis of the osteon
PF	Picosecond laser with fast feed speed (5 mm/s)
PS	Picosecond laser with low feed speed (1 mm/s)
ROI	Region of interest
SC	Shear cutting mode
SCC	Shear-crack cutting mode
SEM	Scanning Electron Microscope
SPH	Smoothed particle hydrodynamics

std dev	Standard deviation
TD	Transverse direction relative to the longitudinal axis of the osteon
TUNEL	Terminal deoxynucleotidyl transferase dUTP nick end labelling
UCT	Uncut chip thickness
VA	Vibration-assisted
VP	Vascular porosity

List of symbols

Symbol	Description	Units
E	Young's Modulus	GPa
K_c	Fracture toughness	MPa×m$^{1/2}$
μ	Friction coefficient	-
h	Depth of cut	µm
V_c	Cutting speed	m/min
i	Sub-index to represent the cutting direction: $i = 1$ → Parallel (PD) to osteons orientation. $i = 2$ → Across (AD) to osteons orientation. $i = 3$ → Transverse (TD) to osteons orientation.	-
G_{IC}	Critical energy release rate of Mode I fracture	J/m^2
$G_{IIC,i}$	Critical energy release rate of Mode II fracture	J/m^2
$G_{(I+II)C,i}$	Critical energy release rate of mixed Mode I and Mode II fracture	J/m^2
h_s	Critical UCT for transition from SC to SCC mode	µm
h_f	Critical UCT for transition from SCC to FC mode	µm
$Ø_i$	Shear angle	°
τ	Shear stress	MPa
τ_s	Shear strength	MPa
τ_{sc}	Shear strength in SC mode	MPa
τ_{scc}	Shear strength in SCC mode	MPa
α	Rake angle	°
λ	Friction angle	°
h_{drill}	Equivalent DOC in drilling, i.e. the feed per lip	µm

f_n	Feed rate	mm/rev
z_n	Flute/teeth number of a drill or milling cutter	-
h_{mill}	Equivalent DOC in milling, i.e. the feed per tooth	µm
V_f	Feed speed	mm/min
$n_{spindle}$	Spindle speed	rpm
θ_{cut}	Angle of rotation of the tool	°
θ	Penetration angle (drilling), i.e. angle between the normal of the surface and the drill axis	°
ω	Half point angle of the drill	°
F_{ski}	Skidding force	N
$C_{Alemnis}$	Nanoindenter's frame compliance	m/N
P	Nanoindenter load (measured from the ASA's load cell)	N
h_{frame}	Displacement of the nanoindenter's frame	m
L_{Pt}	Thickness of the protective Pt layer of the micropillar	µm
E_{Pt}	Young's modulus of platinum (Pt)	GPa
d_{pillar}	Diameter of the micropillar	µm
h_{Pt}	Elastic displacement of the Pt layer of the micropillar	µm
$h_{sink\text{-}in}$	Elastic sink-in displacement of the micropillar	µm
h_{meas}	Raw displacement of the nanoindenter (i.e. as measured, without corrections)	µm
rf_{illet}	Fillet radius at the bottom of the micropillar	nm
v_{bone}	Poisson's ratio of cortical bone	-
σ_{33}	Compressive axial stress	GPa
ε_{33}	Compressive axial strain	µm/µm
σ_{ys}	Yield stress	GPa
σ_{ult}	Ultimate stress	GPa

$V_{f,min}$	Lower bound of the feed speed range for laser machining	mm/s
$V_{f,max}$	Upper bound of the feed speed range for laser machining	mm/s
Ra	Surface roughness	µm
Sa	Area surface roughness	µm
n	Number of measurements	-
T_{max}	Maximum temperature	°
d_{crit}	Threshold micropillar critical diameter to avoid crack development failures	µm
γ_{az}	Ratio between the thickness of the affected zone (az) and the porosity radius	µm
r_{por}	Porosity radius	µm
r_{az}	Affected zone (az) radius	µm
$r_{az,\mu}$	Affected zone (az) radius of the friction coefficient	µm
$r_{az,\tau}$	Affected zone (az) radius of the shear strength	µm
μ_0	Friction coefficient in the bulk material and outside the affected zone (az)	-
β_μ	Reduction ratio of the friction coefficient in the porosity wall (at r_{por}) against the pristine value (μ_0)	-
β_τ	Reduction ratio of the shear strength in the porosity wall (at r_{por}) against the pristine value (τ_0)	-
F_c	Cutting force	N
F_t	Thrust force	N
w	Cutting width	mm
N_y	Number of nodes along the Y direction	mm

List of publications

A list of scientific publications arising from this research is below.

1. Robles-Linares, J.A., Axinte, D., Liao, Z., Gameros, A., 2021. Machining-induced thermal damage in cortical bone: Necrosis and micro-mechanical integrity. Mater. Des. 197, 109215. https://doi.org/10.1016/j.matdes.2020.109215
2. Robles-Linares, J.A., Liao, Z., Axinte, D., Gameros, A., 2022. The effect of interstitial fluid on the machining behaviour of cortical bone. J. Mater. Process. Technol.
3. Robles-Linares, J.A., Winter, K., Liao, Z., 2022. The Effect of Laser Ablation Pulse Width and Feed Speed on Necrosis and Surface Damage of Cortical Bone. Chinese J. Mech. Eng. 35, 52. https://doi.org/10.1186/s10033-022-00740-1
4. Zhang, Y., Robles-Linares, J.A., Chen, L., Liao, Z., Shih, A.J., Wang, C., 2022. Advances in machining of hard tissues – From material removal mechanisms to tooling solutions. Int. J. Mach. Tools Manuf. 172, 103838. https://doi.org/10.1016/j.ijmachtools.2021.103838

Chapter 1 - Introduction to bone and its machining

When I was about 12 years old, my best friend JC and I were playing in a parking lot, and he accidently fell on top of me while we were running. After I stood up, I felt my left arm a bit weird and with very little pain. After inspecting for a few seconds, I realised I had broken my arm. My mom quickly took me to a hospital, were they confirmed a severe fracture on my left humerus. The bone had broken in half! Since then, I have had a total of three surgeries, three implants and more than thirty screws inside my arm that have quite limited my mobility and bring pain from time to time. Interacting with different doctors, I realised that there is a huge gap between manufacturing/machining research and the medical community. In an aim to minimise this gap, I decided to investigate about bone machining and how to improve the technical bone machining knowledge to be employed in real surgeries. With this, I hope that any patient who suffers from severe bone trauma in the future, can fully recover with none or minimum limitations.

During my PhD I explored bone as a material that is subjected to machining, but also as a tissue that is exposed to damage due to the cutting process (i.e. the surgery) itself. This duality in the perspective is what enabled me to explore various routes for damage assessment in cortical bone. As such, with this work I wish to contribute to the understanding that both the research and the medical community have about the damage inducement mechanisms in cortical bone.

In this introductory chapter, the general challenges of bone machining that have motivated this research are outlined along with the problems that these incur in terms of bone damage. From these, a series of aims and objectives are defined and serve as a guideline for the work of this research.

1.1 Motivation

Over the course of history, human bodies have been subjected to surgeries to improve the health condition of individuals, such as treating a disease or removing a tumour. As far back as AD 1000–1250, when no appropriate technology was available, surgeons used stone-made cutting tools, for example, to access the skull (Kurin, 2013). These tools had limited sharpness and resulted in poor cutting action, excessive tissue damage and slow post-surgery recovery or difficulties therein. In modern civilisation, research has enabled the understanding of surgical processes and the development of cutting methods or tools for minimised tissue damage and faster post-surgery recovery.

Tissues subjected to cutting during surgeries can be categorised as either soft (e.g. cartilage (Pang et al., 2020), meniscus (Chen et al., 2021) and skin) or hard (e.g. bone and tooth). Given that hard tissues possess certain strength and hardness, they are more challenging to cut than soft ones. As a result, hard tissues have been a subject of interest not only in cutting, but also in other fields such as bio-inspired composites (Gu et al., 2018), microarchitectures (Torres et al., 2019), biomimetics (Robles-Linares et al., 2019) and bio-micromechanics (Schwiedrzik et al., 2017). Hard tissues, such as cortical bone, cancellous bone, dentin and enamel, not only have a composite-like intricate hierarchical microstructure with a complex anisotropy in properties, but their constituents also vary from person to person and with age and health conditions, introducing difficulties in precisely controlling the cutting process for these tissues. By contrast, they are biological materials and experience cellular death (i.e. necrosis) under the high temperatures that are commonly found in machining. Such necrosis causes a detrimental effect on hard tissue's capacity for regeneration and post-surgical recovery (Mediouni et al., 2019).

Among hard tissues, bone is of vast interest in the research community, as different material removal methods of bone are necessary (e.g. drilling, milling, grinding) for a

wide range of operations in various medical fields, such as orthopaedics, neurosurgery and dentistry. As such, bone was selected as the object of study in this research.

Bone necrosis (i.e. cellular death) is one of the major concerns during its machining; reducing it or eliminating it is the driving force to reduce the temperatures in the cutting of the tissue. However, other types of machining damage, such as cracks (Zhang et al., 2019), can also be induced along with necrosis. Understanding the cutting mechanisms of hard tissues is essential for improving machining processes (Sugita et al., 2009a; C. Y. Wang et al., 2021) and developing effective tooling solutions for various types of surgical cutting, such as milling and drilling (Liao et al., 2017; Shu et al., 2020b), whereby the cutting temperatures and forces are to be minimised to reduce the likelihood of tissue necrosis and other types of damage during a surgical intervention that may incur no only to bone, but also to its surrounding tissue.

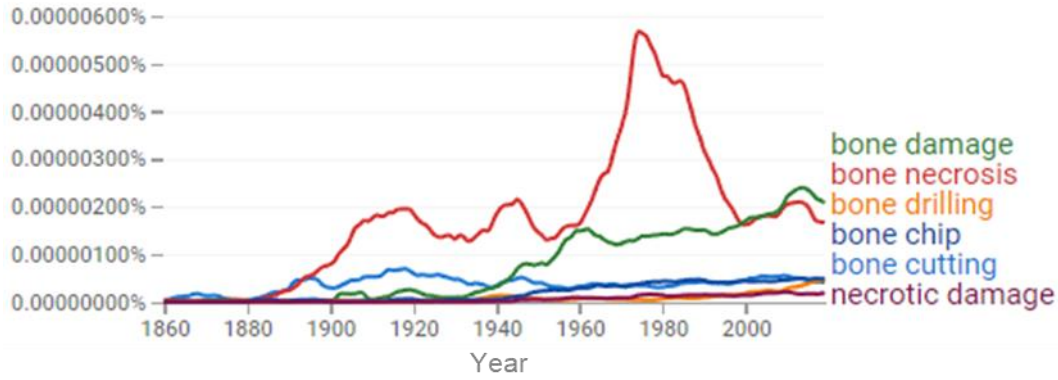

Fig. 1.1. Google Books Ngram viewer with bone machining related terms since 1860. Bone necrosis and damage have been very well reported in books since the early 1900s, but as far as machining-induced necrosis and damage, these terms pose a significant gap.

In the past few decades (Fig. 1.1), a considerable amount of research and development effort has been reported in studying a wide range of topics relating to the machining of hard tissues, including their microstructure and properties, the process and mechanisms of various machining operations, and the improvement of cutting tool design. However, the mechanism of bone necrosis is usually regarded from a medical or biological perspective only, which is why the terms ‘bone damage’ and ‘bone

necrosis' have a significantly larger frequency of use in books (Fig. 1.1) since the early 1900s. However, the terms related to bone machining have a much lower appearance and this is because the machining-induced damage (e.g. necrosis, cracks) has only gained attention until recently.

Table 1.1. The research interest over time of current research topics in hard tissue cutting. The numbers from this table were obtained by searching the keywords using AND/OR operators in Scopus. Both cortical and cancellous bone were considered.

Topic	Keyword 1	Keyword 2	Before 1960	1961-1970	1971-1980	1981-1990	1991-2000	2001-2010	2011-2020	2021-now
Material removal mechanisms	Cortical bone	Orthogonal cutting			2	1		3	13	3
		Drilling process			1		1		34	7
		Drilling force					1	3	25	3
		Drilling temperature			1			3	13	5
		Drilling parameters			1	2	2		26	2
		Milling	1			2	3	11	33	7
		Milling model				1	1	2	15	3
		Grinding			1	3	6	9	18	3
		Vibration-assisted cutting	1		1	1	1	2	20	4
	Cancellous bone	Orthogonal cutting						1		
		Drilling					3	7	20	4
		Milling				1	1	5	11	5
		Grinding				1			2	
Mechanial and thermal damage	Cortical bone	Mechanical damage				1	1	3	15	1
		Thermal damage			1	1	5	6	28	5
		Thermo-mechanical damage						1	2	1
Tool design and process control methods	Cortical bone and cancellous bone	Drill bit	1	1	5	2	3	6	23	1
		K-wire				1	1	8	11	
		Saw				1	2	4	7	
		Milling and grinding tools					1	3	5	1
		Tool cooling system				1	1	4	11	1
		Tool life and coating						2	7	1

Additional to Google Books Ngram viewer, Scopus was employed for studying research trends regarding the material removal mechanisms of cortical bone (Table 1.1). Note how most of the research related to machining of cortical bone and machining-induced damage of cortical bone has been only significantly increasing since after 2010. Additional to this, the research related to the nature or mechanics of the material removal technique is much larger than that related to thermal damage. As such, it is no surprise that a large knowledge gap exists between the research community and the medical community in terms of machining-induced damage in cortical bone. This inherently highlights the importance of in-depth studies of cortical

bone not only as an engineering material, but as a tissue as well, thereby enabling a more significant application of engineering results in the medical community.

1.2 Problem statement and context

The knowledge gap between bone damage and bone machining is the reason why surgical tooling used in orthopaedics is still, on most surgical rooms, state of the art equipment, meaning that conventional surgical cutting tools that were designed several decades ago are still used in surgery, giving only little use to the more novel tool design that bone machining research has achieved. This leads to an imperative need of understanding the damage inducement mechanisms that could occur in cortical bone due to the nature of the material removal technique that is employed. For example, the machining-induced necrosis, phenomenon that is mostly temperature and time dependent, could be expected in material removal methods were high temperatures take place, such as in laser machining or as in drilling at high cutting speeds with low feed rates. However, if drilling were to take place at lower cutting speeds and higher feed rates, the temperatures and drilling time would be much lower, thereby protecting the tissue from necrosis, but these set of machining conditions would also lead to a larger thrust force, thereby enabling the possibility of inducing large cracks into the tissue. This is only an example to highlight the complexity of machining induced damage in cortical bone and the compromise that exists between the nature of the material removal method and how it relates to a specific type of induced damage. This highlights one of the most little-understood problems in bone machining: *how is the material removal process' nature related to the damage it induces to the tissue?*

As an attempt to shed more light into this question, the work of this thesis was done to study the relation between two different material removal techniques in cortical bone: laser machining and drilling. These two were chosen as the material removal

methods not only due to their high application and potential in surgery, but also since they represent two drastically different material removal methods, thereby enabling a comprehensive analysis of bone damage as it relates to a purely thermal, thermomechanical, or mechanical material removal method.

Bone is a natural composite material that is porous and possesses interstitial fluid, blood vessels and nerves embedded on its porosity systems (see Fig. 2.2), giving bone an 'internal irrigation' condition in its alive (i.e. in-vivo) state. This adds another level of intricacy to the machining behaviour of cortical bone, and while there are vast number of studies that have reported on the anisotropic mechanical properties and machining behaviour of cortical bone, these usually lack a clinical relevance since the internal irrigation condition or cortical bone has been traditionally disregarded by the research community. This brings up a second complex question: *what is the role of internal irrigation in bone machining?*

The challenge is that internal irrigation occurs only in-vivo, meaning that studies related to the machining behaviour and machining-induced damage would have to be conducted in a clinical environment right away, but this is very difficult to be done, especially if approached from the machining community. This is also the reason why most of the bone machining studies are conducted with bone in a *dry state* (i.e. without any internal irrigation) and in ex-vivo conditions as it is the most straightforward way to perform machining experiments. Nevertheless, this inherently limits the applicability of whatever results are obtained from the research onto a real medical environment where the bone is alive and irrigated.

Besides studying the bone damage inducement mechanisms in cortical bone, the role of this internal irrigation condition is also addressed in this work. Due to the complex porous architecture of the tissue, orthogonal machining and fly cutting were selected as the material removal methods to study the machining behaviour (i.e. chip formation, forces, temperatures) and damage inducement (i.e. surface topography, cracks,

necrosis) in an irrigated condition of cortical bone and thereby provide a relative comparison to the traditional dry bone cutting process.

Considering all the above, the main challenges faced in this study can be foreseen as follows:

- In cortical bone machining, the relation between machining-induced necrosis and machining-induced mechanical damage is not understood.
- The material removal method's nature (e.g. if it is mostly thermal, thermomechanical, or mechanical) and how it relates to both thermal damage (i.e. necrosis) and mechanical damage (i.e. surface quality and cracks) is not understood.
- The role of internal irrigation in cortical bone is unknown in terms of the chip formation mechanism, the cutting forces and the temperatures that may arise from a mechanical material removal method. Additionally, it is unknown if this is at all different from the traditional dry bone cutting process that is usually employed in the research community.
- If the machining behaviour of internally irrigated cortical bone is different than that from dry bone, this would inherently result in different bone damage mechanisms. As such, the effects that internal irrigation could pose in terms of the machining-induced damage are unknown.

1.3 Objectives of the study

The main objective of this research is to gain knowledge about how the bone damage type, either cellular (i.e. necrosis) or mechanical (i.e. cracks, roughness, failure mode, mechanical properties decay), is related to the nature of the material removal process (e.g. different nature of material removal in drilling than in laser machining, than in orthogonal cutting) and further, how is this influenced by the internal irrigation

condition of cortical bone. To achieve this, specific goals have been defined; these are listed below:

1. Understand the bone damage mechanism induced by machining in dry bone.
    1.1. Study the damage mechanism with two different material removal mechanisms, namely one that is mostly thermal (i.e. laser machining) and another one that is thermomechanical or mechanical (i.e. drilling). This enables the understanding of how the damage relates to the nature of the material removal method.
    1.2. Assess the bone damage following the machining processes. For this, damage must be assessed for both mechanical damage (i.e. surface topography, quality and cracks) and thermal damage (i.e. necrosis).
    1.3. Select one material removal method for an in-depth study of mechanical integrity post-machining and its relation to necrotic damage.
2. Understand the bone damage mechanism induced by machining (with the selected material removal method) in internally irrigated bone.
    2.1. Design and validate an adequate laboratory setup that enables ex-vivo bone cutting testing with an internally irrigated condition. Such a procedure/rig should be capable of mimicking surgery-room conditions by enabling fluid flow through the natural porosities of the bone.
    2.2. Study the material removal mechanism (e.g. chip formation process, cutting forces, temperatures) in internally irrigated bone and compare it to dry bone machining.
        2.2.1. Develop and validate a cutting forces mathematical model for bone cutting in an internally irrigated state.
    2.3. Assess the bone damage following the machining process in internally irrigated bone. For this, damage must be assessed for both mechanical damage

(i.e. surface topography, quality and cracks) and thermal damage (i.e. necrosis) and be compared to the damage obtained for dry bone.

A schematic representation of the structure of the thesis, which was developed to tackle all the previous objectives, is shown in Fig. 1.2.

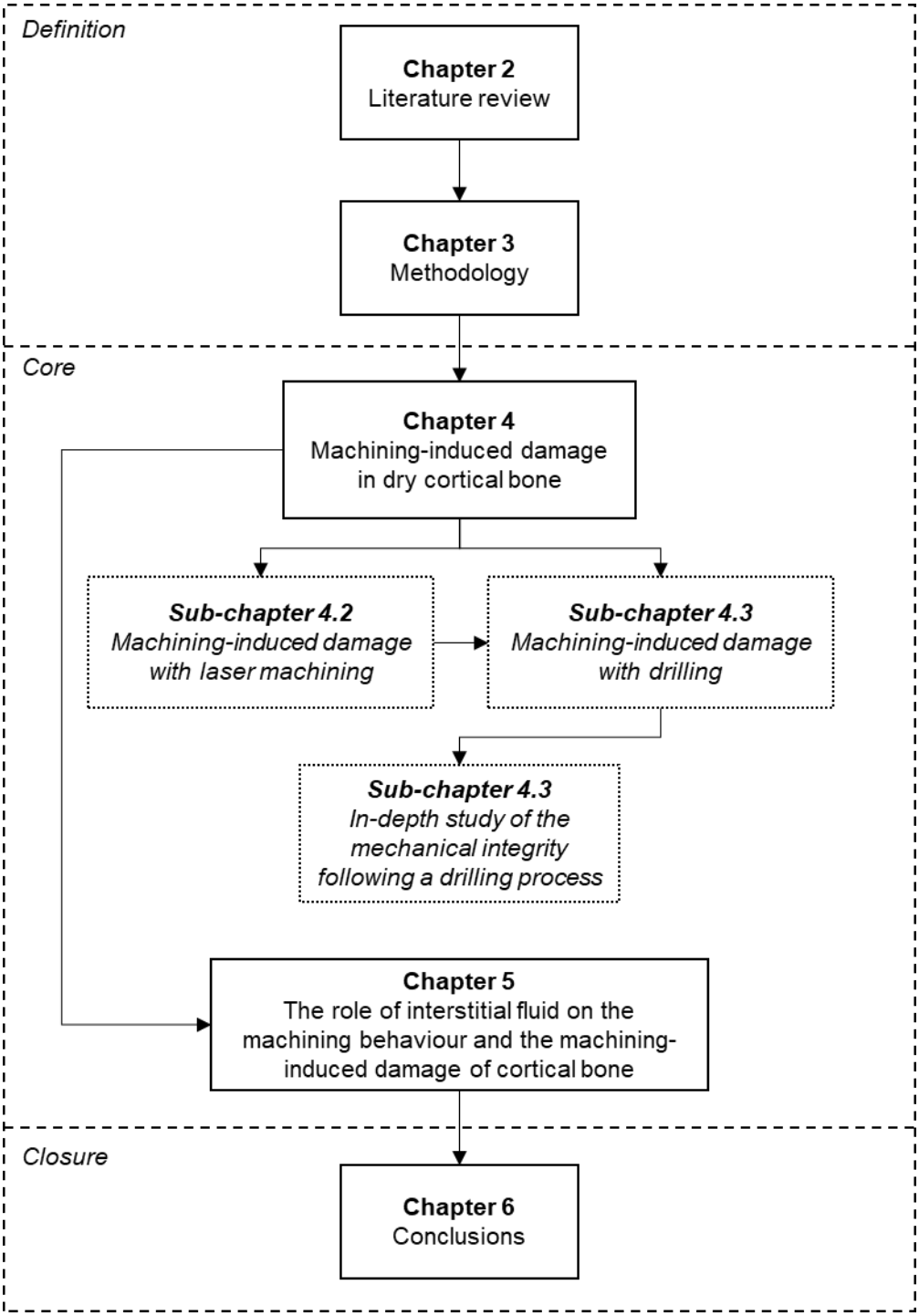

Fig. 1.2. Schematic structure of the thesis.

Chapter 2 - Literature review on bone machining and its surface integrity

Machining of bone has been studied since, roughly, the 1950s but it started gaining more scientific audience with the advance of manufacturing technology, which is why nowadays very complex surgical systems exist in clinical practice. However, to get here, vast amount of research had to be done to explore how bone, a natural anisotropic composite material, behaves in a machining environment not only with the plain analysis of experimental data towards optimisation of machining parameters, but to understand the nature of the material removal process to improve surgical tool design that minimises tissue damage.

In this chapter, the mechanical and biological structures of cortical bone are explained, and their most relevant properties are discussed. This is necessary because the material-related properties that govern the cutting mechanism of cortical bone are responsible for the machining forces, temperatures, and induced damage. As such, knowledge of the anisotropic structure, thermal properties and fracture mechanisms of bone is imperative for supporting the understanding of its cutting mechanisms Further, the material removal mechanisms from different machining techniques are described in-depth to provide a comprehensive understanding of the machining behaviour of cortical bone. Following this, the surface integrity of cortical following a machining process is also discussed, which is an important aspect for this research, as the main techniques (both mechanical and biological techniques) for bone damage assessment are explained. Finally, a summary of the literature is provided with the aim of highlighting the most relevant research gaps that have served to set the aims and objectives of this work.

2.1 The structure and properties of cortical bone

Hard tissues, also known as calcified tissues, are composed of inorganic matter (primarily comprising hydroxyapatite), organic matter (collagen) and water. From the point of view of material composition, hard tissues are a polymer-ceramic particle composite and have the properties of fibrous polymers (i.e. collagen) and ceramic nanoparticles (i.e. carbonated hydroxyapatite) (Peterlik et al., 2006). From the structural perspective, hard tissues possess a specific arrangement like the classic composite materials with unidirectional fibres immersed in a matrix. This directional microstructure contributes to the specific anisotropic characteristics, e.g. varied mechanical properties in different orientations, which has an important influence in the cutting process.

The microstructures of the cortical bone and cancellous bone (i.e. the two types of bone in the human body) are shown in Fig. 2.1. Each bone type has its unique *basic unit*, which is the equivalent to the fibre in a composite material. These are the osteon in cortical bone, and the trabeculae in cancellous bone.

Cortical bone has low porosity and high strength, whereas cancellous bone has a lower strength and a higher porosity (e.g. 79.3% vs. 3.5% of porosity in the human mandibular condylar bone (Renders et al., 2007), 105 vs. 19 MPa of yield strength for cortical bone and cancellous bone, respectively (Tu et al., 2013)) for the cancellous bone filled with bone marrow. Out of these two, cortical bone is of vast interest since it possesses a superior mechanical strength and density over trabecular bone, thus it is of major relevance when it comes to machining.

The osteon has a cylindrical structure of approximately 100–400 μm in diameter and a central Haversian canal with approximately 50 μm in diameter that carries the blood vessels and nerves (see Fig. 2.2). It is surrounded by concentric lamellae, and its length extends along the principal loading direction of the bone (COHEN and HARRIS, 1958), which is parallel to the main axis of long bones.

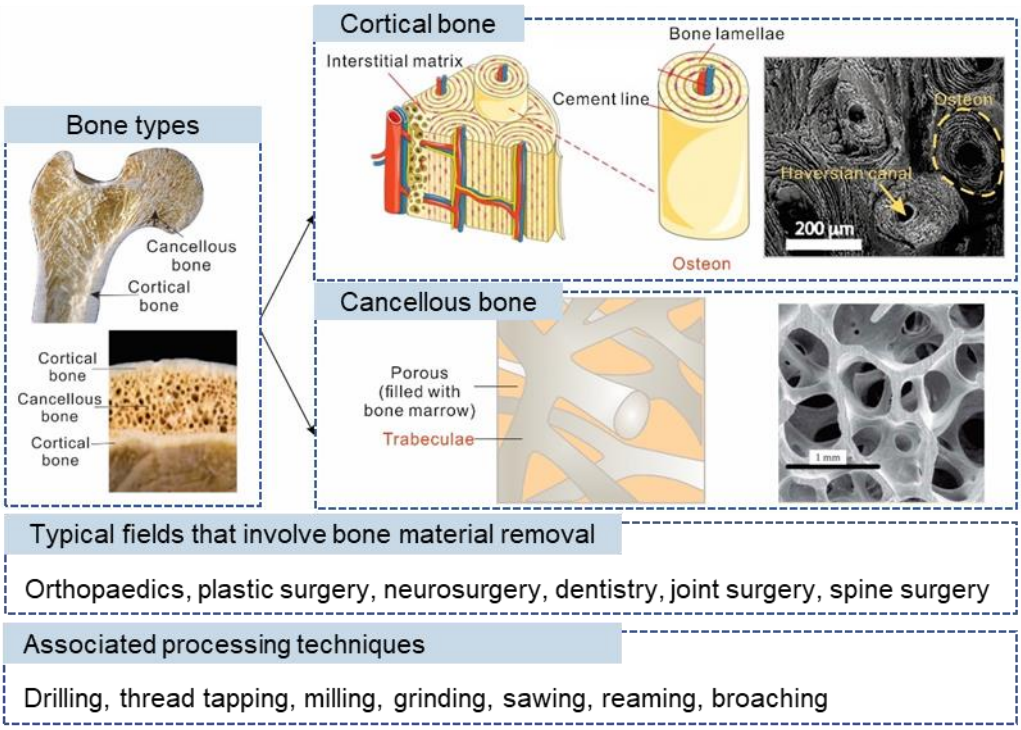

Fig. 2.1. Structure of the two types of bones in the human body, namely cortical bone (Bai et al., 2020; Zimmermann et al., 2014) and cancellous bone (Ritchie et al., 2009). Their associated types of surgeries and processing techniques are listed.

Cortical bone is a highly heterogeneous structure. For instance, interstitial matrixes are interspersed between osteons, and an interface sheath is present between the osteon and interstitial matrix, called the cement line. This interface is denser and plays an important role in the generation and propagation of microcracks during machining (Liao and Axinte, 2016a), which will be discussed later.

As a biological tissue, bone possesses a cellular structure with three main types of cells that keep bone in its living state with appropriate metabolism and remodelling (i.e. capacity to heal itself over time) functions. Osteoclasts and osteoblasts, which are located in the surface of the bone, are the two cells that perform the remodelling process of the bone (i.e. they are responsible of absorbing old or damaged bone and depositing new bone). Osteocytes (see Fig. 2.2b) are a mature form of osteoblasts that are trapped inside the bone in pits called lacunae; these cells act as sensors that monitor the metabolism and remodelling functions of the bone (Hancox, 1972). These cells, altogether, keep the bone in a healthy state and aid in the healing process after the

tissue is exposed to damage (e.g. by machining-induced mechanical and/or thermal loads).

Bone is a tissue that is kept in a living state due to blood flow (Laroche, 2002). In cortical bone, the Haversian and Volkmann's canals contain blood vessels that carry blood with a pressure of 40-60 mmHg (Cowin and Cardoso, 2015). These vessels are 29±14 μm in diameter (Conward and Samuel, 2016) and their blood flow rate depends on the human heart's cardiac output; but it has been shown that between 10% - 15% of this output distributes within the 206 bones in the human body (Tomlinson and Silva, 2014); however, most of the literature assures that intraosseous blood flow rate for a healthy person is within 5-20 ml/min per 100 g of bone (Laroche, 2002).

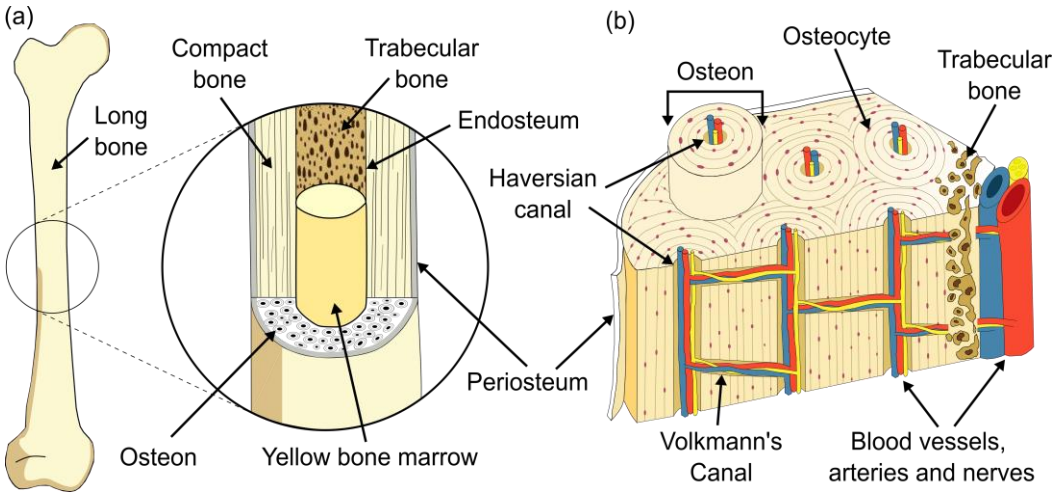

Fig. 2.2. Schematic overview of the bone structure. (a) A long bone possesses two main tissues, i.e. cortical bone in the outermost region and trabecular bone in the innermost region, which encloses the yellow bone marrow. (b) The cortical bone microstructure consists of osteons that run along the principal loading direction of the bone and are immersed in the interstitial lamellae. Inside the cortical tissue two main porosity systems (Haversian and Volkmann's) carry the necessary blood vessels and nerves for maintaining a healthy tissue. The osteocytes (shown as purple dots) are the cells that monitor the metabolism and remodelling process of the tissue. Schematic adapted from (Robles-Linares et al., 2019).

Long bones have three blood supplies: 1) the multiple metaphyseal – epiphyseal vessel complex at the ends of the bones 2) the nutrient artery entering at the diaphysis and 3) the periosteal vessels. However, the main supply comes from the nutrient artery, which

after entering thru the diaphysis it is divided into ascending and descending smaller blood vessels that run thru the Haversian and Volkmann's canals (Cowin and Cardoso, 2015). Fig. 2.2b shows the micro-vessels distribution and arrangement in the cortical bone tissue.

The hierarchical structure, porosity, presence of body fluids and living cells contribute to the anisotropic behaviour of bone (e.g. varied mechanical properties in different orientations) and its thermal response, and hence influence the machining processes. Therefore, machining of bone is intricate due to:

1) Brittle or semi-brittle behaviour of the tissue
2) Orthotropic mechanical properties
3) Highly heterogeneous structure including fibre, matrix and porosity
4) Thermal sensitivity and living cells regeneration capacity
5) Presence of body fluids including blood, bone marrow or others.

2.1.1 Fracture mechanisms of cortical bone

Owing to the brittle nature of hard tissues, microcracks and fractures are usually formed at weak interfaces and easily occur in machining (Sugita et al., 2009a). Therefore, the fracture characteristics and mechanisms of hard tissues are of great significance to the processing theory. Fracture toughness is determined by both the tissue composition and its ability to dissipate deformation energy without the propagation of microcracks. Four different toughening mechanisms, including crack deflection and twist, uncracked-ligament bridging, fibril bridging and constrained microcracking are identified in hard tissues (Fig. 2.3) (Peterlik et al., 2006; Ritchie et al., 2009; Zimmermann et al., 2010). Crack deflection and crack blunting, well known from composites, is attributed to the hyper-mineralised interfaces of the basic units (i.e. cement lines), which provides a microstructurally "weak" pathway. Uncracked

ligament bridging in the weak zone, well-known in ceramics, is an unbroken region formed between a main growing crack and another that initiated ahead of it and thus can carry a large amount of load without propagating the main crack. Fibril bridging, well-known in polymers, is attributed to the unbroken collagen fibrils that bridge the gap formed between a crack and rely on the viscoplastic flow for the dissipation of energy. The formation of microcracks in the vicinity of the developing primary crack compresses the main crack due to stress concentration ahead of the crack tip (Peterlik et al., 2006). However, the magnitude of the effect of each of these toughening mechanisms on the fracture toughness differs. For example, the fracture toughness increase of bone caused by the four toughening mechanisms is 3-20, 1-2, 0.1 or 0.05 MPa×$m^{1/2}$, respectively (Ritchie et al., 2009).

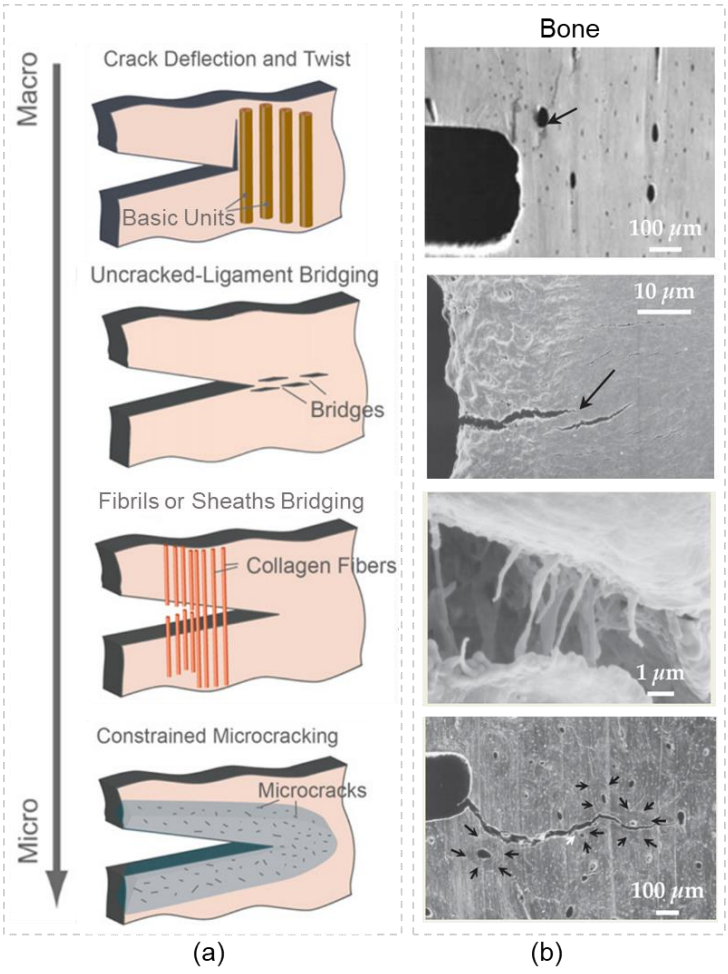

Fig. 2.3. The toughening mechanisms in cortical bone. (a) Schematic diagrams of four toughening mechanisms (Zimmermann et al., 2010). (b) Toughening phenomenon in bone (Ritchie et al., 2009).

Many studies have pointed out the fracture mechanism of cortical bone is related to its anisotropic layered structure. Fractures and microcracks are easier to initiate and propagate along the interface of the matrix or following the cement line because the interface surrounding the osteons is mechanically weaker than the surrounding regions and they require less energy when compared with cracking through the osteon. The Young's modulus (*E*) of interstitial lamellae, cement line and osteon is 14.60, 10.12 and 13.50 GPa, respectively (Idkaidek et al., 2018; Koester et al., 2008; Taylor and Lee, 2003; Zimmermann et al., 2011). Therefore, microcracks propagated along the cement lines can be found in transverse direction (TD), parallel direction (PD) and across direction (AD) (Fig. 2.4), hardly penetrating the osteon in all three directions. The multiple in-plane crack deflections of approximately 90° at the cement line in TD results in osteon pull-out and tortuous crack paths (Koester et al., 2008; Yan et al., 2006). A relatively straight path and a slight tortuous form of microcracks extend among matrix or along cement line are generated in PD and AD, respectively (Koester et al., 2008; Tang et al., 2015). Rough fracture surfaces are more easily generated in TD and AD rather than in RD (Mohsin et al., 2006; Ritchie et al., 2009) due to this reason. About 9920 J/m^2 are required when the angle between fibrils and crack propagation direction is 90°, which is nearly two orders of magnitude than the energy needed to propagate in the direction of the fibril (375 J/m^2) (Peterlik et al., 2006). Therefore, the fracture toughness in TD is significantly greater than that in the other two directions (Table 2.1), and a significantly larger driving /cutting force will be required during machining when cutting along the transverse direction.

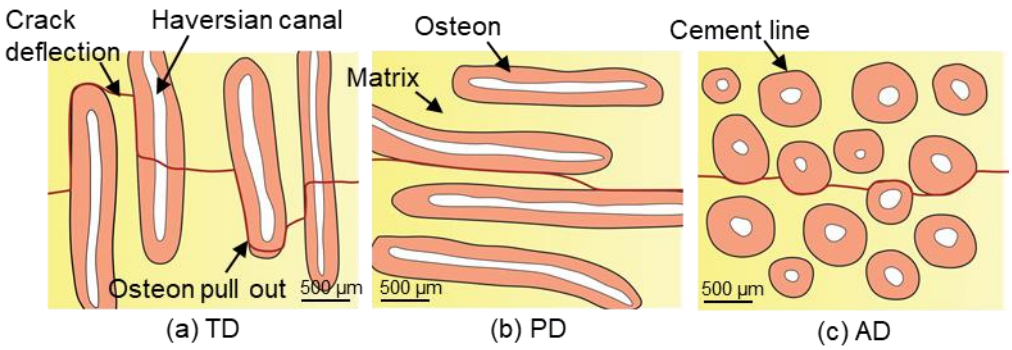

Fig. 2.4. Schematic diagrams of crack propagation in different directions in cortical bone. (a) Microcrack deflection along the cement line in cortical bone in TD, (b) microcrack propagation in the straight path along the matrix or along the cement lines in cortical bone in PD, (c) microcrack deflection and propagation along the cement line in cortical bone in AD (Koester et al., 2008; Ritchie et al., 2005).

In addition to the direction dependency, the fracture mechanism of cortical bone is also strain rate dependent, exhibiting a high sensitivity in the middle strain rate regime of 0.1 s^{-1} to 250 s^{-1} (Bekker et al., 2015). The fracture toughness diminishes by roughly 33% as the strain rate increases from 10^{-5} to 0.01 s^{-1}. At low strain rates of 10^{-5} to 10^{-3} s^{-1}, the fractured surface is rough with a tortuous fracture path with numerous twists and deflections, while the crack defection mechanisms along the cement line appears to be less effective (Zimmermann et al., 2014). The influence of strain rate on fracture properties directly effects the crack generation and fracture surfaces and selection of cutting speed, because these characteristics directly determine the strain rate during cutting of bone.

The fracture toughness of bovine femur was also found to decrease from 7.0 to 4.3 $MPa \times m^{1/2}$ as the temperature increased from 0 °C to 50 °C (Yan et al., 2007). In addition to structure, strain rate and temperature, the porosity, mineral density, species, skeletal area and subject age (Ritchie et al., 2009) also alter the fracture toughness of hard tissues and should be considered when investigating their cutting mechanisms (Greenwood et al., 2015; Tomar, 2009; Yeni et al., 1997).

Table 2.1. Toughness of cortical bone from human (Ritchie et al., 2005) and bovine (Adharapurapu et al., 2006) species.

Species	Directions	K_c (MPa×m$^{1/2}$)	Notes
Human	TD	5.3	-
	PD	3.5	-
	AD	2.2	-
Bovine	PD	3–6	Low strain rate: 2×10^{-2}–0.7×10^{2} s^{-1}
		1–2	High strain rate: 2×10^{5} s^{-1}

2.1.2 Thermal properties and thermal damage in machining of cortical bone

Thermal behaviours are difficult to study because they are sensitive to test conditions, specimen preparation and anisotropic behaviour. Two important thermal properties of the bone are specific heat capacity and thermal conductivity. Contrary to the anisotropic mechanical properties of bone, the thermal properties show an insignificant difference due to orientation and as such, both the thermal conductivity and specific heat capacity are treated as isotropic. However, the bone species does have an impact on the variation of thermal properties (Table 2.2).

Table 2.2. Thermal properties of cortical bone from human (Lundskog, 1972) and bovine (Feldmann et al., 2018) species.

Species	Specific heat capacity (J/ (kg×K))	Thermal conductivity (W/(m×K))
Human	1260	0.68 ± 0.01
Bovine	1216 ± 60	0.64 ± 0.04

A slight difference between human and bovine cortical bone exists. Apart from the slight anatomical disparities of bone between different species, the difference and precision of the measurement apparatus could also be the reason for the deviation

between two samples from different species (Davidson and James, 2000; Feldmann et al., 2018).

Heat generation is inevitable for the material removal and contact friction during hard tissue machining. The tool's cutting action on hard tissue creates the shear and fracture in material removal, which breaks the intermolecular bonds and releases the energy in the form of heat (Fig. 2.5). The friction from the non-cutting surfaces of the rake and flank face of tool acts as additional heat sources (Augustin et al., 2012). Different from metal drilling in which the chips carry away nearly 85% or more of the heat, only a small percentage of the heat is taken away by chips in hard tissue drilling due to its poor thermal capacity and conductivity (Augustin et al., 2012; Karmani, 2006).

Owing to the biological nature of hard tissues, if a critical temperature is withheld for a specific time duration during machining, thermal damage is induced and will affect the cellular functions, such as the natural remodelling process, of the hard tissue (Dolan et al., 2012). The thermal damage may spread to surrounding soft tissue, such as the neurovascular bundles, and result in collateral tissue injury (Fig. 2.5). Bone thermal damage (i.e. necrosis) can occur at a temperature of 47 °C for 1 min, resulting in hindered bone growth after implant collocation (Augustin et al., 2008). However, the precise threshold temperature and the specific time duration for thermal damage of bone remain unclear. Understanding the thermal aspect is important to optimise the bone machining processes for minimum thermal damage. The types of mechanical, thermal and thermomechanical damage, the effect of cutting parameters on damage, and the way to detect these damage will be discussed further.

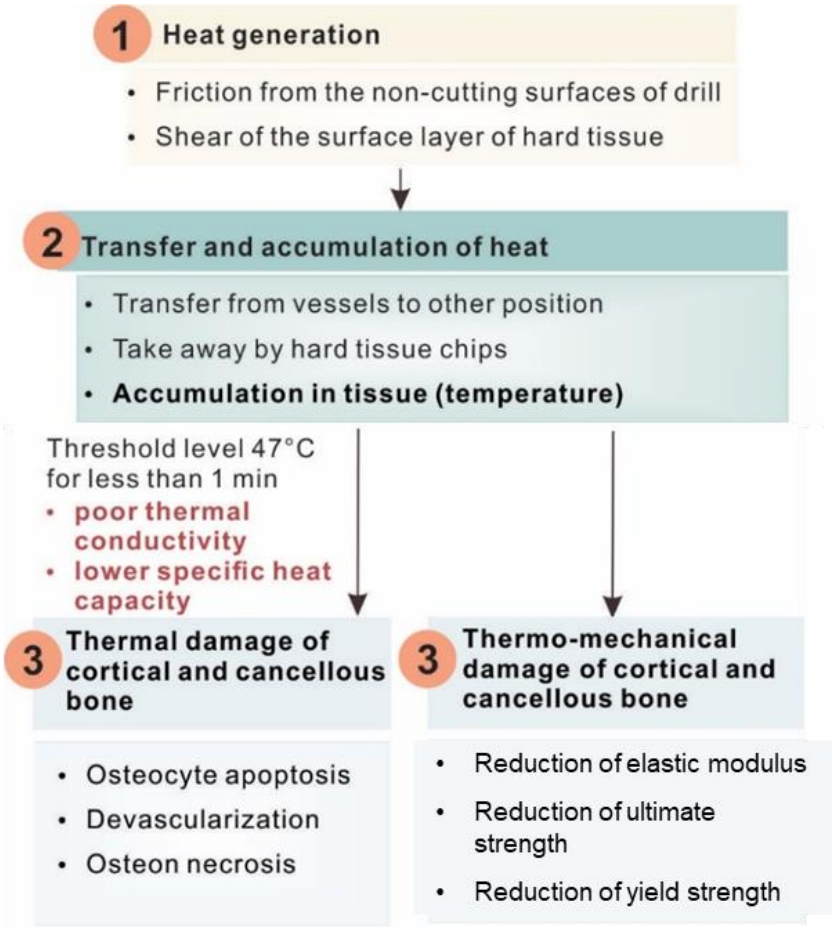

Fig. 2.5. Schematic flow chart of heat generation and thermal damage in bone machining.

2.2 Material removal mechanisms in cortical bone

The intrinsic structure and properties of hard tissues determine their complex material removal mechanisms in machining and damage inducement, such as cracks and necrosis. Understanding the material removal mechanisms of cortical bone, including chip formation processes and predictive models of forces and temperatures, serves as a fundamental guideline for improved tool design and machining systems for surgical equipment. Thus, this section covers the usual material removal techniques (both conventional and non-conventional) of cortical bone.

2.2.1 Conventional machining techniques

Cortical bone's natural anisotropic and composite-like structure makes it an intricate material for machining analysis. Key conventional machining operations in surgery include drilling, milling, sawing and grinding. In a research environment, these operations are studied with the primary concerns being heat transfer and thermomechanical analyses that may affect the material's integrity in terms of thermal and mechanical damage. Additionally, orthogonal cutting is a simplified scenario which can provide good interpretations of the force-chip formation and has been studied extensively. Heat transfer, fracture propagation and chip flow processes during bone cutting are critical for understanding the overall tissue behaviour in surgery because they directly affect surface quality (Liao et al., 2017; Liao and Axinte, 2016a) and necrotic damage (Franssen et al., 2008; Karaca et al., 2011) of the bone as well as are directly related to the contact integrity of the tissue-implant interfaces (Childs and Arola, 2011).

2.2.1.1 Orthogonal cutting of cortical bone

Cortical bone possesses a complex hierarchical and anisotropic structure that inherently results in a direction-dependent machining behaviour, i.e. in relation to the osteon's principal orientation. The cutting force, temperature and chip morphology are dependent on the cutting process parameters and direction. Three principal cutting directions can be identified as parallel, across and transverse. In parallel cutting, osteons' axes are parallel to the feed direction (Fig. 2.6a), in across cutting, the osteons' axes are normal to both the feed and thrust directions (Fig. 2.6b), and in transverse cutting, the osteons' axes are perpendicular to the feed direction and parallel to the thrust direction (Fig. 2.6c). As it will be shown further, these principal directions in cortical bone have a direct correlation with the main cracking orientations from Fig. 2.4.

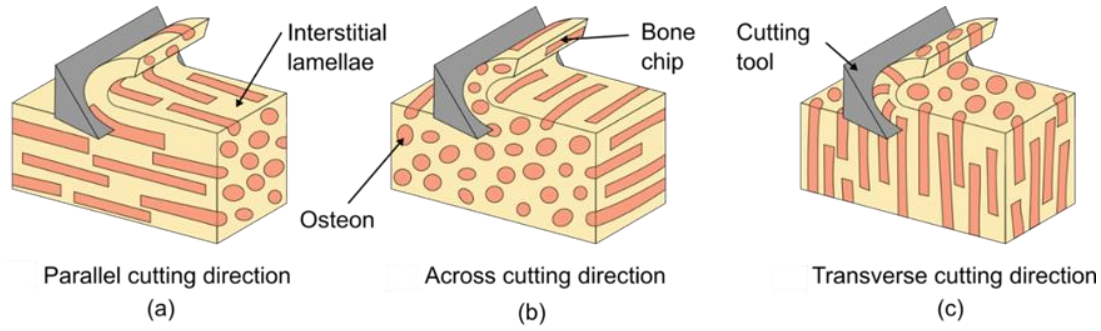

Fig. 2.6. The three principal cutting directions in orthogonal cutting of cortical bone: (a) parallel direction (PD); (b) across direction and; (c) transverse direction (TD).

During orthogonal cutting, various chip formation mechanisms exist, depending on the cutting direction (Fig. 2.6) and machining parameters, particularly the depth of cut (DOC). Owing to the semi-brittle nature of cortical bone, a ductile-to-brittle behaviour transition exists as a response to the increase in DOC. Three chip formation mechanisms or modes have been identified: shear cutting (SC), shear-crack cutting (SCC) and fracture cutting (FC) (Fig. 2.7).

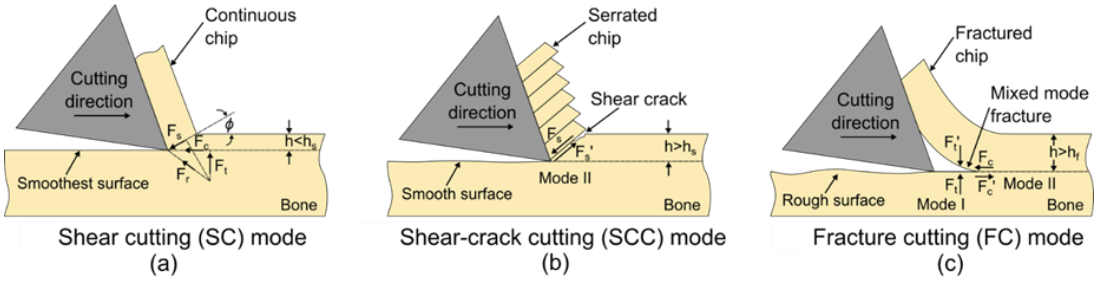

Fig. 2.7. The three cutting mechanisms in cortical bone. (a) SC at small DOC ($h<h_s$), the cutting behaviour is ductile, thus resulting in a continuous chip in compliance with the metal cutting theory. (b) SC at intermediate DOC ($h>h_s$), the shear force induces an energy release rate along the shear plane which overcomes the Mode II fracture toughness of the bone, thus resulting in a shear-crack along the shear plane. (c) FC at the greatest values of DOC ($h>h_f$), the cutting behaviour is brittle because the thrust and cutting forces contribute to overcoming the mixed Modes I and II fracture toughness (Liao and Axinte, 2016a).

The SC mode (Fig. 2.7a) occurs at small DOC (usually lower than 13 µm) in bone cutting. In this mode, the cutting forces produce energy along the shear plane that is smaller than the Mode II in-plane shearing fracture toughness of the bone. The energy is mostly used for crack-free plastic deformation of the chip (Feldmann et al., 2017) and, as consequence, only a continuous chip is produced (Fig. 2.8a,d,g), corresponding

to a shear-driven ductile cutting mode that is in compliance with the classic Ernst-Merchant theory (Sugita and Mitsuishi, 2009). In this mode, at a given DOC, the continuous chip tends to curl at a constant angle, where the curling radius varies depending on the cutting direction.

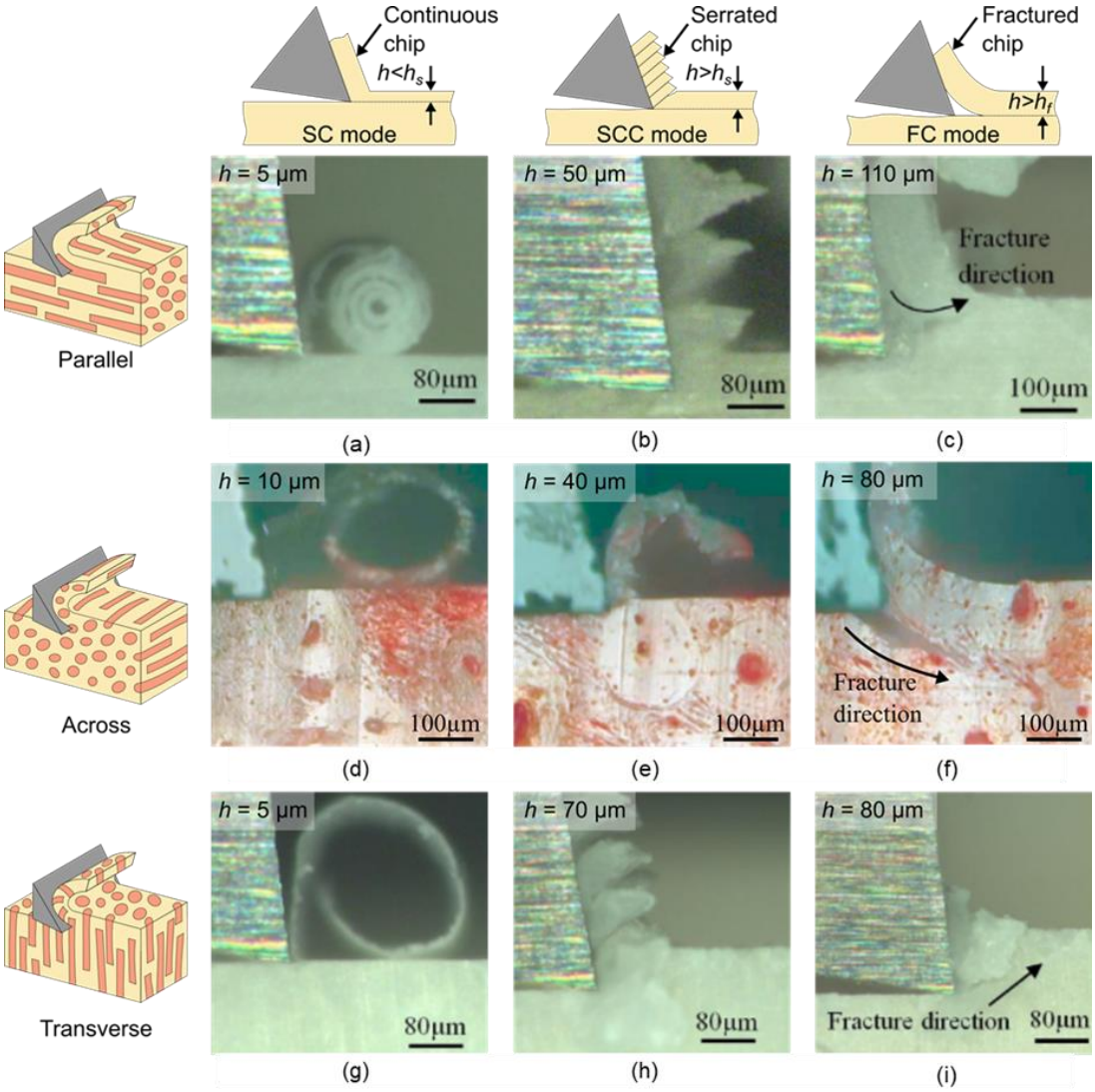

Fig. 2.8. Chip formation as observed under optical microscopy in (a–c) parallel, (d–f) across and (g–i) transverse cutting directions. (a,d,g). At small DOC, SC dominates the process and results in a continuous chip because the energy along the shear plane remains below the fracture toughness of the bone. (b,e,h) Increasing the DOC to intermediate values results in overcoming the fracture toughness (Mode II) in the shear plane, thereby producing an SCC mode characterised by a serrated chip. (c,f,i) Cutting at greater DOC produces an FC mode in which both the thrust and cutting forces contribute to crack propagation. Microscopy images from (Liao and Axinte, 2016a; Sugita and Mitsuishi, 2009).

The SCC mode (Fig. 2.7b) dominates the bone cutting process under intermediate DOC (usually 13–70 μm). In this mode, the larger chip volume hinders plastic deformation and, as a result, the cracking process is enabled (Feldmann et al., 2017). The chip material firstly flows along the shear plane and then is blocked on the free surface, allowing for energy accumulation along the shear plane to take place. Secondly, the induced energy overcomes the fracture toughness of the bone just enough to generate the Mode II fracture along the shear plane (Liao and Axinte, 2016a), resulting in a semi-continuous chip that flows under a brittle regime and gives the appearance of a shear-crack or serrated shape (Fig. 2.8b,e,h). The chip formation at intermediate DOC is consistent with the observations provided on the earliest bone cutting studies provided by Jacobs et al. (Jacobs et al., 1974) and Krause (Krause, 1987), in which they describe a segmented chip morphology that slightly varies depending on the cutting direction and remains consistent for various rake angles and cutting speeds.

The FC mode (Fig. 2.7c) dominates the bone cutting process with the largest (greater than 70 μm) DOC. In this mode, an even larger chip volume is cut, enabling a full fracture mechanism to occur**.** This was first reported by Wiggins and Malkin (Wiggins and Malkin, 1978), where they showed, generally, that the main fracture direction matched the cutting direction. As opposed to SC and SCC modes where the shear force dominates the inducement of energy, in FC, the larger cutting and thrust forces are more significant and both contribute to the fracture formation along the feed direction (Liao and Axinte, 2016a). In FC mode, the energy provided by the cutting and thrust forces is sufficiently large to overcome the mixed Modes I and II fracture toughness and results in a large crack generated, mainly, along the feed direction (Fig. 2.8c,f,i and Fig. 2.4a-c). Nevertheless, the fracture propagation direction is strongly dependent on the cutting direction relative to the osteon orientation (Fig. 2.9), where the cement line serves as a guide for crack propagation (Santiuste et al., 2014).

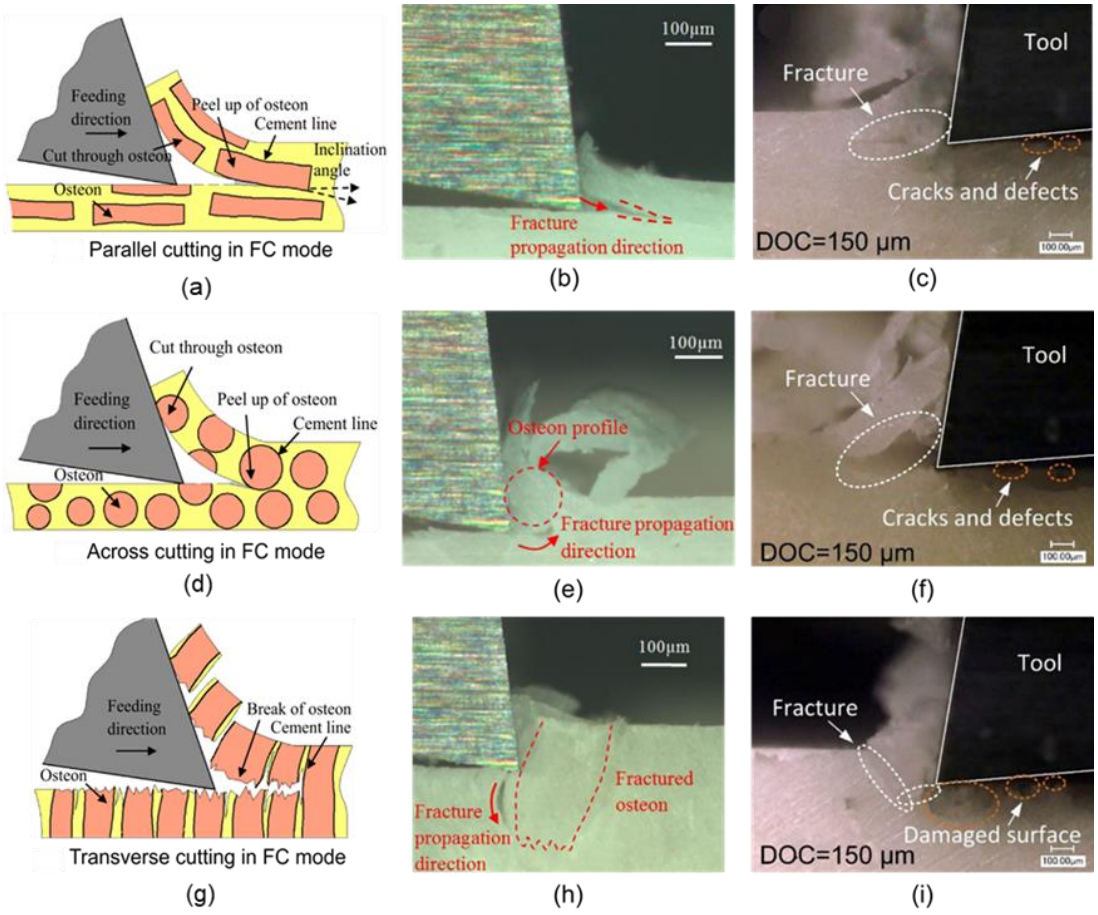

Fig. 2.9. Fracture propagation when cutting at large DOC (i.e. DOC > h_f, FC mode), for the three orthogonal cutting directions: (a–c) parallel, (d–f) across and (g–i) transverse. In general, the fracture tends to propagate along the cutting direction, but will also propagate upwards or downwards into the bone by following the cement line of the osteon being cut, due to the low toughness that it possesses (i.e. as opposed to the tougher structures that the osteon and the interstitial lamellae are). Schematics and microscopy images from (Bai et al., 2020; Liao and Axinte, 2016a).

Given a transition between cutting modes, the shear stress and friction coefficient during the cutting process are not exclusively dependent upon the cutting direction but on the DOC as well. The friction coefficient can be expressed as $\mu = \mu_0 h^C$, where μ_0 and C are experimental calibration constants and h is the DOC (Liao et al., 2019). Similarly, the specific cutting energy is maximum while in the SC mode and it transits to a minimum when cutting in the FC regime, as shown in Fig. 2.10 for the case of transverse cutting. This occurs due to the main failure mechanism: in SC mode, where large friction takes place (Liao and Axinte, 2016a), a large amount of energy is required for producing the plastic flow behaviour that produces the continuous chip.

However, when increasing the DOC and transiting through SCC and FC modes, cracks and fractures occur, thus resulting in a reduction of energy per unit volume of the chip. While the specific cutting energy could be regarded as a relative measure of the associated cutting temperature (Wiggins and Malkin, 1978), the fact that different cutting modes are present highlights the need for a distinction for each mode. For instance, when cutting in the SC regime, all the energy is dissipated as plastic deformation and heat, but when cutting in the FC mode, energy is also dissipated by fractures. The study by Feldmann et al. (Feldmann et al., 2017) has shown that, generally, temperature in the bone workpiece increases with DOC due to the growth in cutting force.

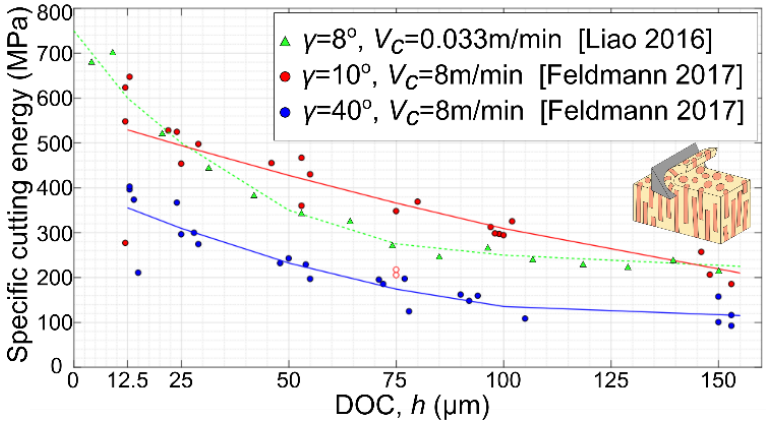

Fig. 2.10. Specific cutting energy respect to depth of cut (DOC) when cutting in the transverse direction (Feldmann et al., 2017; Liao and Axinte, 2016a). In SC mode, plastic flow dominates the process and enables a continuous chip, for which a large amount of energy per unit volume is required. When increasing the DOC and enabling the occurrence of cracks and fractures, the energy is reduced.

Fracture mechanics can be employed to mechanistically model the mean cutting forces and chip morphology. The chip formation mechanism transits from the continuous chip under a dominant SC mode to a segmented chip under a dominant SCC mode when the shear force produces an energy release rate in the shear plane that exceeds the critical release rate of the Mode II fracture (G_{IIC}) of the bone (Liao and Axinte, 2016a). When the DOC (h) exceeds the threshold value of h_s, the cutting mode will transit from SC to SCC (Eq. 2.1). Following this, the larger increase in the DOC will

allow for a transition of cutting modes from SCC to FC due to the larger thrust and cutting forces that contribute to overcoming the energy release rate of the mixed Modes I and II fracture ($G_{(I+II)C}$) of the bone. Thus, when the DOC is larger than the threshold value of h_f, the cutting mode will transit from SCC to FC (Eq. 2.1) (Liao and Axinte, 2016a):

$$h\begin{cases} < h_s & \text{where } h_S = \dfrac{G_{IIC,i}\sin\phi_i}{\tau_{sc,i}} & \rightarrow \text{SC mode} \\ > h_s & & \rightarrow \text{SCC mode} \\ > h_f & \text{where } h_f = \dfrac{\dfrac{G_{(I+II)C,i}\sin\phi_i\cos(\phi_i+\lambda_i-\alpha)}{\cos(\lambda_i-\alpha)+\sin(\lambda_i-\alpha)\tan\phi_i}+G_{IIC,i}\sin\phi_i}{\tau_{scc,i}} & \rightarrow \text{FC mode} \end{cases} \quad \text{Eq. 2.1}$$

where ϕ is the shear angle, τ_{sc} is the ultimate shear strength in the SC mode, λ_i is the friction angle, α is the rake angle, τ_{scc} is the ultimate shear strength in SCC mode and i = 1, 2 and 3 denotes the cutting direction (1 for parallel, 2 for across and 3 for transverse). This model was validated at low cutting speed (0.033 m/min) with an 8° rake angle (Liao and Axinte, 2016a). However, even if the rake angle can have a significant effect in the bone machining behaviour (even more than the cutting speed (Sui et al., 2013)), the study by Feldmann et al. (Feldmann et al., 2017), which was conducted at a more surgically relevant cutting speed (8 m/min), shows consistency with this mechanistic model for increasing rake angles (from 10° to 40°).

In addition to mechanistic modelling, finite element method (FEM) has also been explored to study the chip formation mechanisms (SC, SCC and FC) in orthogonal cutting of cortical bone (Takabi and Tai, 2017). In FEM modelling of metal cutting, the material constitutive models, such as the Johnson–Cook (JC) model, have been adapted to fit the material behaviour of bone. For instance, Childs and Arola (Childs and Arola, 2011), via a pressure-dependent yield stress model, simulated the chip formation mechanism in ductile (Fig. 2.11a, SC mode), transition (Fig. 2.11b, SCC mode) and brittle (Fig. 2.11c, FC mode) manner by adding a limited ductility to the material flow model. Such simulation was done by considering a pressure dependence of the flow stress, where a larger coefficient of pressure dependence resulted in a more

brittle behaviour. All the cutting modes (SC, SCC and FC) can be produced for the same DOC, depending on the coefficient of pressure dependence that is used, which drives the damage accumulation; thus, it could yield misleading results. This type of models can be adapted by giving the bone different isotropic properties based on the location, e.g. different properties for the osteon than for the interstitial lamellae.

Isotropic material models, however, lack the consideration of the intricate structure of hard tissues, so micro-FEM can be used to try to understand the cutting mechanisms. With this technique, the microstructure effect can be accounted for (Hage and Hamade, 2013) by means of the micro-FEM (Fig. 2.11d-f), i.e. FEM modelling with different properties for each micro-constituent of the bone, i.e. osteon, interstitial lamellae, cement line, which requires proper mapping of the cutting sample (Fig. 2.11d,e) or stochastic consideration of the cortical bone microstructure.

Another FEM approach (Santiuste et al., 2014) is to assign anisotropic properties (e.g. an average value of properties in each cutting direction, depending on the osteon's long axes position) with elastic behaviour up to failure using the Hou damage criteria (Hou et al., 2000), a technique widely used in fibre-reinforced composite materials. The latter FEM (Fig. 2.11c) could yield different chip morphologies, degrees of segmentation on the chip, temperatures and cutting forces based on the cutting parameters. However, the relationship between material properties, e.g. shear strengths, coefficients of friction, toughness, and DOC has not been included in the FEM technique. This means that finer tuning is required for improving the relationship between FEM simulation and experimental data not only with mean values of force and temperature, but also in chip morphology and forces variations. The anisotropic modelling at the macroscale has seen closer-to-reality cutting force simulations when compared with isotropic or micro-FEM modelling tactics (Baro and Deoghare, 2018).

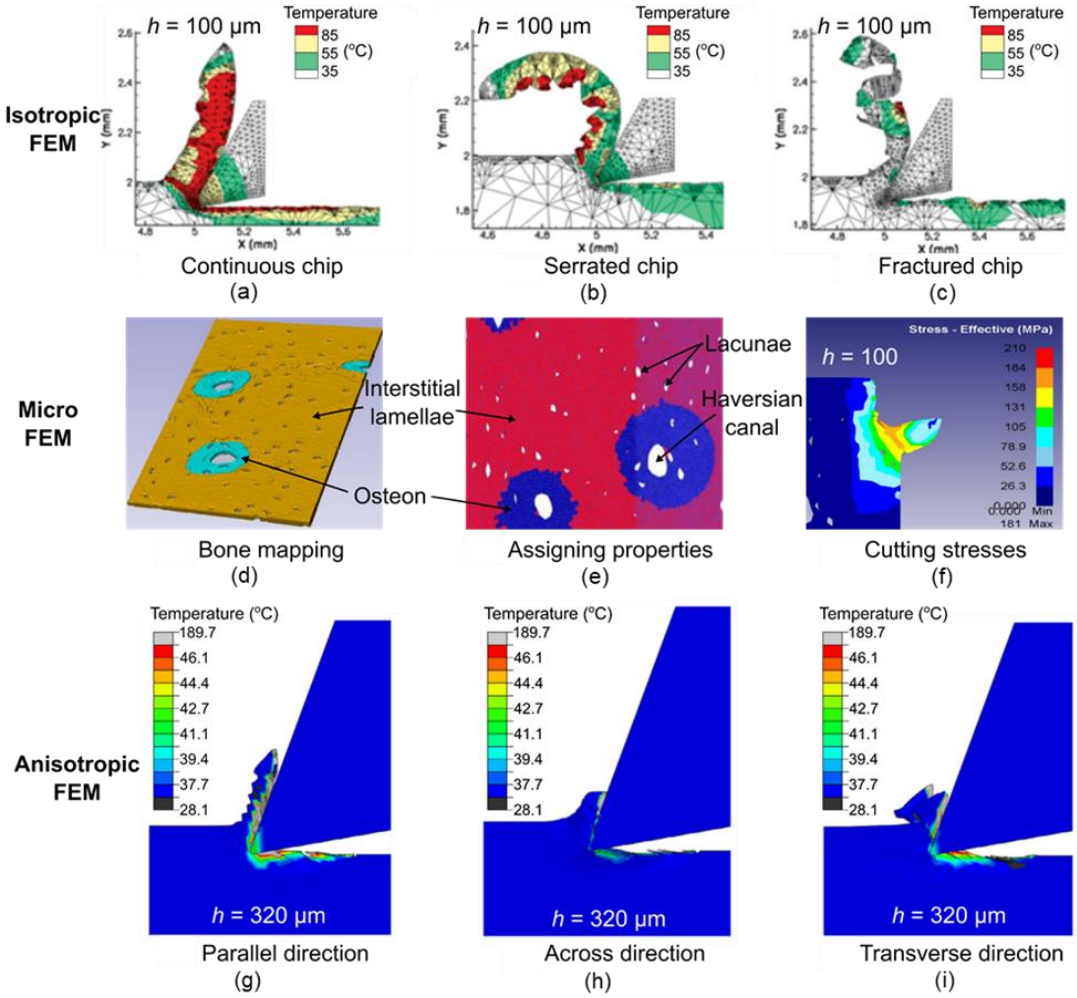

Fig. 2.11. FEM approaches for numerical modelling of orthogonal cutting of cortical bone: (a–c) Chip flow and thermal field as obtained from an isotropic metal-cutting FEM consisting of a pressure-dependent yield stress criterion. This was adapted to the bone material by introducing a ductility by ranking, producing (a) continuous, (b) serrated and (c) fractured chips (Childs and Arola, 2011) for a constant DOC, *h*. (d–f) Micro-FEM model consisting of (d) mapping the bone sample, (e) assigning different mechanical properties to each microstructure and (f) using the JC model in metal-cutting FEM to evaluate cutting stresses and chip morphology (Hage and Hamade, 2013). (g–i) Chip flow and thermal field as obtained from an anisotropic FEM. In this case, the model yields different chip formation and thermal fields depending on the cutting direction (Santiuste et al., 2014): DOC of 320 µm reflects a continuous chip in (g,h) and semi-continuous in (i), while in all cases the chip morphology should reflect a fracture-dominant mechanism due to the large DOC.

The study of orthogonal cutting of cortical bone enables the understanding of the basic cutting mechanisms in this material, which further aids in the understanding of more complex machining methods. For instance, sawing of bone, a machining method widely employed in surgeries, consists of in-series teeth within a blade that enable

cutting small amounts of bone. However, the cutting process of bone sawing could be simplified as orthogonal cutting for each individual tooth, where the cutting direction is orthogonal to the tooth's cutting edge (Dahotre and Joshi, 2016). Similarly, vast number of studies have rather focused on drilling, milling and grinding, which are discussed in detail next.

2.2.1.2 Drilling of cortical bone

Considering that bone drilling is a popular surgical procedure, it is the most studied bone cutting process (Shih et al., 2019). Owing to the low thermal conductivity of the bone and the closed spatial thermal boundary in the drilling process, heat is easily built up in the tool-bone interface. Given that temperature control is crucial for avoidance of necrosis, the drill design must be tailored to minimise bone temperatures and drilling forces. Many experimental studies have focused on researching the aspects, such as drilling parameters and drill design, that most significantly affect the temperature build-up. Studies have also aimed at the development of mathematical and numerical models for the prediction of forces and temperatures, observation and classification of chip morphology and finding the relationship between drilling forces and thermal fields, thereby optimising the drilling conditions for reducing the mechanical and thermal damage.

Owing to the intrinsic composite-like structure of cortical bone with anisotropic behaviour, drilling represents a more intricate process as opposed to orthogonal cutting. During drilling, two main feed directions are radial and axial (Fig. 2.12, relative to the osteons' principal orientation. The cutting direction, i.e. parallel, across or transverse with respect to the osteons (Fig. 2.6) varies along with the drill rotation. In a single revolution, an analogy can be made from drilling to orthogonal cutting; thus, in one revolution the cutting lips cut in all three cutting directions as a function of the drill rotation angle relative to the osteon's principal orientation, as shown in Fig.

2.12. At the starting rotation angle (e.g. 0°, Fig. 2.12b), the cutting lips will only be engaged in the orthogonal parallel cutting direction (Fig. 2.12c). However, after a 90° rotation (Fig. 2.12d), the lips will now be engaged in both the across (Fig. 2.12e) and transverse (Fig. 2.12f) cutting directions. The tool will continue its revolution by respectively alternating between these three orthogonal cutting directions, thereby resulting in a combined cutting action. Furthermore, the drill point angle creates an offset angle in the cutting plane, which results in the osteons being cut at non-perpendicular planes with respect to the feed direction (Cseke and Heinemann, 2018). In drilling, the cutting direction will move back and forth between the three main cutting directions, i.e. parallel, across, transverse, due to the drill rotation, thereby producing a mixed cutting effect between all the three main cutting directions.

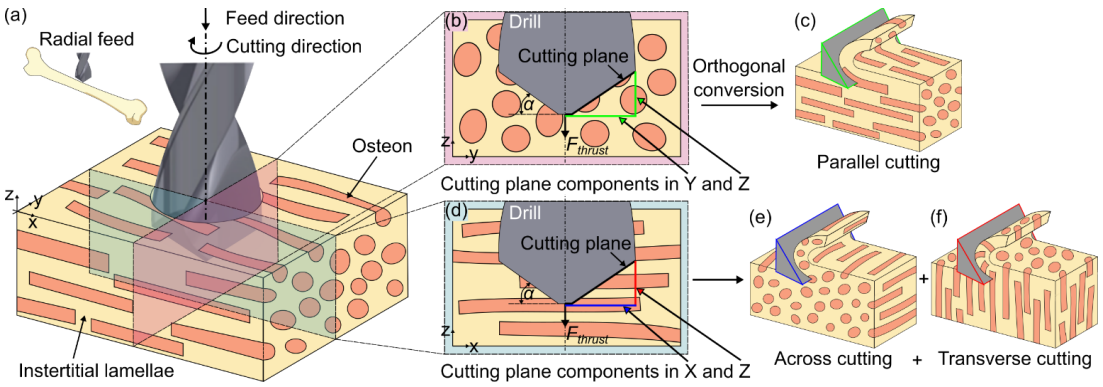

Fig. 2.12. Diagram of different cutting directions in cortical bone drilling with the radial feed direction. In an instant, the cutting edges will be engaged (i.e. performing a cutting action) with the instantaneous cutting direction being parallel to the osteons' axes (pink-coloured plane), thereby showing a similarity to orthogonal parallel cutting. After the tool rotates 90°, the cutting edges will now be engaged in two different principal directions (blue-coloured plane), thereby producing a combined effect of across cutting and transverse cutting.

The drilling process

The feed direction in cortical bone drilling has been mostly disregarded. Most studies have been conducted in the radial direction (Fig. 2.12) due to two main reasons. Firstly, axial feed direction of cortical bone drilling rarely exists in surgery. And secondly ease of access during experimental testing given the natural shape of long

bones. Studies of the feed direction effect have shown no significant differences between axial and radial feed in drilling in terms of forces and torque (Cseke and Heinemann, 2018) as well as in temperature rise (Li et al., 2021). These findings prove, as previously postulated, that axial and radial feed directions in cortical bone drilling are comparable processes.

Making an analogy with orthogonal cutting, where the chip formation mechanism is dependent on the DOC (Liao and Axinte, 2016a), in cortical bone drilling, the material removal mechanism is driven by the combination of the drill rotational speed, feed rate and flute number, i.e. the feed per lip, which can be used to calculate the equivalent drilling DOC, h_{drill}, expressed as (Li et al., 2021):

$$h_{drill} = \frac{f_n \sin \omega}{z_n} \qquad \text{Eq. 2.2}$$

where f_n is the feed rate, ω is half of the drill point angle and z_n is the flute number. The h_{drill} represents the cutting depth of a single lip, per revolution of the drill. The cutting parameters could be adjusted to perform the cutting action in either the SC (Fig. 2.7a) where $h_{drill} < h_s$ ($h_s \cong 13\ \mu m$), SCC (Fig. 2.7b) where $h_{drill} > h_s$, or FC (Fig. 2.7c) where $h_{drill} > h_f$ ($h_f \cong 70\ \mu m$) (Liao and Axinte, 2016a). This rationale could explain why large cracks form along the drilled surface when drilling at large h_{drill} (> 70 µm) values and a smooth surface when drilling at small h_{drill} (< 13 µm) values. During drilling, the bone temperature rises considerably, especially at small h_{drill} when the SC mode is present (Liao and Axinte, 2016b). The high temperature in the bone could have biological (i.e. necrosis) and mechanical (i.e. changes to mechanical properties and failure modes) effects. Contrary to orthogonal cutting (where temperature has little effect due to the open thermal boundaries), in bone drilling (where the closed thermal boundary facilitates the temperature build-up), the cutting mechanism depends on the DOC, h_{drill} and is also affected by the thermal aspects of the drilling process.

Liao and Axinte (Liao and Axinte, 2016b) conducted a series of drilling experiments using a 1 mm drill and h_{drill} within 0.42–1.68 µm that is well below the 13 µm threshold value for the SC mode. By varying the cutting speed from 6 to 60 m/min, a significant increase in bone temperature rises and a change in the chip morphology were observed (Fig. 2.13), producing more powdery chips at increased cutting speeds in drilling. In the similar range of cutting speed (13–75 m/min) and h_{drill} within 3.6–21 µm including both SC and SCC modes, Xu et al. (Xu et al., 2014) showed a similar trend in the chip morphology affected by cutting speed and DOC. This finding proves that the cutting mechanism during drilling is influenced by both h_{drill} and cutting speed as well as directly correlated with the bone temperature (Li et al., 2021). In conclusion, the cutting mechanism cannot be assumed to be exclusively DOC-driven in bone drilling.

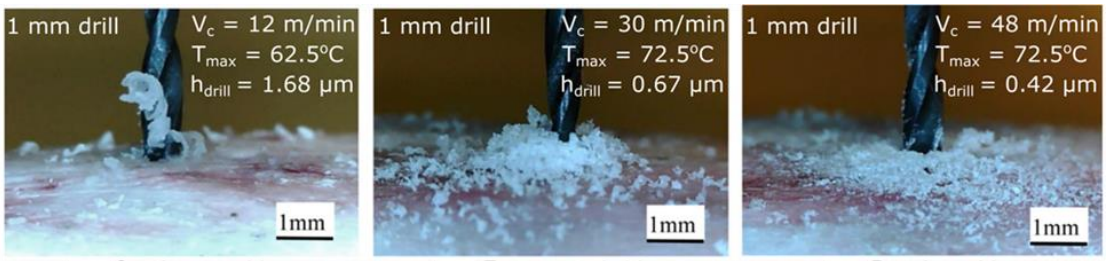

Fig. 2.13. Chip morphologies in cortical bone drilling (Liao and Axinte, 2016b) **at low h_{drill}:** (a) continuous shape chip at low cutting speeds, (b) fragmented chip ay higher cutting speeds, moderately sized chips with intermittent cuts by microfractures and (c) further segmented chips by microfractures at the highest cutting speeds, displaying a powdery form. Since these experiments were conducted at low h_{drill}, the variation in chip morphology is driven primarily by the cutting speed.

As reported by Wiggins and Malkin (Wiggins and Malkin, 1976), even if the chip formation resembles that of metal cutting at the macroscale, the microscale analysis could reveal a chip composed of sliding series of segmented and micro-fractured chips. In orthogonal cutting, three main chip types (sheared, serrated, fractured) depend mostly on the DOC as show in 3.1.1 (Feldmann et al., 2017; Liao and Axinte, 2016a). But in drilling, continuous, fragmented and powdery chips forms can be obtained

(Liao and Axinte, 2016b) (Fig. 2.13), depending on the cutting speed and the DOC per revolution per lip (h_{drill}).

The bone cutting mechanism in drilling is complex because, firstly, the cutting action in a single revolution cut through all the orthogonal directions (Fig. 2.12), thereby giving a mixed cutting mode as a result. Secondly using the analogy of orthogonal DOC in drilling (Eq. 2.2) is not sufficiently describing of the process. Thirdly temperature build-up is facilitated, potentially dehydrating the bone. Finally different chip morphologies exist (Fig. 2.13) depending on the cutting speed (Liao and Axinte, 2016b), but not necessarily on h_{drill} nor the temperature. All these challenges make bone drilling modelling very complex.

Drilling temperature measurement

Another problem arising from cortical bone drilling is temperature measurement. Given that the highest temperature occurs at the drill-bone interface on the drilled wall (Fig. 2.14), the direct measurement in this specific region during bone drilling is not possible. Four techniques have been studied to compare the bone temperatures during the drilling process: an infrared camera pointing directly at the drill exit (Li et al., 2021; Shu et al., 2020b), an infrared camera pointing at the drill entrance and thermocouples embedded in the bone at specific distances from the drilled wall via micro-drilled holes parallel or vertical to the hole axis (Alam, 2015; Amewoui et al., 2020; Sui et al., 2020, 2015). The main advantage is that using thermocouples, compared with a thermal camera, is that the exact position of measurement is known and can be more objectively compared with a mathematical or FEM thermal model, such as discussed late. Using thermocouples is an invasive technique; delicate precautions must be put in place to ensure that no damage is induced to the bone during the thermocouple micro-hole preparation and thermocouple insertion. Additionally, the thermocouple micro-holes also interfere with the heat transfer within the bone. Thermography is a more suitable method to observe the temperature distribution in

the hard tissue in a 2D plane. Although only the surface temperatures can be measured, thermal imaging provides a non-invasive view of the overall temperature distribution and the main sources of heat, especially at the drill exit (Shu et al., 2020b). However, the disadvantages of thermography are that it depends on the bone's emissivity and that it requires some level of extrapolation, and in the case of chip temperature, the readout might be hindered by the curled chip and its accumulated temperature effect (Feldmann et al., 2017). To predict the temperature distribution by simulation models, heat conduction equations can be used for analysis. The heat generation of specific cutting mechanisms, thermophysical properties, geometry and material phase transformation of both the hard tissue and the cutting tool are required as inputs.

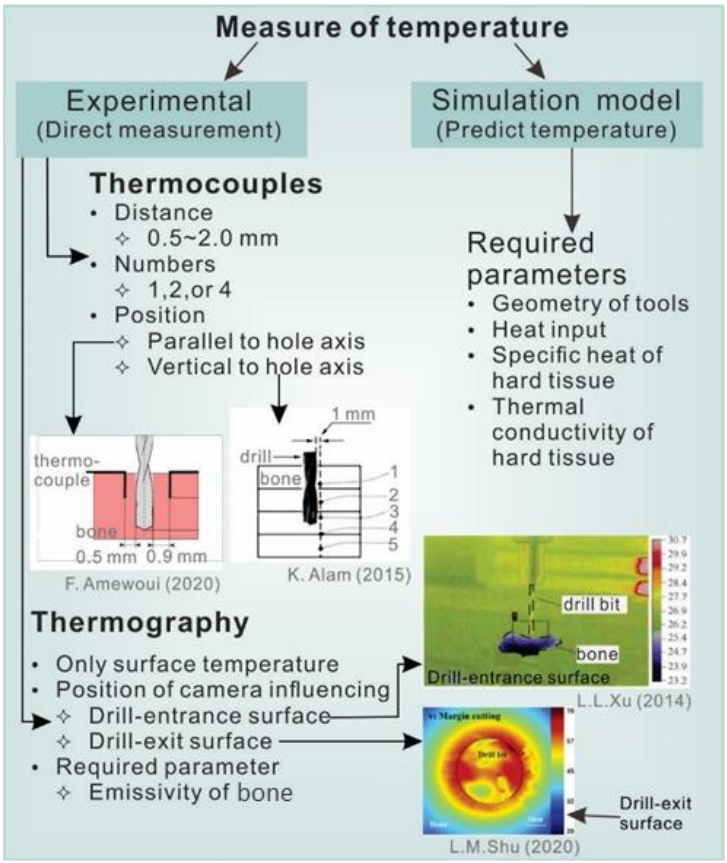

Fig. 2.14. Temperature measurement techniques in cortical bone drilling. The two preferred methods for experimental measurements of temperature are thermocouples and infrared thermography, whereas simulations are also employed for thermal fields predictions (Alam, 2015; Amewoui et al., 2020; Shu et al., 2020b; Xu et al., 2014).

Modelling of the drilling process

Mechanistic, FEM and smoothed particle hydrodynamics (SPH) models have been developed to study bone drilling (Takabi and Tai, 2017). These models can predict the bone drilling forces and temperatures as well as provide a more fundamental understanding of the effect of drill specifications and process parameters on bone temperature. FEM thermal analysis based on commercial software (Sezek et al., 2012; Tu et al., 2008) and coupled with classic metal cutting theory (Davidson and James, 2003) for bone drilling has been carried out. These models have limited capability and cannot fully describe the bone drilling process with anisotropy of the bone material, drill geometry and thermal modelling. During drilling, the cutting action occurs at the chisel edge and cutting lips. The chisel edge in the vicinity of the drill axis has a low cutting speed and mainly indents and pushes the bone material to the cutting lip (Wiggins and Malkin, 1976). The chisel edge contributes significantly (50% or more) to the thrust force but has little effect on torque (Lee et al., 2012a; Sui et al., 2014) (Fig. 2.15a,b). The cutting lips have a higher cutting speed to perform the material removal process and are the main contributors of heat and torque in bone drilling (Shu et al., 2020b). Analytical models of the chisel edge and the cutting lips in bone drilling have been developed and show good agreement with experimentally measured thrust force and torque (Lee et al., 2012a; Sui et al., 2014).

Shu et al. (Shu et al., 2020b) measured the drill-exit temperature with an infrared camera and showed that: 1) a concentrated heat zone is located in the centre of the hole where the chisel edge is engaged, 2) the temperature increases considerably within the hole diameter and in the drill side wall and 3) the heat does not propagate deep into the bone when both the chisel edge and the lips are engaged (Fig. 2.15c–e). Due to the heat concentration in the hole wall, the bone is susceptible to thermal damage (i.e. necrosis) caused by a high temperature for a short period rather than a lower temperature for a longer period (Li et al., 2021).

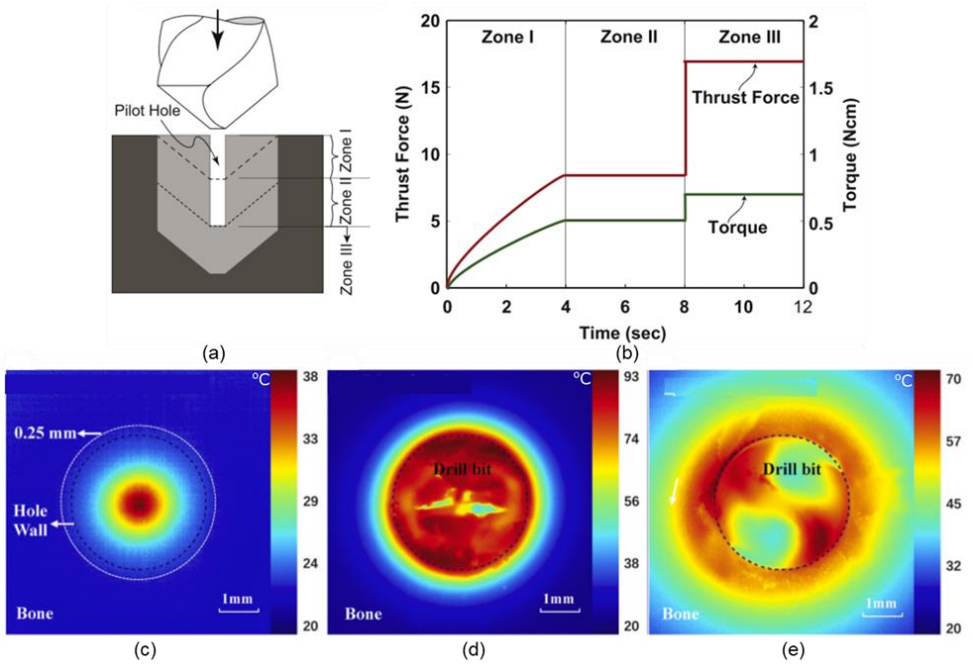

Fig. 2.15. Effects of the specific regions on drilling force, torque and temperature in cortical bone. (a) Using a pilot hole with the same diameter as the chisel edge length allows for observation of the individual effects of the chisel edge and the cutting lips. (b) Partial and increasing engagement of the cutting lips increases both the torque and thrust force in Zone 1, full engagement of the cutting lips in Zone II, engagement of both the cutting lips and the chisel edge with a significant increase in thrust force but a less significant effect on torque in Zone III (Lee et al., 2012a). Thermal images at the drill exit of the hole: (c) a concentrated heat zone when only the chisel edge is engaged, (d) a considerable temperature rise in the hole diameter and in the drill side wall that does not propagate deep into the bone when both the chisel edge and the lips are engaged and (e) the temperature decreases and diffuses deeper into the bone when the entire drill is engaged (Shu et al., 2020b).

The main difficulty is to accurately measure peak temperatures and temperature gradients in the immediate vicinity from the drill. Thermocouples are currently only capable of measuring the temperature at a specific distance, e.g. 500 µm, from the drill. The use of mathematical models is required to predict the heat generation rate and bone temperature. Aghvami et al. (Aghvami et al., 2018) predicted the peak temperature in the drill-bone interface and showed that it is much higher than that at immediate radial positions from the drill site (Fig. 2.16) based on the analytical thermal model.

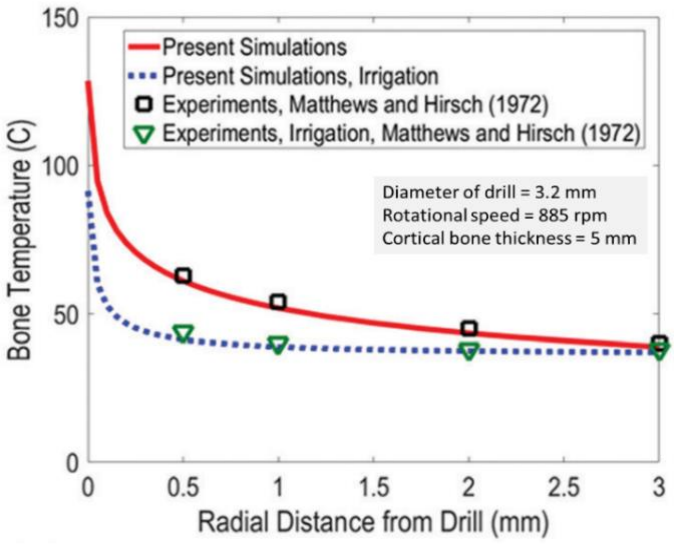

Fig. 2.16. Effect of point of temperature measurement radially away from the drilled hole (Aghvami et al., 2018).

FEM has been used for simulating the cortical bone drilling process. Lee et al. (Lee et al., 2011) developed a thermal FEM model (Fig. 2.17a) that accounted for heat generation at the drill tip, heat diffusion of the bone and the heat transfer among the drill, chip, workpiece and environment. Enhancements to this FEM model by applying a lumped-parameter approach, based on the concepts of thermal resistors and capacitors as well as considering the friction between the chips with both the drill flutes and the bone have been carried out (Maani et al., 2014). Results showed a positive correlation between feed rate and bone temperature. However, this finding is opposite to most research findings (Table 2.3). As suggested by Sui et al. (Sui et al., 2015), the heat partition ratio that flows into the workpiece was misused as the fraction of shear deformation that transforms into heat. This consideration, in parallel with a mechanistic force modelling approach (Sui et al., 2014), yielded an improved FEM model that agreed with experimental data (Sui et al., 2015), even considering convective effects by air or water (b).

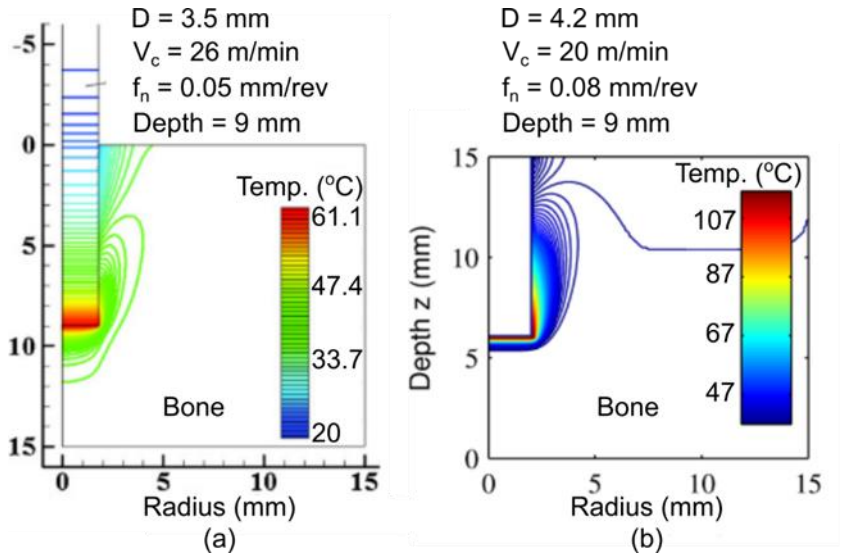

Fig. 2.17. Comparison of FEMs developed for cortical bone drilling temperature rise. (a) FEM results from Lee et al. (Lee et al., 2011) yield a maximum temperature of 61 °C and (b) FEM results from Sui et al. (Sui et al., 2015) show a much higher temperature of 107 °C. The observed contrast in temperature could be due to the differences in numerical modelling, in the cutting parameters and the tool diameter.

Current FEM studies of bone drilling require the use of experimental calibration parameters and are based on isotropic material properties. The bone microstructure is not included and, therefore, the variation in force values due to the anisotropy of the bone (Fig. 2.12) cannot be predicted. Advancing, the bone drilling modelling to include bone anisotropy is needed, as is gaining an improved understanding of the heat dissipation through the bone that causes cellular damage. Feldmann et al. (Feldmann et al., 2016) proposed a force and temperature prediction model for in-vivo bone drilling based on the radiodensity (measured in Hounsfield units) and via a computed tomography (CT) scan of the bone. Along the drilling path, local zones with higher bone density, which produces larger force/torque and a higher temperature in drilling, will be identified. Although this modelling approach captures the variation of bone properties in drilling due to the density distribution, it is still constrained to experimental calibration and isotropic material considerations.

Additional to FEM and mechanistic models, smoothed particle hydrodynamics (SPH), a technique usually employed in fluid dynamics, has been proven useful to model the

bone cutting process in a meshless manner, thereby avoiding mesh-related problems in FEM, such as excessive distortions or displacements (Takabi and Tai, 2017). In fact, they (Tajdari and Tai, 2016) were able to model K-wire bone drilling three-dimensionally by coupling FEM with SPH, being the interface between the two on the drill wall and the SPH domain defined only in the bone volume directly below the K-wire's tip. Their model showed the SPH method can capture the effect of small and fragmented bone debris that is produced during the cutting process, aspect that is not achievable by FEM.

Effect of drilling parameters upon the loads of the cutting process

Necrosis is a major concern in bone drilling, and as such, high temperatures must be avoided in bone cutting (Augustin et al., 2008). Research has focused on the effects that drilling process parameters (e.g. cutting speed, feed rate and drilling depth) and drill geometry (e.g. diameter, helix angle, drill point angle and chisel edge) have on bone temperature, thrust force and torque (as summarised in Table 2.3). Inconsistencies have been documented among research studies, mainly due to the differences in the drilling process, as well as in the experimental and modelling setups. The correlations listed in Table 2.3 have been summarised from the literature and serve as a guideline. Rationales that lead to these conclusions are briefly discussed next.

Table 2.3. Correlations between drilling parameters and drill specifications with temperature, thrust force and torque. The table lists data obtained from experiments as well as mechanistic and numerical models.

Drilling process parameters and drill specifications	Main effect on temperature	Main effect on thrust force	Main effect on torque
Cutting speed	(+) Positive[1]	(−) Negative[2]	(−) Negative[3]
Feed rate	(−) Negative[4]	(+) Positive[5]	(+) Positive[6]
Drilling depth	(+) Positive[7]	(+) Positive[8]	(+) Positive[9]
Drill diameter	(+) Positive[10] or (−) Negative[11]	(+) Positive[12]	-

Helix angle	(−) Negative[13]	-	-
Drill point angle	(+) Positive[14]	(+) Positive[15]	(+) Positive[15]

Data compiled from: [1](Augustin et al., 2008; Basiaga et al., 2011; Davidson and James, 2003; Hillery and Shuaib, 1999; Lee et al., 2012b, 2011; Maani et al., 2014; Reingewirtz et al., 1997; Saha et al., 1982; Sezek et al., 2012; Sui et al., 2020, 2015; Tahmasbi et al., 2017; Xu et al., 2014; Yang et al., 2010), [2](Abouzgia and James, 1995; Alam et al., 2011; Basiaga et al., 2011; Hillery and Shuaib, 1999; Sui et al., 2014; Tu et al., 2008; Xu et al., 2014; Yang et al., 2010), [3](Alam et al., 2011; Basiaga et al., 2011; Hillery and Shuaib, 1999; Sui et al., 2014), [4](Augustin et al., 2008; Davidson and James, 2003; Lee et al., 2012b, 2011; Maani et al., 2014; Sezek et al., 2012; Shakouri and Ghorbani, 2020; Singh et al., 2016a; Sui et al., 2020, 2015; Xu et al., 2014), [5](Alam et al., 2011; Lee et al., 2012a; Sui et al., 2014; Wiggins and Malkin, 1976; Xu et al., 2014), [6](Lee et al., 2012a; Sui et al., 2014; Wiggins and Malkin, 1976), [7](Davidson and James, 2003; Erikssons et al., 1984; Hillery and Shuaib, 1999; Lee et al., 2012b, 2011; Maani et al., 2014; Sui et al., 2020, 2015; Yacker and Klein, 1997), [8](Hillery and Shuaib, 1999), [9](Lee et al., 2012a; Wiggins and Malkin, 1976), [10](Augustin et al., 2008; Davidson and James, 2003; Maani et al., 2014; Sezek et al., 2012; Sui et al., 2020, 2015; Tahmasbi et al., 2017), [11](Lee et al., 2011; Sui et al., 2020, 2015), [12](Saha et al., 1982; Tahmasbi et al., 2017), [13](Davidson and James, 2003; Lee et al., 2011; Maani et al., 2014; Sui et al., 2020, 2015; Ueda et al., 2010), [14](Basiaga et al., 2011; Lee et al., 2011; Maani et al., 2014; Sui et al., 2020, 2015), [15](Basiaga et al., 2011)

Cutting speed: An increase in the cutting speed creates a higher shear strain rate in the primary shear deformation zone (Sui et al., 2015). The chips rapidly evacuate from the drilled bone and result in frictional heat between the bone drilled hole wall and drill. A higher cutting speed in bone drilling will manifest higher temperatures and lower forces and torques.

Feed rate: At an increased feed rate, the DOC (h_{drill}) is larger, more shearing energy is required and the thrust force and torque increase. While these conditions favour heat generation, the heating time is also reduced (at increased feed rate, the drilling takes a shorter time), potentially result in a reduced heat diffusion in the bone and lower bone temperatures. A sensitivity study of bone drilling (Tahmasbi et al., 2017) showed that the feed rate increase could result in either a positive or negative correlation with bone temperature depending on combinations of cutting speeds and drill diameter. This observation is consistent with the experimental results by Li et al. (Li et al., 2021) that the feed rate–cutting speed–temperature relationship shows both positive and negative trends and is not trivial.

Drilling depth: At the beginning of the bone drilling, minimal material is removed. When the drill advances into the bone, the flutes tend to clog by hot chips that hinder

the heat dissipation and drill rotation, consequently yielding larger thrust forces, torques and temperatures (Wiggins and Malkin, 1976).

Helix angle: An increase in the helix angle reduces the engagement length of the cutting edge, producing shorter chips that facilitate chip evacuation (Ueda et al., 2010). The quick chip evacuation minimises frictional heat between the chip and the bone, thereby producing lower temperatures.

Drill point angle: A larger drill point angle (i.e. the flatter drill) produces decreased rake angles along the cutting lips (Sui et al., 2020). Consequently, a narrower rake implies that more mechanical work is in place, thereby producing a higher shear deformation and greater temperatures during drilling (Lee et al., 2011).

Drill diameter: Increasing the diameter is translated into a larger material removal rate under the same drilling conditions. This phenomenon is synonymous with shearing energy, a condition that favours heat generation and temperature rise. A larger drill diameter also enlarges the convective and conductive areas in the drilled bone wall, allowing an improved heat transfer to take place and result in lower bone temperatures (Sui et al., 2020). Both scenarios could occur based on the specific drilling and experimental conditions (Sui et al., 2020, 2015).

2.2.1.3 Milling of cortical bone

The principle of cortical bone milling is similar to orthogonal cutting (0). Owing to the rotation of the milling cutter, the chip formation exhibits the transition from one orthogonal cutting direction to another every 90° of tool rotation. When milling along the parallel (Fig. 2.18a) or across (Fig. 2.18b) directions, the milling action can be decomposed to a mixed mode of parallel-to-transverse cutting mechanism that depends on the rotation of the milling tool. Owing to the bone's anatomy, when milling along the TD (Fig. 2.18c), the cutting edges are only engaged in the across cutting

direction at all rotation angles of the tool. Forces for milling in the PD and AD are similar, whereas milling in the TD exhibits lower forces (Chen et al., 2020).

Similar to drilling, the chip formation in milling is not as simple as in orthogonal cutting due to the mixed mode cutting action. As explained in drilling of cortical bone, making an analogy between orthogonal cutting DOC and the feed per tooth of the milling tool can provide a rough understanding of the chip formation mechanism in milling. The corresponding DOC in milling is the feed per tooth (h_{mill}):

$$h_{mill} = \frac{V_f}{n_{spindle}\, z_n} \qquad \text{Eq. 2.3}$$

where V_f is the feed speed, n is the spindle speed and z_n is the teeth number. The h_{mill} represents the cutting depth of a single tooth, per revolution of the tool. In milling, the chip will form by SC (Fig. 2.7a) if $h_{mill} < h_s$ ($h_s \cong 13\ \mu m$), SCC (Fig. 2.7b) when $h_{mill} < h_f$ ($h_f \cong 70\ \mu m$) or FC (Fig. 2.7c) when $h_{drill} < h_f$ ($h_f \cong 70\ \mu m$) (Liao and Axinte, 2016a). High cutting speed milling (125 m/min) showed that when $h_{mill} < 5\ \mu m$ (well below h_s), the ploughing force is significant for the chip formation process; it facilitates crushing of the lamellar structure, thereby resulting in chips that tend to form by crushing (Fig. 2.19a). For h_{mill} of up to 16 µm (Fig. 2.19b-d), a shear-formed continuous chip is obtained (Conward and Samuel, 2016). Additionally, the failure is related to the individual constituent, e.g. cement line, Haversian canal, osteon and lamellae being cut at a given time and showing inter-osteonal failure, i.e. chip breakage at osteon radius length.

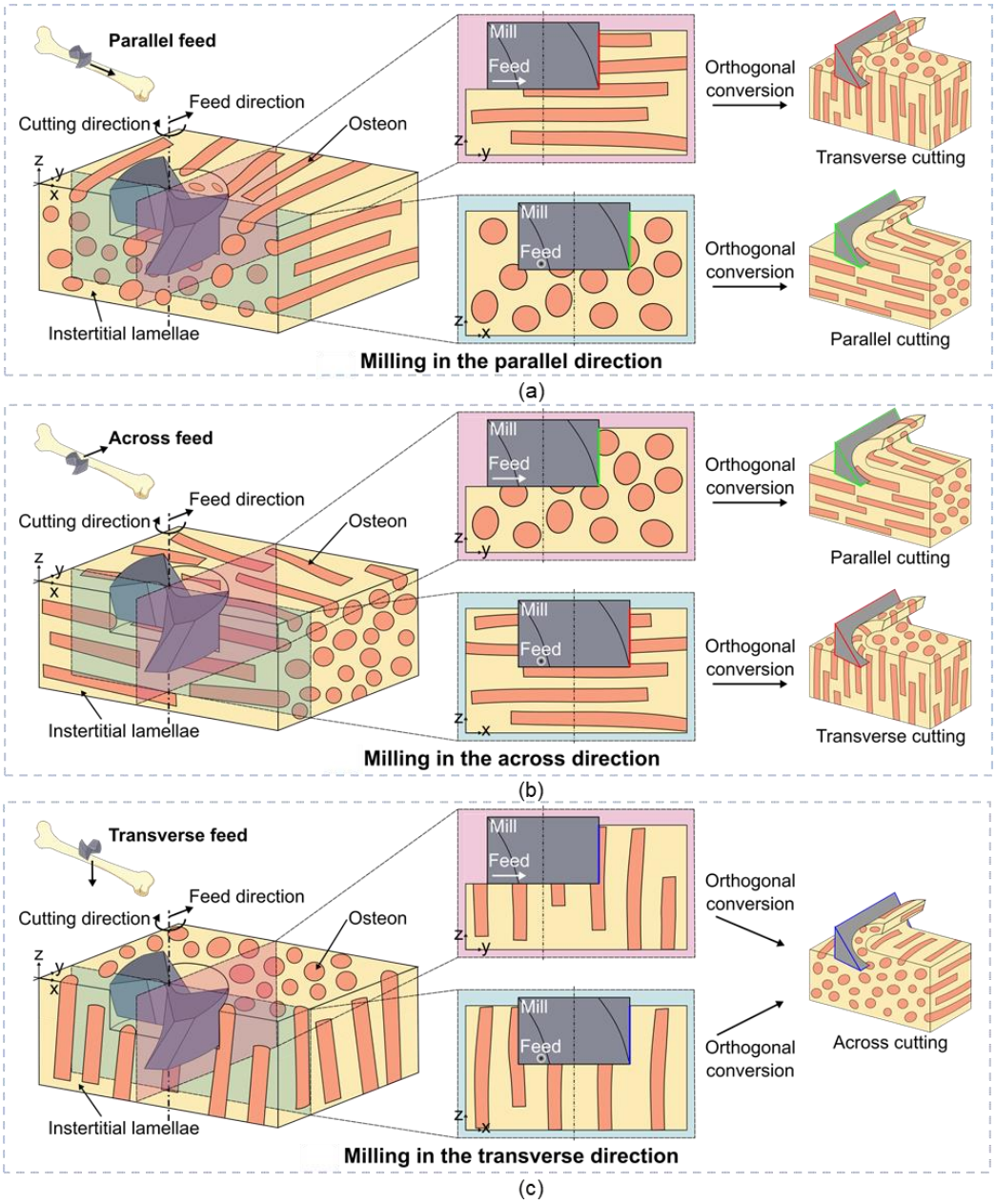

Fig. 2.18. Orthogonal cutting simplification in cortical bone milling. (a) Milling along the PD results in a mixed mode between orthogonal parallel and transverse cutting due to the rotation of the tool. (b) Milling along the AD results in the same orthogonal cutting directions. (c) Milling along the TD results in across cutting throughout the entire revolution of the tool. These analogies from milling to orthogonal cutting are limited due to the flute angle of the milling tool.

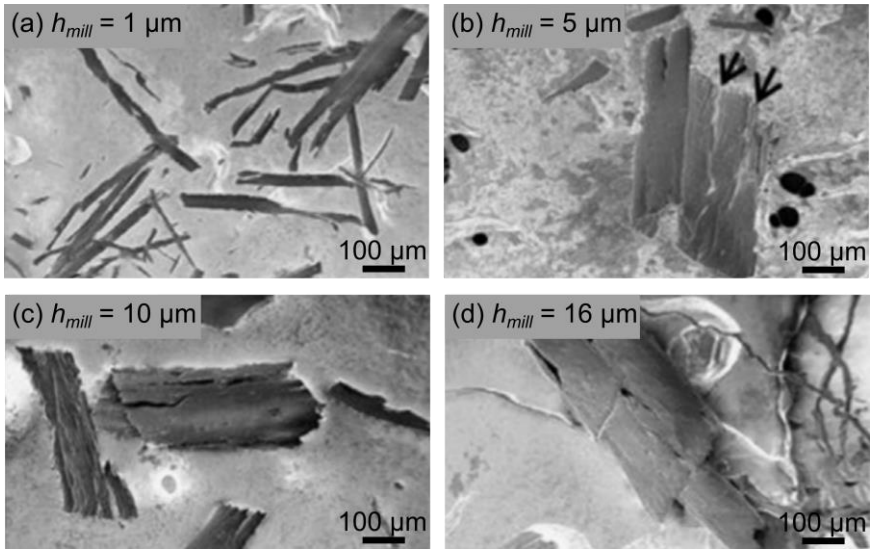

Fig. 2.19. Chip morphology in cortical bone micro-milling at a different feed per tooth (h_{mill}) and 125 m/min of cutting speed (Conward and Samuel, 2016)**.** (a) Owing to the low feed, the ploughing force is important and aids to a crushing failure mode, in which the chip is heavily segmented. (b-d) Increasing the feed per tooth produces thicker segments of chip, i.e. shows a more continuous chip with inter-osteonal failure (black arrows in (b)).

Modelling of the milling process

Mathematical models have been proposed to describe the cortical bone milling process. Normally, the specific cutting force (i.e. cutting force per unit area of cut) is required for modelling the milling force that can be either predicted through milling (Mitsuishi et al., 2004) or orthogonal cutting (Liao and Axinte, 2016a) experiments. Modelling can be based on the orthogonal cutting properties as a function of the tool rotation (Chen et al., 2020). Owing to the anisotropy properties of cortical bone, the instantaneous coefficient of friction and shear stress will vary along with the rotation angle of the tool, θ_{cut} (0) and the DOC (Liao and Axinte, 2016a). The shear stress is a function that can be expressed as (Liao et al., 2019):

$$\tau(\theta_{cut}, h_{mill}) = (C_1 + C_2 \sin(C_3\theta_{cut} + \theta_0)) \left(\frac{6V_c}{h_{mill}(\theta_{cut})[\tan\alpha + \cot\phi]}\right) \quad \text{Eq. 2.4}$$

where C_1, C_2 and C_3 and θ_0 are experimental constants, V_c is the cutting speed, α is the rake angle and ϕ is the shear plane angle as defined by the Ernst Merchant principle. The result is a mechanistic model that allows for force predictions, even

while considering the ploughing force effect. This model was coupled with a mechanistic 2D thermal analysis by considering an arc-shaped moving heat source along with the bone structure while considering anisotropy. The force and thermal models (Liao et al., 2019) were both validated with milling experiments while feeding along the PD and showing the potential for modelling the necrotic depth post-machining.

Thermal modelling of bone milling can assess the necrosis and predict the maximum temperatures at the tool-bone interface, which are complex to validate experimentally. Infrared thermometry (Shin and Yoon, 2006) and embedded thermocouples (Liao et al., 2019) along with extrapolation and the consideration of the moving heat source have been studied to estimate the maximum temperature in the tool-bone interface. When no cooling is employed and high cutting speeds are present, high bone temperatures (>100 °C) are built up and can create necrotic damage of up to 1.9 mm (Shin and Yoon, 2006).

To achieve low-temperature bone milling, the feed per tooth can be increased, but this increase comes at the expense of larger surface roughness and possible microfractures when h_{mill} exceeds the h_f fracture threshold. The correlation between feed per tooth with temperature and force has been reported as positive and negative, respectively, which is consistent with the results in drilling. Contrary to drilling, an increase in the cutting speed decreases the bone temperature because the rotational heat source is not fully immersed in the bone and reduces the heat transferred to the bone. These correlations have been validated for human bone at a h_{mill} of 10–550 µm and a cutting speed of 63–141 m/min for a 10 mm mill (Denis et al., 2001), and for lower cutting speeds of 7.9–157 m/min and h_{mill} of 15–375 µm in porcine femurs (Sugita et al., 2009b). Furthermore, an increase in the tool diameter or milling without coolant resulted in larger forces (up to a factor of 2.5) and higher temperatures (up to a factor of 2.4) in human skull bone (Federspil et al., 2003).

2.2.1.4 Grinding of cortical bone

Bone grinding is a cutting process less used in orthopaedics but more used in neurosurgery, e.g. the endonasal approach to the skull base in neurosurgery (Shih et al., 2012). Bone grinding enables accurate removal of bone around critical tissues (e.g. nerves) and organs (e.g. brain and spinal cord). High heat generation and low thermal conductivity of the bone may produce high bone temperatures and result in necrosis, thermal damage to the surrounding tissues (e.g. nerves) or coagulation of blood creating clots and blockage (e.g. in the carotid artery in skull-based bone grinding) (Shih et al., 2012). Bone grinding is a critical process in bone machining, where thermal modelling has been the main topic in bone grinding, with the goal of minimising the temperature rise.

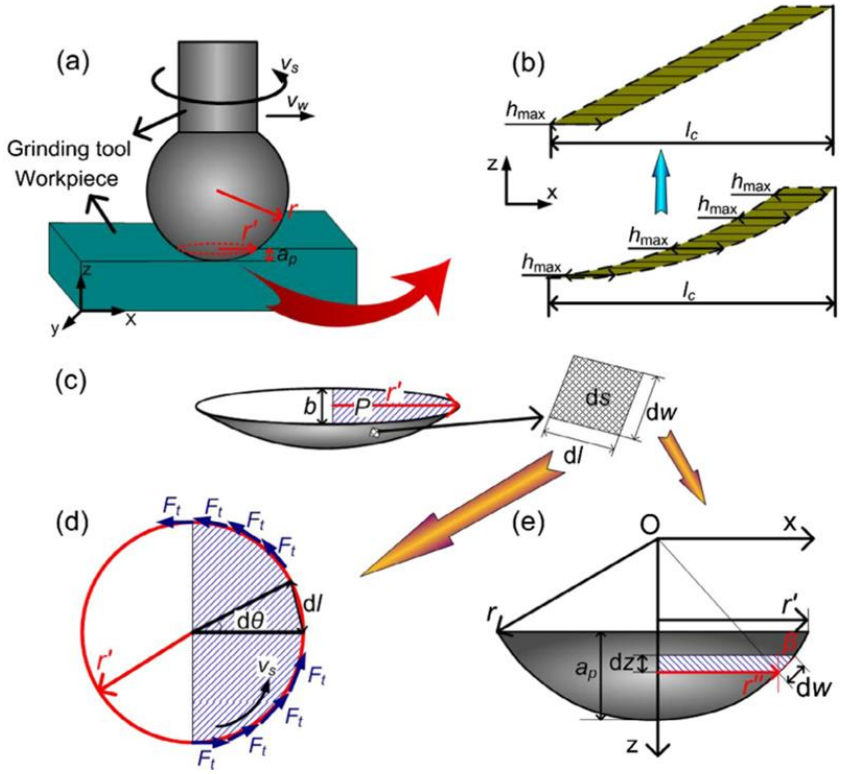

Fig. 2.20. Description of the machining mechanism in bone grinding (Yang et al., 2017). (a) Grinding tool rotating at a constant spindle speed and feed speed, (b) DOC, *h*, for all the arc-shaped contact region of the tool within the contact length, l_c, (c) the partial spherical shaped region that is cut by the grinding wheel, (d) the integral arc length (*dl*) showing the tangential force direction in the XY plane and (e) integral cutting width (*dw*) in the XZ plane.

In bone grinding, the tool is usually a spherical grinding wheel with embedded diamond particles (Tai et al., 2013b, 2013a). As opposed to orthogonal cutting, drilling and milling, where the material removal is shear-driven, abrasion is the key material removal mechanism, and the chip formation, cutting forces and thermal analyses are different in bone grinding (Fig. 2.20). During bone grinding, the rotation axis of the tool is not necessarily orthogonal to the feed direction (Tai et al., 2013b, 2013a), as the cutting usually occurs at a specific tilt angle (Fig. 2.21); this condition adds another variable to the bone machining process. However, considering an orthogonal position of the rotation axis of the grinding wheel in Fig. 2.20a (Yang et al., 2017), a force model has been developed based on experimental data and localised forces for each portion of the grinding wheel contact area with the bone. The heat flux in the grinding wheel-bone interface is analysed to predict the bone temperatures.

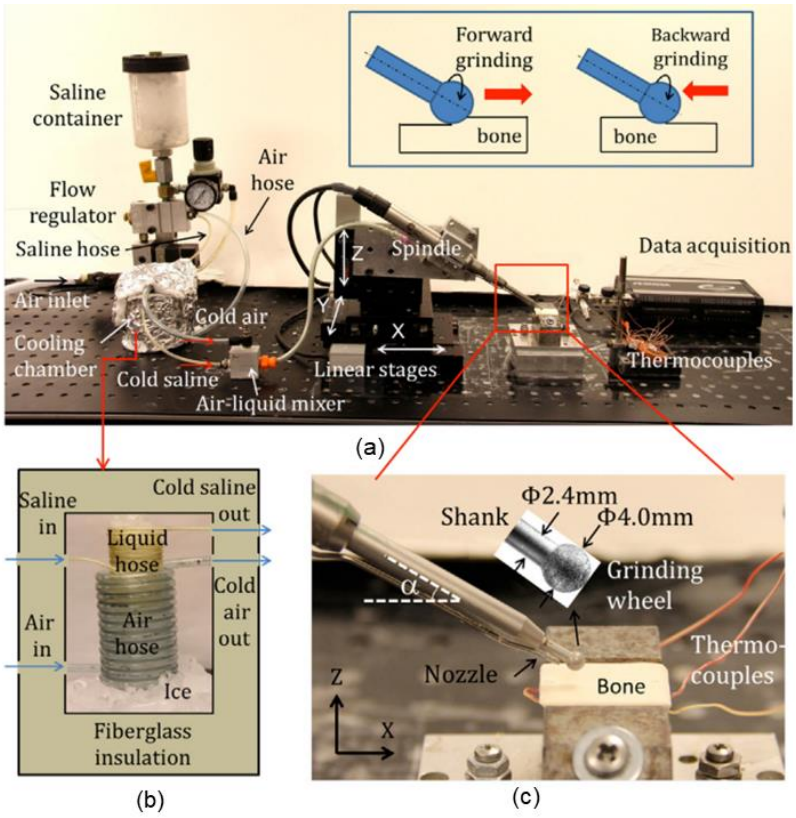

Fig. 2.21. Bone grinding setup (Zhang et al., 2013a). (a) Overview of the setup which comprises the machining equipment and mist cooling system. (b) Close-up view of the cooling chamber used for the coolant delivery (i.e. mist cooling). (c) Close-up view of the bone, grinding wheel and nozzle for fluid delivery.

Most studies in bone grinding are aimed to predict the temperature distribution in the bone, usually with the aid of thermocouples, while comparing various grinding setups (e.g. motor electrical power (Tai et al., 2013b, 2013a) and convective cooling (Yang et al., 2018; Zhang et al., 2013a)) or modelling approaches (e.g. elemental modelling (Zhang et al., 2013b), micro-modelling (Yang et al., 2017) and time-varying heat flux (Wang et al., 2016)). Thermal power should not exceed 0.5 W to protect the optic nerve from thermal damage (Shih et al., 2012). The thermal damage may extend up to 3 mm if no cooling is used (Zhang et al., 2013b) and that temperature rise can be minimised by using lower rotational speeds, feed speeds and DOCs (Shakouri and Mirfallah, 2019). These studies use high rotational speeds (45,000–60,000 rpm) with a 4 mm grinding tool, which is translated to the 565–754 m/min cutting speed. The concept of mist cooling has been introduced to bone grinding (Fig. 2.21), where, similar to minimum quantity lubrication, instead of using conventional flood cooling, a controlled low temperature cryogenic saline mist is accurately delivered to the grinding area, resulting in lower heat generation and bone temperature (Zhang et al., 2013a).

Usually, these grinding models and studies are only applicable to a set of specific to conditions in neurosurgery (Tai et al., 2013a), limiting the scope of the past bone grinding studies. Investigating the chip formation and grinding forces based on the mechanistic modelling approach is still needed to explain the fundamental material removal mechanisms and be compared with those in orthogonal cutting, drilling and milling.

2.2.2 Non-conventional machining techniques

During surgical procedures, machining-induced bone fractures should be avoided. Given that these can be generated when the DOC exceeds the fracture threshold ($h_f > 70\,\mu m$) with conventional machining methods (milling, drilling and orthogonal

cutting), non-conventional methods to allow greater DOC while maintaining a continuous or serrated chip form and better surface quality.

Since mechanical machining poses a great challenge in terms of machining-induced damage avoidance, non-conventional machining techniques could represent a promising approach towards improving the material response during machining. As such, this section covers the recent advances in the non-conventional machining techniques of cortical bone, namely vibration-assisted machining and laser machining, as these two are representative of those with potential or current use in surgeries.

2.2.2.1 Vibration-assisted machining techniques

Vibration-assisted (VA) machining is a promising technique for biomaterials like bone (Alam et al., 2011) and it also improves the cutting of other materials (Yang et al., 2020). From the early 2000s, the ultrasonic bone curette started to be used for osteotomy to replace the conventional high-speed rotary bone drilling in dental, skull base and spinal surgeries. The concept of using ultrasonic vibration for bone cutting was first proposed by Catuna in 1953 (Catuna, 1953) and Volkov and Shepeleva in 1974 (Volkov and Shepeleva, 1974) and first applied in rabbits bone cutting experiments in 1981 by Aro et al. (Aro et al., 1981). VA cutting is s a hybrid machining process in which conventional machining is coupled with a vibration pattern with a known amplitude and frequency (Alam et al., 2011; Zhang et al., 2017). VA machining is usually in the ultrasonic frequency range which has been applied to orthogonal cutting (Bai et al., 2021; Shu and Sugita, 2020), drilling (Gupta et al., 2017a) and grinding (Babbar et al., 2019) of cortical bone.

Compared with conventional machining, the material removal in VA machining is different due to the interaction of the tool vibration paths with the bone, characterised by a combination of extrusion and impact-based material removal (Alam et al., 2011; Bai et al., 2021). The elliptical-shaped vibration pattern enables continuous or

semicontinuous chips even when the DOC exceeds the threshold value for fracture generation if conventional methods were used in bone cutting at DOC larger than 100 µm and 400–1600 Hz frequency (Fig. 2.22) (Shu and Sugita, 2020). In VA machining, the cracks mainly propagate along the shear direction and produce small triangular chips which quickly leave the tool rake face (Bai et al., 2021). Although increased frequency improves the cutting performance in terms of lower forces and minimising fractures in VA bone cutting, it comes at the expense of greater temperatures owing to the frictional contact between the tool and the bone that is increased at a higher vibration frequency.

An opposite trend in the temperature effect was reported in VA bone drilling when compared with conventional drilling. The VA drilling process produced lower forces and torque; it also generated lower temperatures than conventional drilling (Gupta et al., 2017a). This finding is contradictory to the results in (Shu and Sugita, 2020) with a positive correlation between the vibration frequency and temperature rise in VA orthogonal cutting. The conventional bone drilling was assessed using a 4.5 mm diameter surgical bone drill, whereas the VA bone drilling was evaluated with a hollow diamond-coated tool of the same diameter. Two different drills were used, thereby hindering the comparison between the two techniques. Another VA bone drilling study (Wang et al., 2014) conducted with standard 4 mm drills showed that the temperature decreases with increasing amplitude and frequency, once again contradicting the trend observed in temperature in VA orthogonal cutting (Shu and Sugita, 2020). The orthogonal bone cutting study was conducted at a high frequency and low amplitude (400–1600 Hz and 3.75–15 µm), whereas the bone drilling was done at low frequency and high amplitude (5–20 Hz and 100–500 µm). The contact time between the tool and the bone is reduced and frictional heat generation is eased in VA bone drilling. Thus, the effect of VA machining in temperature is not trivial and depends on the specific VA machining conditions (e.g. vibration frequency and amplitude). Higher VA frequency and lower amplitude in VA machining facilitate

frictional heat generation, but the lower frequency and higher amplitude reduce the contact time and friction heat generation. Although VA machining of cortical bone can effectively reduce the cutting forces of the process and yield a smooth surface (Alam et al., 2011; Shu and Sugita, 2020), the vibration parameters must be carefully chosen to minimise the thermal damage that the vibrations may induce.

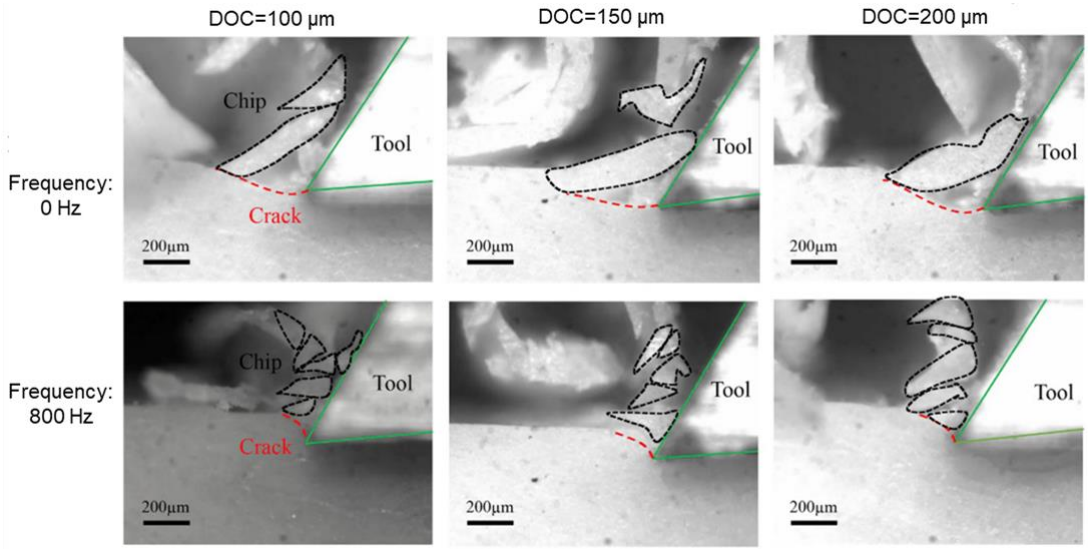

Fig. 2.22. Chip formation mechanism in vibrational-assisted orthogonal cutting of cortical bone (Shu and Sugita, 2020). In conventional orthogonal cutting (i.e. 0 Hz of frequency), the FC mode dominates the process since in all cases the DOC exceeds the threshold value for fracture ($h_f > 70$ μm). However, when cutting at the same DOC but with 800 Hz of vibration frequency in an elliptical shape pattern, the chips are segmented and exhibit low crack lengths in an upward manner, thereby protecting the bone from crack damage.

2.2.2.2 Laser machining

Laser (e.g. pulsed or continuous lasers) machining can remove material through a range of mechanisms. Pulsed laser ablation is a technique that removes material through the use of a high intensity, focused laser beam, with a short pulse width (Cha et al., 2019) which leads to energy absorption by the material, subsequently vaporising/ionising it. On the other hand, lasers with longer or continuous pulses may have fluencies below the ablation threshold – leading to a more thermally based material removal mechanism such as melting (Villerius et al., 2019).

Additionally, laser machining provides an improved cutting geometry and precision over conventional tools due to reduced/no mechanical loads (K. W. Baek et al., 2015). Therefore, laser ablation represents a non-conventional machining approach that could improve the bone cutting process by eliminating the mechanical effect. However, the thermal and shock waves from the laser beam can propagate deep into the bone, thus resulting in possible damage even in regions far from the machined or ablated zone (Amini-Nik et al., 2010). Due to the fully thermal phenomenon and considering the low thermal conductivity of bone (Feldmann et al., 2018), necrosis becomes more relevant.

The three most common lasers used in hard tissues, like cortical bone, are CO_2, Er:YAG and Nd:YAG types. The reason for these relies on the optical absorption properties of the tissue, and more specifically, on the ones from its individual constituents (e.g. protein, DNA, water, collagen, haemoglobin) (Vogel and Venugopalan, 2003). For instance, the CO_2 laser wavelength (i.e. 10.6 µm) is within the optical absorption spectrum of hydroxyapatite (i.e. 9 – 11 µm) (Krause et al., 1997), one of the most important constituents from the bone's mineral, being the mineral phase the main constituent of bone (Liu et al., 2016). The wavelength of Er:YAG lasers (i.e. 2.94 µm) is similar to one of the largest absorption peaks of water (ca. 3 µm), the third main constituent of bone (Liu et al., 2016). The wavelength from Nd:YAG lasers is 1.094 µm, but this value can be shortened by frequency doubling, meaning that it can be tailored to minimise water absorption (Nguendon Kenhagho et al., 2021), thus maximising the laser penetration depth into the tissue in water-rich (e.g. with coolant) environments.

Rayan et al. (Rayan et al., 1992) did in-vivo CO_2 laser cutting without coolants in cortical bone and reported that tissue carbonisation is easily induced along with necrosis; however, the laser pulse width was kept constant at 0.1 ms along with a frequency of 2 kHz. Krause et al. (Krause et al., 1997), also using a CO_2 laser without coolants, reported a necrotic depth ranging from 30 – 200 µm when the laser energy

density is within 160 – 2062 J/cm^2; however, a comprehensive assessment is hindered since the pulse width (5 ms, 10 ms and continuous) and frequency (10 Hz, 20 Hz, continuous) varied for each energy density condition. Frentzen at al. (Frentzen et al., 2003) also employed a CO_2 laser (80 µs pulse width) in ex-vivo bone cutting, but due to the usage of external coolant (fine air-water spray), both necrosis and tissue carbonisation were totally avoided.

Since laser machining implies a lower material removal rate as opposed to conventional machining, studies on improving the cutting efficiency in cortical bone have also been explored. For instance, a research using an Er:YAG laser (300 µs pulse width and 20 Hz frequency) (Pandurić et al., 2012) proposed a set of laser processing parameters that could result in lower cutting time, when compared to conventional drilling, even producing less heat. However, the laser was coupled with a water spray cooling system and the conventional drilling parameters were intentionally produced with a low speed, thereby hindering the understanding of the real material response both in terms of necrosis and cutting efficiency. Baek et al. (Kyung Won Baek et al., 2015) showed that mechanical machining, often resulting in a smear layer in the cut surface, blocks the bleeding of the bone, whereas laser machining eases the bleeding by leaving an open wound without smearing on top; this is the reason why laser machining could result in an improved healing time. It is known that an increased pulse laser energy will inherently result in a larger ablation volume but regarding the effect of pulse width, Beltran et al. (Beltran et al., 2017) showed, in a limited width range (i.e. microsecond range, 244 – 388 µs) that there was no direct relation and instead proposed that the driving factor in the ablation efficiency is only the pulse energy. Additionally, Beltran et al. (Beltran Bernal et al., 2018) explained how the ablation rate (i.e. ablated bone in depth per unit time) depends on both the feed speed and the number of passes of the laser beam, generally showing that for a single laser pass, the ablation rate increases while lowering the feed. However, they also suggested that a single pass results in a more uneven trench (i.e. with ripples), thereby showing

that there is a non-trivial relationship between feed speed, cutting efficiency and surface quality.

2.3 The surface integrity of bone following a material removal process

Hard tissue cutting in orthopaedics and dentistry is usually followed by the allocation of an implant or restoration material on the machined surface. Achieving and maintaining high-quality implantation or restoration is important for successful surgical operations, which are affected by the primary and secondary stabilities (Vollmer et al., 2020). Primary stability is related to mechanical and thermomechanical damage of local tissue quality, including the surface roughness and defects, microcracks, burrs, etc, from a mechanical perspective after machining. Secondary stability is determined by the bone regeneration and remodelling phenomena, which are mainly influenced by thermal damage, including osteocyte necrosis. Fig. 2.23 shows manifestations of mechanical and thermal damage in bone. Owing to the unique nature (e.g. semi-brittle and anisotropic) of this tissue, two main drivers of these damage to the surface, subsurface and surrounding tissues are large forces and higher temperatures.

Primary stability also has an important role in metals and composites when parts need to be installed or assembled; this role has been widely studied (Garcia Luna et al., 2020; la Monaca et al., 2021; Liao et al., 2021; B. Wang et al., 2021). Secondary stability is a unique feature of biological tissues for both themselves and the surrounding tissues that are biologically active. Microcracks also affect secondary stability because they could produce osteocytes necrosis (Noble et al., 2003). To achieve sustainable orthopaedic surgery, a surgeon must try to control these damage on the surface and subsurface of the machined area. Therefore, this section focuses on reporting the surface and subsurface integrity and biological activity when machining

cortical bone with conventional (i.e. orthogonal cutting, drilling, milling, grinding) and non-conventional (i.e. ultrasonic-assisted machining) machining processes.

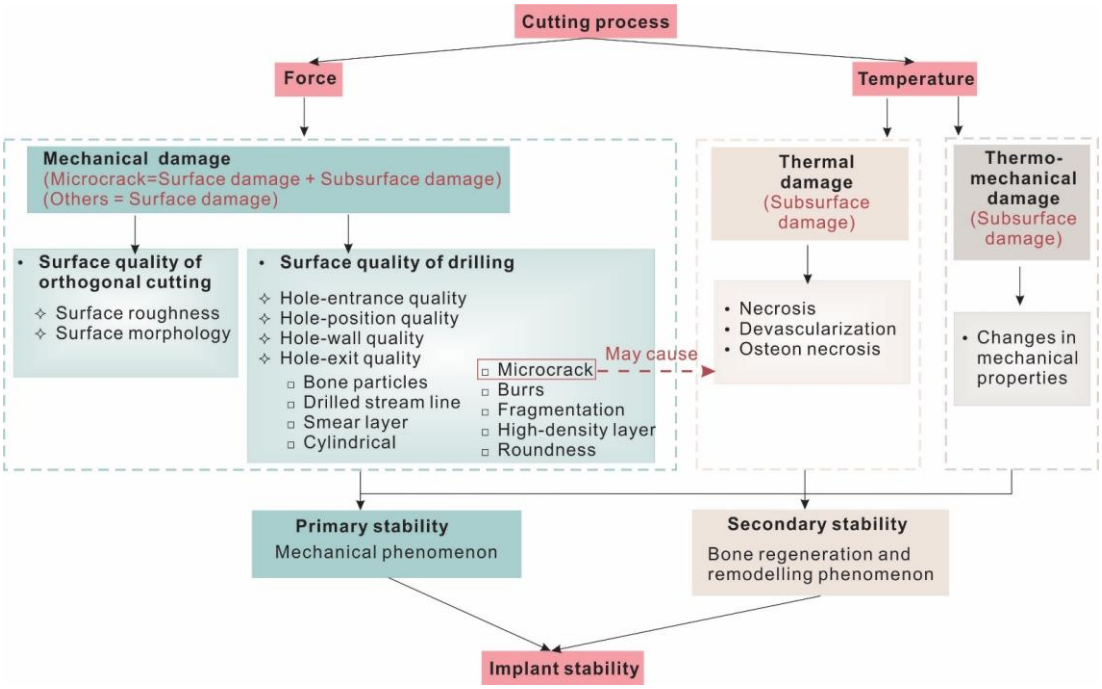

Fig. 2.23. Types of mechanical, thermal and thermomechanical damage, and the relationship between type of damage and implant stability.

2.3.1 Mechanical damage – Surface morphology and roughness in orthogonal cutting of cortical bone

Fracture and crack propagation are the basic characteristics of cortical bone processing due to its semi-brittle and anisotropic properties. The cutting directions play important roles in the machined surface morphology for the different chip formation mechanisms and fracture propagation properties which have been discussed in previously (Fig. 2.7 and Fig. 2.8). Under the same cutting speed and DOC, the TD and PD result in the largest and lowest surface roughness (Yeager et al., 2008) (Fig. 2.24), respectively, because of the downward propagation of cracks along the cement line following, which facilitates the osteon pull-put and "crater defects", thereby producing a rough surface in TD.

Similar to material removal mechanisms, DOC also plays an important effect on the surface morphology and roughness. Few defects or even no evident defects on machined surface and subsurface were found at small DOC (Fig. 2.24). Increasing crack and defect formation is observed at a large DOC of 70 µm. Severe craters, defects, cracks and exposed Haversian canals are presented when the DOC increases to 140–150 µm in all cutting directions (Liao and Axinte, 2016a; Yeager et al., 2008). As explained before, the quality of surface morphology is affected by the cutting mode, fracture mode and material removal mechanism (Fig. 2.9) (Bai et al., 2020; Liao and Axinte, 2016a). In practice, surgical operations are performed at a large DOC for efficient operation, potentially causing serious damage to the bone surface. Developing innovative cutting technologies to reduce damage in relevant bone cutting operations is crucial.

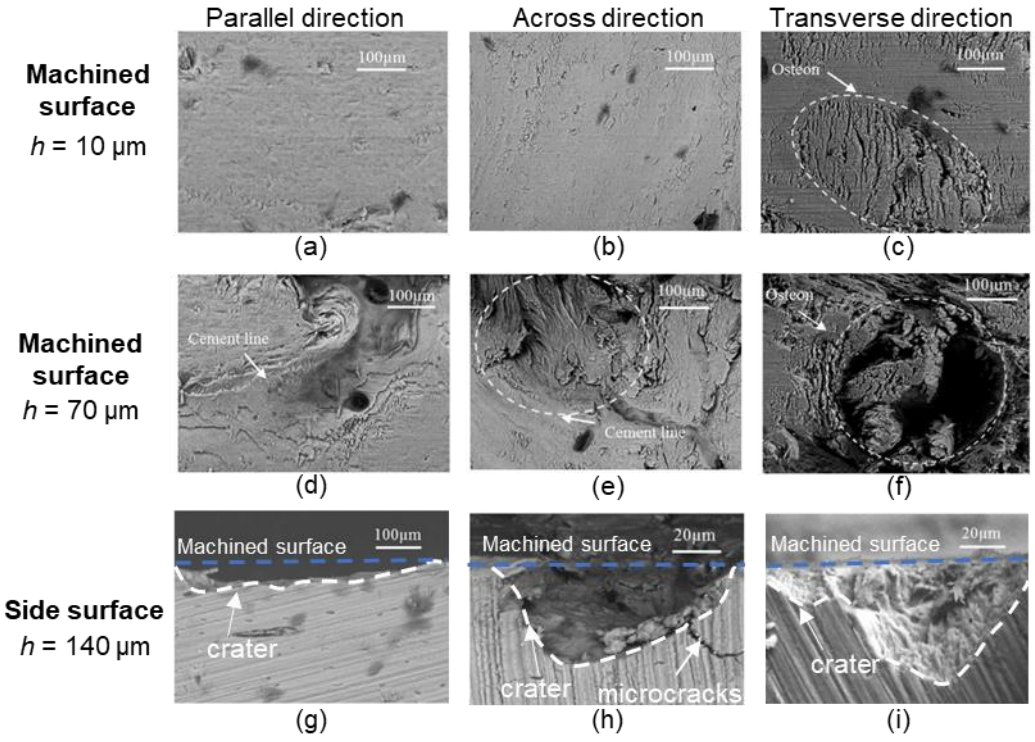

Fig. 2.24. SEM images of the machined and cross-sectional surface morphology of cortical bone in three orthogonal cutting directions and three DOCs (Liao and Axinte, 2016a). (a–c) Machined surface for a small DOC, (d–f) machined surface and (g–i) cross-sectional surface for a large DOC (*h*). The employed tool was a straight cutting edge with 8° rake angle, 8° clearance angle and a 33 mm/min cutting speed was used.

The rake angle of the tool also affects the surface roughness and morphology. Cutting with a high (30°) positive rake angle produced low surface roughness in TD. While cutting with negative rake angles (up to –30°) had low surface roughness due to the smearing of a thin layer of mineralised bone matrix on the machined surface (Yeager et al., 2008) (Fig. 2.25). This smear layer phenomenon also was found after bone drilling, as it will be shown further.

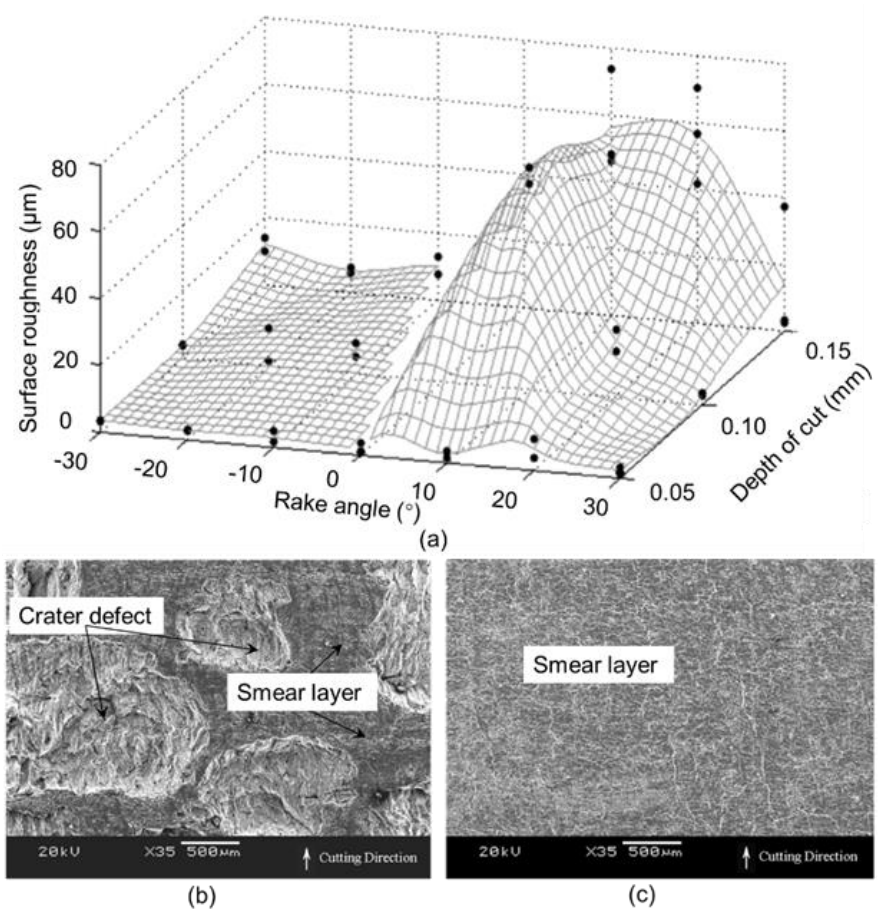

Fig. 2.25. Rake angle and DOC effects on surface roughness and SEM images of machined surfaces after orthogonal cutting in TD (Yeager et al., 2008)**.** (a) Average surface roughness under –30° to 30° rake angles and 0.05 to 0.15 mm DOCs, (b) machined surface morphology with 150 µm DOC, 20° rake angle, and (c) machined surface morphology with 150 µm DOC, −20° rake angle.

2.3.2 Mechanical damage – Hole quality in drilling of cortical bone

As mentioned before, the hole quality is critical for the primary stability of the implantation or restoration after surgical operation since it affects the bone-implants

interface strength and cellular response. When considering the removal of screws, a strong integration between bone and fixation components is a disadvantage. According to related studies, the hole quality of cortical bone can be divided into the following categories from a mechanical perspective: hole-entrance quality, hole-position accuracy, hole-wall quality and hole-exit quality (Fig. 2.26). The specific damage form and the influence of drilling process parameters, tools, environments, and techniques to improve the hole quality are discussed below.

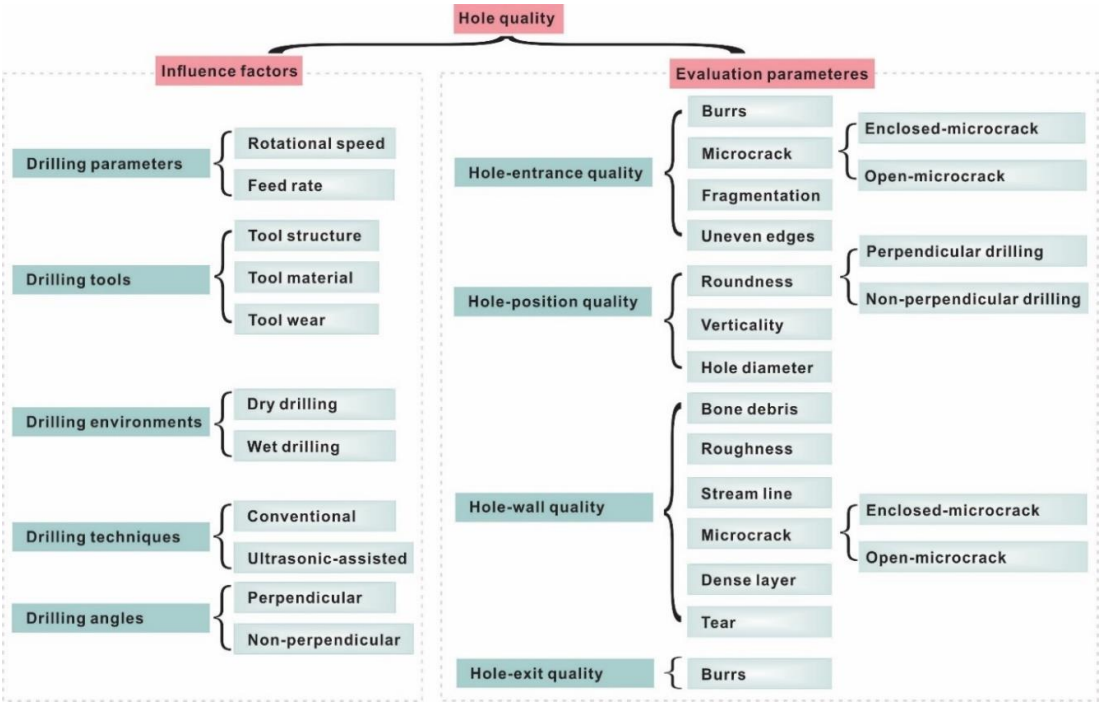

Fig. 2.26. Review scope of bone hole quality after drilling.

2.3.2.1 Hole entrance quality

To ensure the hole-implant interface contact area and stress distribution, the ideal hole in surgery is damage-free, round and has a size equal to that of the drill (Fig. 2.27a) (Ohashi et al., 1994; Singh et al., 2016b). However, various defects, including burrs, delamination, enclosed microcracks (fractured surface in contact) and open microcracks (separated fracture surface), occur at the hole-entrance during drilling of cortical bone (Fig. 2.27b-f).

The drill design and drilling parameters are important to burr formation and circularity of bone hole-entrance. Compared with abrasive-coated and hollow drills, twist drill gives fine and circular holes in perpendicular drilling due to the sharp cutting edges give shear-driven material removal mechanisms. Abrasive-coated and hollow drills generate burrs and non-circular holes by given abrasion-driven material removal mechanisms because the chip evacuation flutes are lacking (Gupta et al., 2017b; Singh et al., 2016b). The burr information and circularity of hole-entrance could be detrimentally affected by drilling with an increasing feed speed from 50 to 200 mm/min and a rotational speed from 1000 to 2000 rpm (Ying et al., 2020). Compared to the penetration angle (the angle between the normal of the surface and the drill axis, θ), the point angle, helix angle and web thickness have a less significant effect on the burr and microcracks around the hole edge (Noorazizi et al., 2017). The number, length and width of microcracks around the hole-entrance surface lack investigation.

Another significant parameter affects hole surface quality were penetration angle, since the non-perpendicular drilling occurs due to the uneven bone surface or specific surgical location. Penetration angle of 30° gives the rough hole surface compared to perpendicular drilling (θ=0°) because larger penetration induces skidding of drill (Noorazizi et al., 2017). Considering the drill skidding mechanisms under non-perpendicular drilling, a unique step tip with a thinned wed thickness as 17%, an optimal point angle of first step as 45°, point angle of second step as 90° and a transition arc as 0.6 mm could improve the hole-entrance quality with fewer closed microcracks and defects by switching the cutting mechanism from FC and SCC modes to the SC mode when compared with a conventional twist drill (Shu et al., 2020b).

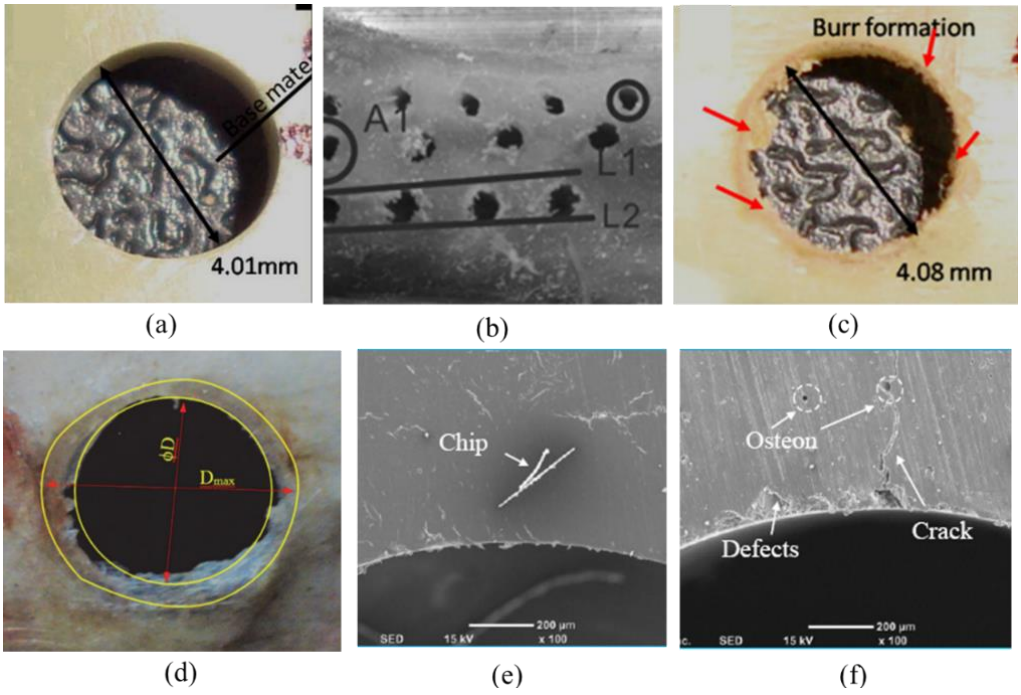

Fig. 2.27. Hole entrance quality after drilling of cortical bone. (a) Ideal hole quality (Singh et al., 2016b), (b–c) hole with burrs (Singh et al., 2016b), (d) delamination measurement (Koluaçik et al., 2020), (e) "closed" cracks at entrance surface (Shu et al., 2020b), (f) "open" cracks at entrance surface (Shu et al., 2020b).

Delamination at hole entrance (Fig. 2.27d) is one of the most common problems encountered in drilling of composite materials, including cortical bone. The average value of delamination increased with the rotational speed from 400 to 3000 rpm, the feed speed from 10 to 240 mm/min, drill point angle from 60° to 140° or helix angle from 12° to 35°. Because of the increase of rotational speed, feed speed or drill point angle, the production of different sizes and numbers of chips that could get stuck at the interface of drill bit or erode the machined surface and hole's wall increased, thereby inducing larger frictional forces and shear stresses. The increase of helix angle facilitates easy removal of the chips during drilling, thus avoiding the additional force induced by the clogging of drill bit and reducing the percentage of delamination. Among all of these factors, feed speed was found to be the most dominating factor affecting the delamination during bone drilling (Koluaçik et al., 2020; Pandey and Panda, 2015; G. Singh et al., 2021). Twist drills produced poor hole quality with delamination layers. Such defects were inexistent in the hole produced by a hollow

drill with a 80-100 grit diamond-coated (Gupta et al., 2017b). Compared with conventional drilling, the delamination observed in the VA drilling with a frequency greater or equal to 20 kHz is slight or even non-existent, because segmented small-size chips were generated by the intermittent contact during VA drilling. And these chips are easily evacuated from the drilling zone during the retraction of the tool due to the longitudinal vibrations of the tool, phenomenon that does not occur in conventional drilling (Gupta et al., 2017c; G. Singh et al., 2021; Singh et al., 2015).

2.3.2.2 Hole position and geometric errors

The hole shape can be non-cylindrical due to the axis of the holes deviating from the intended axis of the hole when drilled by the surgeon without a guide plate or robotic assistance (Fig. 2.28a,b). Drill geometry affects the deflection of the hole walls (Zhang et al., 2019). The incremental spindle speed and feed rate values cause the cylindrical and circular hole shapes to deteriorate to oval (Koluaçik et al., 2020). Hole diameter is another important parameter because it directly affects the stability of the screw implantation. The ultrasonic vibration amplitude applied on drill affects the hole diameter for hole forming due to the elastic recovery of bone tissue after tool removal. However, this phenomenon of increased hole diameters only reported by (Li et al., 2016).

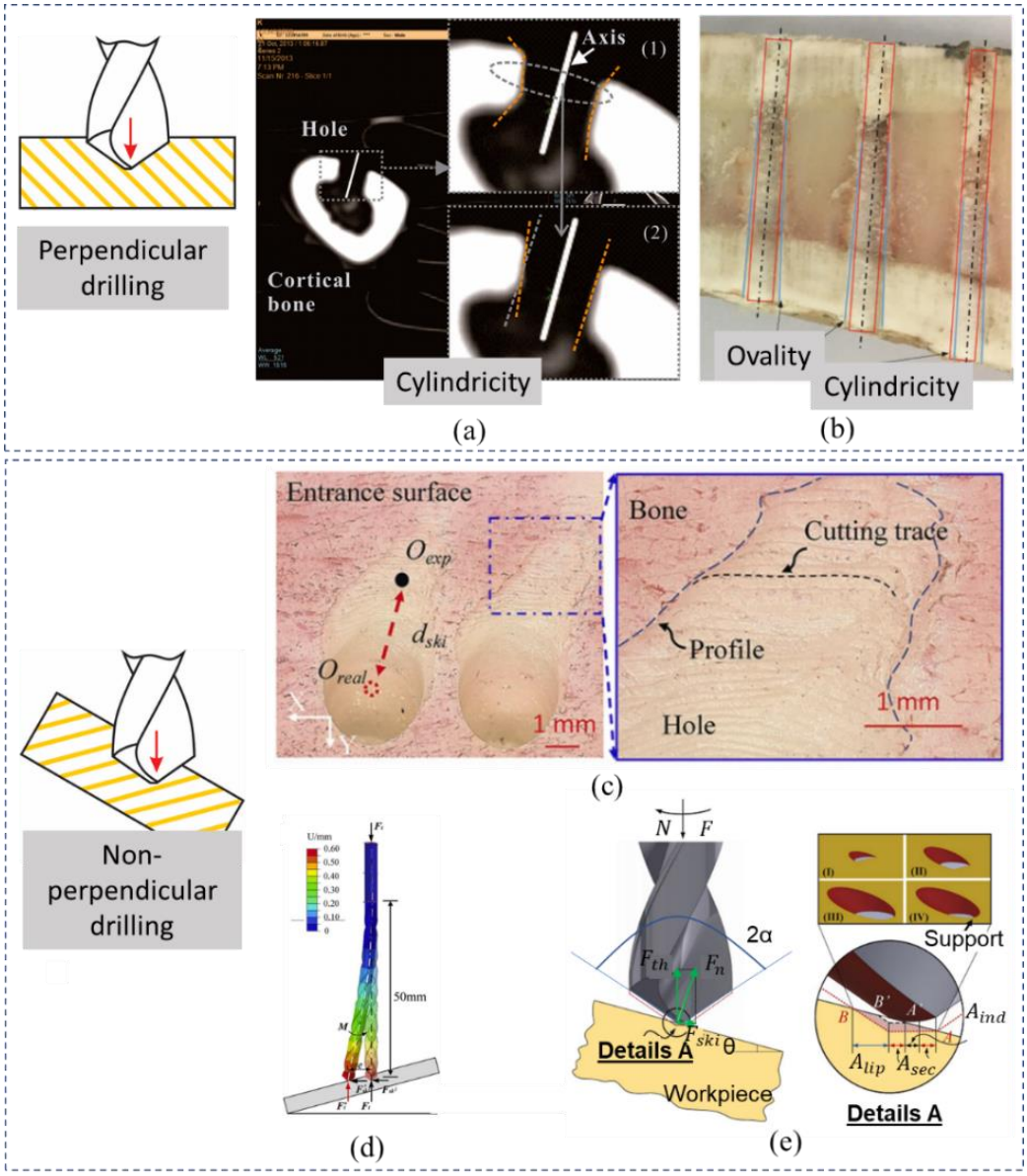

Fig. 2.28. Hole position quality after drilling of cortical bone. (a) CT images of bone hole cylindricity (Zhang et al., 2019), (b) optical images of hole ovality and cylindricity (Koluaçik et al., 2020) and (c) non-circular hole in non-perpendicular drilling (Shu et al., 2020b).

Skidding of drill bit along bone surface directly affects the accuracy of hole position and the screw or pin to be placed in the hole (Fig. 2.28c). Drilling high aspect-ratio holes are common in orthopaedic surgery. The large-aspect-ratio drill bit (typically longer than 60 mm and smaller than 4.2 mm diameter) are more prone to skidding and bending. The surgeon's ability to drill accuracy (within ± 4° error) is limited, particularly at penetration angles larger than 30° (Brioschi et al., 2016).

The skidding mechanism of $0<\theta<90-\omega$, where θ is penetration angle, 2ω is the point angle of drill bit, is discussed below (Fig. 2.28e). At the beginning of drilling, only the cutting lip and the unilateral secondary cutting edge are initially in contact with the bone surface, therefore, a skidding force (F_{ski}) is generated because of the asymmetry of the cutting areas on both sides of the X-plane. Subsequently, F_{ski} increases with the indentation zone and the entire secondary cutting-edge penetrating the bone surface. Drill skidding is inclined to be reduced as a support bone emerges on the lower side of the hole while increasing the cutting depth (Shu et al., 2020b). The improvement of the chisel edge is critical for preventing drill skidding because the cutting action of the chisel edge bears most of the thrust force during bone drilling. Several studies have been conducted to prevent drill skidding in bone drilling and recommended using three-fluted drills for it to have a higher bending stiffness (Bertollo et al., 2010, 2008) or using a step drilling bit with a small point angle of 45° followed by a second one of 90° and thinned web as 17% (Shu et al., 2020b).

2.3.2.3 Hole wall quality

Surface roughness is a direct indication and the most widely used variable to characterise the surface characteristics of the machined surfaces, which depends on the drilling parameters, drill bit geometry and drilling techniques. At high cutting speeds of 3000 rpm with diameter of 4 mm, chips erode the surrounding walls with larger centrifugal force thus increase the surface roughness. In this case, the surface roughness increases with the feed speed (from 50 to 150 mm/min) because larger feed leads to an increase of chip volume removed per unit time, which is translated into thicker chip size removed in the SCC or FC modes, as elaborated in previously (Koluaçik et al., 2020; Singh et al., 2016b). Twist drill gives a better surface with lower surface roughness than abrasive coated and hollow tools because the differences of cutting mechanisms (Liao et al., 2017; Singh et al., 2016b). Cutting fluid (distilled water or saline solution) and VA drilling can improve the surface roughness due to the

reduced cutting force and easier chip evacuation (Alam et al., 2009; Sheng, 2016). For example, the arithmetic average roughness of conventional and VA drilled hole surfaces is 1.75 and 1.37 µm, respectively (Singh et al., 2015). The repeated use of surgical drill also affects surface roughness because wear of the drill cutting edges results in blunter cutting lips leading to fragment bone particles trapped on the hole surface and causing increased friction force (Alam et al., 2020).

Bone debris, drill streaming line, tissue tearing, dense layer, closed microcracks, open microcracks and smearing also be found on the inner hole wall surface (Fig. 2.29). Bone particles and parallel streamlines (Fig. 2.290a,b) on the hole inner surface support the results of surface roughness and can also lead to an increase of stress within the bone-implant interface. Feed speed in the range of 10 to 40 mm/min shows a more significant impact on the particles and streamlines than the spindle speed in the range of 600 to 2400 rpm with diameter of 4 mm though both of them have a positive correlation with the quantity of particles and streamlines (Jindal, 2016). Tissue tearing (Fig. 2.29c) was founded by histological analysis with mm-scale slicing of the bone tissue, which can inherently induce cracks, was only reported by Zhang et al. (Zhang et al., 2019) and lack a clear understanding.

The number, width and length of microcracks generated increased with the decrease in rotational speed or increase of feed rate for both conventional drilling and VA drilling. For example, a longer, wider and larger number of cracks produced at a lower rotational speed of 1000 rpm than at a higher speed of 3000 rpm in conventional drilling. The length and width of cracks increased as the feed speed increased from 10 to 50 mm/min (Gupta et al., 2017c; R. P. Singh et al., 2021). A significant decrease in the number, dimensions and density of microcracks produced on the inner drilled surface with VA drilling in comparison to conventional drilling because the drilling force generated (Gupta et al., 2017c; Singh et al., 2015; R. P. Singh et al., 2021; Wang et al., 2013). The maximum length of microcracks generated by conventional drilling exceeded 300 µm could lead to bone fracture and/or deterioration in areas of weak

bone structure for they can penetrate the osteons. While the mean length of microcracks for vibrational drilling is 100 µm, approximately, which might be repaired by self-remodelling of bone (O'Brien et al., 2005; R. P. Singh et al., 2021; Wang et al., 2013). All these studies demonstrated that the cutting force and torque are related to the microcracks generated during drilling.

Pull-out strength of screws, a force required to pull a screw out of its foundation from bone, was used to understand the influence of processing parameters on bone remodelling (Agarwal et al., 2020; Bertollo et al., 2010; R. P. Singh et al., 2021). The increase in the intensity and width of microcracks reduced the stability between the inserted screw and the bone, therefore, reducing the pull-out strength of the screw. Greater surface roughness of the drilled hole in a bone exhibits greater pull-out strength because more anchoring is provided by the roughened surface. However, the relation of surface roughness and crack formation, which can cause implant failure, is still unclear.

The dense layer (Fig. 2.29d) on the hole wall was only reported on a VA micro-hammering investigation owing to the repetitive "forging" and "squeezing" action on the fractured bone lamellae. The thickness of the dense layer can be reduced by the high amplitude of 75 µm and hammering with conical tip. It is thinner at larger point angles (120° with respect to 60°) because the squeezing action that pushes bony tissue aside is weaker when the drill tip becomes blunter (Li et al., 2017, 2016).

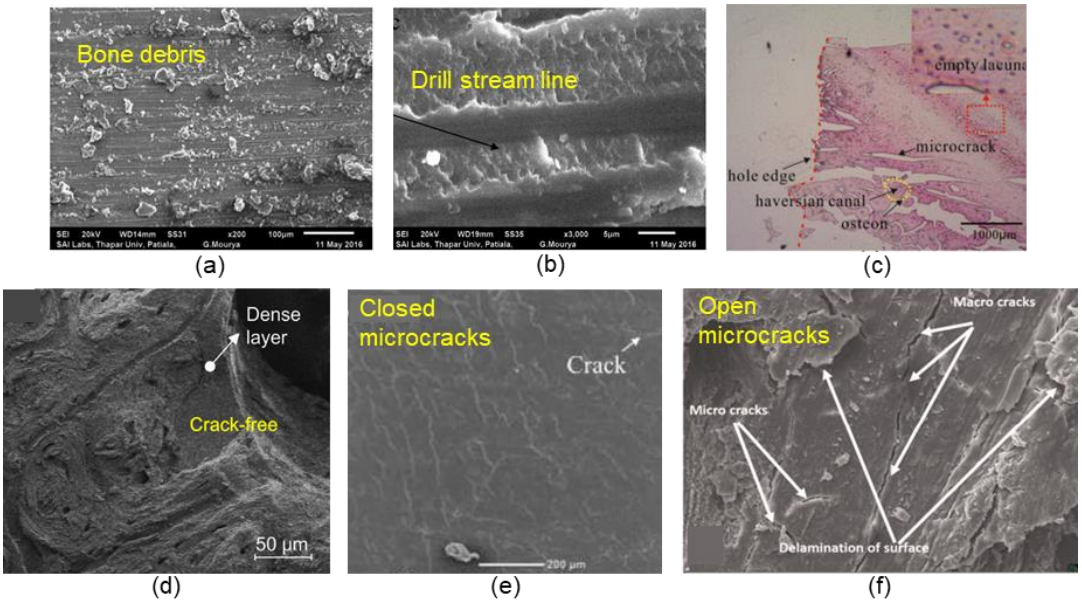

Fig. 2.29. Hole wall quality after drilling of cortical bone. (a) Bone particles(Jindal, 2016), (b) drill stream line (Jindal, 2016), (c) histological analysis of the hole edge morphology of hole wall (Zhang et al., 2019), (d) high-density surrounding layer produced by ultrasonic micro-hammering (Li et al., 2016), (e) closed microcracks (Shu et al., 2020b), (f) open microcracks (Singh et al., 2015).

2.3.2.4 Hole exit quality

A pyramid burr with multiple facets (usually between 3 and 5) is generated in the hole-exit when hammering by an VA conically tipped tool because the last few layers of bone lamella cannot withstand the thrust force and will bulge during drilling (Fig. 2.30). Cracks initiate and propagate along the radial direction due to the tensile stress in the bulged bone lamellae. The generation of the exit bur is thought to be related to crack propagation in the mineralised collagen lamellae. This hole-exit characteristic was investigated only by VA micro-hammering which has the "forging" and "squeezing" action that has been discussed before (Li et al., 2017, 2016). Whether this phenomenon would be induced during the conventional drilling process is unclear. Delamination and burr were also found around the hole-exit but lack of detailed research on the effect of cutting parameters, drill geometries and drill techniques (Koluaçik et al., 2020).

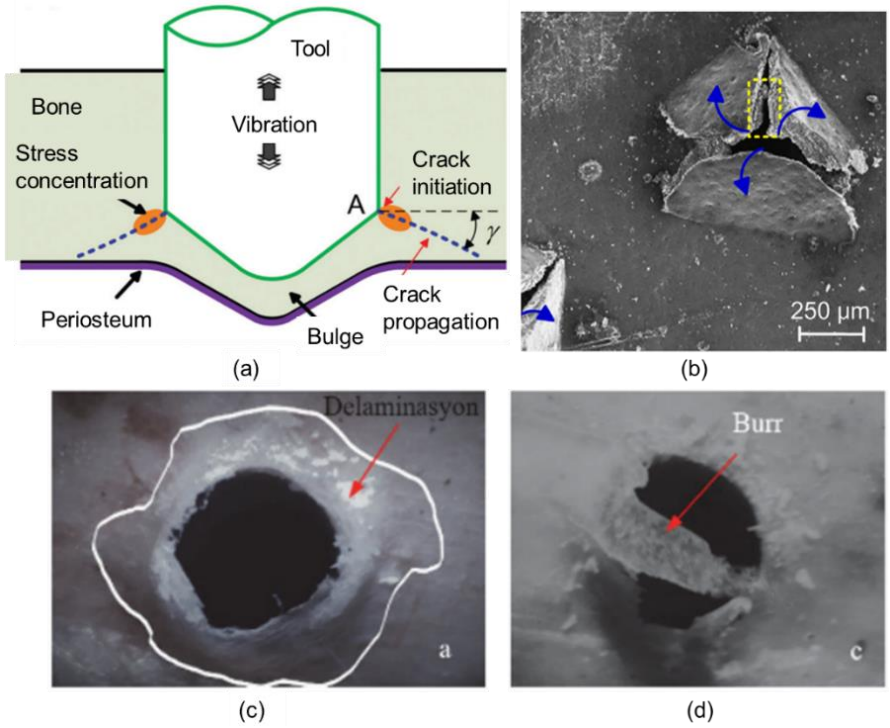

Fig. 2.30. SEM images of exit burr generated at the bottom surface of skull bone. (a) Overview of the exit burr generation (Li et al., 2016), (b) the pyramid burr generated by conically tipped tools (Li et al., 2016), (c) delamination (Koluaçik et al., 2020) and (d) burr formation (Koluaçik et al., 2020).

2.3.3 Thermal damage – Machining-induced necrosis in cortical bone

Thermal necrosis of bone, induced by the degree of temperature and the duration of exposure, has been of vital concern in bone machining surgical operations. In 1925, Brock et al. (Timon and Keady, 2019) described the local effects of heat during orthopaedic surgical operations. In 1941, Gillies et al. noticed necrosis around pins inserted into bone. In 1943, Anderson and Finlayson (Karmani, 2006) proposed the terms aseptic necrosis for local cauterisation, which they observed after pin insertion.

Though direct comparison between various investigations analysing the thresholds for thermal issue injury to bone are difficult to make as the studies have explored various exposure time, different criteria for tissue injury and observation at disparate points. Three types of thermal necrosis of bone, namely, necrosis, devascularisation and

osteon necrosis, detected by different methods were found in bone (Fig. 2.5 and Fig. 2.31).

Histological analysis, which requires haematoxylin and eosin staining (H&E staining, Fig. 2.31a) of μm-scale bone slices, is common to measure the degree of necrosis after machining. The death of osteocytes will leave empty lacunae (contain no discrete cell or nucleus) under light microscopy (Dahotre and Joshi, 2016; Franssen et al., 2008; Zhang et al., 2019). Terminal deoxynucleotidyl transferase dUTP nick end labelling staining (TUNEL staining) and Annexin V-FITC/PI staining can detect the extent of death of osteocytes (Aghvami et al., 2018; Shu et al., 2020a). In TUNEL staining (Fig. 2.31b), a zone of necrosis (marked by an arrow) is evident around the edge of the osteotomy (dotted line). In Annexin V-FITC/PI staining (Fig. 2.31c), surviving cells and cells undergoing necrosis emit blue and red fluorescence, respectively. The H&E staining is easier to detect than other methods.

H&E staining can also detect the appearance of the vasculature after machining. As shown in Fig. 2.31d, the vessels in the endosteal envelope of drilled bones evenly manifested protein substances present in the blood vessel lumen, especially immediately adjacent to the cutting position. Radiographic images after staining by disulphine blue (Fig. 2.31e) and spalteholz (India ink, Fig. 2.31f) showed substantial haematoma formation, vascular disruption and lower perfusion deficiency in the vicinity of hole (Field and Sumner-Smith, 2002).

The “osteon necrosis”, where the Haversian canal size could be altered with the degree of necrosis within the tissue, is shown in Fig. 2.31g (Zhang et al., 2019). At low levels of necrosis, a relatively complete osteon starts to appear. An increasing necrotic damage increases the Haversian canal’s apparent diameter, resulting in an “eaten” or necrotic osteon. These observations were done via a histological analysis, which required mm-scale bone slicing (i.e. cutting) with a microtome. Further research is

required to identify the exact source of damage because the microtome slicing might induce osteon damage.

Among all thermal damage inspection methods, the depth of empty lacuna (distance between the cutting site and filled osteocyte) detected by the histological analysis is the most common criterion for thermal damage of bone. This depth of damage layer indicates the heat penetration to cause cellular death. Higher temperatures produce deeper necrotic layers in drilling (Karaca et al., 2011). The longer the drilling time, the larger the necrotic depth because the heat source from the drill stays in the tissue for a longer period (Franssen et al., 2008).

The depth of empty lacuna obtained in PD tends to be larger than in TD, whereas cracks in PD are more difficult to occur because more energy is converted to heat in the TD where more cracks are generated and less energy is left for heat generation (Zhang et al., 2019). The necrotic thermal damage could decrease by lowering the cutting speed and increasing the feed rate (James et al., 2014; Karaca et al., 2011; Singh et al., 2018), both resulting in lower temperatures with shorter drilling times but at the expense of larger thrust forces. Variations on drill geometry also result in different heat generation and bone necrotic damage (Augustin et al., 2008; Saha et al., 1982). Lower necrosis is expected for drills with a shorter chisel edge because a larger chisel edge facilitates higher friction (Kanaya et al., 2019; Shu et al., 2020b). The increase of the number of flutes and edges of drills would decrease the depth of empty lacuna due to their enhanced chip evacuation that allows for less heat transfer between the chips and the bone (Zhang et al., 2019). The osteonecrosis region was greater in the specimens of the conventional drilling than VA drilling (Pourgiv, n.d.).

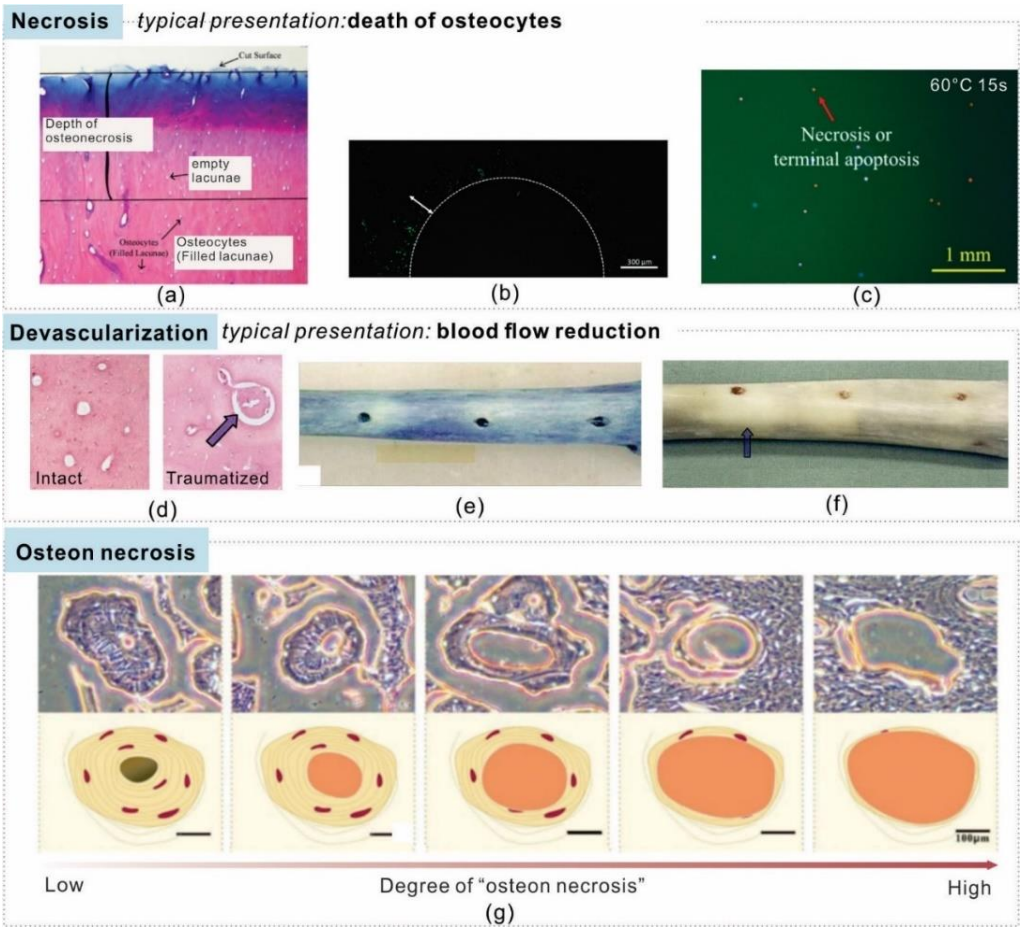

Fig. 2.31. Types of thermal damage and identification methods in cortical bone. (a) H&E staining (Dahotre and Joshi, 2016), (b) TUNEL staining (Aghvami et al., 2018) and (c) Annexin V-FITC/PI staining (Shu et al., 2020a) for assessment of necrosis; (d) H&E staining (Field and Sumner-Smith, 2002), (e) disulphine blue (Field and Sumner-Smith, 2002) and (f) India ink for assessment of devascularisation and vessel trauma (Field and Sumner-Smith, 2002) and (g) H&E staining for assessment of "osteon necrosis" (Zhang et al., 2019).

Mechanical and thermal effects may couple with each other to create damage not only at the biological level but also at the micromechanical in bone machining. The accumulation of microcracks in the mineralised matrix of cortical bone can increase the incidence of stress fracture (Wang et al., 2013) and cause osteocyte necrosis (Noble et al., 2003). However, this is still lacking in-depth investigation.

2.4 Summary of the literature

In this chapter, an extensive review has been conducted regarding the structure and properties of cortical bone, its most usual conventional and non-conventional machining techniques and the usual routes for damage assessment and surface integrity evaluation of cortical bone post-machining.

First, the structure of cortical bone has been provided to understand the intricacies of its hierarchical and anisotropic microstructural arrangements, along with the vital functions that are performed by the cells that are embedded within the structure and that are necessary for keeping the metabolism and remodelling capacities of bone in a proper state. The relevant mechanical and thermal properties of cortical bone have also been included here, as they are of relevance for understanding the material response under loading (e.g. under machining). Second, with the aim of understanding the governing phenomena behind the usual surgically employed machining techniques of cortical bone, orthogonal cutting, drilling, milling and grinding have been reviewed and synthesised to provide a proper understanding of how each material removal method works. Moreover, two non-conventional machining techniques (i.e. vibration-assisted and laser machining) have been reviewed as they are promising techniques that show potential for surgical use. And third, the machining-induced damage, or surface integrity assessment, has also been reviewed with the aim of understanding the usual techniques employed by both the research and the medical community in terms of assessing the quality of the bone following a material removal process.

2.4.1 Research challenges and gaps

After an in-depth review of the presented literature regarding bone machining and its damage assessment techniques, several research gaps have been identified. These are listed below.

- There is no clear understanding on the relation between induced necrosis and the nature of the material removal method. There are only a limited number of studies on the relation of temperature and time with necrosis, but these have so far neglected the nature of the material removal process itself (i.e. if it is purely thermal or purely mechanical) and have focused instead on parameters optimisation to reduce necrosis.
- While several studies report on machining-induced mechanical damage, these mostly focus on superficial crack formation and surface roughness. However, no reports have been documents on the micromechanical integrity of bone near the machined subsurface. This aspect is surprising, since the mechanical properties near the machined subsurface play a major role when it comes to implant bonding and withstanding loading stresses.
- The role of interstitial fluid in cortical bone machining (in terms of cutting mechanism and induced damage) is unknown. This is both surprising (because it is such a characteristic feature of bone that has not been considered) and expected (laboratory setup is limited to ex-vivo bone testing, in which the bone is internally dry).

Chapter 3 - Methodology for the bone machining and damage assessment study

The aim of this research is to understand the machining-induced damage mechanism both in dry bone and in internally irrigated bone, as per different material removal techniques. As such, a significant amount of equipment had to be employed to allow testing in multiple conditions, as well as for performing material characterisation analysis following a machining process. This chapter includes all the experimental techniques and equipment that were employed throughout the work of this research.

The material employed in this research is bovine cortical bone, and since it is a tissue, especial care had to be taken when handling the bone specimens from the moment of acquisition up to the point of testing to prevent any handling damage, especially necrosis. This is the reason why the initial details on this chapter are to carefully describe the optimum bone handling process that avoids damage into the tissue.

Following this, the experimental equipment used for machining is described, including the conventional and non-conventional machine tools employed, along with the respective sensing and recording equipment that allows for analysis of cutting forces, temperatures, and chip formation process.

Finally, to assess the bone's integrity post-machining and to enable the analysis of bone damage as linked to the material removal process, numerous material characterisation techniques were employed, including Engineering, Materials Science and Biology/Medical instruments. These are also listed and described here.

3.1 Bone used in this study

Bovine femur (Fig. 3.1a.) has been used on these investigation as it resembles human bone in the macro- and microstructural composition, healing capabilities, apparent density, mineral content, elastic modulus and ultimate strength (Liebschner, 2004; Pearce et al., 2007). These characteristics make it a suitable human bone model for mechanical and biological testing on both the macroscale (e.g. tensile tests, impact tests, machining tests) and microscale (e.g. microindentation, micropillar compression, histology).

All bone samples were acquired from a local butcher with pre-discussed arrangements to receive the specimens as fresh as possible. Following this, the sample preparation procedures and machining trials were carried out immediately, with most machining tests occurring on the same day of acquisition and keeping the samples in a saline soaked gauze at -20 °C when not in use. Imperative care was taken to minimise the time between bone acquisition and bone testing (including sample preparation time) in order to preserve the mechanical and biological properties of bone as much as possible. In all instances, a control sample was used to guarantee that handling of the samples did not induce necrosis.

3.1.1 Sample preparation and handling

Immediately after acquisition from a local butcher, the femurs were manually cut with a reciprocating saw (Bosch PSA 700E, see Fig. 3.1b) at room temperature under abundant saline solution (Goh et al., 1989; Zhang et al., 2018) to extract the mid-diaphysis specimens (see Fig. 3.1c). The mid-diaphysis were further manually cut with the same tool to obtain rectangular prismatic bone sections suitable for being manually ground and polished into their final shape for the experimental trials.

At all times, when bone samples were not in use nor prone to immediate use, they were kept at -20 °C in a saline soaked gauze (Zhang et al., 2018) to prevent both biological and mechanical degradation.

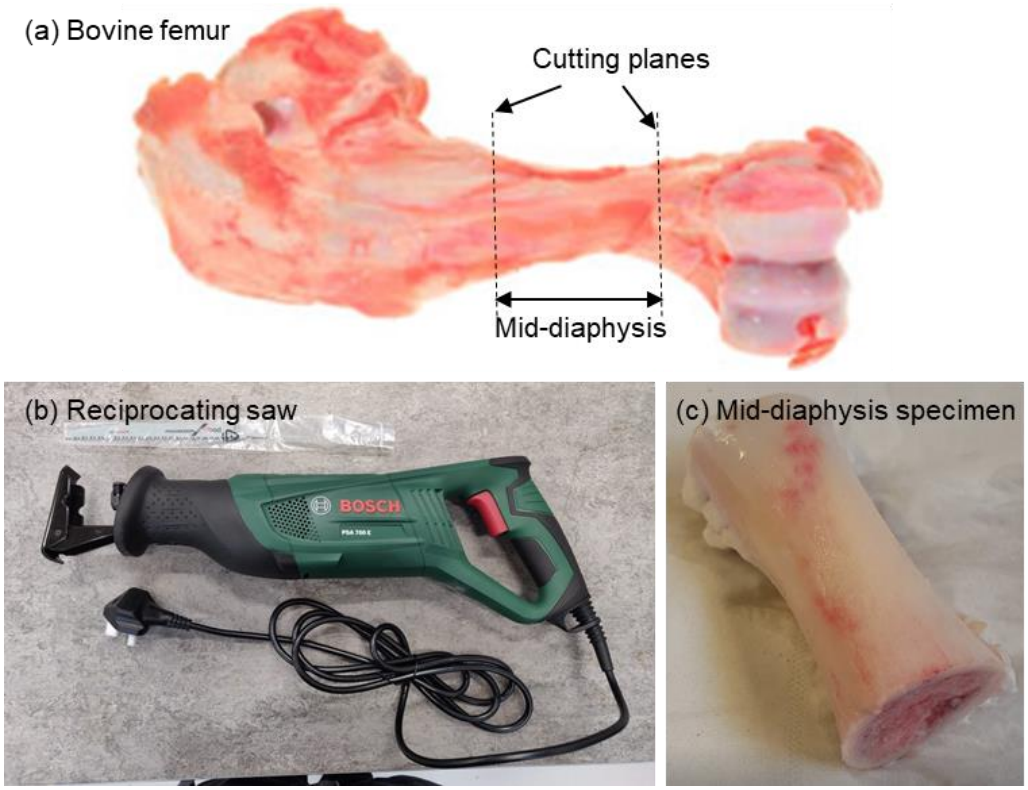

Fig. 3.1. Example of a bovine femur, the selected bone type in this study due its strong similarities to human bone. (a) Bovine femur as acquired from the local butcher. (b) A reciprocating saw Bosch PSA 700E was used to cut the bone in (a) along the dashed lines to extract the mid-diaphysis specimens. (c) Example of an extracted mid-diaphysis. Copious amounts of saline solution were used during the sawing process to ensure tissue preservation.

3.1.2 Grinding and polishing

Since micromechanical testing was employed in this research, it was ensured that sample grinding and polishing was performed in line with the appropriate standards for micro-testing ("BSI Standards Publication Metallic materials — Instrumented indentation test of hardness and materials parameters Part 1 : Test method," 2015). As a conservative measure, the same protocol of sample grinding and polishing was

performed for all samples, regardless of if they were to be used in micromechanical testing or not. This way it is ensured that all samples are of comparable surface quality.

The rectangular prismatic bone samples (see section 3.1.1) were manually ground and polished in a polishing machine (Tegrapol-21, Struers) under abundant saline solution with various SiC grit sizes (200 to 1200) and diamond particle suspension (6 to 1 µm) and 0.06 µm colloidal silica, employing fresh saline water rinsing (i.e. ultrasonic bath) after each step (Altman, 2009). Diamond particle suspension and colloidal silica steps were done in separate polishing cloths (MetPrep AlphaCloth Ref. 16 25 94).

The grinding and polishing set of steps were done manually (i.e. without mounting bone samples into resin or any other media) to prevent media infiltration into the porosities of the bone and to preserve tissue integrity in terms of cellular structure. This sample preparation process was used for all the experiments that required smooth flat surfaces, such as for general machining, Raman spectroscopy and micromechanical testing.

Fig. 3.2. Polishing machine (Tegrapol-21, Struers) used in this research. All samples were ground and polished manually (i.e. without embedding the samples in resin nor using the polishing head).

3.2 Novel design to mimic in-vivo conditions of cortical bone during machining

To mimic the in-vivo conditions of cortical bone during machining, a setup was designed to allow intraosseous flow through the natural porosities (i.e. Haversian and Volkmann's canals) of the bone; i.e. to enable an internally irrigated condition. This way, machining experiments could be conducted in a laboratory environment, while also considering the intraosseous flow condition that bone possesses in a normal surgical condition where body fluids and blood flow through the cortical tissue. Thus, the use of this setup enables a "closer to reality" condition of bone that can be employed to tackle objectives 2.1 to 2.3 (see section 1.3). The design of the mimicking setup is described in detail here.

The setup is made up of three main parts, which are additively manufactured: fluid pool base, channelled base and clamps (see Fig. 3.3 and Fig. 3.4).

1. **Fluid pool base:** this part serves several purposes. First, it is a rigid component that allows connection of the system to the dynamometer, hence permitting the measurement of cutting forces during experimental procedures. Second, the design has enough space to allow for the channelled base to be fixed inside of it, while also providing enough surrounding material with an appropriate wall height as to enable fluid collection (therefore the name 'fluid pool base'). This is designed this way to protect the dynamometer and the CNC table from getting any fluid that exits the bone.

2. **Channelled base:** this component has two primary functions. The first one is to allow for the bone sample to be clamped onto it for the machining experiments. The second, and most important one, is to allow fluid transfer from the fluid source (i.e. a syringe or pump) onto the bone sample. This is achieved by a small L-shaped channel that connects a standard hose connector (i.e. the syringe or pump tubing is

attached to this) to the lower part of the bone sample (see Fig. 3.4b,c). Importantly, the upper portion of the L-shaped channel ends in a cupule (i.e. half-sphere shape) that is protruding from the part, as shown in Fig. 3.4b. This sits beneath a half-sphere slot (milled) on the bottom of the bone sample. In-between these two, an O-ring serves to seal the space and allow for a small chamber of fluid to be located between the bone and the channelled base. This way, when a small pressure is applied to the fluid inlet, the flow is forcefully directed to exit through the bone, having no other option than to flow through the natural porosities of the bone.

3. **Clamps:** the clamps simply enable to fix the bone sample against the channelled base. Since an O-ring is used in the cupule, other O-rings are also added through the whole length of the bone, as to level it properly.

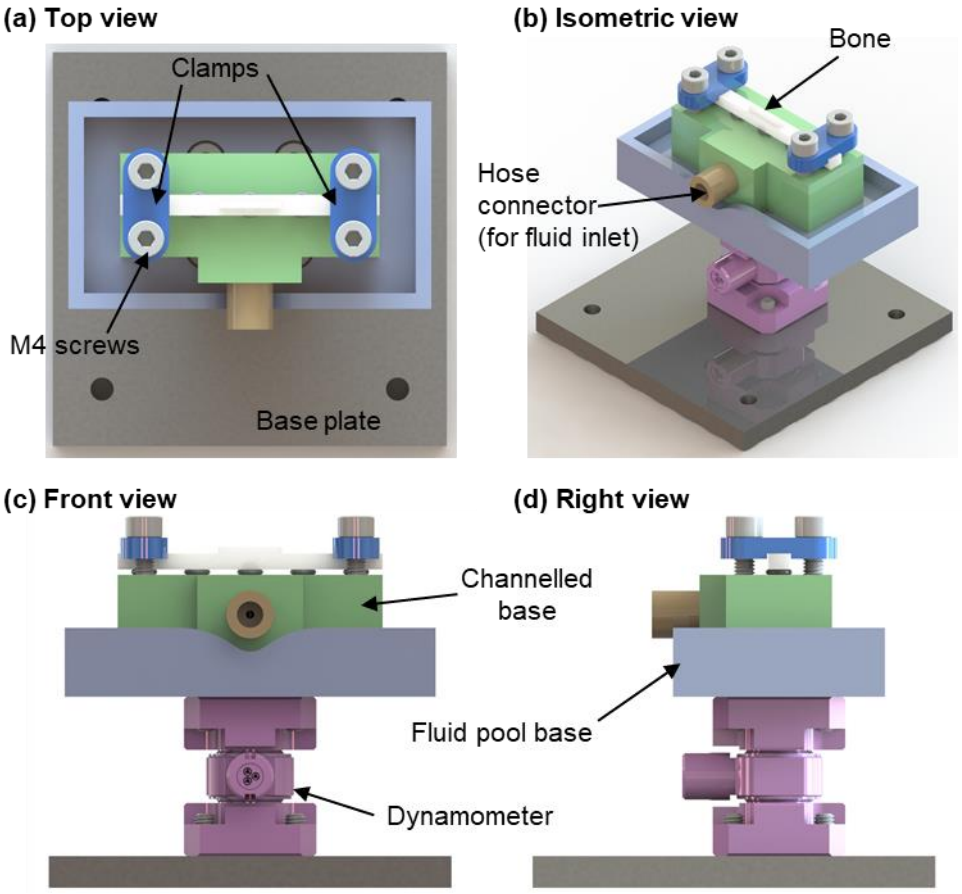

Fig. 3.3. Experimental setup designed to mimic in-vivo conditions of cortical bone during machining. Different views of the assembly, showing the most relevant components of the design. The clamps, channelled base and fluid pool base were produced via additive manufacturing.

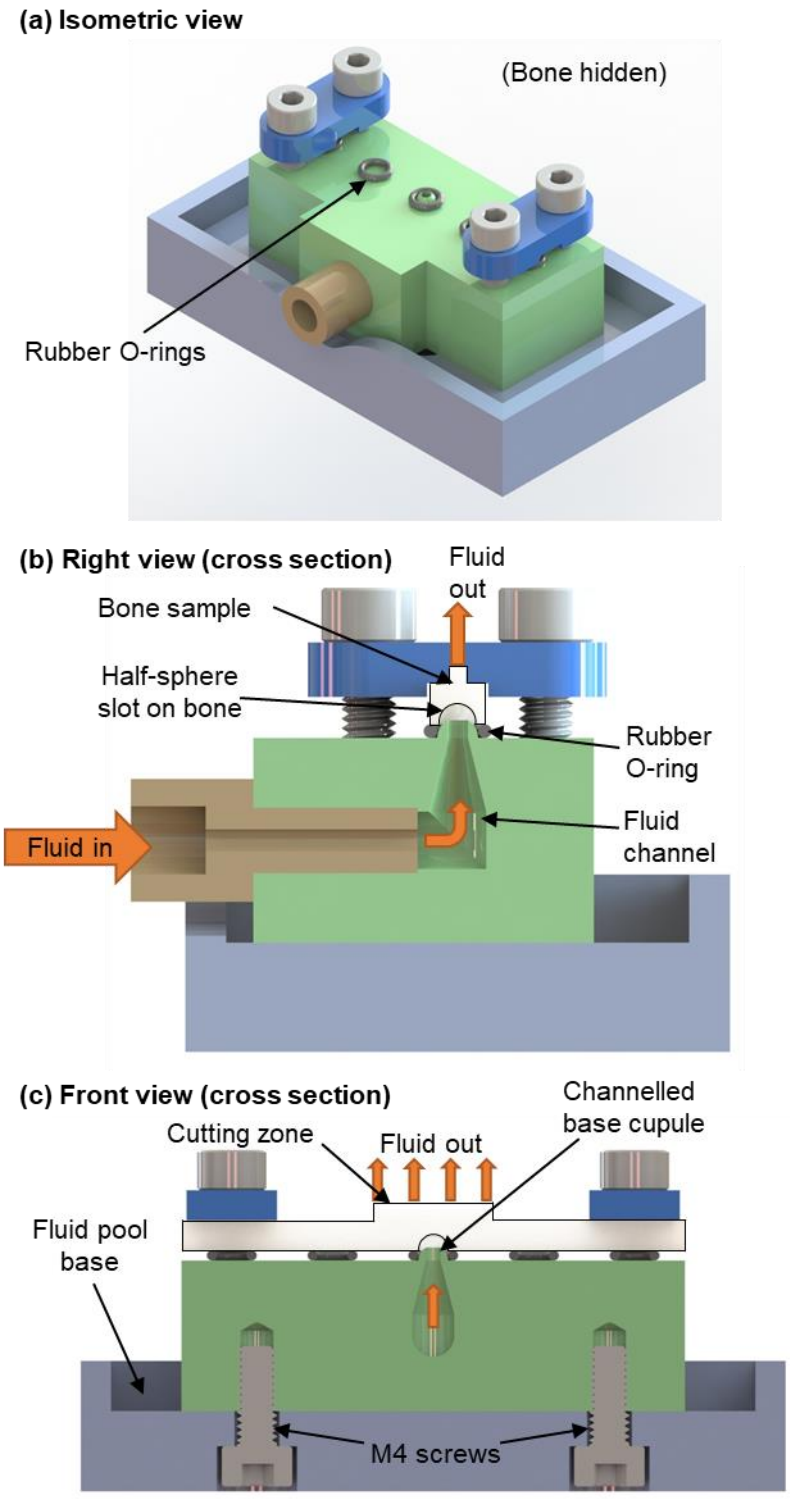

Fig. 3.4. Detailed and cross section views of the design. (a) The O-rings are located beneath the bone sample to properly level it. Moreover, the middle O-ring serves also as a sealing component for the fluid located in the bone's half-sphere slot. (b) Right view (cross section) of the design. The channelled base has a protruding cupule of material that seats beneath the bone, which is why a spherical slot is milled to the bone on this side, with the O-ring clamping and sealing in-between. (c) Front view (cross section) of the design. Orange arrows designate the direction of the fluid flow.

The additively manufactured components were produced with stereolithography, using a Formlabs Form 3+, employing *Durable* and *Rigid* resins and a 100 µm layer thickness. All the components (including the dynamometer) were assembled and fixed onto a base plate (see Fig. 3.3), which enabled clamping onto the milling machine table. All the fluid flow was controlled manually with a syringe that was connected to the hose connector.

This design enabled the possibility of internally irrigating the bone samples that were used in this research, thus enabling the understanding of the role of interstitial fluid in the behaviour of cortical bone under machining conditions.

3.3 Experimental equipment for material removal trials

This section includes a detailed description of the machine tools and experimental measurement equipment (e.g. sensors) employed during this research.

3.3.1 Conventional machining equipment, tooling and sensors

3.3.1.1 CNC milling machine

A milling machine tool (770 PCNC Tormach, Fig. 3.5) was employed to perform conventional machining trials on bone samples, including drilling, orthogonal cutting and fly cutting processes. The selected machine tool allows feed speeds of up to 3.4 m/min in X and Y, while up to 2.8 m/min in Z; and a spindle speed in the 175-10000 rpm range. This set of capabilities allow the replicate cutting speeds that could be encountered in surgical environments (e.g. 8 m/min when drilling with a 3 mm drill at 1000 rpm (Feldmann et al., 2017)), making it suitable for the scope of this research.

Fig. 3.5. Milling machine (770 PCNC Tormach) used in this study for orthogonal cutting and drilling trials.

Prior to any machining process, the samples were manually prepared according to sections 3.1.1 and 3.1.2 and they were kept in a hydrated condition (i.e. immersed in saline solution) up to being positioned in the CNC table. All machining experiments were conducted at room temperature. If the samples were frozen prior to machining, they were thawed at room temperature prior to commencing the trial.

3.3.1.2 Drilling setup

Drilling experiments (see Fig. 3.6) were performed on the 770 PCNC Tormach milling machine (Fig. 3.5). The bone samples were clamped with a state-of-the-art vice and a flat surface was first machined on the top surface using mild machining parameters and copious amounts of saline solution to achieve flatness prior to the drilling tests. Additionally, to prevent inducing corrosion into the machine due to the use of saline solution, an acrylic box (visible in both Fig. 3.5 and Fig. 3.6a) was used to contain all the fluid and the bone chips that resulted from the cutting action, thereby protecting

the CNC's table from corrosion. The drilling experiments were carried out with a 4.5 mm drill, as it is representative of those used in surgery.

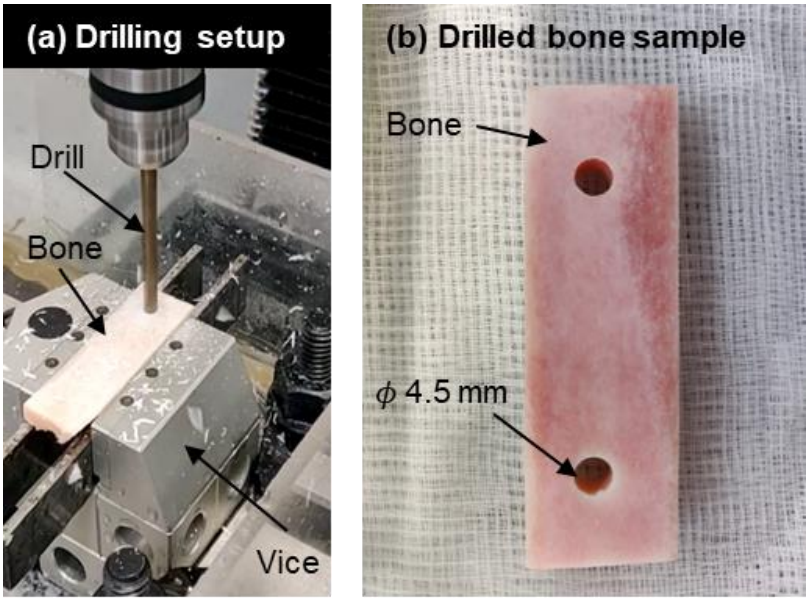

Fig. 3.6. Drilling setup. (a) Experimental drilling setup in the milling machine. (b) Example of a drilled sample.

3.3.1.3 Orthogonal cutting setup

Orthogonal cutting trials (see Fig. 3.7) were performed on the 770 PCNC Tormach milling machine (Fig. 3.5). The bone samples were clamped in place with an in-house designed additively manufactured fixture, as shown in Fig. 3.7a. The reason for this is that such a fixture not only serves as a clamping device but is also allows fluid pumping through the porosities of the bone sample, aspect that is discussed in-depth in Chapter 5 to study the role of internal irrigation in the tissue during machining.

The samples for this type of test were pre-machined to produce a small orthogonal cutting section on their top surface, as shown in Fig. 3.7b,c. A solid carbide 2 mm cutting edge with rake angle α=8°, clearance angle of 8° and edge radius of 1 μm from Seco Tools was subsequently employed to perform the cutting trials.

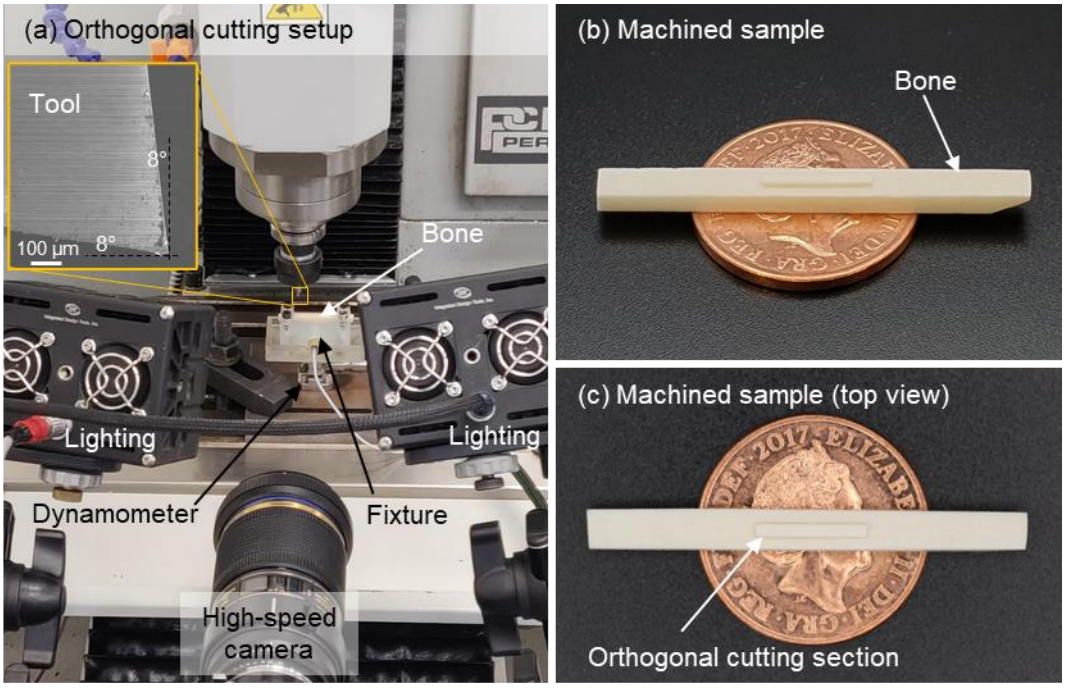

Fig. 3.7. Orthogonal cutting setup. (a) Experimental orthogonal cutting setup in the milling machine. The setup shows also additional equipment required for the experiments (i.e. high-speed camera, lighting and dynamometer). (b) Perspective view of a machined (i.e. after the orthogonal cutting test) bone sample. (c) Top view of the same sample.

3.3.1.4 Fly cutting setup

Fly cutting trials were performed on the 770 PCNC Tormach milling machine (Fig. 3.5), using the same setup and sensing equipment as those used in orthogonal cutting. However, the fly cutting tests were performed with the primary goal of studying thermal damage in bone, while the orthogonal cutting trials were performed to study the chip formation process and the involved cutting and thrust forces. In these tests, a single straight tooth milling tool (HSS) of 6 mm in diameter was employed.

3.3.1.5 Sensing equipment

For the purposes of this research, three main aspects were measured and recorded during the material removal process: forces, temperatures and chip formation.

Dynamometer

A Kistler type 9317C miniature 3-component piezoelectric dynamometer (Kistler Instruments LTD) was used for measuring the orthogonal components of the forces involved in the cutting processes. The dynamometer is 25 x 25 x 30 mm^3 (see Fig. 3.8) and can measure forces of up to 2kN, which is enough for the experiments due to the small depths of cut that were employed.

The dynamometer was mounted directly below the fixture for holding the bone (see Fig. 3.7a) during the machining process and it was connected to a Kistler charge amplifier and a National Instruments data acquisition card that permitted the recording of the forces in a computer, using the software Signal Express, by National instruments. All the forces were measured at 10 kHz acquisition rate and the data was processed in a custom code in MATLAB.

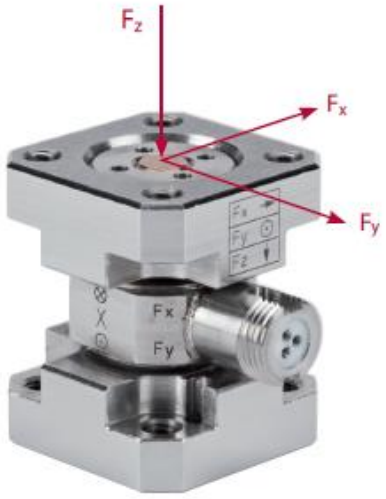

Fig. 3.8. Dynamometer (Kistler 9317C) used for forces measurements during cutting.

High-speed imaging

An IDT Y4-S2 Motion Pro high-speed camera (Integrated Design Tools Inc.) was used for recording the orthogonal cutting processes performed on the bone workpieces with the objective of observing the chip formation mechanism on each cut (see Fig. 3.9a,b). It was included in the setup to record the machining processes at an acquisition rate of

5 kHz. Motion Studio was used to process the videos recorded during the bone cutting procedures. The video processing consisted mainly in adjusting the brightness, contrast, playback speed and zoom-in area of the recorded videos. The camera was connected to its own power supply and one set of led lights was used to illuminate the section of interest. The video was saved after each cutting procedure on a computer by using the Motion Pro software by IDT.

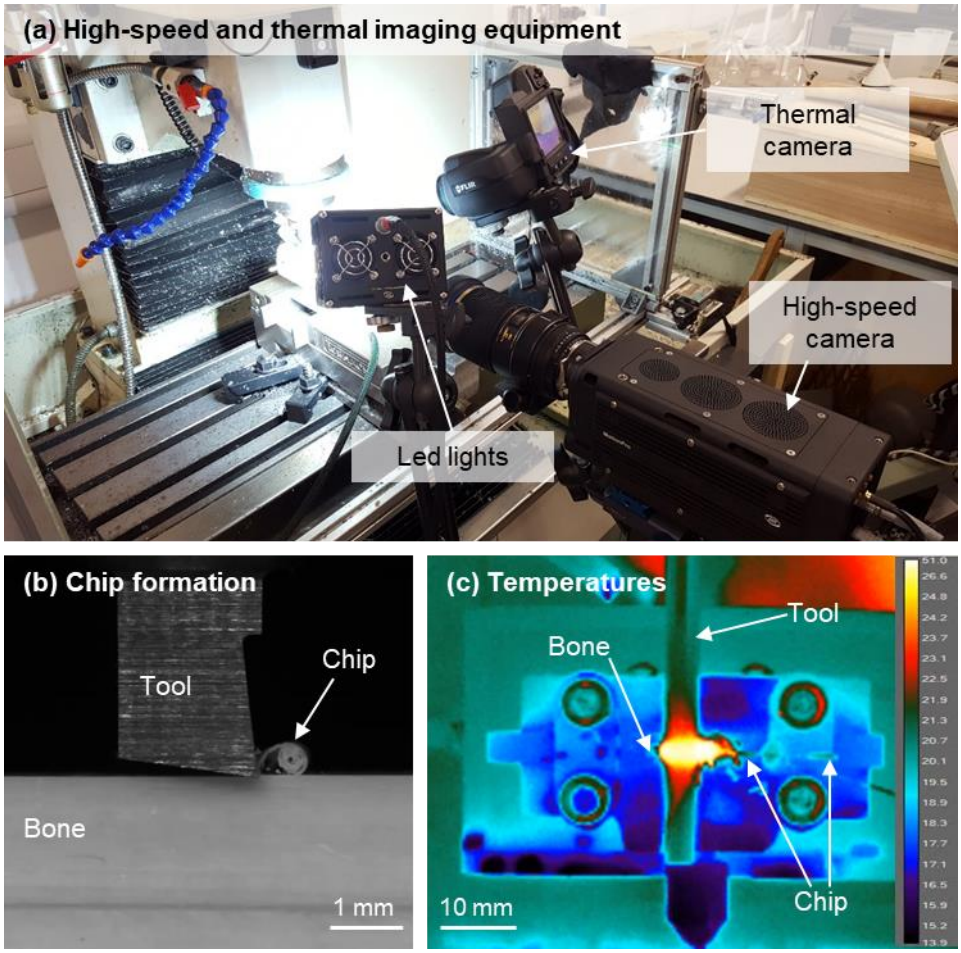

Fig. 3.9. High-speed and thermal imaging equipment used in this research. (a) Overview of the equipment as it is set up in the machining environment. (b) Example of a chip formation video frame obtained with the high-speed camera. (c) Example of a video frame obtained with infrared thermography.

Infrared thermography

As explained in Chapter 2, temperature measurements in the tool-bone interface is challenging, and while using thermocouples offers a greater accuracy (regarding the temperature location), it also implies that the bone samples need to be pre-machined

with micro-holes for placing the thermocouples, which could induce damage to the tissue. However, since the objective of study is damage inducement in bone, using thermocouples could not be a feasible option. As such, the selected method for measuring the thermal fields was infrared thermography, as it provides a "damage free" application.

Two different cameras for infrared thermography were employed. For the drilling experiments, a FLIR T460 thermal imaging camera (FLIR Instruments) with 30 Hz capacity was employed; this camera is shown in Fig. 3.9a. However, for the fly cutting experiments, a FLIR A655SC (FLIR Instruments) with 50 Hz frame rate was used instead; an example of an acquired image from this camera is shown in Fig. 3.9c.

Regardless of the camera model, the camera was set to capture the thermal frames with an emissivity value of 0.95, which is the expected value for bony tissue (Feldmann and Zysset, 2016). All data extracted from the IR cameras was post-processed in the ResearchIR software (developed by FLIR). The post-processing consisted on defining the region of interest within the frame and exporting the data to a text file, which was then processed in a custom MATLAB code.

3.3.2 Non-conventional machining equipment

Laser machining was used in this research as a non-conventional material removal method for cortical bone. Three Nd:YAG laser types were used with varying pulse widths (Fig. 3.10), i.e. picosecond pulsed (60 ps), nanosecond pulsed (200 ns), and continuous wave.

Besides the lasers, the experimental setup consists of a vertical translator (Aerotech AVS125), X and Y translation stages (Aerotech ALS130), a rotary stage (Aerotech ACS150) and a galvanometric scanner (Aerotech AGV-10HP) equipped with an F-theta lens (No. 4401-302-000-21). This multi-axis position system enabled an adequate control of the feed speeds for all the laser machining experiments (Fig. 3.10).

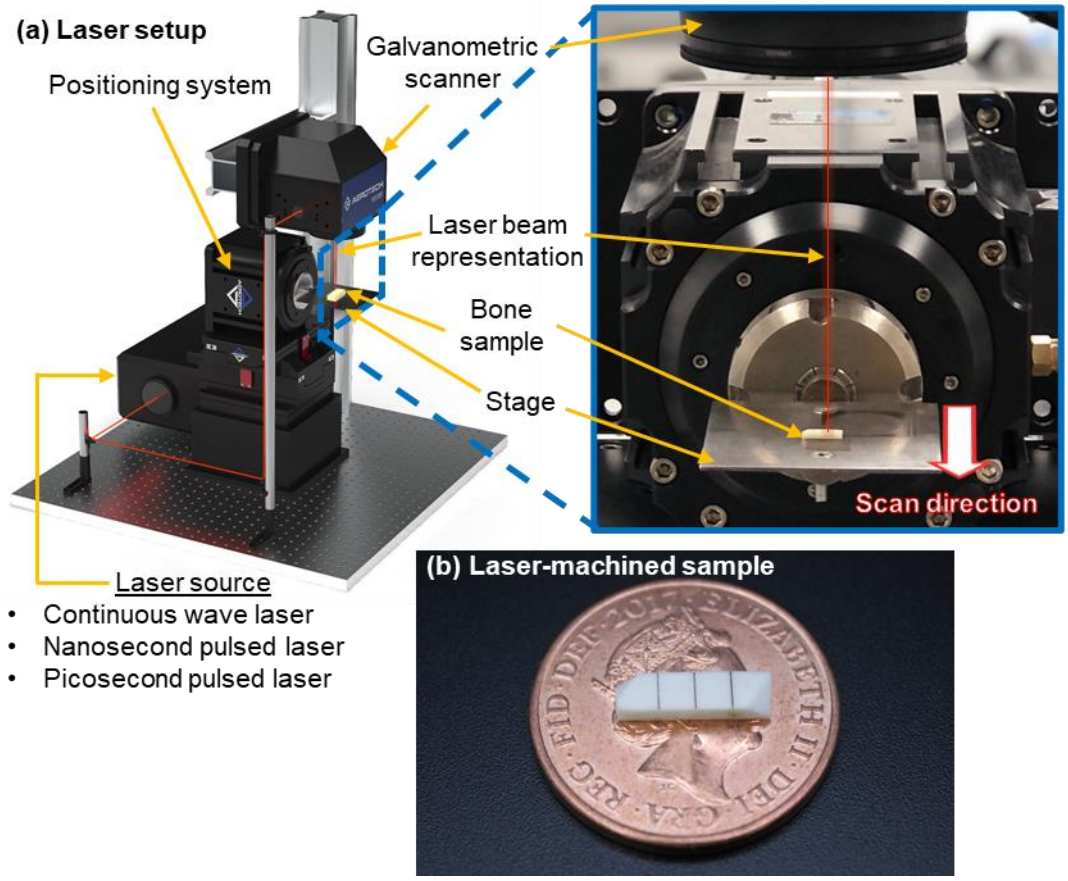

Fig. 3.10. Diagrammatic overview of the experimental setup for laser machining single trenches in bone. (a) The experimental setup uses three different lasers (represented as a single laser source for clarity) and a galvanometric scanner in conjunction with a multi-axis positioning system to control the feed speeds for machining single trenches in the bone sample. (b) Example of a machined sample with three separate trenches (visible charring).

Prior to the laser machining trials, the samples were manually prepared according to sections 3.1.1 and 3.1.2 . The samples were kept in a hydrated condition (i.e. immersed in saline solution) up to being positioned in the laser machining stage.

3.4 Material analysis techniques

Multiple material analysis techniques and surface characterisation methods were employed with the aim of assessing the surface and subsurface integrity of bone following a material removal process. These are detailed here.

3.4.1 Raman spectroscopy for bone quality assessment

The chemical composition of biological specimens can be obtained with Raman spectroscopy (Morris and Mandair, 2011); hence this technique was used to validate that the bone used in this study was chemically acceptable (i.e. within values stated in literature for healthy bone) to be employed for the experiments. A mapping was performed on the bone samples in dry condition (48-hour air-drying) using a confocal Raman microscope (Horiba LabRAM HR), employing a 785 nm laser excitation wavelength to minimise the fluorescence effect (Bachman and Ellis, 1965), 25 seconds of acquisition time, grating of 600 lines/mm and a 50x objective with numerical aperture of 0.55. To avoid tissue damage to the microstructure and cells, laser power was maintained below 5 mW (Notingher et al., 2003).

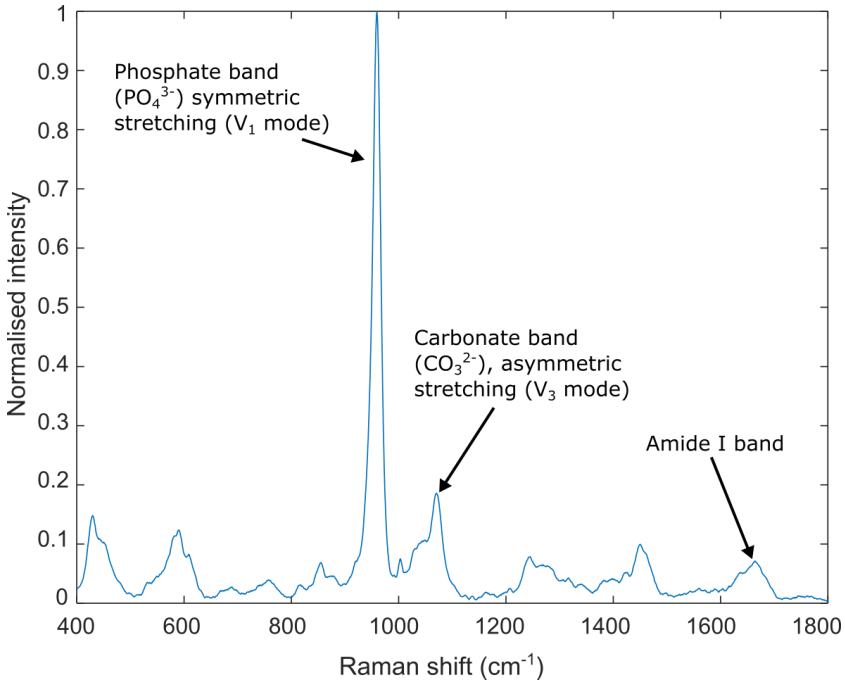

Fig. 3.11. Example of the obtained Raman spectra for the control sample. The most relevant bands are shown. Mineralisation is the amplitude ratio of the PO_4^{3-} band to the amide I band, carbonate substitution is the ratio of the PO_4^{3-} band to the CO_3^{2-} band and the crystallinity is the full width at half maximum (FWHM) of the PO_4^{3-} band.

The raw data extracted from the measurements was post-processed in a custom MATLAB code that was written to:

- Perform a baseline correction of the signal to remove sample background florescence.
- Clean the signal using a Savitzky-Golay filter of order 2.
- Normalise the amplitude of the signal.
- Identify the peaks of interest (see Fig. 3.11), which correspond to a specific mode of vibration:
    - The phosphate band (PO_4^{3-} symmetric stretching) in the 960 cm^{-1} mark.
    - The amide I band vibration of collagen (i.e. peptide carbonyl, CO) in the 1663 cm^{-1} mark.
    - The carbonate band (CO_3^{2-} symmetric stretching) in the 1071 cm^{-1} mark.
- Calculate the following (Akkus et al., 2004; Schwiedrzik et al., 2014b):
    - *Mineralisation:* this is the ratio of the phosphate band to the amide I band, which represents the mineral-to-protein (i.e. hydroxyapatite-to-collagen) ratio of the tissue. A larger value of mineralisation indicates a more mineralised collagen matrix.
    - *Carbonate substitution:* this is the ratio of the phosphate band to the carbonate band, which represents the inverse of the substitution of carbonate ions in the locations of phosphate ions. A larger value of carbonate substitution indicates a lower amount of carbonate ions replacing the phosphate ions.
    - *Crystallinity:* this is the full width at half maximum (FWHM) of the phosphate band. The lower the FWHM, the greater the crystallinity of the bone, implying a crystal lattice that is well-ordered.

A representative Raman spectrum of the bone utilised in this study is shown in Fig. 3.11. The plot is an average of a 22-point mapping on the bone surface, which resulted in a mineralisation of 12.12 ± 1.50 (average ± std dev, n = 22), a carbonate substitution of 8.19 ± 0.28 (n = 22) and a crystallinity of 19.29 ± 0.63 cm^{-1} (n = 22), which is in good agreement with values reported previously for ovine (Schwiedrzik et al., 2014a) and human (Yerramshetty et al., 2006) bone. This guaranteed that the samples used in this research exhibited a proper chemical quality.

3.4.2 Scanning Electron Microscopy (SEM)

Scanning Electron Microscopy (SEM) allows for high resolution imaging up to the nanometric scale, thereby superseding optical microscopes. As such, SEM has been largely employed in this research with the aim of assessing the surface quality of bone.

A FEI Quanta 650 SEM (Fig. 3.12a) has been used in this research to do general imaging of bone samples in high vacuum (HV) and low vacuum (LV) conditions. HV imaging allows to do sharper imaging, provided that the samples are dry and conductive, while LV imaging permits to image wet/hydrated samples at the expense of possible image charging. Due to the poor electrical conductivity of cortical bone, using this SEM provided the main advantage of allowing the samples to be imaged either wet (i.e. when the bone was fresh) or dry (i.e. when the bone was dry). In the case of dry bone imaging, the bone samples were additionally coated with a 25-nm gold layer via sputtering to minimise drift due to charging. Additional to imaging, this SEM was also used for in-situ micromechanical testing, as it is discussed in section 3.4.5 .

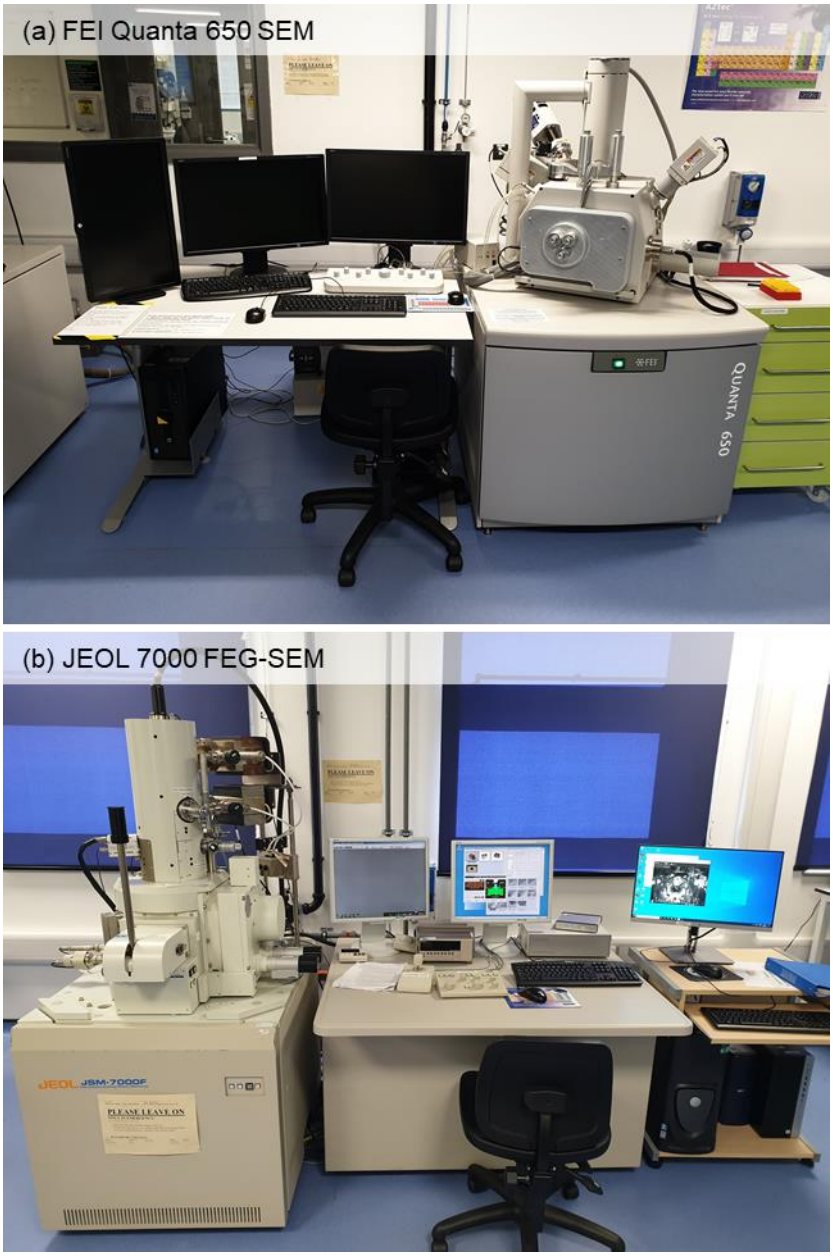

Fig. 3.12. Scanning Electron Microscopes (SEMs) used in this study for imaging. (a) A FEI Quanta 650 SEM was used for imaging in both HV and LV conditions. (b) A JEOL 7000 FEG-SEM was used for superior resolution imaging only in HV conditions.

A JEOL 7000 FEG-SEM (Fig. 3.12b) was additionally used for achieving superior resolution imaging in HV conditions. This is possible due to the Field Emission Gun (FEG) that enables higher voltages than the ones that are achieved with a tungsten filament SEM (such as that of the FEI Quanta 650).

Prior to any imaging, the samples were glued to standard aluminium SEM stubs using a silver adhesive (Agar Scientific).

3.4.3 Surface topography (Alicona)

3D inspection of machined bone samples was completed using the Bruker Alicona InfiniteFocus G4 (Fig. 3.13). The samples were inspected by non-contact probing with focus variation which allowed for measurements of the trench depths in the case of laser-machined specimens and surface defect and damage depths in the case of orthogonally machined specimens. This surface topography inspection allowed to assess the surface morphology of the samples post-machining. All the data was processed using the MountainsMap Premium software from Digital Surf.

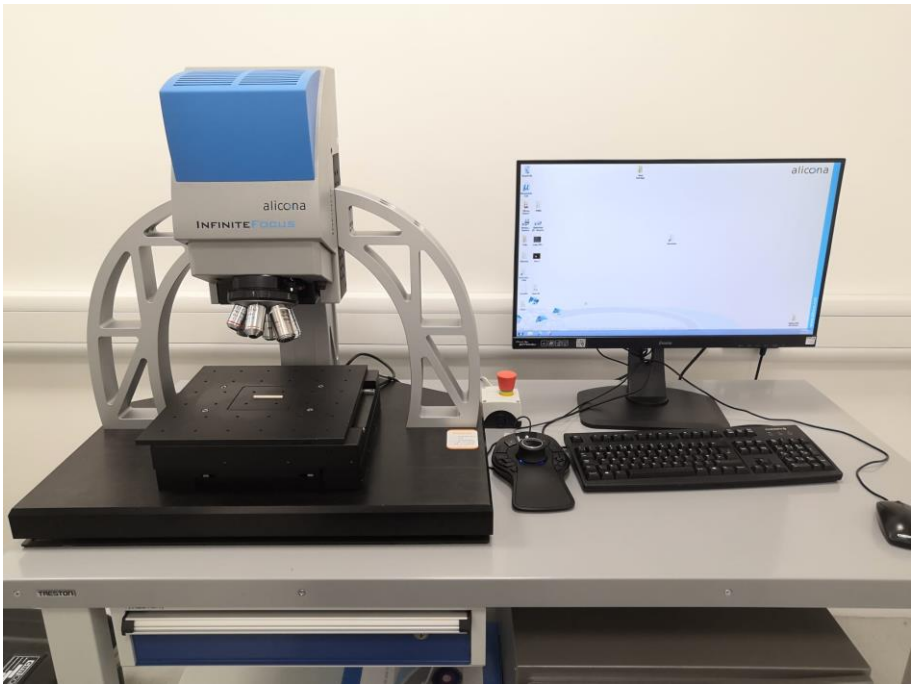

Fig. 3.13. Bruker Alicona InfiniteFocus G4 used in this research for surface topography analysis.

3.4.4 Focused Ion Beam (FIB) milling

Focused Ion Beam (FIB) systems could be regarded as an extension or add-in to an SEM, in which the FIB column employs a finely focused beam of ions (usually Ga ions) that can be operated similarly as a regular SEM. However, upon impact on the sample's surface, the ion beam removes material by sputtering it away, which is why this process is usually referred to as *FIB milling*. At high ion beam currents, the beam

is more aggressive upon the sample and is like a roughing material removal process. At lower currents, the ion beam is gentler upon impact, thereby relating more to a finishing process. Additional to this, if the region of interest of the sample is large enough, a low current could also be employed for imaging instead.

In this work, FIB milling (FEI Quanta200 3D FIB-SEM, Fig. 3.14a) was employed to fabricate micropillars beneath the bone's machined surface, as these were then compressed for micromechanical properties and failure mode analysis using an in-situ micromechanical testing unit (details can be found in section 3.4.5).

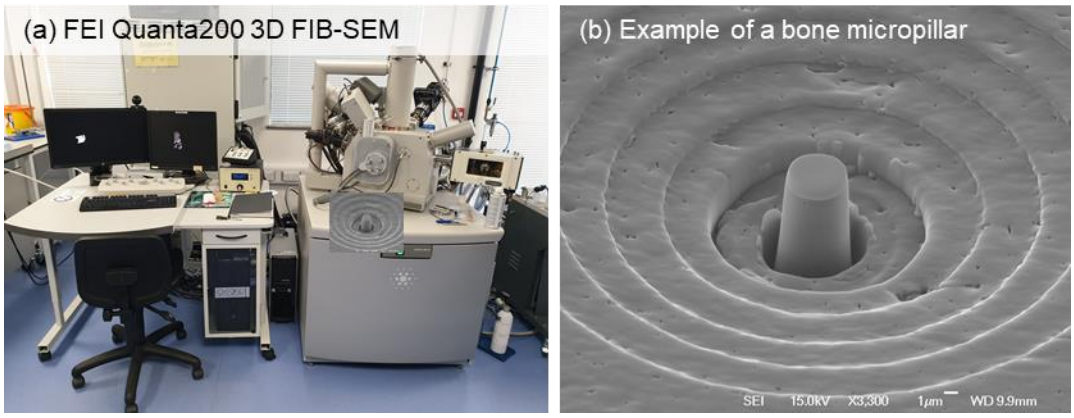

Fig. 3.14. Instrument used for FIB milling of bone micropillars. (a) A FEI Quanta200 3D FIB-SEM was employed for FIB milling bone samples. (b) Example of a FIB-milled bone micropillar (SEM image acquired with the JEOL 700 FEG SEM shown in Fig. 3.12b) with a specimen tilt angle of 50°.

The samples used for micromechanical testing were polished according to section 3.1.2 and were allowed a 12-hour period for air-drying, subsequently being coated with a 25-nm gold layer via sputtering to minimise drift due to charging. Prior to micropillar FIB milling, a 1.25 µm platinum (Pt) protective layer was deposited on top of each pillar location (the Pt layer is visible in Fig. 3.14b and Fig. 3.15a). Afterwards, each micropillar was milled similarly to a previously established protocol (Schwiedrzik et al., 2014a): circular trenches of 45 µm in diameter were milled at 7 nA to obtain 15 µm diameter posts (Fig. 3.15a,b); then, these were milled at 3 nA to obtain 7 µm diameter posts (Fig. 3.15c) that were finally polished at 0.3 nA to obtain

the final micropillar size of 5 µm in diameter and 10 µm long (examples shown in Fig. 3.14b and Fig. 3.15d).

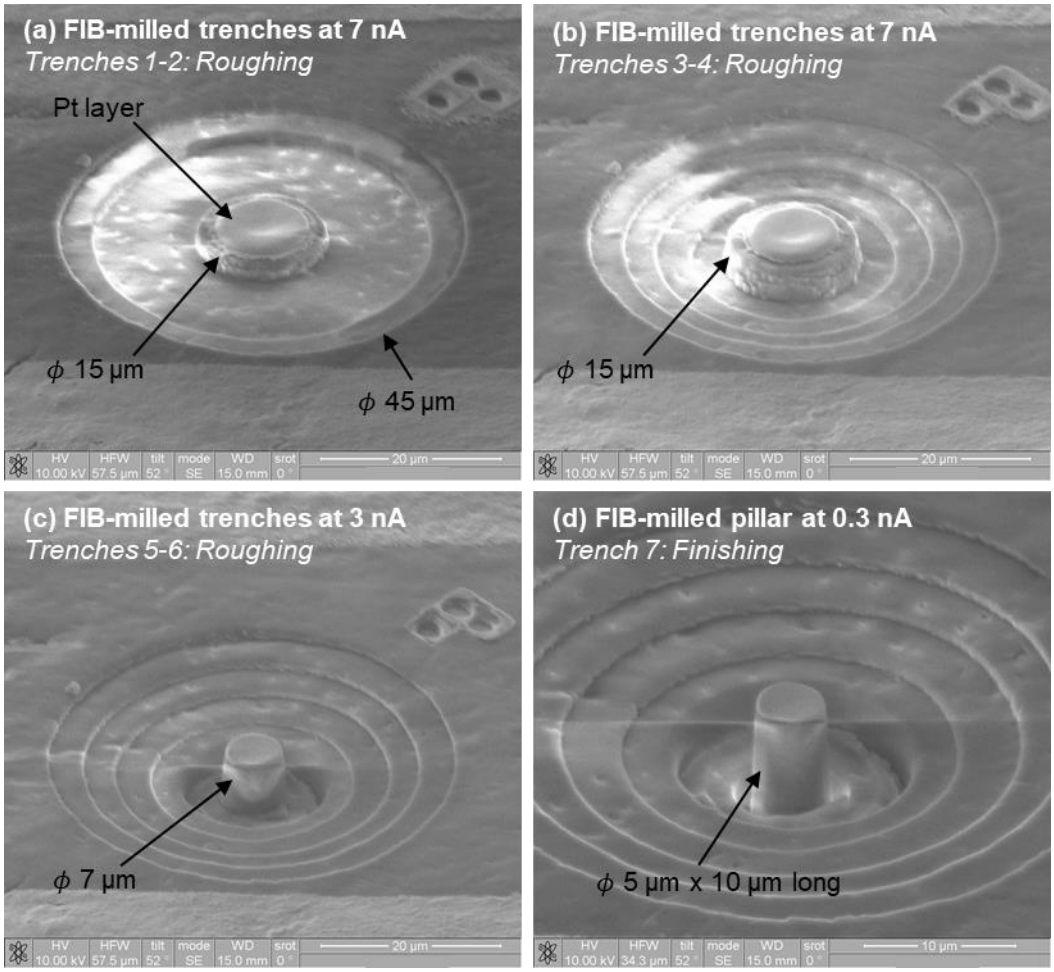

Fig. 3.15. FIB milling strategy for micropillar fabrication in cortical bone. (a) Pillar state after milling the first two trenches (1 and 2) at 7 nA. (b) Pillar state after milling trenches 3 and 4, also at 7 nA. (c) Pillar state after milling trenches 5 and 6 at 3 nA. (d) Finished pillar after a 0.3 nA polishing/finishing pass.

3.4.5 Micromechanical testing unit

Micromechanical testing, in the form of micropillar compression testing, was employed throughout this research for the purposes of micromechanical properties assessment and failure mode analysis in the machined subsurface of bone samples. To this end, an Alemnis Nanoindenter has been used in-situ within the FEI Quanta 650 SEM (Fig. 3.12a) for compressing the FIB-milled micropillars described in section 3.4.4 .

The Alemnis Nanoindenter is a versatile instrument that can be employed for micro- and nanoindentations, nanoscratching, micropillar compression, microbending testing, among other micro- and nanometric scale tests that yield a set of data corresponding to a localised material behaviour in both the elastic and plastic zones. This is achievable by designing a testing profile that can be either load-controlled or displacement-controlled. In the case of micropillar compression testing, displacement controlled was employed to have control over the micropillar compression strain rate.

In this case, the Alemnis Standard Assembly (ASA), as shown in Fig. 3.16a, was employed in this research. The ASA was fixed inside the FEI Quanta 650 SEM (Fig. 3.12) and all imaging and testing was done in HV conditions to minimise load and displacement drifts.

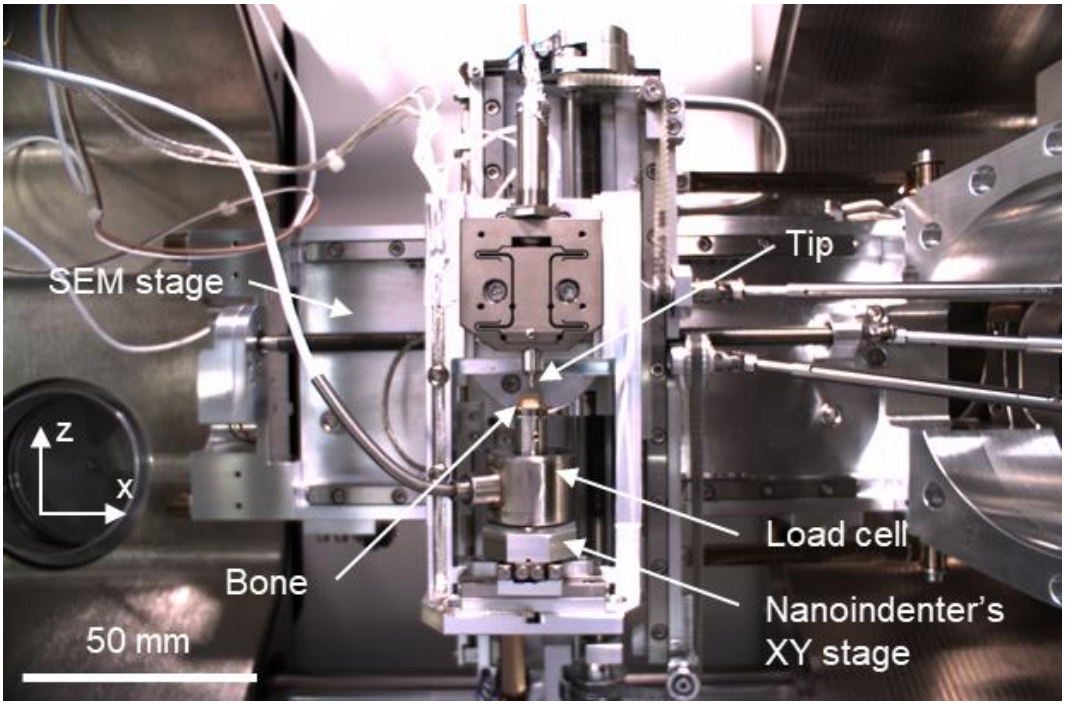

Fig. 3.16. In-situ micromechanical testing unit employed for micropillar compression testing. The Alemnis Standard Assembly (ASA) was mounted inside the FEI Quanta 650 SEM, thereby enabling in-situ micromechanical testing. The nanoindenter is equipped with an XY stage to move the sample, a load cell for force measurements and a piezoelectric transducer for precise motion control of the tip along the Z axis.

Raw load and displacement data was obtained for each pillar and was corrected for compliances associated with the nanoindenter's frame, platinum layer and sink-in effect (schematic shown in Fig. 3.17).

The Alemnis nanoindenter is a compliant system, implying that some portion of the measured raw displacement corresponds to the compliant displacement of the nanoindenter's frame. Since the compliance of the ASA was measured by Alemnis as $C_{Alemnis}$ = 0.0000043 m/N (according to the Alemnis Materials Mechanics Data Analyzer software, i.e. AMMDA), this enables to calculate the corresponding displacement of the nanoindenter's frame as a function of the load (P) as:

$$h_{frame} = PC_{alemnis} \qquad \text{Eq. 3.1}$$

Another source of compliance is the protective platinum (Pt) layer on top of each pillar. While the Pt is deposited to protective the pillar's material from FIB damage, it also implies that the pillar is not fully made of bone, resulting in two different materials being compressed during the test (see Fig. 3.17). Nevertheless, since Pt's modulus of elasticity (E_{Pt} = 168 GPa) is larger than that of bone (i.e. <20 GPa), its corresponding displacement (h_{Pt}) can be regarded as fully elastic and in accordance with the classic theory of Mechanics of Materials (Ashby and Jones, David, 2012). As such, h_{Pt} is a function of the thickness of the Pt layer (L_{Pt}) and the pillar's diameter (d_{pillar}):

$$h_{Pt} = \frac{4\,L_{Pt}}{E_{Pt}\,\pi\,d_{pillar}^2} \qquad \text{Eq. 3.2}$$

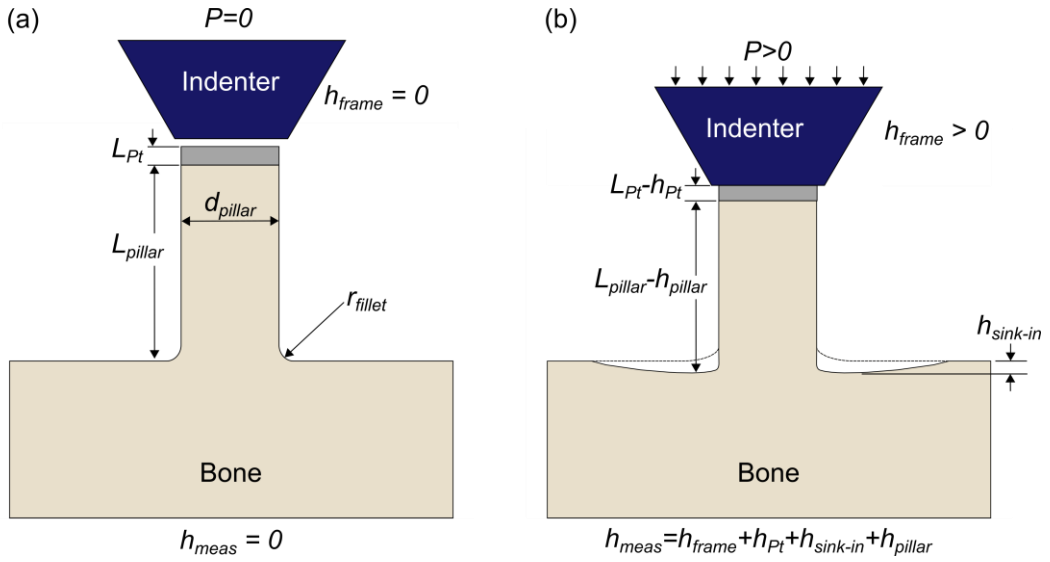

Fig. 3.17. Compliance analysis in micropillar compression. (a) Before testing, the measured displacement and force (*P*) are zero. (b) During testing, a portion of the h_{meas} is due to the nanoindenter frame (h_{frame}), the platinum layer (h_{Pt}) being elastically compressed, and the sink-in effect of the pillar into the bulk material ($h_{sink-in}$), which is also elastic. Since all of these are known, the real displacement of the pillar (h_{pillar}) can be straightforwardly calculated from the experimental data.

Additionally, another type of compliance is present during the test. Due to the pillar being attached to the bulk material on its bottom face, during the test, the pillar elastically sinks into the bulk material, creating a *sink-in* effect (see Fig. 3.17). To account for this, Sneddon (Sneddon, 1965), was able to derive the compliance of the flat punch's base in contact with an elastic half-space; and the solution was later modified to account for the fillet radius (r_{fillet}) that is created during FIB milling at the bottom of the pillar (Zhang et al., 2006), being this denominated as the *Sneddon correction*. Since the pillar and the substrate are both from the same material (i.e. bone), the displacement corresponding to this compliance can then be calculated as (Sneddon, 1965; Zhang et al., 2006):

$$h_{sink-in} = h - \frac{h}{1 + \left(\frac{L_{pillar}}{\frac{d_{pillar}}{2} + r_{fillet}}\right)\left(\frac{2}{\pi(1-\nu_{bone}^2)}\right)} \qquad \text{Eq. 3.3}$$

where υ_{bone} = 0.3 is the Poisson's ratio of cortical bone and L_{pillar} denotes the length of the pillar. Additionally, the fillet radius for the pillars was considered constant as r_{fillet} = 300 nm in order to be consistent with previous bone micropillar testing research (Schwiedrzik et al., 2014a).

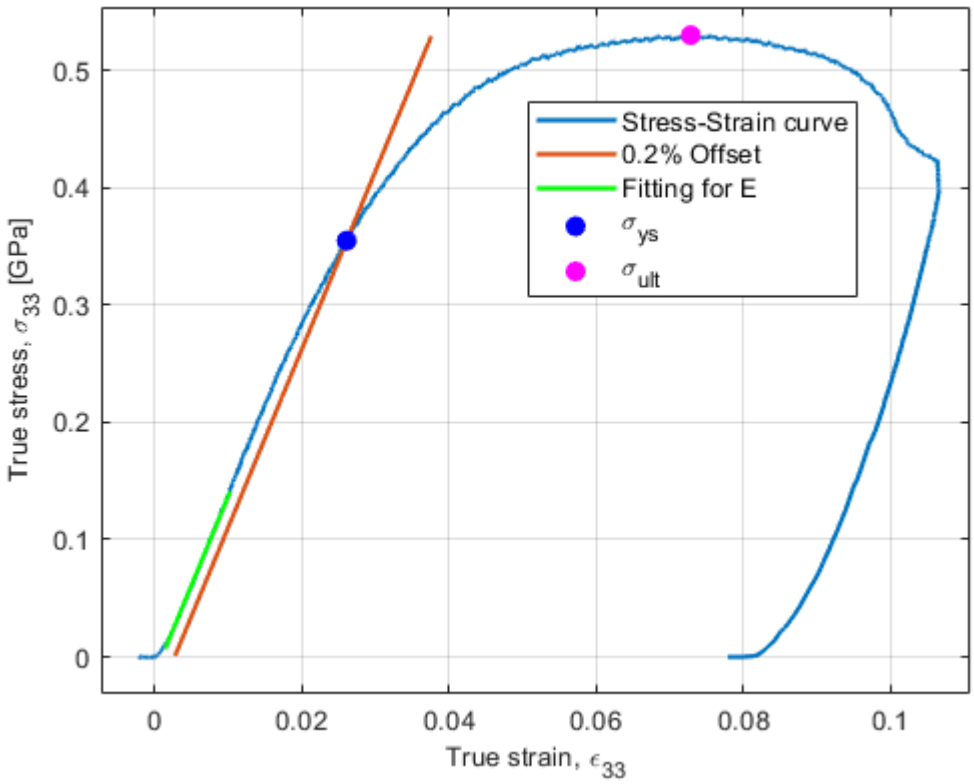

Fig. 3.18. Example of stress-strain analysis from a micropillar compression test. The true stress-strain data is calculated from the compliance-corrected displacement and load, while employing the assumption of negligible volume change. A portion of the loading region within the elastic zone is used for a linear curve fitting to calculate the Young's modulus of the material. Subsequently, a 0.2% offset curve is used to calculate the yield point (σ_{ys}), and the maximum stress prior to failure is taken as the ultimate stress (σ_{ult}).

After compliance correction, engineering stress-strain data was obtained following established protocols (Schwiedrzik et al., 2014a; Tertuliano and Greer, 2016) and true stress-strain data was derived with the assumption of negligible volume change (Ashby and Jones, David, 2012). Additionally, the yield point was calculated with the 0.2% offset rule and the ultimate stress was obtained as the maximum stress prior to failure. Data analysis was done both in AMMDA (Alemnis, Switzerland) and a custom MATLAB code.

3.4.6 Histological analysis for necrosis assessment

Histological analysis was employed in all experiments for studying the necrotic damage induced by a specific machining technique. Immediately (i.e. within 5 minutes) after the machining process, the histology samples were fixed for 48 hours in 10% neutral formalin at room temperature to preserve the tissue and its cells (i.e. osteocytes) (Bancroft and Cook, 1994; Iwaniec et al., 2008). Afterwards, for decalcification, the samples were kept in a solution of 40 ml 65 vol% nitric acid, 20 ml 10 vol% formaldehyde and 340 ml deionised water for 10 days. The solution was changed for a fresh one each second day (Karaca et al., 2011). After this, the samples were dehydrated in a tissue processor (Leica TP 1020, Fig. 3.19) by immersion in different alcohol baths with increasing alcohol percentage (i.e. 70%, 80%, 90%, 100%, 100%, 100%) for 1.5 hours in each of the 70-90% alcohols and 1 hour in each of the 100% alcohols. This was followed by two immersions in xylene for 1.5 hours each and then finalised the dehydration process by immersion in two separate 2-hour baths of paraffin to infiltrate into the porosities of the bone. Afterwards, each sample was mounted in paraffin (Leica EG 1150 H, Fig. 3.19b,c), taking essential care of the machining direction to leave the outermost cortical region of the sample in the cutting end of the paraffin-mounted section (se Fig. 3.19c,d). Mounting was ensured by allowing at least 1 hour of solidification in a cold environment. Paraffin-mounted samples were sectioned with a microtome (Leica RM2245, Fig. 3.19e,f) to obtain 7 μm thick slices (see Fig. 3.19g) that were stained with haematoxylin and eosin (H&E), as shown in Fig. 3.19h,i, to allow improved morphological observation of the tissue (Bancroft and Cook, 1994) under light microscopy. After staining, the samples were mounted in a mixture of distyrene, plasticiser and xylene (i.e. DPX) media (Fig. 3.19j) and left to dry for at least 24 hours prior to light-microscopy observation (Axioplan, Zeiss). Necrotic depth evaluation (i.e. measurement from the machined surface to the disappeared osteocytes extent) were made in Fiji (ImageJ). Measurements were done

manually for each image by measuring the normal distance from the machined surface to the location with filled lacunae.

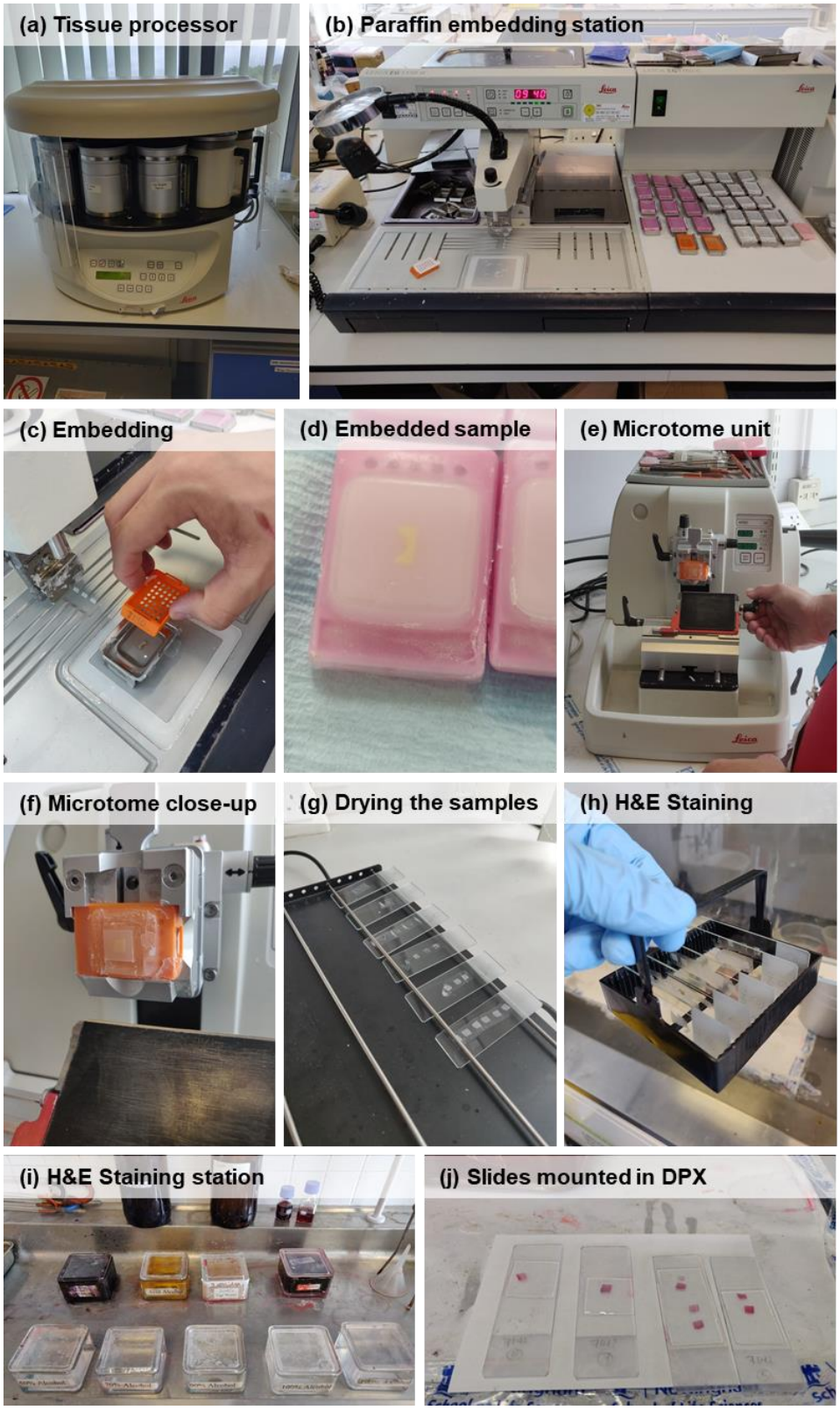

Fig. 3.19. Histological analysis technique for bone. (a) Firstly, a tissue processor for dehydration and paraffin baths is used for all samples overnight. (b) All samples are then

moved onto the paraffin embedding station. (c) Example of embedding a sample with paraffin. (d) Example of a paraffin-embedded sample after the paraffin has cooled down; the bone sample is visible in the middle. (e) The mounted samples are then cut into 7-µm thick slices using a microtome. (f) The microtome's blade enables a continuous set of slices to be done. (g) After collecting the strip of slices from the microtome, these are placed on top of a warm water surface, which flattens the bone and paraffin sections of the slices. These are then collected (and therefore adhered) to the microscope slides, which are left to dry. (h) Once dry, the slides are ready to be stained. (i) A series of a predetermined baths in various chemicals (e.g., alcohol, acids, staining media) are used for completing the H&E staining process. (j) Once the slides have finalised the H&E staining process, these are protected with a crystal-clear lid using PDX embedding media. Once these are dry, they are suitable for light microscopy.

Chapter 4 - Machining-induced damage in cortical bone

Bone is a complex material for machining analysis, and regardless of the thousands of surgeries occurring daily, there is little understanding on the damage that the they induce to the bone. Consequently, it must be imperative to understand the bone damage inducement mechanism and how it is driven by the nature of the material removal process. With this in mind, this chapter covers the experimental results and analysis of machining-induced damage analysis from two different material removal methods: laser machining (thermally driven) and drilling (mechanically or thermomechanically driven).

First, to study a mostly thermally driven material removal method, laser machining trials were conducted, and the surface integrity was then assessed. From this, a set of conclusions are drawn regarding the relation of the laser removal method and the induced damage. Afterwards, drilling, a mechanically/thermomechanically driven material removal method, is similarly reported and analysed. After comparing the two methods of material removal, drilling was subsequently selected for an in-depth study of micromechanical properties and failure mode analysis, which is discussed in detail too. This shows the relation that exists between necrotic damage and micromechanical damage within the tissue following a conventional machining method that is highly employed in surgery. Finally, concluding remarks regarding the damage assessment in dry cortical bone are highlighted

4.1 Introduction

Bone is an important tissue in the human body as it allows vital locomotive functions of humans to take place, such as providing stiffness, walking or jumping (Croker et al., 2009). However, bones are also load-sensitive and semi-brittle (Liao and Axinte, 2016b, 2016a) and, therefore, prone to injuries. As a result, bone surgical interventions are a daily task in orthopaedics, neurosurgery, and dentistry. However, many of these involve the mechanical material removal by principally cutting (i.e. milling, sawing, drilling) (Liao et al., 2019) or abrading (i.e. grinding (Zhu and Beaucamp, 2020)) the tissue to perform the surgery (e.g. total knee arthroplasty, hole drilling, implant or screw insertion), whereby the bone, being of semi-brittle nature, can easily get damage induced to its subsurface (Yin et al., 2018) due to mechanical machining, similarly as it occurs in other difficult-to-cut materials, such as composites (Gavalda Diaz et al., 2019) or metals (B. Wang et al., 2021); nevertheless, bone also possess a unique self-healing capacity (Zhang et al., 2020). These two characteristics make bone an interesting and complex material from both an engineering and medical perspective.

During conventional machining, the mechanical effect may induce sufficient strain that facilitates crack propagation from the cutting zone and into the material (Bai et al., 2020). Additionally, the cutting energy will also dissipate in the form of heat, and as a biological material, the cellular integrity of the tissue may be compromised if the temperature is high enough (Augustin et al., 2008) (see Fig. 4.1). In general, if the tissue is exposed to a temperature of 47 °C or 50 °C during 60 or 30 seconds, respectively, necrosis (i.e. death of osteocytes) will occur, which implies that the healing, remodelling and metabolism functions of the bone will be hindered either temporarily or permanently (Mediouni et al., 2019; Yang et al., 2020). Additionally, much less time is required for necrosis to occur if the temperatures are larger. As such, should tissue necrosis (i.e. cellular death) occur in a clinical context (e.g. orthopaedic surgery), it will represent a serious problem for the patient.

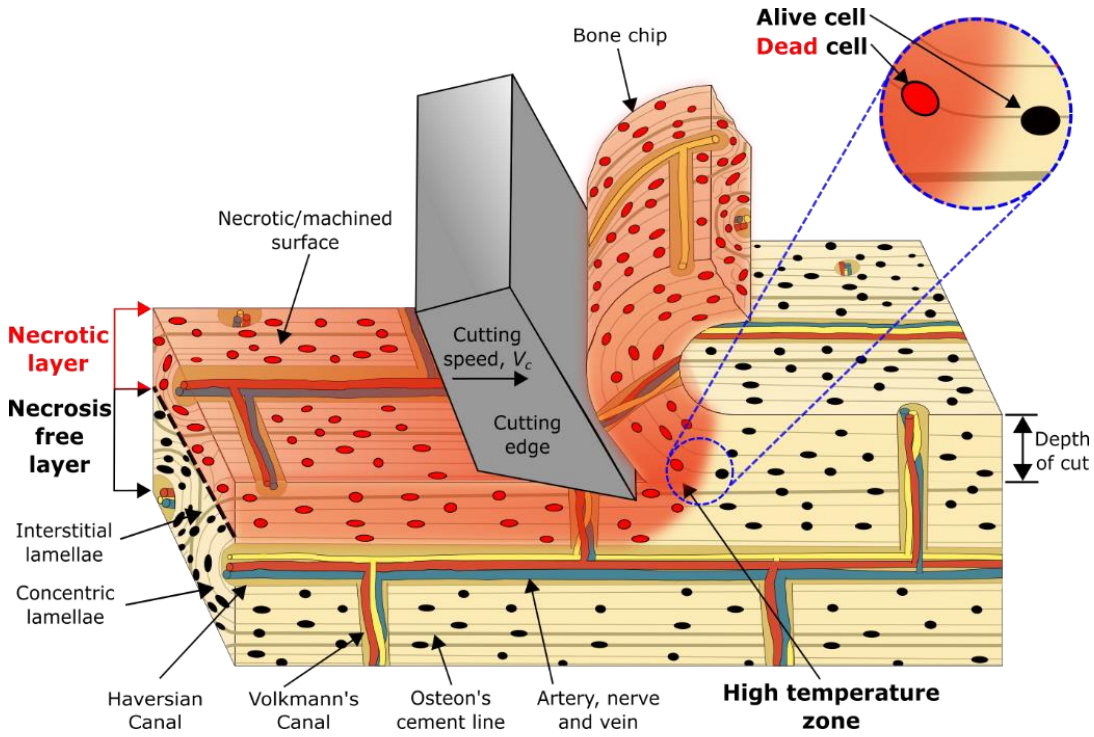

Fig. 4.1. Schematic of the machining-induced thermal damage in cortical bone, which results in the formation of a layer with necrosis and a damage-free layer. As the cutting edge removes material, it leaves behind a machined surface heated by the dissipation of the cutting energy. This heat propagates deeper into the bone and, if the temperature is high enough (47 °C (Augustin et al., 2008)), it causes osteocyte necrosis (dead cells shown in red colour) and the lacunae to empty. The regions far enough from this heat source (cutting edge) remain with their osteocytes alive and undamaged inside their respective lacunae (represented in black colour).

Besides being a useful technique for monitoring the regeneration process of bone (Ventura et al., 2020), histology is considered the gold standard for necrosis assessment, since it allows in-situ analysis of its cells (Iwaniec et al., 2008). With this technique, the ‘alive’ or ‘dead’ states are determined by the appearance of the osteocytes (Hancox, 1972). In ‘dead’ bone, the lacunae appear empty, implying that when necrosis occurs, the osteocytes disappear from the lacunae (Hancox, 1972).

In this section, bone damage is evaluated with histology to assess the necrotic depth induced by both thermally driven (i.e. laser machining in Section 4.2) and thermomechanically driven (i.e. drilling in Section 4.3) material removal techniques and is complemented with traditional material assessment techniques, such as SEM and surface topography analyses. Following this, one of these machining techniques

was selected and studied in-depth via micromechanical testing (Section 4.4) to understand the thermomechanical damage relation of necrosis and micromechanical properties in the machined subsurface.

4.2 Machining-induced damage in non-conventional bone machining

Bone machining via non-conventional methods is under current investigations towards making the process a more reliable one in surgical environments. However, there is still lack of understanding on the relation between laser type (in terms of laser pulse width) and induced necrosis, as most of the aforementioned studies always employ cooling methods to the laser machining process. Additionally, most studies aiming on improving the cutting efficiency (i.e. maximising material removal rate per unit time) have been limited to a fixed pulsed width laser, thus making the processing recommendations pulse-width dependent.

To bring more light into these aspects, here, the effect of pulse width of the laser beam on damage cortical bone both in terms of its surface characteristics (e.g. cracks, roughness) and necrosis is investigated. This was done for an Nd-YAG laser with pulse widths in the nanosecond, picosecond, and continuous ranges. Additionally, various feed speeds (i.e. 0.25 – 45 mm/s) were employed to understand the machining efficiency of each case. Histological analysis was used as a gold standard technique for assessment of the necrotic depth after machining, while metrology equipment was used for evaluation of the machined trench profiles post-machining. In this section, the relation of laser pulse width with necrosis inducement is shown to be non-trivial, highlighting that variations of pulse width can produce both carbonisation and necrotic damage, as well as mild machining with minimum damage. It is also shown that the use of pulse widths in the picosecond range can shift the material removal mechanism from thermal to optomechanical, thereby reducing the inducement of thermal damage.

4.2.1 Experimental methodology for non-conventional machining-induced damage in cortical bone via laser machining

4.2.1.1 Samples acquisition and preparation

Laser machining bone samples were prepared according to section 3.1.1 to obtain bone samples of roughly 15 x 15 x 15 mm^3. These were subsequently ground and polished to final shapes of 5 x 5 x 5 mm^3, as per the protocol stated in section 3.1.2 . These cuboid specimens were then used for performing the laser machining trials on them.

4.2.1.2 Laser ablation tests

To machine the trenches, three laser types were used with varying pulse widths (Fig. 3.10), i.e. picosecond pulsed, nanosecond pulsed, and continuous wave. The picosecond laser used was an Nd:YAG laser with an ultra-short pulse width of 60 ps with the pulse energy of 0.88 mJ and average power output at 3.5 W. For the histological evaluation, two feed speeds were selected (*Pico-Fast* (PF) = 5 mm/s, and *Pico-Slow* (PS) = 1 mm/s). The continuous wave laser (i.e. non-pulsed) used was an Nd:YAG laser operating at 20% (19.5 W) of the maximum output power (measured at 97.5 W) and a feed speed of 20 mm/s (*CW*) was used to limit the total energy supplied to the sample. The nanosecond laser used was an Nd:YAG laser with the pulse energy of 0.52 mJ, average power output at 18.3 W, and a pulse width of 200 ns. A feed speed of 5 mm/s was used in the histological evaluation of the nanosecond laser sample (*Nano*) to provide comparison with both: (1) The total energy transferred to the sample in PS; and (2) the average output power in CW. The complete laser parameters can be found in Table 4.1. As a rule of thumb, the laser processing parameters were determined by two primary factors: (1) avoidance of visible charring of the bone at low feed speeds; and (2) acceptable material removal efficiency at high feed speeds. The laser machining was completed without cooling/irrigation of the bone

samples, they were conducted in a fresh state to understand the material behaviour and response to machining by different laser types as opposed to broadening the scope to become an exercise in process optimisation.

Table 4.1. Laser machining parameters for necrosis inspection.

	PF	**PS**	**CW**	**Nano**
Laser Type	Picosecond	Picosecond	Continuous wave	Nanosecond
Wavelength (nm)	1064	1064	1090	1062
Pulse width	60 ps	60 ps	N/A	200 ns
Repetition rate (Hz)	4000	4000	N/A	35000
Average output power (W)	3.5	3.5	19.5	18.3
Peak pulse power	14.6 MW	14.6 MW	N/A	2.6 kW
Spot size (µm)	40.0	40.0	30.0	51.5
Pulse energy (mJ)	0.88	0.88	N/A	0.52
Feed speed (mm/s)	5	1	20	5
Trench length (mm)	3.5	3.5	3.5	3.5
Total pulses along trench length	2800	14000	N/A	24500
Total interaction time (s)	1.68×10^{-7}	8.40×10^{-7}	0.175	4.90×10^{-3}
Total energy (J)	2.45	12.25	3.41	12.81

Temperature measurements were completed using the same laser parameters as the necrosis investigation (Table 4.1). The temperature was measured by infrared (IR) thermography (FLIR A655SC Long Wavelength IR camera with a 2.9x magnification lens). The camera is calibrated for three temperature profiles (-40^{o}C to 150^{o}C (Fig. 4.2a), 100^{o}C to 650^{o}C (Fig. 4.2b), and 300^{o}C to 2000^{o}C (Fig. 4.2c)), as the temperature that the bone is elevated to during laser machining did not always remain in one of these profiles, the recording was repeated three times to obtain a dataset in each of the temperature profiles for each sample. This method facilitated the accurate temperature

recording (±2% accuracy) at both: (1) the lower (~50°C) region for investigating the spatial dissipation of heat, and (2) the higher (>1000°C) region for measuring the maximum instantaneous temperature. Spatial measurements of the temperature relative to the radial distance from beam centre were measured as well as the maximum temperature across a radial profile relative to time (Fig. 4.2).

To understand the mechanisms of material removal taking place during the different laser processes, high-speed imaging was also employed with the continuous wave and nanosecond-pulsed lasers.

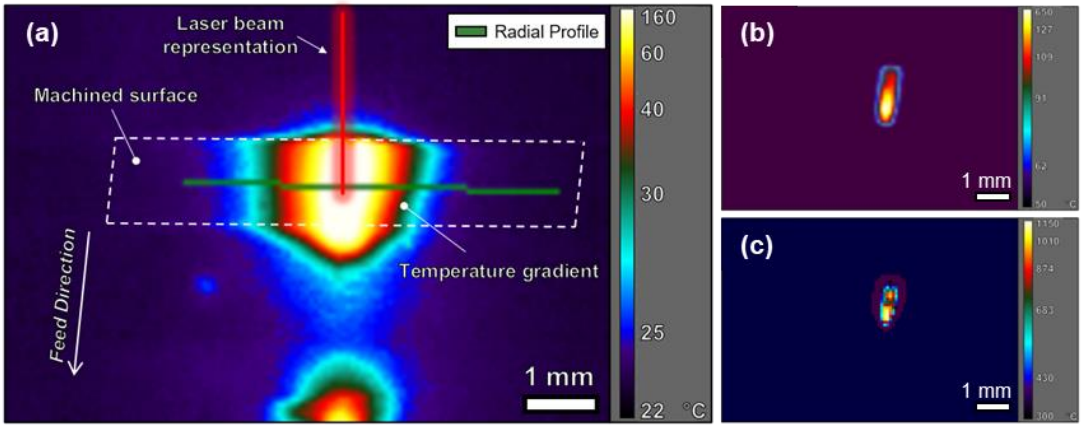

Fig. 4.2. Schematic overview of thermal imaging methodology. The schematic depicts the experimental methods used to investigate the thermal properties in the surface of the bone sample during laser machining. The radial profile is used for both the spatial and temporal plots. It should be noted that the colour bar is non-linear and uses plateau equalisation to improve the contrast for the entire scene. As there is not one camera calibration profile to cover the complete temperature range, three recordings were used: (a) Low-range, (b) mid-range, (c) high range.

4.2.1.3 Surface inspection

To further evaluate the effects of the total interaction time between the laser and bone sample on the surface morphology after machining by each of the three laser types, single trenches were machined across a range of feed speeds, V_f, (mm/s) (Table 4.2). As the samples for this stage were prepared prior to the completion of the histological analysis, the upper ($V_{f,max}$) and lower ($V_{f,min}$) bounds were chosen based on the level of carbonisation observed visually by optical microscopy after iterative pre-experimental

trials. More specifically, the $V_{f,min}$ bounds were selected due to an elevated level of bone carbonisation whereas the $V_{f,max}$ bounds typically had minimal discolouration. The V_f steps were subsequently calculated to ensure that a linear V_f range was evaluated over nine trenches for each of the three laser types. All the operating parameters not dependent on V_f for each of the lasers were kept identical to those used for the necrosis inspection (i.e. wavelength, pulse width, repetition rate, average power output, spot size, pulse energy).

Table 4.2. Laser machining feed speeds for surface morphology inspection.

Parameter	Picosecond	Nanosecond	Continuous wave
$V_{f,min}$ **(mm/s)**	0.25	2.50	5.00
$V_{f,max}$ **(mm/s)**	6.25	6.50	45.00
Step (mm/s)	0.75	0.50	5.00
Machined feature	Single trench	Single trench	Single trench

Following the laser machining of the samples, 3D inspection of the trenches was completed using the Bruker Alicona InfiniteFocus G4. The scans were first levelled in the vertical direction based on the mean surface height of the unaffected areas surrounding the trench to obtain an accurate reference plane to measure the trench depth from. A series of cross-sectional profiles of the trench were taken to calculate the mean depth across the profile, these were subsequently plotted and centred on the maximum trench depth. The maximum trench depths for the range of feed speeds (Table 4.2) were also studied to investigate the linearity of the trench depth relative to feed speed.

4.2.1.4 Histology

Histology was performed as per Section 3.4.6 on a set of 5 samples. Additionally, a control sample (i.e. non-machined) was employed to confirm that the sample

preparation process did not induce necrosis to the tissue. In total, 5-7 slices per sample were inspected.

4.2.2 Results of non-conventional machining-induced damage in cortical bone via laser machining

4.2.2.1 Surface topography analysis

Surface integrity is an important aspect in conventional materials, such as metals (Liao et al., 2021), since the surface condition post-machining can alter the material behaviour in-service and possibly lead to early-stage failures if abusive cutting conditions occur (la Monaca et al., 2021). In cortical bone this is also the case; thus, to understand the influence of laser type (in terms of pulse width) on the machining efficiency, a metrological assessment of the machined trench and bone surface was completed. Topological maps (see Fig. 4.3) observing a plan view of the machined surface revealed the variation in single trench geometry for the laser types. Moreover, two feed speeds (1.0 mm/s and 4.0 mm/s) for samples machined by the picosecond laser to determine the extent to which feed speeds affect the single trench geometry and surface morphology for lasers in the same pulse width region.

It was found that the lowest kerf width (54 µm) was achieved by the picosecond laser at a feed speed of 4.0 mm/s (Fig. 4.3a) which contrasted the slower picosecond laser (V_f = 1.0 mm/s) (Fig. 4.3b) that had a kerf width of (83.50 µm) – a 55% increase. The kerf edges were also more defined in the faster picosecond laser than the slower, where the latter showed surface cracks propagating perpendicularly to the feed direction. The faster picosecond laser also produced a smoother trench floor (Ra = 3.22 µm) than the slower (Ra = 15.05 µm). This combination of well-defined kerf edges and a smoother trench floor in the faster picosecond sample suggests that for machining trenches with multiple passes, the decrease in single trench depth may be offset by optimised surface,

i.e. the laser beam focus would be more controlled throughout multiple passes compared to a rougher surface where the undulations in surface height would not remain in optimal focus.

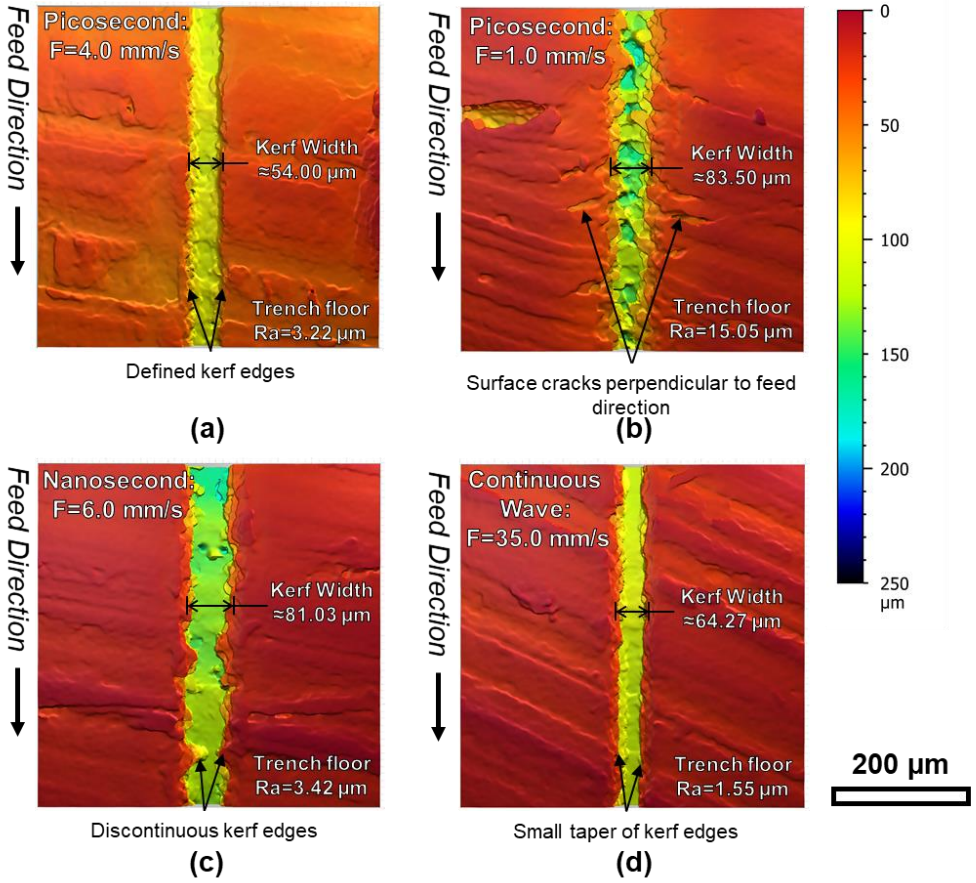

Fig. 4.3. Surface topography maps after laser machining. The surface topography maps observing a single trench machined by (a) the picosecond laser at a feed speed of 4.0 mm/s. (b) The picosecond laser at a feed speed of 1.0 mm/s where cracks that are propagating perpendicular to the feed direction from the kerf edges are visible. (c) The nanosecond laser at a feed speed of 6.0 mm/s. (d) The continuous wave laser at a speed of 35.0 mm/s.

On the other hand, the kerf width of the trench machined by the nanosecond laser at a feed speed of 6.0 mm/s (Fig. 4.3c) was measured at 81.03 µm, which was similar to that in the slower picosecond laser (V_f = 1.0 mm/s), however the trench floor was similar in roughness (Ra = 3.42 µm) to that of the faster picosecond laser (V_f = 4.0 mm/s). Although the trench floor roughness in the sample machined by the continuous wave laser (V_f = 35.0 mm/s) (Fig. 4.3d) was the lowest measured (Ra = 1.55 µm), there

is a small kerf taper which widens the kerf width (64.27 µm) at the machined surface due to the convergence/divergence of the beam above and below the focal point.

If the machining efficiency was the only goal, then the key factors influencing the decision of laser type would be one which achieves a deep trench depth at a fast feed speed. From a clinical frame of reference however, this decision is more nuanced; requiring a higher weighting to be given to the later discussed necrotic damage (see Fig. 4.8). To address the efficiency problem, the mean cross-sectional trench profiles were calculated (Fig. 4.4) for the bone samples machined with identical parameters as those used in the histological assessment and curves plotting the mean trench depth over a range of feed speeds (Fig. 4.5) were used to investigate the linearity of the relationship. The mean profile width of the nanosecond (V_f = 5 mm/s) laser trench was the broadest due to the graduation of the kerf, whereas the continuous wave laser trench profile was the slenderest. It could be posited that a narrower kerf would be a beneficial characteristic of the laser in a clinical setting, allowing for precise cutting paths. This precision, however, would need to coincide with a high degree of predictability to be accurate. When the trench depth machined by the continuous wave laser is compared with feed speed (Fig. 4.5), there is a low coefficient of determination between the variables (R2=0.77) compared to those machined by the picosecond laser and nanosecond laser (R2=0.90 and R2=0.93 respectively). This leads to the implication that the reliability and stability of the laser source is an important factor to consider. For feed speeds > 3.5 mm/s, the trenches machined by the nanosecond laser increase greatly in their depth, and the sharp decrease as feed speeds increase offer an exceptionally narrow window of operation for this laser despite the high fit. Conversely, over a similar range of feed speeds, the trench depths after machining by the picosecond laser occupied a far narrower span of depths whilst also maintaining a comparatively high fit.

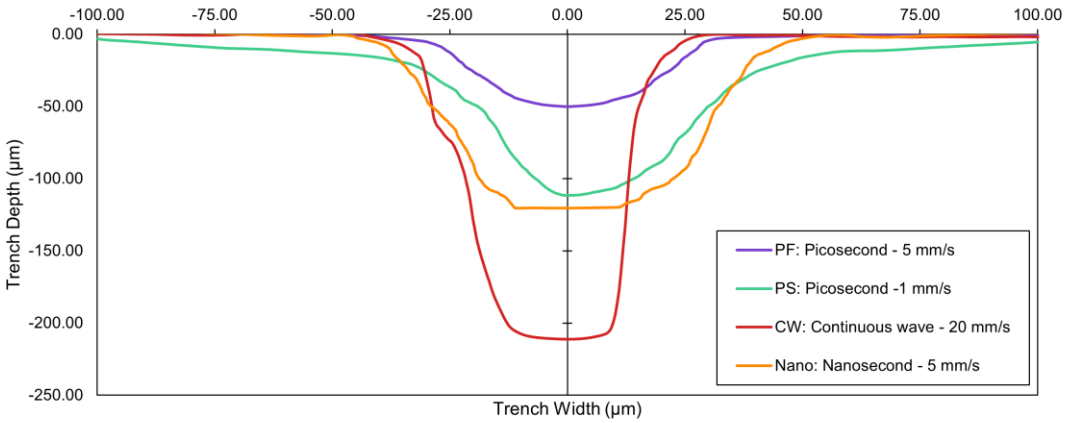

Fig. 4.4. Mean cross-sectional trench profile. The mean cross-sectional trench profiles were plotted for samples machined with identical process parameters as those used in the histological analysis.

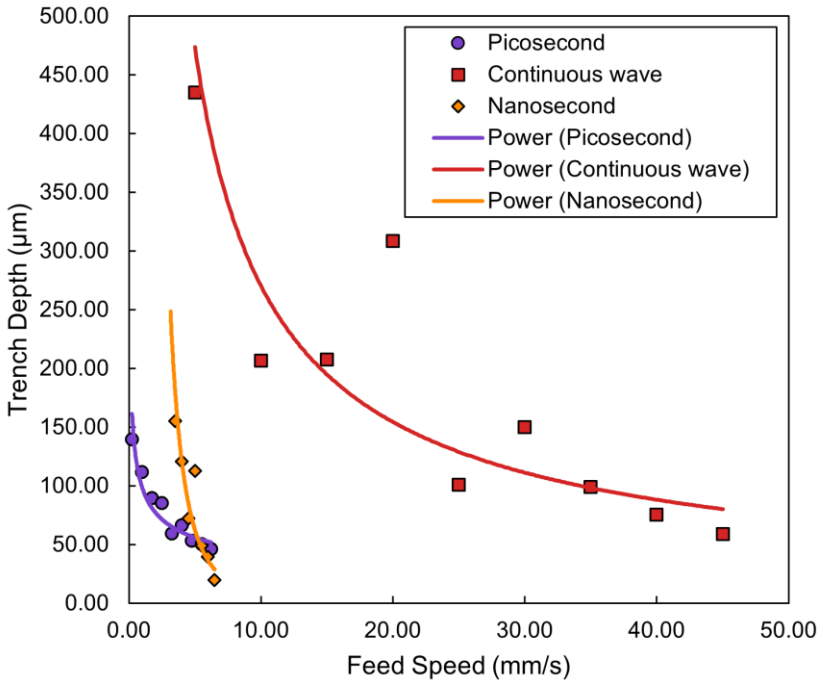

Fig. 4.5. Investigation into the effect of feed speed on the trench depth. The maximum trench depth taken from the mean cross-sectional profiles were plotted over a range of feed speeds to compare the efficiency and predictability of machining by the different laser types

4.2.2.2 Thermal behaviour analysis

To understand the causes non-linear relationship between trench depth and feed speed for the different laser types, an investigation into the thermal behaviour of the

machined bone was completed (Fig. 4.6). By plotting temperature across the radial profile taken at the time when the radius that was greater than 50 °C was at a maximum (Fig. 4.6a), the thermal penetration depth can be considered. Comparing this spatial data with the temporal data (Fig. 4.6b) measured across the same profile allows us to obtain a clearer understanding of the mechanisms which influence the machining efficiency and the level of necrosis. The distance where the temperature of the bone >50 °C was the highest after machining by nanosecond laser (1550 µm) which is far greater than the samples cut by the other lasers. Despite the continuous wave laser increasing the surface temperature to 1318 °C compared to the nanosecond laser (830 °C), there is a far greater rate of cooling in the former. The distance that temperature was elevated >50 °C after machining by the picosecond laser was substantially smaller for both tested feed speeds, which can be explained by the high rate of cooling observed in them after reaching their peak temperature. The low thermal penetration depth and high cooling rate observed in the faster (5 mm/s) picosecond laser sample leads to the prediction of positive results in the later necrosis assessment.

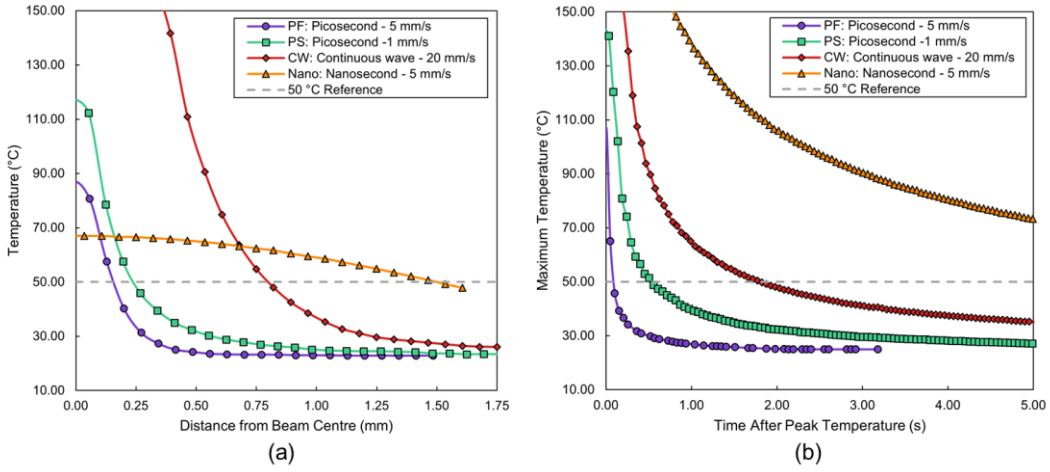

Fig. 4.6. Investigation of thermal effects after laser machining. (a) The thermal penetration depth is plotted relative to the radial distance from the laser beam centre measured by infrared thermography. The profiles were selected from the recorded frame where the radial distance from the beam centre at a temperature greater than 50 °C was at a maximum. A 50 °C reference line is also plotted. (b) The cooling behaviour was studied using temporal plots evaluating the maximum temperature along a radial profile from the beam centre relative to the time passed since peak temperature was achieved.

4.2.2.3 Material removal mechanism analysis

Using high speed imaging whilst machining by the continuous wave laser and nanosecond pulsed laser, the difference in material removal mechanisms was observed (Fig. 4.7). In the nanosecond pulsed laser (Fig. 4.7a), the initiation of plasma generation (Fig. 4.7aii) followed by the subsequent micro-explosions (Fig. 4.7aiii) caused pressure waves to propagate through the surface (Fig. 4.7aiv). These explosions cause the expansion of the plasma plume leading to the ejection of vapourised and melted material from the surface. On the other hand, machining with the continuous wave laser (Fig. 4.7b) was not explosive, rather, the material removal was almost entirely a thermal mechanism. Some ionisation of the surface material was present at the beginning of the laser interaction (Fig. 4.7bii), and during this period the bone was heated, initiating a melt pool (Fig. 4.7biii). Further heating by the laser caused a bubble to form which also contained carbonised debris (Fig. 4.7biv). The contents of the bubble were seen to be rotating and growing in volume over time. The bubble then overcame the surface tension of the surrounding melt pool and was ejected from the surface – removing both the molten material and carbonised debris. This difference in material removal mechanisms for a continuous wave laser and nanosecond pulsed laser highlights the transition from thermomechanical to thermal when longer/continuous pulse durations are used.

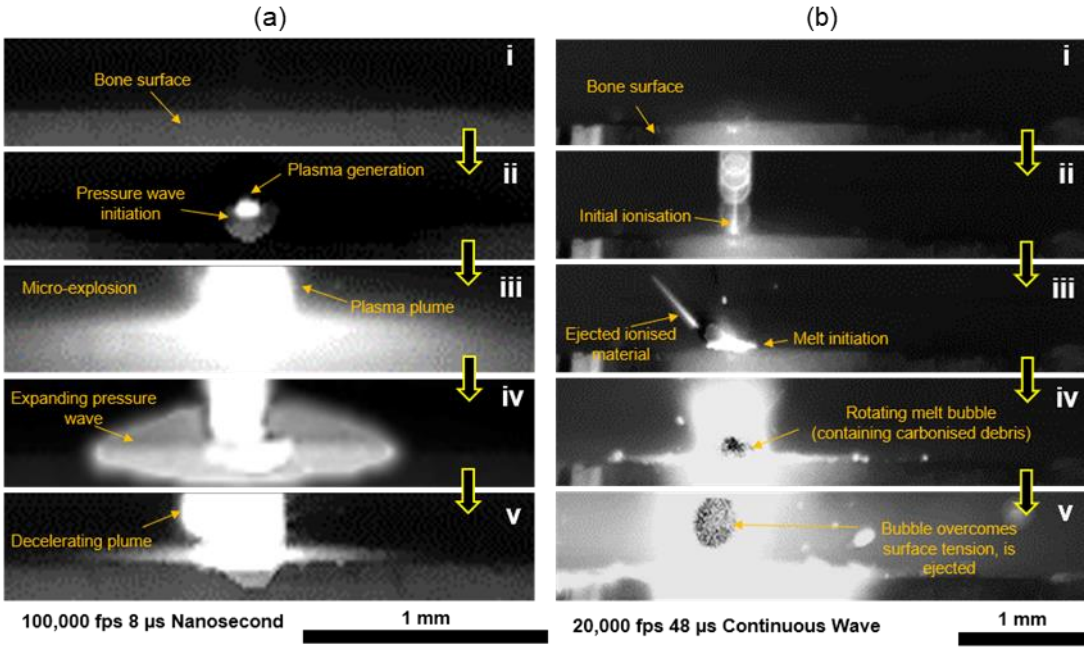

Fig. 4.7. High-speed camera investigation of material removal mechanisms during laser machining. The bone surface was imaged perpendicular to the beam direction during (a) Nanosecond pulsed laser machining and (b) Continuous wave laser machining. Sequence (a) was captured at 100,000 fps with an 8 µs exposure time; due to the high repetition rate (35 kHz) the image sequence was not able to be taken from an individual pulse. Sequence (b) was captured at 20,000 fps to allow for a greater vertical field of view, and a 48 µs exposure time was used.

4.2.2.4 Necrotic damage assessment

Conventional machining processes (i.e. drilling, milling) have shown that temperatures as low as 50 °C can produce necrotic damage in cortical bone if withheld for 30 seconds (Augustin et al., 2008); however, should larger temperatures occur, they will induce necrosis much faster. Nevertheless, in laser machining, the mechanical effect is removed due to the thermally dominant process that is laser ablation and as a result, heat generation can be enough to cause thermal necrosis in bone (Krause et al., 1997), but this can be minimised with the use of air and water spraying during the laser cutting process (Frentzen et al., 2003). While the use of coolants is necessary in clinical environments as a precautionary measure for necrosis avoidance, in a research environment it does not allow a straight-forward analysis of the material response to different types of lasers. Thus, with the intention of studying

the effect that the native laser (i.e. without any coolant) could have on the tissue in terms of thermally induced necrosis, the samples were assessed with histological analysis (see Table 4.3 and Fig. 4.8). Necrosis was evaluated by measuring the normal distance from the trench site until the extent within the tissue at which the lacunae stopped from being empty (i.e. with dead osteocytes) to being filled (i.e. with osteocytes).

It is observed that a larger temperature does not necessarily imply a larger necrotic depth if the acting time of the temperature is short (Table 4.3). Machining with the picosecond laser at 5 mm/s (PF) produced a maximum temperature of 122 °C and resulted in a necrotic depth of 79 ± 7 µm, while also depicting the shallowest trench (Fig. 4.8b). Slowing down the feed rate by 5 times (i.e. 1 mm/s, PS) produced a maximum temperature of 143 °C and a necrotic depth of 190 ± 39 µm (Fig. 4.8c), clearly showing that a longer exposure to same-power laser will inherently facilitate temperature build-up and, therefore, increase necrosis. The continuous wave laser at 20 mm/s feed (CW) produced the highest temperature of all tests with a maximum value of 1318 °C, but the necrotic depth was not the greatest, with a value very close to that achieved in PS conditions: 194 ± 19 µm (Fig. 4.8d). Cutting at 5 mm/s with the nanosecond laser (Nano) produced a temperature of 813 °C, which resulted in the largest necrotic value of 268 ± 67 µm (Fig. 4.8d). Note how even when the PS produced a larger maximum temperature than the Nano, the nanosecond laser produced carbonisation in the tissue, which is visible along the trench profile in Fig. 4.8e; phenomenon that is not visible in (Fig. 4.8c). Thus, this inherently shows that the necrosis is strongly affected by the laser power and acting time in tissue, but also proves that the pulse time of the laser will result in a different material response.

Table 4.3. Necrotic depth for all the laser conditions.

Alias	Laser/test	Feed speed, V_f, (mm/s)	T_{max} (°C)	Duration of sample above 50 °C (s)	Necrotic depth (µm), avg ± std dev	Number of measurements, *n*
PF	Picosecond	5	122	0.085	79 ± 7	48
PS	Picosecond	1	143	0.530	190 ± 39	56
CW	Continuous wave	20	1318	1.790	194 ± 19	52
Nano	Nanosecond	5	830	11.000	268 ± 67	62

A separate control sample subjected to the same experimental conditions, but excepting the laser ablation process, was also assessed with histology to confirm that the handling, preparation, and storage processes did not induce necrosis to the tissue (Fig. 4.8a). The evaluation showed no evidence of necrosis neither in the vicinity of the free surface nor in the bulk region of the sample, i.e. all the lacunae appear filled. Consequently, this confirms that the followed methodology is appropriate for this study and that the necrotic damage from PS, PF, CW and Nano samples was induced by the thermal effect of the laser machining process.

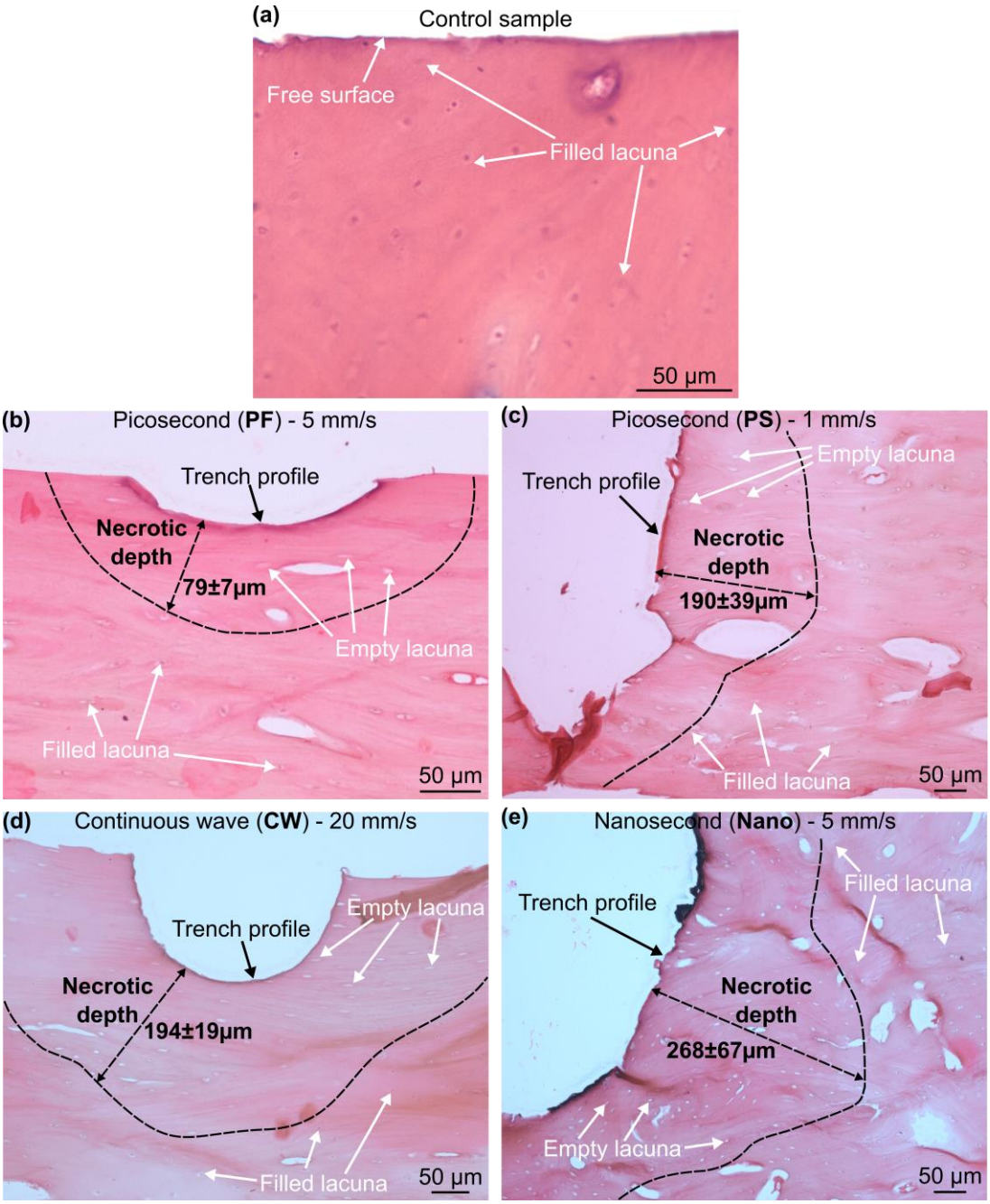

Fig. 4.8. Histological analysis for necrosis assessment. The necrotic depth was assessed by measuring the normal distance from the trench profile to the dashed black line, which marks the interface between the zone with empty lacunae (i.e. necrotic zone) and the zone with filled lacunae (i.e. necrosis-free zone). (a) Control sample free of necrosis, as all lacunae are filled with osteocytes. (b) Picosecond laser machining at 5 mm/s (PF) exhibits a necrotic depth of 79 ± 7 µm, while also depicting the smallest trench; (c) Picosecond laser machining at 1 mm/s (PS) shows a necrotic depth 190 ± 39 µm and shows a trench depth that almost reached the bottom of the sample; (d) Continuous wave laser machining at 20 mm/s caused a necrotic depth of 194 ± 19 µm, which is similar to the one in (c), but in this case the trench is much shallower; (e) Nanosecond laser machining at 5 mm/s showed a necrotic depth of 268 ± 67 µm, while also exhibiting a deep trench and carbonisation traits in the trench profile.

4.2.3 Discussion on the effect of the laser pulse width upon the damage inducement and bone's integrity post-machining

Bone machining under conventional methods such as milling, grinding, or sawing, involves the mechanical removal of material, which inherently produces a mixed thermomechanical process that induces damage to the tissue in various forms (e.g. cracks, mechanical properties decay, necrosis, carbonisation, etc.). Altogether, these forms of damage alter the bone regeneration capacity and the healing process (i.e. the remodelling process of the bone is hindered) (Mediouni et al., 2019), being also able to affect any implant bonding process (Axinte et al., 2019a).

An approach to reduce these types of damage is to use non-conventional machining techniques, such as laser machining. Here, the effect that the laser pulse width and the feed speed have on necrosis inducement and trench profile were explored. To do so, gold-standard technique of histology has been employed towards biological tissue analysis for necrosis assessment post-machining. Additionally, the trench profiles under various feed speeds and laser pulse widths were measured and analysed in accordance with the respective laser processing parameters.

The metrology assessment showed a non-linear relationship between the feed speed and trench depth (Fig. 4.5) in all laser types (i.e. picosecond, nanosecond, and continuous wave). As found in the thermal analysis during machining (Fig. 4.6b), the maximum temperature of the bone can be increased significantly in a rapid time period. With all the samples recording >100 °C temperatures, some vaporisation of the water, which is a key constituent of bone (Rajitha Gunaratne et al., 2017), would initially be expected from a purely thermal viewpoint. This would alter the composition of the bone so that there is a non-constant ratio of the volume of the constituent (e.g. water:collagen:hydroxyapatite), thus contributing to non-linear optical properties (i.e. the wavelength dependent optical absorption coefficient). The non-linear absorption characteristics have also been discussed in an investigation of

laser machining trabecular bone (Pantawane et al., 2020), where it was theorised that the bone marrow, consisting of water and other organic material, would be vapourised in the initial stages because of their lower vaporisation temperature than that of hydroxyapatite.

Surface cracks propagating perpendicularly from the trench direction were also found in the slower picosecond sample (V_f = 1.0 mm/s) (Fig. 4.3b). As the temperature in this sample was not raised to the elevated temperatures recorded after machining by the continuous wave and nanosecond laser, which did not show cracks, it is unlikely that thermally induced stresses were their cause. A more likely explanation is that the comparatively higher fluence (i.e. energy per unit area) of the picosecond laser (69.67 J/cm2), when compared to the nanosecond laser (25.11 J/cm2) with the longer pulse width, was the source of these cracks. This high fluence and the high associated peak pulse power (picosecond = 14.6 MW, nanosecond = 2.6 kW) would introduce non-linear optical breakdown, where the increased photomechanical effect caused by the explosive generation of plasma – introducing cracks (Sotsuka et al., 2014). This theory is supported by the high-speed imaging investigation (Fig. 4.7) where the nanosecond pulsed laser removed material by a thermomechanical mechanism as opposed to the continuous wave laser which was thermal. Combining these findings with those from the thermal investigations (Fig. 4.6), it could be suggested that decreasing the pulse width further (i.e. to the picosecond region) would reduce the thermal effects seen in the nanosecond laser sample, transitioning to photomechanical effects instead. It is also interesting how the cracks were not present after picosecond laser machining with a faster feed speed (V_f = 4.0 mm/s), potentially due to less dehydration of the bone coupled with the lower associated temperature increase preventing the bone becoming more brittle and therefore, less susceptible to crack initiation by the plasma induced pressure wave. This lack of thermal damage also suggests the promising possibility of using lasers with a short pulse width and higher feed speeds in a clinical setting to

substantially minimise the necrotic depth observed in the lasers with a longer to continuous (Payne et al., 2001) pulse width.

Necrosis evaluation (Table 4.3) showed that the greatest necrotic depth occurred for the nanosecond (Nano) laser with a value of 268 ± 67 µm, which is an interesting outcome, given that the maximum temperature was recorded for a different laser (i.e. the CW laser reached a peak value of 1318 °C and necrotic depth of 194 ± 19), while the Nano just reached a maximum of 830 °C. Nevertheless, by looking at Fig. 4.6a the peak temperature drops to a necrotic threshold value (i.e. 50 °C) at ca. 750 µm from the laser beam centre, while the Nano depicts a deeper propagation up to almost twice the distance (1500 µm); thus, showing that even if the peak temperature was lower, it penetrated deeper into the bone. Additionally, from Fig. 4.6a, the Nano laser machining natural cooling time after laser exposure remained above 50 °C much longer than any of the other laser combinations used for histology (see Table 4.3). The reason for this is that the Nano laser frequency (35 kHz) in combination with the pulse energy of 0.52 J (see Table 4.1) results in the greatest laser energy input towards the bone (i.e. 12.81 J), even if the laser interaction time was not as great as with continuous wave. This implies that the nanosecond laser conditions employed, produced the greatest heat generation and heat transfer into the tissue, thus resulting in increased carbonisation and a higher necrotic depth.

It is interesting to note that the total input energy from the picosecond laser with slow feed (PS) also has a similar input energy of 12.25 J; however, the necrotic depth for PS was evaluated as 190 ± 39 µm. The picosecond laser, having its pulse width about 3000 times shorter than the nanosecond, allows for a larger pulse energy and a lower frequency. Therefore, these conditions favour the natural convection that cools down the sample after each laser pulse; these is the reason why the PS and PF laser conditions produced the minimum necrosis values. It is also interesting that even when the feed speed was 5 times larger in PF against PS, the peak temperature was only lower by 21 °C; however, the difference in necrotic depth is much more noticeable

(i.e. 79 ± 7 µm in PF vs. 190 ± 39 in PS); in this case, being the faster feed the only difference, laser interaction time is minimised and therefore less temperature and necrosis will occur.

The increased heat generation after nanosecond laser machining may be explained by the frequency dependent pulse overlap. This can be demonstrated by comparing PF with Nano, with the respective frequencies of 4 kHz and 35 kHz, coupled with the spot sizes of 40.0 µm and 51.5 µm. In PF, there is an overlap of 96.9% (38.75 µm) compared with 99.7% (51.36 µm) in Nano. At the feed speeds in PF there are 32 individual pulses in the time taken to travel the distance of 1 spot diameter as opposed to 1802.5 in Nano, when also considering the pulse widths it becomes clearer how Nano suffers a longer cooling time.

When comparing the effect of PS and CW lasers in histology, the necrotic depth could be regarded as equal; even though there are evident differences in temperature behaviour (see Fig. 4.8). The CW laser, while not allowing intermittent natural convection (i.e. cooling between each pulse), eases heat conduction through the tissue, which is why carbonisation occurred in CW and not in PS. The reason for achieving a similar necrotic depth could be that even if the total input energy from PS is 12.25 J (i.e. 4 times larger than that from CW), the laser interaction time is very little (i.e. 8.4×10^{-7} s), while in CW the interaction time is 0.175 s. The drastic difference in laser interaction time between PS and CW (which is dependent on the pulse width and frequency) allows to achieve similar necrotic damage, but due to the large feed speed of CW (i.e. 20 times faster than PS), the machined trench is shallower than that from PS (see Fig. 4.8c, d).

In all cases, the peak temperature exceeded 100 °C, which could produce dehydration in the tissue (Samuel et al., 2016). Additionally, the exceedingly large temperatures here measured (i.e. >800 °C for Nano and CW lasers), even when only lasting a fraction of a second in the tissue, were high enough to produce carbonisation in the

tissue, another type of damage different from necrosis. Carbonisation traits, which are expected to be removed during the histological analysis processing, are even visible in the trench profile from the histological slices (see Fig. 4.8e), which is coherent with this sample also exhibiting the greatest necrotic depth.

While it is known that laser machining of bone is a promising technique towards intelligent tooling systems for surgical interventions, laser processing parameters imperatively need optimisation to compete with conventional machining processes, which are characterised by a much larger material removal rate (Beltran Bernal et al., 2018). The findings from these trials show that the pulse width in laser machining of bone plays a major role both in the surface quality, trench depth (i.e. which is related to the material removal rate) and in cellular damage (i.e. necrosis). Here, it is shown that greater energy density can be employed in the laser processing parameters only if narrower pulse widths are employed, but the frequency should be chosen to allow enough convection between each pulse.

4.3 Machining-induced damage in conventional bone machining

In the previous section, a potential thermally driven machining technique was explored in terms of damage inducement into the tissue. While many advantages exist with such a material removal method, it is still required to supersede non-conventional machining in terms of not only precision, but also efficiency (i.e. time) to obtain real use in surgery. For instance, conventional drilling is one of the most employed material removal techniques in not only cortical bone, but all hard tissues. As such, to provide a comparative perspective, drilling is studied in this section.

Histology has been used to evaluate the necrotic depth caused by drilling into bone, revealing that higher cutting speeds and lower feed rates yield higher temperatures near the drilled surface, leading to greater necrotic depths (Franssen et al., 2008;

Karaca et al., 2011). Research on this field shows that most studies aimed at evaluating machining-induced bone damage have focused on finding the relationship of the necrotic depth with different cutting conditions that may occur during surgery (e.g. speeds, temperatures, forces). As a consequence, bone cutting tool design has been tailored to minimise temperature rise (Liao et al., 2017; Shu et al., 2020b).

In this section, cortical bone drilling is studied under low and high generation conditions to understand the thermal and mechanical damage induced to the tissue via conventional machining.

4.3.1 Experimental methodology for conventional machining-induced damage in cortical bone via drilling

4.3.1.1 Sample acquisition and quality

Drilling samples were prepared according to section 3.1.1 and 3.1.2 to obtain bone samples of roughly 50 x 40 x 9 mm^3. These samples were used for the drilling tests, but also for the in-depth micromechanical study detailed in section 4.4 .

4.3.1.2 Drilling tests

Since drilling is highly used in orthopaedic surgeries (e.g. total knee arthroplasty, trauma interventions), it was chosen to study the damage induced to the sub-surface of the bone tissue by machining operations.

To avoid tissue degradation as much as possible, the drilling tests (Fig. 4.9) were conducted 6 hours after the bone was acquired from a local butcher. After obtaining the 50 x 40 x 9 mm^3 samples and prior to the drilling processes, the samples were kept at room temperature and immersed in saline solution. All samples were retrieved from a single mid-diaphysis bovine femur.

The drilling operations were performed with a typical surgical drill bit (i.e. 2 flutes, 4.5 mm diameter) (Pandey and Panda, 2013) in the radial direction relative to the long axis of the bone (i.e. transverse direction relative to osteon orientation), as shown in Fig. 4.13. Twelve different drilling conditions were employed, with various spindle speeds (i.e. 600, 1200, 3000, 9000 rpm) and feed speeds (i.e. 30, 60, 120 mm/min), with no coolant whatsoever. Considering the intent of this research is to study the thermal damage, these cutting conditions were chosen to intentionally create both low and high temperature drilling scenarios in which the minimum temperature was higher than the necrosis threshold of 47 °C (Augustin et al., 2008). To verify this, a thermal camera (FLIR T460) was included in the experimental setup at ca. 500 mm away from the workpiece (Fig. 4.9) and pointing at the tool-bone interface at the drill entrance to measure the cutting temperatures. This provided a relative comparison of temperature rise for all the employed drilling conditions.

The two selected cutting conditions produced the lowest (62 °C) and highest (110 °C) cutting temperatures, respectively, and therefore are expected to induce different levels of thermal damage to the bone. From here on, these two conditions are referred to as low temperature, LT, (cutting speed V_c = 8.5 m/min, feed rate f_n = 0.2 mm/rev, maximum temperature T_{max} = 62 °C) and high temperature, HT, (i.e. V_c = 42.5 m/min, f_n = 0.01 mm/rev, T_{max} = 110 °C), conditions, respectively.

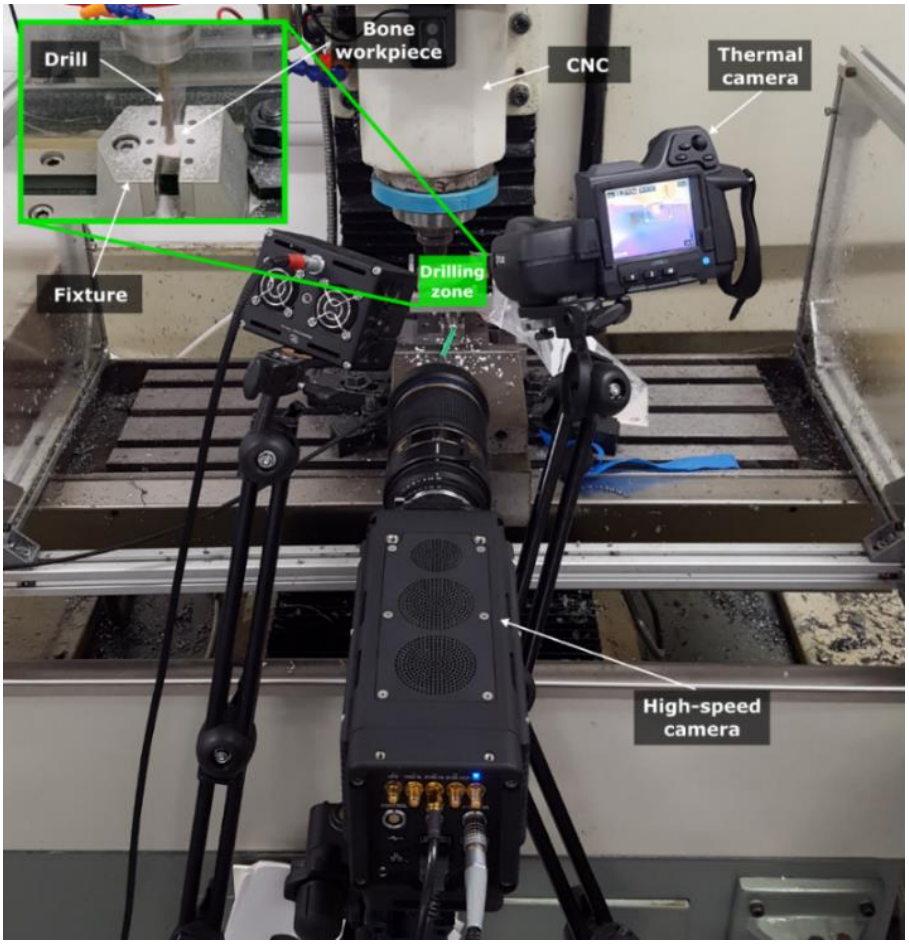

Fig. 4.9. Drilling trials setup. A CNC milling machine tool (770 PCNC Tormach) was used for making the drilling experiments. A thermal camera (FLIR T460) and a high-speed camera (IDT Y4-S2 Motion Pro) were used during each drilling test to record the experiment data.

Table 4.4. Selected sample drilling conditions for histological and micromechanical analyses.

Drilling condition	Cutting speed, V_c (m/min)	Feed rate, f_n (mm/rev)	Coolant	Maximum measured temperature, T_{max} (°C)
Low temperature (LT)	8.5	0.20	None	62
High temperature (HT)	42.5	0.01	None	110

4.3.1.3 Histology

Histology was performed as per Section 3.4.6 . At least 4 measurements were done for each slice and a total of 32 slices were used for the LT sample, while a total of 37 were used for the HT sample. A separate control sample (i.e. non-machined) was also used for histology to confirm that the sample handling (i.e. polishing and manual grinding and cutting) did not induce necrosis to the tissue.

4.3.2 Results of conventional machining-induced damage in cortical bone via drilling

4.3.2.1 Macro-damage on the machined bone surface

As initial investigatory step (i.e. before histology and micromechanical analyses), a separate set of the LT and HT drilled samples were inspected for macro-damage by using SEM in a low vacuum (LV) environment. Initially, it seemed that the HT condition exhibited a smooth "crack-free" surface (Fig. 4.10a), while the LT condition sample presented large cracks on the machined surface (Fig. 4.10c). Such an effect is unexpected as the latter drilling condition presented a lower temperature (i.e. 62 °C) and as such, should not present a large extend of surface damage.

To verify if the operating vacuum conditions of SEM might have played a contribution to crack propagation of the bone's composite structure, the samples (after three days of air-drying) were coated with gold and inspected again under SEM in a high vacuum (HV) environment. The LT sample (Fig. 4.10d), showed no signs of crack growth. Contrary to this, the HT sample, which previously presented "crack-free" and smooth surface, now revealed the appearance of some minor cracks (Fig. 4.10b). This implies that some of the machined surface of the bone was smeared due to the high cutting speed and slow feed rate, creating a 'deceiving' smooth appearance with minor cracks laying underneath.

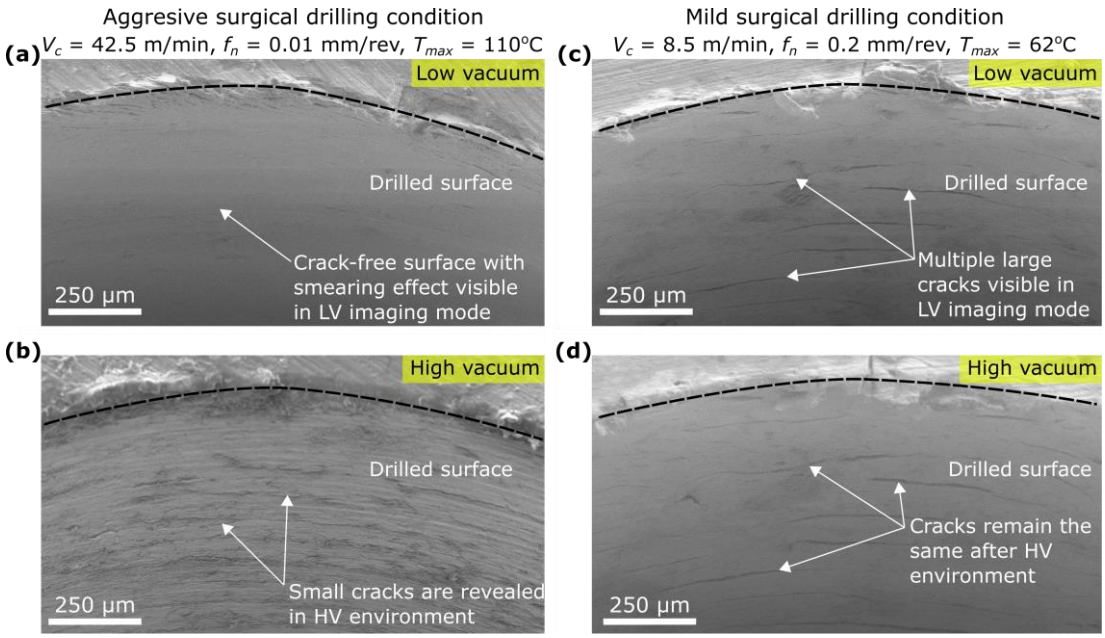

Fig. 4.10. Macro-level effect of drilling conditions upon crack formation and surface smearing when using high (HT) and low (LT) temperature drilling conditions in low and high vacuum SEM. (a,b) As-machined bone surface with HT drilling conditions yielding intensive thermal fields (T_{max} = 110 °C): (a) LV imaging immediately performed after drilling revealed a deceiving "crack-free" surface with a smearing effect, giving it a smooth appearance; (b) HV imaging carried out after 72 hours of air-drying revealed minor cracks that were not visible in LV SEM. (c,d) As-machined bone surface with LT conditions yielding lower level of thermal fields (T_{max} = 62 °C): (c) LV imaging immediately performed after drilling revealed a surface with large cracks; (d) HV imaging carried out after 72 hours of air-drying revealed no further crack growth.

The smearing effect was not seen following low temperature drilling conditions, with damage appearing immediately after the cutting operation in the form of large cracks. At first instance, this was not expected as it is envisioned that a high temperature drilling condition will generate more cracks than a lower-temperature one. However, two points need to be addressed: (i) The LT drilling condition is adopted to minimise the cutting temperature, and hence to minimise the necrotic depth, but this does not inherently result in a better surface quality after drilling. (ii) The lack of cracks in the HT sample can be explained with the cutting mechanics of bone. Cortical bone exhibits different chip formation mechanisms (Liao and Axinte, 2016a), one of which is fracture mode at the largest chip thicknesses, which results in a cracked surface. Another is shearing mode at the lowest chip thicknesses, resulting in a smooth surface.

Since the HT condition has a considerably lower (20 times) feed rate than the LT condition, it results in lower thrust forces with a smoother chip type and an uncracked surface. However, even though the HT condition induces less macro-cracks to the tissue, it is the one that affects the most in terms of necrosis and micromechanical properties, as it will be shown further.

This macro-level analysis reveals that the cutting process has a considerable effect on the bone surface and temperature, depending on the cutting conditions. Furthermore, the hierarchical and biological nature of the bone raises questions about the effects of such behaviour to the micromechanical properties of the tissue, as well as the repercussions to the living cells near the drilled surface. Therefore, the understanding of the micromechanical behaviour in the machined sub-surface and the necrotic depth into the bone by means of micromechanical testing and histological analysis can reveal an integrated and comprehensive damage evaluation.

4.3.2.2 Necrotic damage in the machined bone sub-surface

Thermal necrosis is induced to the tissue depending on both the maximum temperature and the amount of time that said temperature is held within the tissue. Temperatures as low as 47 °C and 50 °C are enough to cause necrosis if maintained for periods of 60 and 30 seconds (Augustin et al., 2008), respectively. After drilling, a portion of each sample was analysed by histological means (see Fig. 4.13) to understand the relationship of necrotic depth to cutting conditions (e.g. temperature), by measuring the semi-annular thickness of the zone with dead osteocytes (empty lacunae).

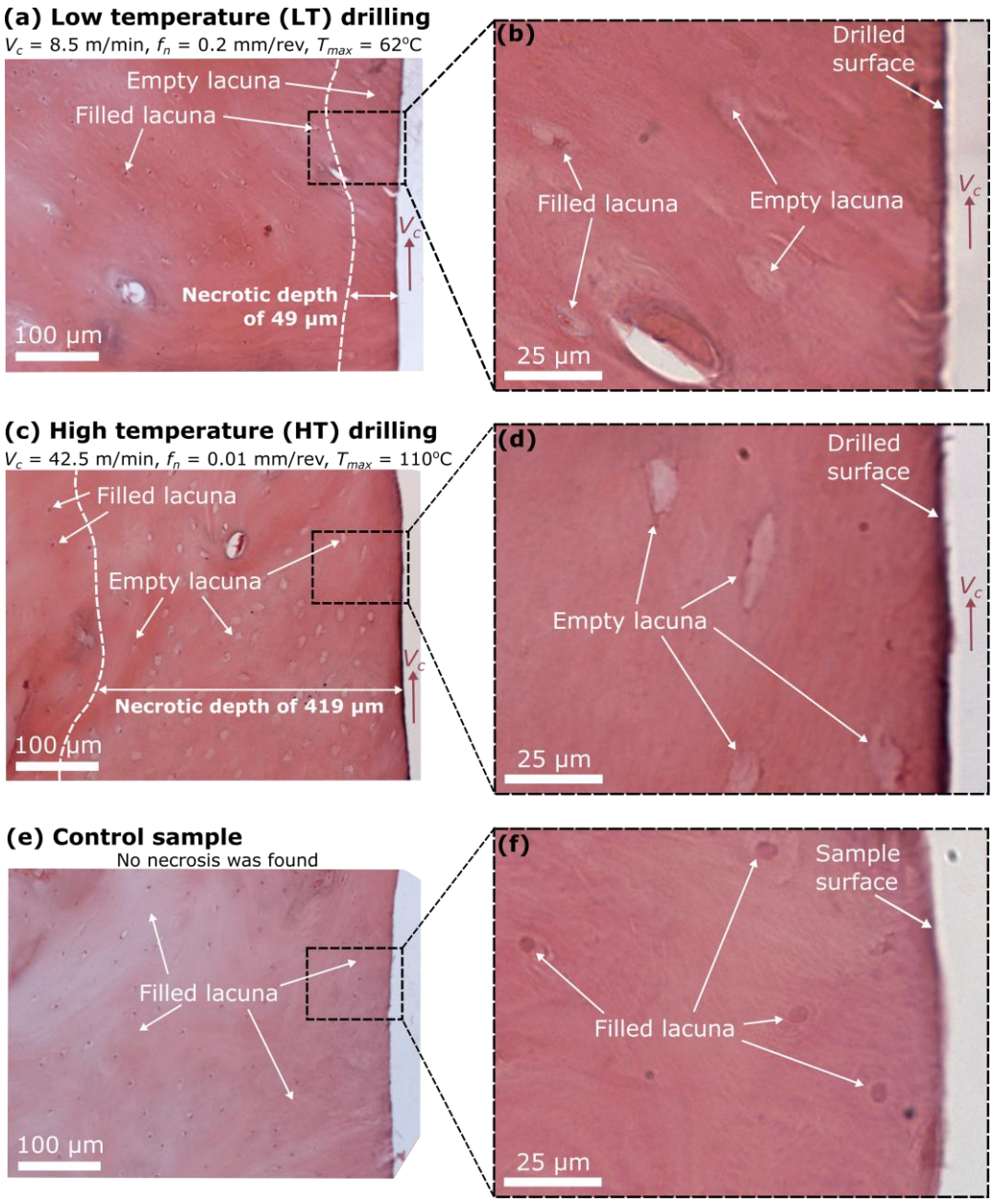

Fig. 4.11. Evaluation of the necrotic depth by histological analysis on the bone surface after using low (LT) and high (HT) temperature drilling conditions. (a,b) At LT conditions: (a) At low magnification, most lacunae seem to be filled with osteocytes both near and far from the surface; (b) Higher magnification reveals that empty lacunae are confined to a necrotic distance of 49 ± 3.9 µm (n = 162). (c,d) At HT conditions: (c) Even at low magnification it is evident that the greater cutting temperature induced an 8-times larger necrotic depth of 419 ± 33.2 µm (n = 185) in average; (d) Higher magnification shows that all osteocytes near the drilled surface disappeared during drilling due to the high temperatures achieved in the sub-surface. (e,f) The control sample showed no signs of necrosis, as all lacunae are filled, both near and far from the surface.

As expected, greater temperatures produced larger necrotic zones (see Table 4.5), since the LT condition (T_{max} = 62 °C) created a necrotic depth of 49 ± 3.9 µm (n = 162) (Fig. 4.11a,b), while the HT condition (T_{max} = 110 °C), possessing a more intense thermal field, yielded a necrosis penetration zone of 419 ± 33.2 (n = 185) (Fig. 4.10c,d).

Table 4.5. Necrotic depth measurements, as obtained with histological analysis.

Drilling condition	Maximum measured temperature, T_{max} (°C)	Necrotic depth (µm), avg ± std dev	Number of measurements, n
Low temperature (LT)	62	49 ± 3.9	162
High temperature (HT)	110	419 ± 33.2	185

Under both sets of conditions, the necrotic zone locally hinders the bone healing capacity due to the lack of osteocyte activity; this makes the recovery more difficult for implant bonding and localised healing (Axinte et al., 2019a; Gupta et al., 2017a). Nevertheless, the healing capabilities of necrotic tissue are not within the scope of this research.

To confirm that sample handling and preparation (i.e. polishing, manual grinding and cutting) did not induce a necrotic effect to the bone, a control sample was analysed as well (Fig. 4.10e,f). The histological analysis showed no signs of necrosis whatsoever, as all lacunae appeared filled, effectively proving that the followed protocol is acceptable and does not induce any necrotic damage to the tissue. Hence, the previously mentioned necrotic depths for the LT and HT conditions were induced only by the drilling operation.

It is also interesting to observe that the Raman spectra before and after drilling (in the drill site) remains unchanged since the high temperatures achieved during the drilling experiments (max. 110 °C) are unable to create significant chemical changes in the bone that could be measured with this technique, as shown in Fig. 4.12. This is consistent with other studies where thermal damage assessment with Raman

spectroscopy is difficultly employed when bones are burned at temperatures lower than 700 °C (Mamede et al., 2018).

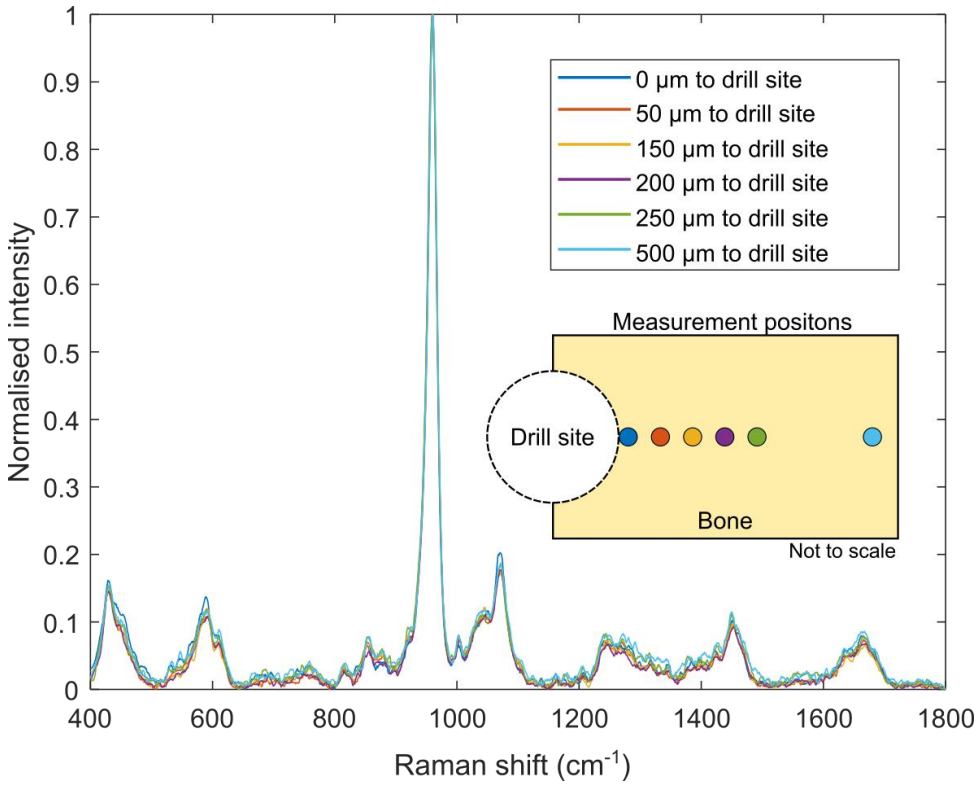

Fig. 4.12. Raman spectra near the drill site after high temperature drilling (T_{max} = 110 °C). Raman spectroscopy was employed to quantify the thermal damage in the HT sample. However, for positions both near (within the necrotic region) and far (outside the necrotic region) from the drill site, the spectrum remains unchanged and in congruence with that of Fig. 3.11. For all points, the crystallinity, mineralisation and carbonate substitution are consistent (i.e. within standard deviation) with that of the control sample (Fig. 3.11).

4.3.3 Brief discussion on necrotic damage of cortical bone via drilling and laser machining

During bone cutting, besides the possibility of inducing cracks at the macroscale, the cells within the tissue are also exposed to damage (i.e. necrosis) by the thermal loads applied during the machining process. To assess this type of damage (i.e. cellular death), histology has been used as the gold standard for many years, and therefore it was employed in this work to assess the necrotic depth for both cutting conditions studied, clearly revealing that a higher temperature (i.e. 110 °C) results in a deeper

necrotic layer (419 ± 33.2 µm, n = 185) when compared to a lower temperature drilling (i.e. 62 °C) with less necrosis (49 ± 3.9 µm, n = 162).

Laser machining, as reported in the previous section, induced comparable levels of damage to the tissue, especially necrotic damage. For instance, the maximum necrotic depth due to laser machining was measured as 268 µm, but this occurred after a single laser pass that removed ca. 0.0336 mm^3 of bone, with a cut duration of 0.7 s (i.e. removal rate of ca. 2.88 mm^3/min). However, in high temperature drilling, the necrotic depth was measured as 419 µm; but in this case, the material removed was 143 mm^3 (i.e. 4256 more times than in the laser) with a drilling time of 18 s (i.e. only 25 times more than the laser), which is traduced to a removal rate of 477 mm^3/min. This highlights that if laser machining was to be employed for removing the same amount of material as in drilling, it would take about 165 times longer, at the expense of inducing much more necrotic damage than with drilling due to the increased time of the heat source (i.e. laser) being in interaction with the tissue. Additionally, if laser machining is to be employed without external coolant, the processing time would even have to be larger than 165 times to enable cooling periods to keep the necrosis at a comparable value as those with drilling.

As a result, it can be said that even while laser machining offers the main advantage of improving precision, it requires a much longer processing time (as opposed to conventional drilling) to achieve the same material removal rates with minimum damage inducement. With this in mind, drilling was the selected material removal method for an in-depth study of micromechanical characterisation, which is discussed next to analyse the micromechanical response of the necrotic zone, aspects that not yet been addressed in the literature.

4.4 In-depth study of the selected machining operation

Being a material that sustains mechanical loads in the human body, mechanical damage (e.g. mechanical properties changes, failure mechanism shifts) should also be of relevance and employed in parallel with histology for a full material integrity assessment. A promising approach on mechanical damage assessment is micromechanics, as it allows for localised (i.e. near the machined surface) material testing (Davis et al., 2020).

Micromechanical testing of bone has been employed since the 1980s with the aim of mapping the elastic properties (Rho et al., 1997, 1993) of its different constituents (e.g. osteons (Ascenzi et al., 1990), trabeculae (Kuhn et al., 1989)) and to characterise the bone repair mechanism (Kong et al., 2020). Moreover, recent research has raised attention to the post-yield behaviour of the bone structure since there is a ductile-to-brittle failure mechanism transition going from the micro- to the macroscale, respectively (Tertuliano and Greer, 2016). Microindentation and micropillar compression are useful techniques for comprehensively evaluating the mechanical behaviour in both the elastic and plastic regions of the material (Oliver and Pharr, 1992; Schwiedrzik et al., 2014a), and so could be used to evaluate damage (Lloyd et al., 2017; Poundarik et al., 2012). Even though these techniques have been used for bone characterisation in dry (Rho et al., 1997; Schwiedrzik et al., 2014a) and wet (Bushby et al., 2004; Schwiedrzik et al., 2017) conditions, they have not been explored for assessing machining-induced micromechanical alterations. Moreover, as opposed to the complex analysis that microindentations require, micropillar compression allows for a straightforward analysis that enables understanding of the energy dissipation of the material under both the elastic and plastic domains. Therefore, micropillar compression testing is an important micromechanics technique that could be employed for damage assessment in bone.

Bone mechanical assessment in this direction has been made focusing on the mechanical behaviour at the macroscale (Ma et al., 2017; Varvani-Farahani and Najmi, 2010) and microcracks formation (Zhang et al., 2019), but these have so far failed to successfully capture microscale effects in terms of mechanical properties or localised failure mechanisms. However, it is at this micro-level of detail where one can start to understand the true extent of bone damage after machining, from both the micromechanical and biological perspectives, allowing evaluation of any implications this could have on the bone's functionality.

Following these propositions, here, three questions are investigated: What are the micromechanical characteristics (i.e. modulus of elasticity, compressive yield strength and compressive ultimate strength) and failure mechanisms of cortical bone in areas near and far from a machined surface? How does the micromechanical behaviour of the bone change as a function of distance from the machined surface? What is the relationship between the necrotic depth and the micromechanical properties? To address these questions, the drilled samples (i.e. those used in section 4.3) were sectioned and micropillars were fabricated with a Focused Ion Beam (FIB) milling technique in the drilled sub-surface to conduct micromechanics tests with an in-situ SEM method. This study reveals, for the first time, the micromechanical characteristics of damaged cortical bone after drilling operations.

4.4.1 Experimental methodology

After drilling (see section 4.3.1), the samples were immediately (i.e. within 20 minutes of drilling) cut into two sections along the hole axis (Fig. 4.13) and used for damage evaluation of the bone machined sub-surface. One half was used for histological analysis (i.e. necrosis evaluation) and the other one for micromechanical testing (i.e. changes in the micromechanical behaviour). However, to study the effects

of high and low temperature drilling, only two of the twelve drilled samples were used for histology and micromechanics (Table 4.4).

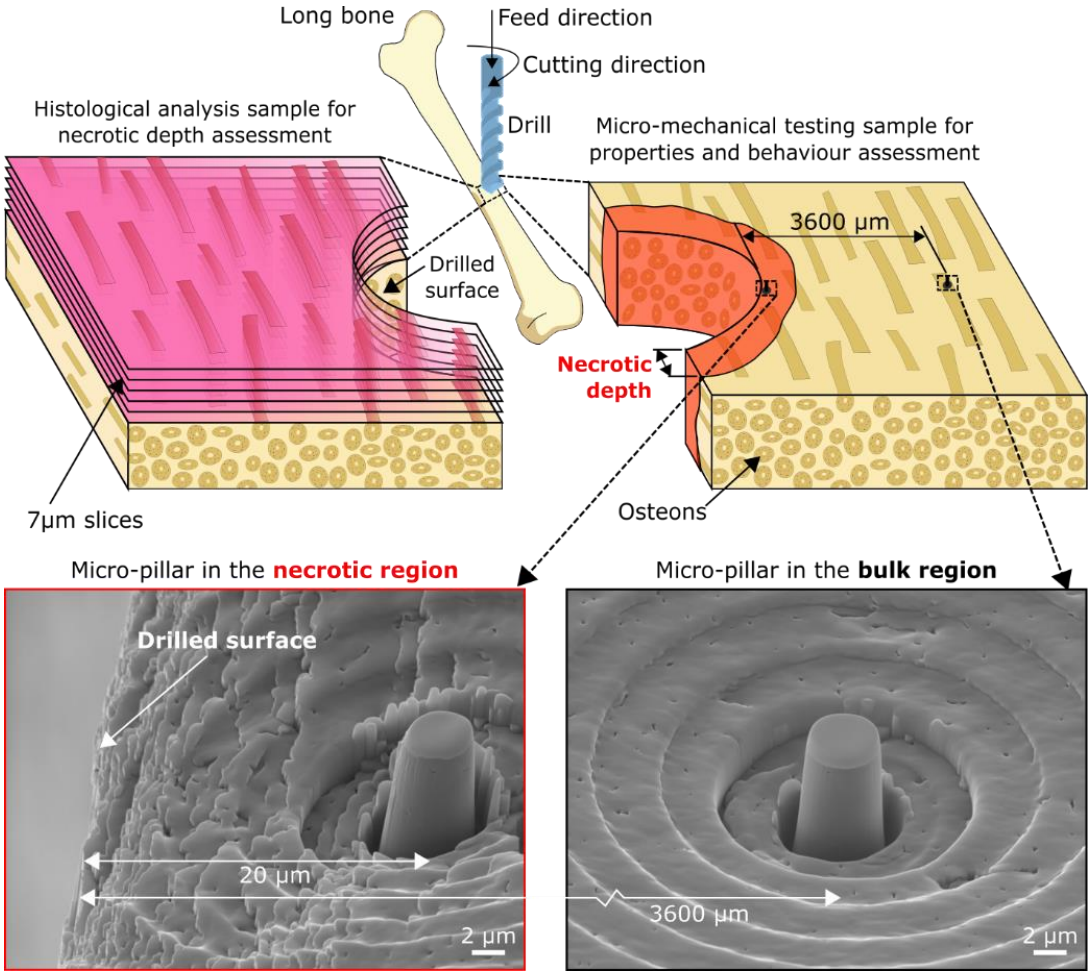

Fig. 4.13. Location of micropillars inside and outside the necrotic zone, and histological analysis of the drilled holes. After drilling, one half of the specimens (i.e. hole) was used for histological analysis (shown as pink slices) to evaluate the necrotic depth. The other half was used for fabricating micropillars with FIB inside the necrotic region (shown in red) and in the bulk material (shown in black) for evaluation of elastic and plastic properties, as well as to perform failure mode observations.

4.4.1.1 Micromechanics

To assess machining damage in terms of mechanical performance and properties, micro-testing (i.e. micropillar compression) was used as an approach for evaluating elastic and plastic properties inside and outside the necrotic (N) zone that was evaluated with the histological analysis (zones defined in section 4.3.2.2).

Micropillars were located in the bulk (B) material (i.e. 3600 µm radially away from the drilled surface) and in the necrotic (N) region (see Fig. 4.13) for both drilling conditions. In the LT sample 6 micropillars were fabricated (2 in the necrotic zone and 4 in the bulk zone); in the HT sample 9 micropillars were fabricated (4 in the necrotic zone, 3 in the bulk zone and 2 in between these zones). A total of 15 micropillars were successfully compressed.

Investigations on micropillar compression in brittle materials (Gerberich et al., 2009) have shown that pillars exceeding a threshold critical diameter, d_{crit}, are prone to crack development failures, whereas those with $d_{pillar}<d_{crit}$ tend to fail with ductile mechanism (Östlund et al., 2011). Furthermore, according literature (Schwiedrzik et al., 2014a), $d_{crit}>5$ µm for ovine cortical bone in the radial direction. Therefore, all micropillars were fabricated with a nominal diameter of 5 µm and an aspect ratio of 2 (Zhang et al., 2006). In this manner, it is assured that any failure mode transition (i.e. from ductile to brittle) that could be observed is a result of machining damage and is not related to micropillar size.

After fabrication, each pillar was inspected via SEM with a 50° specimen tilt and with different rotation angles for (i) a comprehensive pre-testing geometrical characterisation and (ii) to confirm the pillar was not located above a lacuna (Fig. 4.14). The micropillars were measured to be 4.94 ± 0.27 µm (n = 15) in diameter with an aspect ratio of 2.22 ± 0.21 µm (n = 15), making them of appropriate size for micropillar compression testing (Zhang et al., 2006).

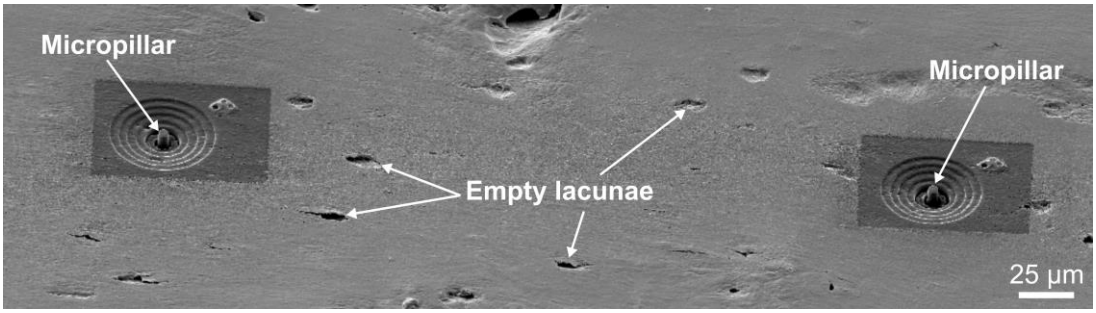

Fig. 4.14. Example of a cluster of two micropillars in the high temperature drilling conditions sample. The empty lacunae are easily visible since they normally are within 5-20 µm long (Noble, 2008), which makes them comparably larger to the nominal diameter of the micropillars (i.e. 5 µm).

During inspection, it was detected that micropillars located at 20 to 50 µm away from the drilled surface (e.g. micropillar in the necrotic zone shown in Fig. 4.13) exhibited a rougher surface around them when compared to micropillars located in the bulk region due to the edge effect caused by FIB milling during the roughing pass. However, this edge effect does not adversely affect the use of these micropillars for compression testing since a finishing pass was also included in the FIB milling process that yielded a smooth micropillar surface. This was confirmed with several micropillars that behaved mechanically the same (i.e. both in stress-strain performance and failure mode) in the edge of the sample and in the bulk material (as shown in Fig. 4.15a).

All micropillars were compressed at a strain rate of 1.35×10^{-3} s^{-1} until failure. This was done using a nanoindenter (Alemnis ASA, Switzerland) with a 6-µm flat diamond tip inside an SEM (FEI Quanta 650) under high vacuum conditions.

4.4.2 Results of conventional machining-induced micromechanical damage in cortical bone via drilling

4.4.2.1 Micromechanics of the machined bone sub-surface

To assess the micromechanical behaviour of bone near the drilled surface, micropillar compression tests have been performed in the sub-surface at different radial distances in two distinct regions: (i) on the bulk (B) material, where no damage is expected (3600 μm beneath the drilled surface) and (ii) on a region near the machined sub-surface (within the necrotic (N) zone and near the drilled surface). Refer to Fig. 4.13 for visual representation of the locations.

Micropillars in the low temperature (LT) drilling condition sample

The micropillars in both the bulk (Fig. 4.15a - B_{LT}, sky colour) and necrotic (Fig. 4.15a - N_{LT}, black colour) regions of the LT drilling condition behaved similarly in terms of stress-strain. These pillars displayed an elastic modulus of 15.78 ± 1.56 GPa (n = 6), yield strength of 0.34 ± 0.02 GPa (n = 6) and ultimate strength of 0.67 ± 0.04 GPa (n = 6), in fair agreement with previously published results of micropillars in damage-free cortical bone in the transverse direction (Schwiedrzik et al., 2014a). Besides displaying such an unaffected micromechanical behaviour, the post-yield mechanism until failure was exclusively governed by slipping along a single shear plane (Fig. 4.15b), clearly showing the characteristic shearing failure mode of undamaged cortical bone in the microscale (Schwiedrzik et al., 2014a). These results indicate, for the first time, that low temperature (T_{max} = 62 °C) machining produces no changes in the micromechanical behaviour, implying that micromechanical damage is inexistent in both the necrotic (N_{LT}) and bulk (B_{LT}) regions of the machined sub-surface.

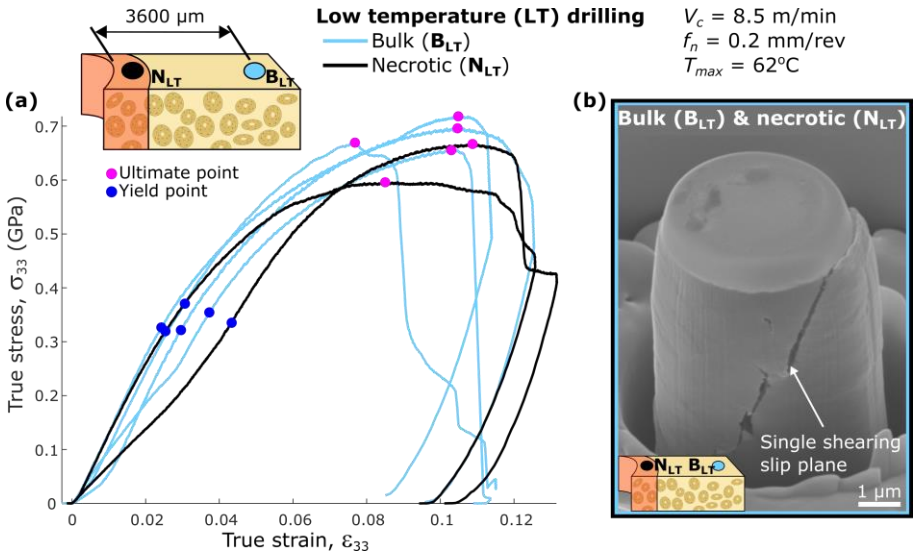

Fig. 4.15. Stress-strain curves and failure micrograph of micropillars from the low temperature (LT) drilling condition in the necrotic (N_{LT}) and bulk (B_{LT}) regions. (a,b) Micropillars in the bulk and necrotic zones of the LT drilling condition exhibited the classic behaviour of undamaged cortical bone. (a) Stress-strain curves showing no difference between mechanical performance in the bulk (B_{LT}) and necrotic zones (N_{LT}) obtained in LT drilling conditions. (b) Representative micropillar of both the bulk (B_{LT}) and necrotic (N_{LT}) zones, which failed exclusively by slipping along a single shear plane.

Micropillars in the high temperature (HT) drilling condition sample

The micropillars in the bulk material (Fig. 4.16a - B_{HT}, blue colour) of the HT sample revealed a congruent stress-strain behaviour (i.e. within standard deviation) as those from the LT drilling sample, with elastic modulus of 16.01 ± 0.72 GPa (n = 3), yield strength of 0.36 ± 0.04 GPa (n = 3) and ultimate strength of 0.65 ± 0.01 GPa (n = 3). Furthermore, these micropillars (B_{HT}) also failed by shearing (Fig. 4.16b), as those from the LT drilling conditions (Fig. 4.15b); in both cases, the failure mode is clearly identifiable and in agreement with another bone micropillar compression study (Schwiedrzik et al., 2014a). This behaviour confirms that in high temperature drilling (T_{max} = 110°C), the micromechanical behaviour of bone is not affected at far distances (i.e. 3600 µm) from the drilled surface (away from the necrotic layer).

Micromechanical damage was detected for micropillars closer to the drilled surface in the HT sample in the form of reduction of properties. The pillars within the necrotic layer (Fig. 4.16a - N_{HT}, green colour) exhibited an elastic modulus 42% lower (9.20 ±

1.54 GPa, n = 4) than the unaffected bone. Ultimate strength was also lower by 41% (0.39 ± 0.02 GPa, n = 4). Nonetheless, the yield strength was less affected, with only a 15% reduction (0.29 ± 0.03 GPa, n = 4). All the pillars confined to this region (N_{HT}) failed by splitting of axial cracks (Fig. 4.16e) which corresponds to a brittle failure mode.

This behaviour shows that if high temperatures occur during drilling, the damaged zone is not only constrained to a greater cellular death extent, as histological analysis suggests (Fig. 4.10 and Table 4.5), but also to a considerably different micromechanical post-yield behaviour with smaller elastic and plastic regions.

To assess the existence of a transition zone between the necrotic (N_{HT}) and the undamaged (B_{HT}) regions of the HT sample, additional micropillars were fabricated on intermediate (I) regions (i.e. I_1 and I_2) outside of the necrotic area (refer to Fig. 4.17 and the legend of Fig. 4.16). These intermediate locations for pillars I_1 and I_2 were set to 2700 and 1500 µm from the drilled surface, respectively. The analysis revealed that the pillar closer to the bulk material (Fig. 4.16a – I_1, yellow colour) behaved similarly to the pillars in the bulk region (Fig. 4.16a – B_{HT}, blue colour), with elastic modulus and yield stress within the standard deviation of the pristine values (15.17 GPa and 0.35 GPa, respectively); and just the ultimate stress lower by 20% (0.53 GPa).

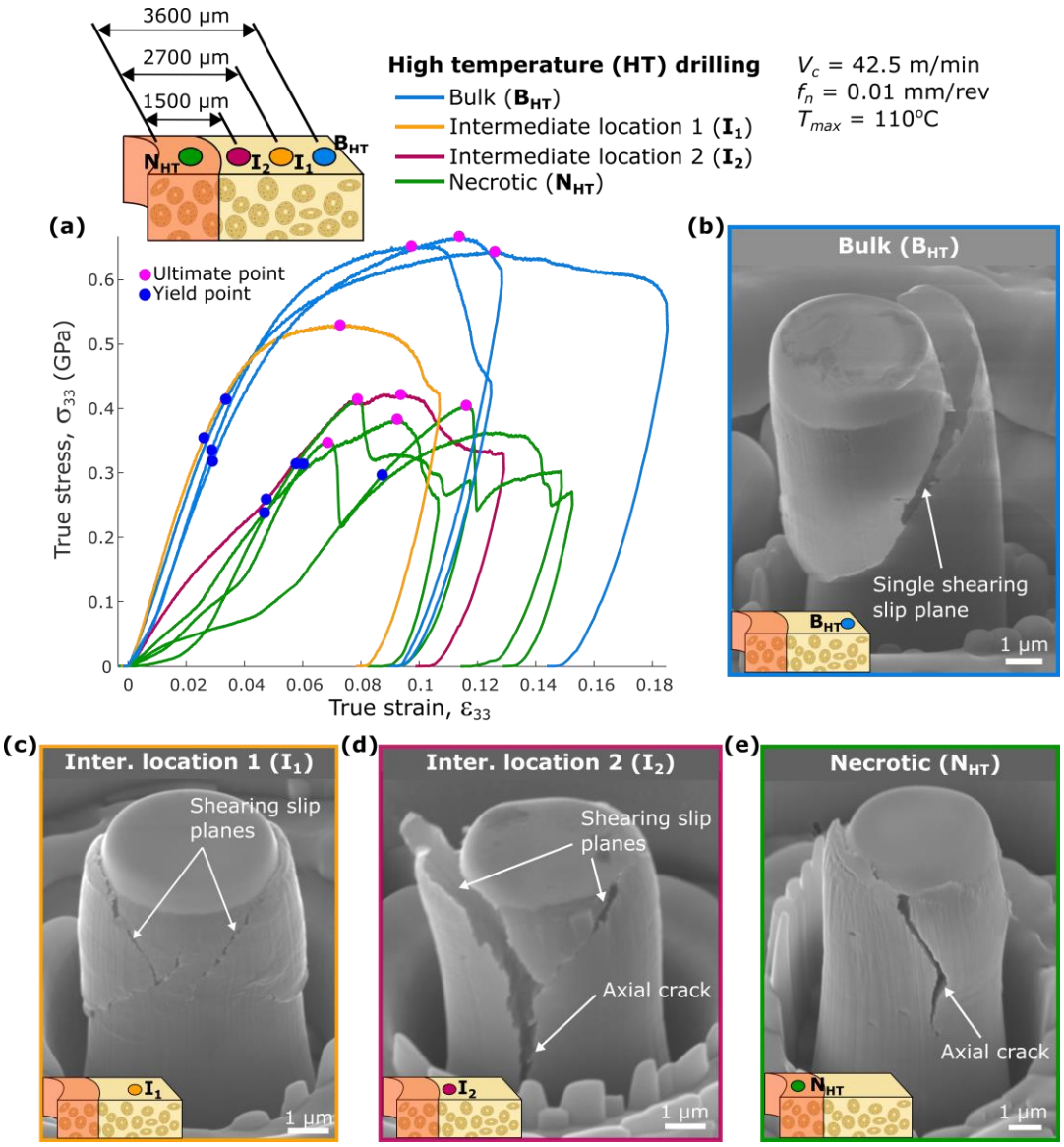

Fig. 4.16. Stress-strain curves and failure micrographs of micropillars from the high temperature (HT) drilling condition in the necrotic (N_{HT}), intermediate (I) and bulk (B_{HT}) regions. Micropillars from the HT sample exhibited different behaviours depending on their location. (a) Stress-strain curves, showing that bulk micropillars (B_{HT}) behaved as undamaged bone (i.e. similar to Fig. 4.15a) and that the performance decreases as the micropillar location gets closer to the drilled surface. (b) Micropillars located in the bulk region (B_{HT}, blue colour) failed by slipping along a single shear plane. (c) The micropillars located in intermediate location 1 (I_1, yellow colour) exhibited a two-plane shearing failure mechanism. (d,e) Micropillars located in intermediate location 2 (I_2, magenta colour) and necrotic (N_{HT}, green colour) zones failed by axial splitting.

Nonetheless, the pillar closer to the necrotic region (Fig. 4.16a – I_2, magenta colour) behaved similarly (i.e. within standard deviation) to the pillars inside the necrotic layer (Fig. 4.16a – N_{HT}, green colour), exhibiting an elastic modulus, yield stress and

ultimate stress of 8.86 GPa, 0.26 GPa and 0.41 GPa. These results confirm that the mechanical properties of the bone degrade in a gradual manner from the pristine behaviour in the bulk (B_{HT}) material to a weakened performance in the necrotic (N_{HT}) layer. This phenomenon only occurs if high temperatures occur during the cutting operation, such as with HT conditions (Table 4.4).

Failure mode analysis of the micropillars in the transition layer showed that pillars in intermediate location 1 (I_1, yellow colour) failed by the development of two slip planes with localised shear (Fig. 4.16c), while the pillars in intermediate location 2 (I_2, magenta colour) failed by axial splitting (Fig. 4.16d). This proves that the mechanical properties are gradually transitioning from the undamaged (B_{HT}) region to the necrotic (N_{HT}) zone, and so does the failure mode. The failure mode shifts from single-plane shearing (bulk region, B_{HT}) to two-plane shearing (intermediate region) and then to axial splitting in the necrotic (N_{HT}) region, indicating a ductile-to-brittle transition going from the undamaged bulk (B_{HT}) region to the necrotic (N_{HT}) zone.

According to classic fracture mechanics (Anderson, 2017), cracks can propagate in one of three main modes ((I) opening; (II) in-plane shearing; (III) out-of-plane shearing), depending on the direction of loading. The observed brittle failure (axial splitting, Fig. 4.16d,e) corresponds to a Mode I fracture, consisting of the axial crack that propagates from the intersection point of two slip planes, as shown in Fig. 4.16d. This type of fracture can be modelled at the nano- and microscales employing dislocation-based models (Östlund et al., 2009). The micropillar's critical energy release rate, G_{Ic}, for this case can be calculated as (Schwiedrzik et al., 2017):

$$G_{Ic} = \frac{1}{16E}\pi\sigma_{ult}^2 d_{pillar} \sin\phi_{pillar} \cos^3\phi_{pillar} \qquad \text{Eq. 4.1}$$

where E is the elastic modulus, ϕ_{pillar} is the shear plane angle, σ_{ult} the ultimate stress and d_{pillar} the pillar diameter. Calculations for each pillar yielded an average G_c of 6.68 ± 1.14 J/m2 (n = 9) for the pillars that failed with ductile mechanism (Figs. 8b & 9b,

& Supplementary Movie S1) and 4.24 ± 1.03 J/m^2 (n = 5) for the pillars that failed with axial splitting (Fig. 4.16d,e). These results indicate that pillars in the necrotic zone of high-temperature drilling have a mode I G_c that is 37% lower than those from pillars in the damage-free bone, implying that they require less energy to fail by splitting and are more susceptible to behave in a brittle manner. Such reduction in toughness, as well as the weaker elastic performance, makes the machined sub-surface more prone to this type of fracture under a brittle regime if subjected to stress.

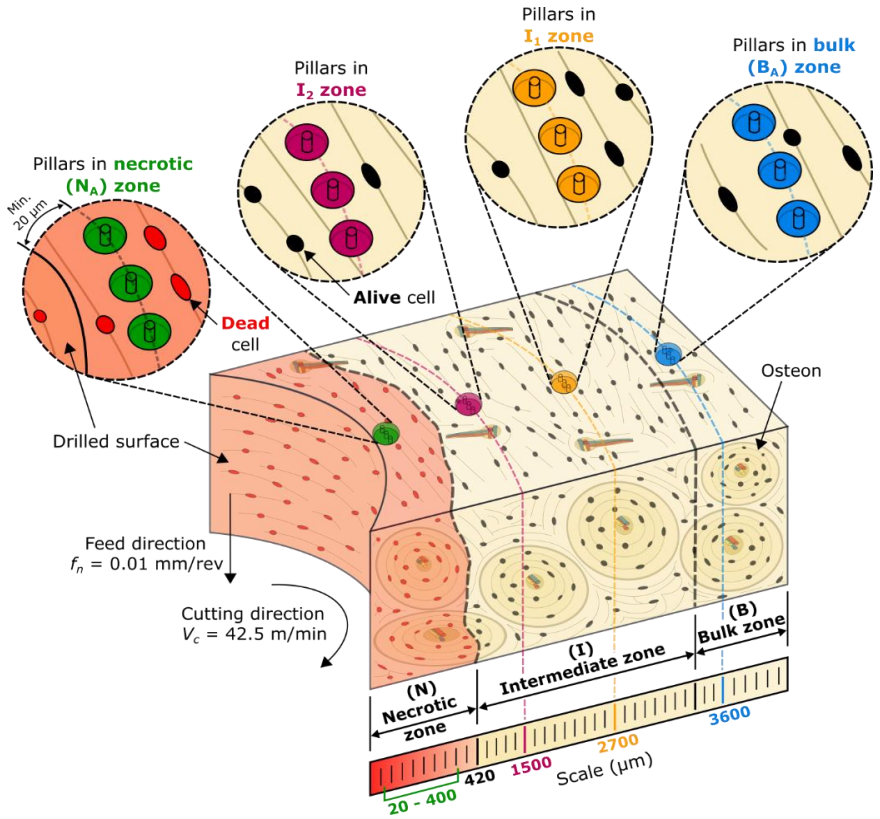

Fig. 4.17. Schematic of the micropillar cluster locations in the high temperature (HT) drilling conditions sample. The micropillars in the necrotic zone (N_{HT}, green colour) are located within 20 to 400 µm away from the drilled surface, since the necrotic (N) depth in this condition is 419 ± 33.2 µm (n = 185) (Fig. 4.10c,d). Micropillars in the bulk material (B_{HT}, blue colour) are located at 3600 µm from the drilled surface. To assess if there is a transition of the micromechanical behaviour between the necrotic (N_{HT}, green colour) and bulk (B_{HT}, blue colour) zones, additional pillars were fabricated in two intermediate locations (i.e. I_1 and I_2, shown in yellow and magenta colours, respectively).

4.4.3 Discussion on the drilling thermomechanical effect upon the bone's integrity post-machining

From an engineering standpoint, bone could be regarded as a structural component of the human body, as it sustains mechanical loads. Therefore, not only its biological assessment (i.e. necrosis evaluation) is of relevance, but also its mechanical performance. With the intention of studying the material behaviour at the microscale after been exposed to large temperature via a machining process, micromechanical testing (i.e. micropillar compression) was performed inside (near the machined surface) and outside (in the bulk region) the necrotic region.

The micromechanical tests showed no changes nor in properties (i.e. exhibited pristine properties) nor in failure mode (e.g. exhibited ductile failure with shearing mechanism) for pillars located in the low temperature (LT) sample, both inside the necrotic (N_{LT}) region and in the bulk (B_{LT}) zone. This was also the case for the micropillars in the high temperature (HT) sample located in the bulk (B_{HT}) region. Nevertheless, reduction in properties was quite significant for micropillars located in the necrotic (N_{HT}) region of the high temperature (HT) sample, displaying an elastic modulus, ultimate strength and yield strength reduced by -42%, -41% and -15%, when compared to the undamaged pillars. Furthermore, these set of pillars (N_{HT}) displayed a dominant brittle failure characterised by a mode I fracture (i.e. axial crack, Fig. 4.16d,e).

The observed failure mode shift (from ductile to brittle) raises questions of the nature that drives such a drastic change in the microstructure to behave this way after exposure to high cutting temperatures (i.e. 110 °C). One or more phenomena could be occurring in the bony structure that makes it shift this way, such as a local dehydration effect surrounding the drill site.

Bone naturally possesses water at all its hierarchical levels, including pore-level water in the microstructure (i.e. within the Haversian canals, Volkmann's canals and the

lacuno-canalicular system), loosely bound water in its ultrastructure and nanostructure (i.e. within the lamellae, the collagen chains and the mineral crystals), and tightly bound water at the molecular scale and at the structural level (i.e. in the apatite structure) (Granke et al., 2015). Prior to the drilling experiments, the samples were kept at room temperature and immersed in saline solution; hence, it is expected that they retained a significant amount of water up to when the drilling started. During the high temperature drilling process, the measured temperature reached a maximum of 110 °C, which by itself is above the boiling temperature of water at atmospheric pressure. Therefore, it could be intuitively thought that bone regions near the drill site, which were exposed to the highest temperature build-up, lost some of their water content due to the exposure to such a high temperature; hence, creating a local dehydration effect. Furthermore, it is well known that dehydration increases the brittle behaviour in bone (Granke et al., 2015; Maghsoudi-Ganjeh et al., 2020; Samuel et al., 2016) both in compressive and tensile loading, which could explain the observed micropillar failure mode shift from ductile to brittle shown in Fig. 4.16. However, the literature also points out that as the brittle behaviour increases with dehydration, the stiffness and strength of the bone should also increase, which is opposite in this case: with high temperature drilling the brittle behaviour increased, but the stiffness and strength decreased. This does not inherently imply that local dehydration is not the explanation behind these results, but that it could be occurring in parallel with other phenomena.

Some explanations for the decremental properties in the locally dehydrated region are, for example, thermally induced residual stresses that are able to leave the material in a pre-loaded state, or changes to the nanostructure and molecular structure related to temperature but not to water. Nevertheless, these are other fields of study by themselves and out of the scope of this research. Whether any of them are occurring or not, more in-depth research is required to properly address them, as they are only plausible explanations of the underlying phenomena behind the presented results of

micropillar compression testing for assessing machining-induced thermal damage in cortical bone.

In addition, cortical bone is a porous structure (Cowin and Cardoso, 2015), meaning that the localised porosity in each micropillar may vary. Therefore, some serrated trends in the stress-strain curves may be observed (see Fig. 4.16a - N_{HT}, green colour) due to the collapse and densification process that occurs when a local porosity is collapsed during compression of the micropillar. In the future, it will be valuable to include local porosity assessments to improve the understanding of the stress-strain behaviour of bone under uniaxial compression micro-testing.

Usually, following the bone cutting process in a surgical environment, an implant is placed in intimate contact with the machined surface and, to prevent early stage failures of the implant, bone overheating must be avoided (Kate et al., 2016). The main reason for this precaution is based on histological analysis, since at greater temperatures the osseointegration process is hindered with necrosis. Nevertheless, here it has been shown that once high temperatures do occur, not only the necrotic layer is deeper, but an even greater heat-affected transition zone extends beyond the necrotic region. This implies that a larger volume of the bone is negatively affected from the mechanical perspective than from the biological standpoint, i.e. more volume of affected bone surrounding the implant when considering altered mechanical properties than when considering the quantity of dead cells. The hindered osteocyte activity in parallel with the lower mechanical strength could significantly alter the remodelling process of bone, since it has been proven that the remodelling process is not only sensible to necrosis, but also to the induced loads in the tissue (Christen et al., 2014). Nevertheless, the results shown here are limited to ex-vivo bone in a non-clinical environment, and so further research would be required to study the bone micromechanical surface integrity and its impact on implant applications and the bone healing process.

With this research, an important aspect that has not been reported before comes to light: thermal damage manifests not only as necrosis in a bone machining operation, but also as micromechanical properties reduction and increased brittle behaviour near the machined sub-surface. In our studied case, when high temperatures (110 °C) occur during bone cutting, a weak micromechanical layer in the machined sub-surface is generated. This layer is larger than the necrotic region and exhibits a brittle behaviour with lower modulus (-42%), ultimate strength (-41%) and yield strength (-15%) than healthy undamaged bone. This has successfully been proven this for high temperature drilling condition, where the micropillars in this region failed by axial splitting due to their reduction (-37%) in toughness for this type of fracture (i.e. critical energy release rate of Mode I fracture). These findings unveil new knowledge about the complex material behaviour of bone from an engineering perspective.

4.5 Concluding remarks

Two material removal method were compared in terms of induced damage in cortical bone. Firstly, laser machining was studied to provide machining-induced damage that is mostly driven by thermal loads. Secondly, drilling was studied to contrast the damage when the material removal process is not purely thermal, but thermomechanical.

The laser machining study was performed to assess the surface quality (i.e. roughness, trench depth, cracks) and induced cellular damage (i.e. necrosis) in ex-vivo bovine cortical bone, following laser machining processes at various feed speeds (i.e. 1 – 20 mm/s) and laser pulse widths (i.e. 60 ps, 200 ns, continuous wave). Thermal measurements showed that peak temperatures during processing can reach up to 1318 °C for an instant, but the thermal distribution is affected by the cooling time (i.e. time between each pulse). Surface inspection showed that there is a non-linear relationship between feed speed and trench depth and a notably, a large depth variation over a small

feed speed range for the nanosecond laser when compared to a similar feed range by the picosecond laser. Surface cracks were also found on the sample machined by the picosecond laser at a slow feed speed (V_f = 1.0 mm/s), the absence of these cracks in the other samples indicates that their formation may be caused by the production of an explosive plasma pressure wave and is potentially exacerbated by dehydration of the bone. Histological analysis revealed that the 200 ns pulse width produced the greatest necrotic damage and carbonisation, whereas the 60 ps pulse width produced the minimum; being the main reason that a shorter pulse width facilitates intermittent convection between each pulse (favoured cooling).

The laser machining study reveals how the choice of laser type (i.e. pulsed or continuous wave) needs to be considered for the further development of laser osteotomy. Additionally, it exposes how pulse duration and frequency leads to large variations in the thermally induced effects imparted to the bone during machining. This highlights the potential for the use of ultra-short pulse widths (i.e. in the picosecond range) to shift the material removal mechanisms from thermal to optomechanical, reducing the temperature-dependent necrotic depth and in-turn, the opportunity to improve healing times in a clinical scope.

The drilling study was carried out to assess the machining-induced thermal damage in cortical bone after drilling with low (LT) and high (HT) temperature drilling conditions, which produced mild (T_{max} = 62 °C) and intense thermal fields (T_{max} = 110 °C), respectively, during the machining operation. SEM analysis showed that the gross appearance of the machined surface could be deceiving, as LT drilling produced evidently large cracks, while HT drilling produced a smearing effect that might appear smooth, but in fact has minor cracks lying underneath. Histological analysis and in-situ micropillar compression tests revealed that high temperature drilling produces an 8-times larger necrotic depth (419 ± 33.2 µm, n = 185), when compared to low temperature drilling (49 ± 3.9 µm, n = 162); clearly showing that the higher the temperature, the larger the necrotic damage. Furthermore, in high temperature drilling,

the micropillar failure mode analysis revealed that the microstructure shifts from being ductile in the bulk, to brittle and mechanically weaker (up to -42% reduction in elastic modulus, -41% in ultimate compressive strength and -15% in yield strength) near the machined surface. It was found that this brittle layer can extend to at least 1500 μm away from the machined surface, which is more than 3 times the necrotic depth. This brittle layer was found to be inexistent in low temperature drilling, where micropillars in the necrotic layer retained both their pristine properties and their ductile failure mode.

The drilling study reveals that the traditional histological analysis, which is valuable for assessing the amount of cellular death, could be complemented with micromechanical analysis to yield a full bone damage evaluation that accounts for both biological and mechanical assessments. Furthermore, the method here presented (i.e. micromechanical testing) should be extrapolated to assess in-vivo or in-vitro bone after a surgical intervention where temperature build-up could occur in the bone-tool interface (such as in drilling, burring, milling, grinding or sawing associated with orthopaedics, dentistry, maxillo-facial surgery or neurosurgery) to study the micromechanical integrity of the tissue both as machined and as it heals post-surgery.

It is important to mention that in both laser machining and drilling, the machining was performed in dry condition (i.e. no external coolants were used to allow for a more native material response to various laser conditions and drilling parameters) and with ex-vivo specimens. This enabled a proper understanding of the material response in a ‘material state’ (i.e. dry, without internal nor external irrigation) that has been traditionally employed by the research community.

Chapter 5 - The effect of interstitial fluid on the machining of bone and its induced damage

Up to this point, the research has focused on understanding the machining-induced damage in cortical bone not only with gold-standard Histology, but also employing micromechanical testing to unveil the degree of micromechanical damage near the machined subsurface. This is a necessary precursory assessment towards understanding the native material response of cortical bone as it is usually tested worldwide in the research community: in dry state. However, the question about the role of the internal irrigation of cortical bone remains unanswered. As such, this chapter reports the effect that the interstitial fluid has both in terms of the machining behaviour and in terms of the machining-induced damage.

To understand the effect of interstitial fluid on the cutting process, first a set of experiments dedicated to studying the chip formation and the validation of a cutting forces model is detailed here while employing a novel laboratory setup that enables mimicking an 'in-vivo-like' state of the bone samples during machining. This is followed by an analysis of the material response in terms of mechanical and thermal damage.

This chapter enables a more realistic understanding of bone not only as a material, but as a tissue being cut. This is done by contrasting the drastic differences that exist between traditional dry bone machining and internally irrigated (i.e. as in surgeries is the case) bone machining.

5.1 Introduction

Bone cutting is a common process in orthopaedics, dentistry and neurosurgery that comprises both simple interventions (e.g. hole drilling) and complex procedures (e.g. joint replacement involving machined surface matching implant surface). However, bone cutting is challenging both in terms of machining analysis (Liao and Axinte, 2016a) and damage assessment due to its intricate hierarchical composite-like microstructure (Tan et al., 2021). Engineeringly, cortical bone consists of an arrangement of osteons (i.e. the fibres, running through the principal loading direction in the bone) (Heřt et al., 1994) within an interstitial lamellae (i.e. the matrix) composed of old osteons that have been partially resorbed during the remodelling process of the bone (Currey, 2002). Further, its porous structure contains the blood, nerve and interstitial fluid supplies (Cowin and Cardoso, 2015) that are necessary for the living tissue. As consequence, machining-induced strains and temperatures in cortical bone are difficult to analyse; therefore, vast amount of research has focused on improving the understanding of bone as a material that is subjected to mechanical loads, such as under machining conditions.

Orthogonal cutting of bone has been extensively studied with the principal aim of understanding its cutting mechanisms under different machining conditions. Even the earliest reports on the cutting mechanisms of cortical bone (Jacobs et al., 1974; Wiggins and Malkin, 1978) showed a dependency of the chip morphology on both the cutting direction (i.e. relative to the principal osteon direction) and the depth of cut (DOC), where a small DOC was associated with continuous chips and a smooth surface, and a large DOC with a fractured or segmented chip and a rough surface. Additionally, the interface between the osteons and the interstitial lamellae (i.e. the cement line) was associated with crack propagation due to its lower strength when compared to both the osteons and the interstitial lamellae (Krause, 1987). More recent studies have confirmed that continuous or semi-continuous chips occur with a DOC

lower than 80 µm at low (12.5 µm/s) (Sugita and Mitsuishi, 2009), intermediate (8 m/s) (Feldmann et al., 2017) and high (>15 m/s) (Sugita et al., 2014) cutting speeds, thus highlighting that bone's anisotropy and DOC are far more relevant in the cutting mechanism than the strain rate itself.

Contrary to the machining of soft tissues, which exhibit a large viscoelastic behaviour (Chen et al., 2021), bone possesses a ductile-to-brittle performance. Three main cutting modes can be identified in bone machining, and these depend on both the cutting direction and, mainly, the DOC (Axinte et al., 2019b). The modes show a transition of a ductile behaviour at low DOC to a brittle behaviour at large DOC. When the DOC is small (usually less than 13 µm), the cutting energy promotes plastic deformation, but not cracking (Feldmann et al., 2017), thereby producing a continuous chip (i.e. ductile behaviour) that is in compliance with the Erns-Merchant principle (Shaw, 2005); this cutting mode is known as shear cutting (SC) mode. Further, when the DOC is at intermediate values (usually between 13 and 70 µm), the chip volume is larger and it hinders plasticity, while enabling cracking to occur along the shear plane, thereby producing a series of discrete segments of chip (Liao and Axinte, 2016a); this cutting mode is referred to as shear-crack cutting (SCC) mode and is characterised by its semi-brittle nature. Finally, when the DOC is large (>70 µm), the cutting and thrust forces play a more important role since their combined actions is enough to surpass the fracture toughness of the bone, thereby enabling a fracture cutting (FC) mode (i.e. brittle behaviour) in the chip formation mechanism (Liao and Axinte, 2016a). Naturally, these cutting modes have a direct effect on the machined surface quality, where a SC mode can be associated with smooth surfaces, while the FC mode with rougher surfaces (Bai et al., 2020).

Due to the complexity of the bone cutting process, modelling it is a challenging task. As such, a significant number of papers have been reported, principally employing Finite Element Method (FEM) for the prediction of temperatures, cutting forces and chip formation (Marco et al., 2015). This has been usually done by adapting isotropic

metal cutting models (e.g. Johnson-Cook model) (Baro and Deoghare, 2018; Childs and Arola, 2011), considering anisotropy by assigning different properties to each microconstituent of the bone (Hage and Hamade, 2013; Shu and Sugita, 2020) or by simply designating distinct properties depending on the cutting direction at the macroscale (Santiuste et al., 2014).

Empirical models have also been proposed for describing the orthogonal cutting process. For instance, it has been shown that the friction coefficient (μ), necessary for predicting the cutting and thrust forces, could be modelled as a function of DOC, in the form $\mu = \mu_0 h^c$, where μ_0 and h are the experimental calibration constants (Liao et al., 2019). Cutting temperature predictions during machining could also be performed empirically, based on the density distribution of the bone by assuming that a denser region produces a larger cutting force value, thereby increasing heat generation (Feldmann et al., 2016); however, this requires experimental constants and local density measurements, also accompanied by FEM.

Due to the semi-brittle nature of cortical bone, a fracture mechanics based cutting model has been proposed to explain the chip formation and cutting process in orthogonal cutting, by allowing the calculation of the mean cutting and thrust forces mechanistically (Liao and Axinte, 2016a); thereby also providing the threshold DOC between each cutting mode (SC, SCC, FC). This mechanistic model only requires the mean values of the mechanical properties of the bone in the different cutting directions and for each cutting mode.

Additionally to understanding the cutting mechanism in cortical bone, there is also the imperative need to assess bone damage post-machining because, being a living tissue, not only is the mechanical integrity of relevance, but the wellbeing of the cells (i.e. osteocytes) is of upmost importance. For the cells to perform their vital functions, they must remain below a certain temperature-time threshold (Hancox, 1972); usually defined as 47°C for 1 min (Augustin et al., 2008) or 55°C for 30 s (Hillery and Shuaib,

1999), which can be easily surpassed during a machining process. When the temperature surpasses this threshold, it generates cellular death (i.e. necrosis), which compromises the metabolism and remodelling process of the bone. Machining-induced necrosis can be directly assessed with histology by directly measuring the necrotic depth in the machined bone subsurface, which is enabled due to the clear distinction between 'death' and 'alive' osteocytes that histological methods generate (Hancox, 1972). To minimise necrosis, external cooling (i.e. saline solution) is usually employed with the intention of minimising the cutting temperatures.

While all the above cutting mechanisms and cutting models are valuable for understanding bone under machining conditions, they have typically neglected the in-vivo conditions bone, as they have been conducted in dry cutting conditions and considering bone as a block of solid material. However, bone is a porous structure that contains fluid flow within; in fact, intraosseous blood flow and interstitial fluid can help to dissipate the heat generated during the bone cutting process (Hillery and Shuaib, 1999), and consequently this should have a direct effect on the necrotic damage that is assessed with histology. Additionally, bone has a very low thermal conductivity (Feldmann et al., 2018), but it has been shown that blood flow and interstitial fluid significantly increases the effective thermal conductivity of the tissue (Li et al., 2014), which implies that necrosis should be hindered due to the fluid presence in the internal porosities of the bone. It is believed that this internal irrigation condition can also affect other properties that impact the cutting process (e.g. friction coefficient, shear strength). Nevertheless, no studies have shown the effect of blood and interstitial fluid on machining of cortical bone.

While dry bone cutting studies are useful, realistic and necessary for understanding the bone cutting mechanisms (i.e. cutting forces, chip formation), they are not comprehensive due to their lack of consideration of internal irrigation (i.e. presence of fluid flow in the vascular porosities of the bone), as the fluid presence in the porosities will locally affect the lubrication in the bone-tool interface. Moreover, while external

flood cooling has typically been employed as a precautionary measure for avoiding necrosis, it does not allow for understanding the effect of internal irrigation in terms of neither temperature distribution nor necrotic damage, as the fluid presence in the porosities will not only affect the lubrication, but also the cooling mechanism in the cutting zone.

To investigate the role of internal irrigation (i.e. cooling, lubricating) on the cutting mechanism and necrotic damage of cortical bone, this chapter presents a novel laboratory setup that allows for mimicking in-vivo conditions (i.e. internally irrigated bone) by pumping a fluid through the natural vascular porosities of the bone, so that the real (i.e. closer to a surgical environment) cutting conditions can be replicated. Additionally, a mechanistic model was developed to consider the local variations of friction and shear strength due to the fluid supply via internal irrigation and a series of tests have been performed to show the relevance of internal irrigation in the cutting mechanism and necrosis of cortical bone. As such, this research emphasises, for the first time, that internal irrigation (i.e. which mimics in-vivo conditions) has a clear importance when studying the cutting mechanisms of bone and its response to cutting parameters.

5.2 The importance of internal irrigation and its influence on the bone cutting mechanism

Up to now there are no studies of the cutting mechanism of bone in-vivo. This is not surprising as, usually, the machinist requires additional equipment (e.g. high-speed cameras, thermocouples, load cells, etc). Indeed, there are studies on bone cutting done on experimental setups, but these are far from reality as the bone is a living structure where the blood and interstitial fluid are supplied via the vascular channels (i.e. Haversian and Volkmann's canals), and as mentioned above, there might be an

influence of this local fluid (i.e. blood, interstitial fluid) supply upon the cutting mechanisms.

Here, a novel method is proposed to study the influence of local lubrication (see Fig. 5.1) that is provided by the blood and interstitial fluid supplied through the vascular porosities upon the cutting mechanism of the bone and its further influences on the level of damage on the living cells during cutting.

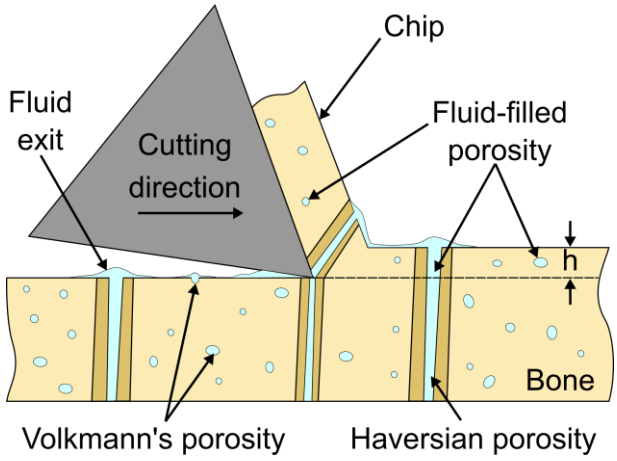

Fig. 5.1. Schematic representation of bone cutting in-vivo without external cooling, where the vascular porosities are filled with interstitial fluid, thereby acting as local lubrication points.

As such, Fig. 5.1 presents the real cutting conditions of living bone since the interstitial fluid presence in the natural porosities of the bone is considered. During the cutting process, the cutting edge will be in close contact with both bone material and porosities. However, due to the in-vivo conditions, the porosities are not empty, as they possess interstitial fluid inside (Cowin and Cardoso, 2015). This phenomenon enables a localised fluid effect on the cutting edge as it removes material: greater lubrication and cooling will take place in portions with fluid, whereas fluid-free portions will depict a dryer cutting behaviour (i.e. minimised cooling and larger friction).

As this might be an interesting and relevant problem in cutting bone structure, an original laboratory method to study this localised fluid effect during machining has been developed (see Fig. 5.2 and Fig. 5.3). This setup offers the possibility to study

the specifics of cutting mechanisms of bone and make adaptations of the cutting models to reflect the influence of local lubrication provided by the pumped fluid through the bone sample, which ultimately mimics the interstitial fluid flow presence.

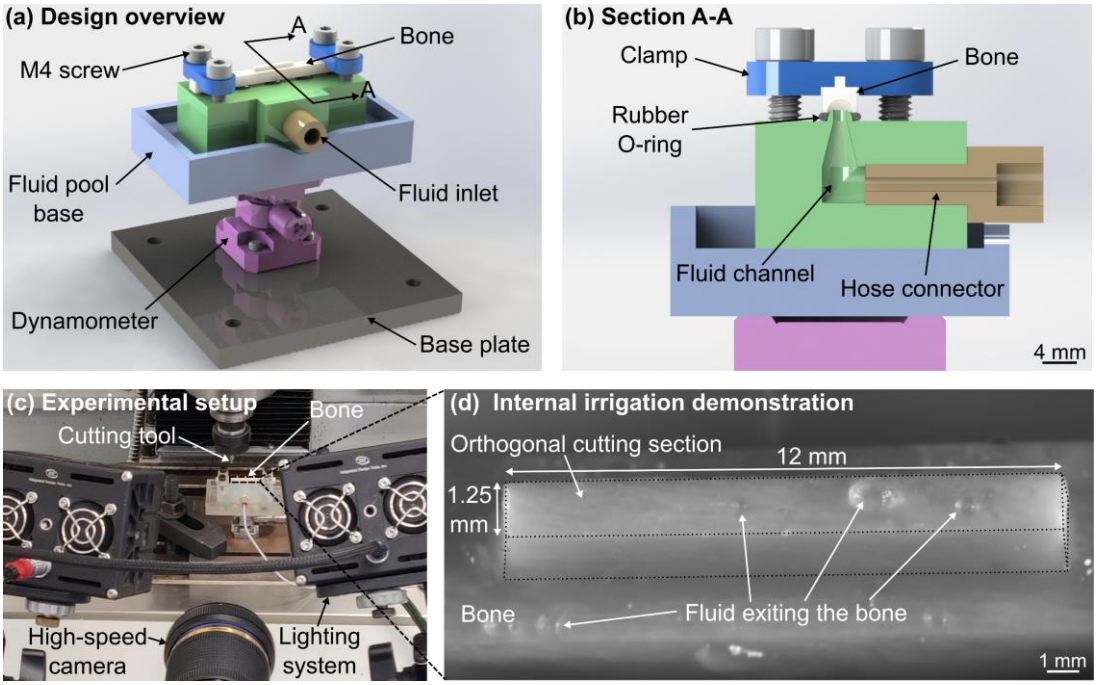

Fig. 5.2. Fixturing and pumping system for enabling the delivery of the interstitial fluid through the bone porosities during machining to mimic in-vivo conditions. (a) Design overview of the setup. (b) Cross section of the system, where the fluid channels that allow pumping fluid into the bone are visible. (c) Experimental setup. (d) Example of a bone sample with internal irrigation.

The setup (details in section 3.2) consists of an additively manufactured assembly which serves to clamp a small bone sample over a dynamometer (Kistler type 9317C) for a machining operation (see Fig. 5.2a), while also allowing for fluid pumping to take place, being the fixture the fluid inlet and the bone the fluid outlet (see Fig. 5.2b). This design offers the main advantage of permitting to pump fluid through the natural porosities of cortical bone (i.e. the Haversian and Volkmann's canals), thereby enabling a more realistic (i.e. closer to an in-vivo condition) laboratory setup for bone machining testing in a laboratory environment (see Fig. 5.2c). As an example, Fig. 5.2d depicts an orthogonal cutting section of cortical bone mounted on the setup and

having saline solution pumped through its natural porosities. Additionally, refer to Fig. 5.3 for a more detailed setup overview and examples of the machining tests.

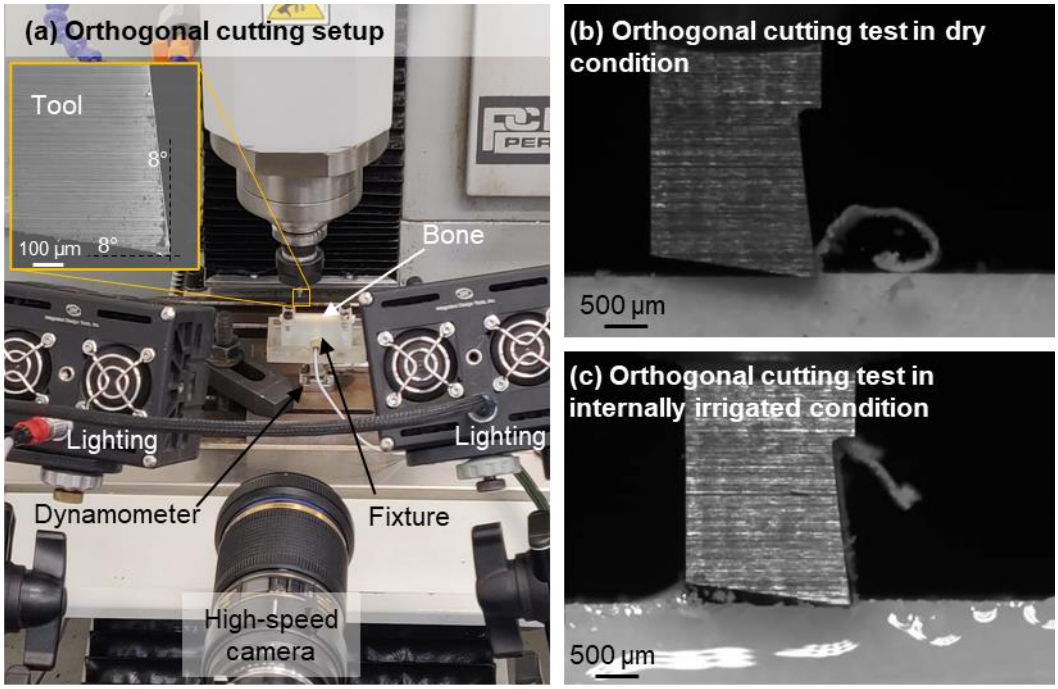

Fig. 5.3. Orthogonal cutting experimental setup and examples of tests with and without internal irrigation. (a) The setup enables to pump fluid through the bone via a fluid supply and the natural porosities of the bone. (b) Example of an orthogonal cutting test using the rig, but without the internal irrigation supply (i.e. dry cutting test). (c) Example of an orthogonal cutting test using the rig and with the internal irrigation enabled.

This will be useful to understand the magnitude of living bone structure during and after cutting. During the cutting process, the involved forces and chip formation mechanisms can be measured, recorded and analysed, which yields a more comprehensive machining understanding of this material. After cutting, the sample can be assessed with traditional engineering methods (e.g. SEM, surface roughness) and, additionally, the sample can be studied histologically to measure the necrotic extent induced by machining, thus enabling a damage evaluation that is highly relevant in the medical community. It is expected that all these measurable aspects depict a significant difference between dry bone (i.e. as traditionally tested in the scientific community) and irrigated bone (i.e. as enabled by the novel setup for mimicking in-vivo conditions).

5.2.1 Modelling of bone cutting considering the influence of local irrigation

Cortical bone machining research, usually conducted in dry, wet (external coolant delivery) or frozen states, have so far neglected the effect of interstitial fluid presence in the vascular porosity (VP) system (i.e. Haversian and Volkmann's canals) of the bone. Nevertheless, as explained previously this fluid presence is expected to alter the machining behaviour of cortical bone. Thus, to tackle this, local gradients of shear strength and friction coefficient near the VP pores have been considered to occur due to the permeability (Cowin and Cardoso, 2015) of bone near the VPs.

It is considered that the Haversian and Volkmann's porosities are filled with interstitial fluid and blood (see Fig. 5.4) and that due to the permeability of the bone, the fluid is radially absorbed into the cortical tissue, thereby increasing the lubrication near the canals and decreasing the shear strength of the bone in these zones. However, the effect is not the same throughout all this annular zone of lower properties. The region immediately surrounding the porosity will be highly permeable and therefore it is expected to have a lower friction coefficient (μ) and shear strength (τ) than regions away from the porosity in contact with the cutting edge. Therefore, an *affected zone* is introduced for both the friction coefficient and shear strength, where their values will be lower than in the bulk region away from the fluid.

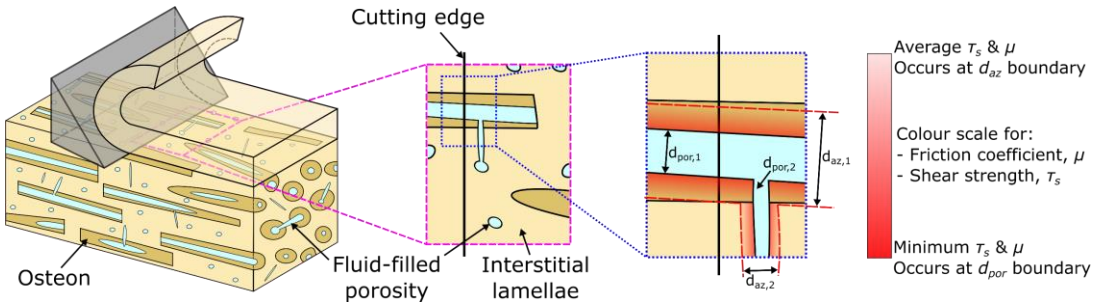

Fig. 5.4. Effect of interstitial fluid during bone machining. Near-porosity sites (i.e. affected zone) depict a linear gradient in shear strength and friction coefficient due to the permeability of the bone.

To model the effects of interstitial fluid in the cutting process, it is necessary to consider variations in porosity and microstructural arrangements (i.e. interstitial lamellae, osteons and porosities exact locations) along the toolpath. To this end, an algorithm has been developed to have the capability of constructing a bone volume of specific dimensions, microstructural arrangements (including the VP) and randomness. This is based on a previous work (Robles-Linares et al., 2019), but some changes have been put in place to improve its usage in this specific application (i.e. bone cutting forces modelling).

In short, a set of inputs are fed to the algorithm, such as porosity range, cutting direction and osteon density (see Stage 1 in Fig. 5.6). Using Boolean logic and vectorial algebra, the program yields a set of data that contains the location, direction and radius of each porosity in the bone workpiece. By defining a specific plane and cutting direction, the cutting surface is then obtained (see Stage 2 in Fig. 5.6), yielding with exactitude the positions of the microstructures (i.e. interstitial lamellae, osteon, porosity) that will be in contact with the cutting edge along the toolpath; an example is shown in Fig. 5.5a for the case of transverse cutting direction. To this end, each porosity is regarded as an individual vector of specific length, direction and thickness (i.e. radius). Thus, by considering that the affected zone radius (r_{az}), as defined in Fig. 5.4, is a function of the porosity radius (r_{por}) then:

$$\gamma_{az} = \frac{r_{az} - r_{por}}{r_{por}} \qquad \text{Eq. 5.1}$$

where γ_{az} represents the ratio between the thickness of the affected zone and the porosity radius, which can be obtained experimentally.

Regarding the effect of the fluid within the affected zone radius, several aspects must be considered. First, the porosity volume (where $r < r_{por}$) is filled with fluid (i.e. not bone); as such, it can be regarded as a void that does not contribute neither to shear strength nor to producing friction with the cutting edge, thus resulting in contributing

with zero values to the cutting forces. Second, regions of the bone away from the affected zone (i.e. $r > r_{az}$) will behave as pristine bone, retaining unaffected properties. Third, the affected zone region ($r_{por} \leq r \leq r_{az}$) will depict a linear variation of its properties, where they will be at a minimum value larger than zero in the porosity wall ($r = r_{por}$) and a pristine value at the end of the affected zone ($r = r_{az}$). Thus, for the friction coefficient (μ):

$$\mu = \begin{cases} 0, & \forall\, r < r_{por} \\ \mu_0(1-\beta_\mu) + (r - r_{por})\dfrac{\mu_0\beta_\mu}{r_{az,\mu} - r_{por}}, & \forall\, r_{por} \leq r \leq r_{az,\mu} \\ \mu_0, & \forall\, r > r_{az,\mu} \end{cases} \qquad \text{Eq. 5.2}$$

where β_μ represents the reduction ratio of the friction coefficient in the porosity wall (r_{por}) when compared to the pristine value of the friction coefficient outside the affected zone (where $\mu = \mu_0$). Similarly, for the shear strength:

$$\tau = \begin{cases} 0, & \forall\, r < r_{por} \\ \tau_0(1-\beta_\tau) + (r - r_{por})\dfrac{\tau_0\beta_\tau}{r_{az,\tau} - r_{por}}, & \forall\, r_{por} \leq r \leq r_{az,\tau} \\ \mu_0, & \forall\, r > r_{az,\tau} \end{cases} \qquad \text{Eq. 5.3}$$

where β_τ represents the reduction ratio of the shear strength in the porosity wall (r_{por}) when compared to the pristine value of the shear strength outside the affected zone (where $\tau = \tau_0$). Note how from Eq. 5.2 and Eq. 5.3, the affected zones and their respective reduction ratios are considered independently from each other when relating to either the friction coefficient ($r_{az,\mu}$ and β_μ) and the shear strength ($r_{az,\tau}$ and β_τ), respectively. This is conservatively considered this way, since it cannot be assumed that the fluid will affect two different properties in the same manner.

Therefore, in the bulk material (i.e. regions outside of the affected zone), the bone will possess its pristine properties of shear strength and friction coefficient, but as the cutting edge approaches the porosity, it will see a decrease in both shear strength and friction that goes from their average value (i.e. μ_0, τ_0) in the farthest region from the porosity ($r \geq r_{az}$), to a minimum value (i.e. defined by β_μ and β_τ) in the porosity wall

($r = r_{por}$). A set of machining trials conducted in bone samples with induced controlled porosities (i.e. micro-drilled holes) enabled the calculation of such experimental constants, which were found to be $\gamma_{az,\mu}$ = 2.18 and β_{μ}=0.08 for the friction coefficient and $\gamma_{az,\tau}$ = 1.63 and β_{τ}=0.50 for the shear strength. An example of this is shown in Fig. 5.5b and Fig. 5.5c for the case of shear strength along the toolpath when cutting in the transverse direction.

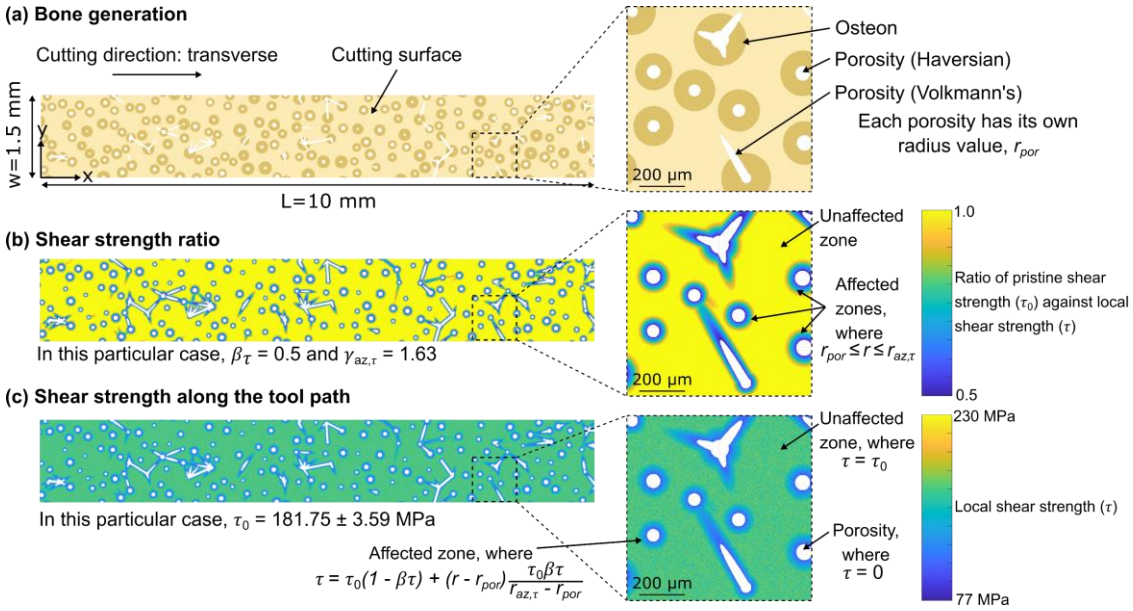

Fig. 5.5. Example of properties mapping (shear strength) along the toolpath for the case of transverse cutting direction. (a) Bone cutting surface generation. (b) Calculation of local property ratios with a linear gradient in the affected zones. (c) Calculation of the local value of properties.

This part of the model could be regarded as the properties mapping stage (see Stage 3 in Fig. 5.6), and it works in three main steps. First, a cutting surface is produced, where the microstructural arrangements along the toolpath are obtained via the bone generation algorithm (Fig. 5.5a). Second, the calculation of the ratio of shear strength and friction coefficient is done along the cutting surface, using the reduction ratios and affected zones (example shown in Fig. 5.5b).Third, once the ratio of each property is known along the surface, the local values are calculated for each node (Fig. 5.5c) by considering the mean value of the pristine property, its standard deviation and the local reduction ratio.

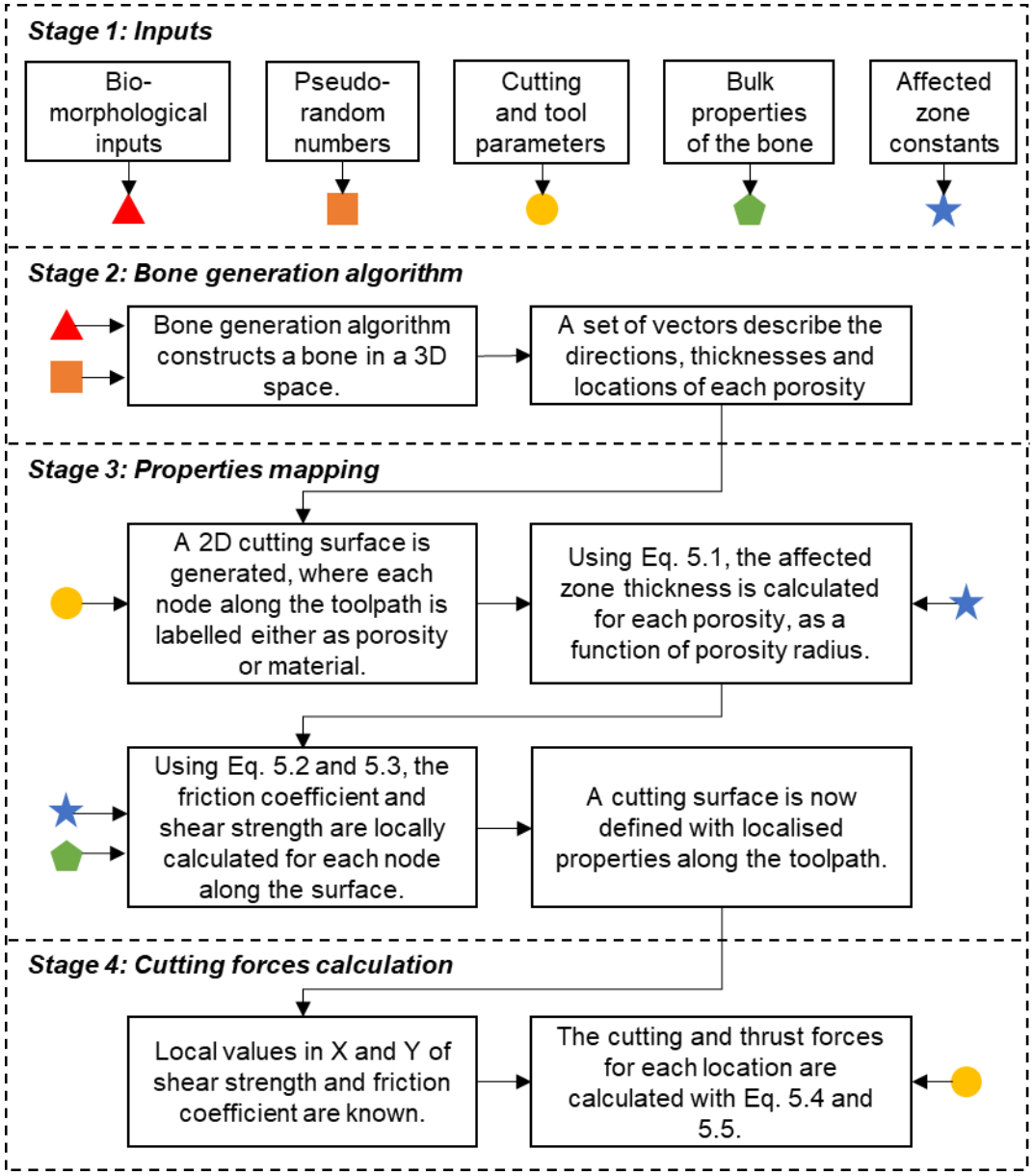

Fig. 5.6. Flowchart of the cutting forces model. After a set of inputs are fed to the program, a bone is constructed, and depending on the cutting direction relative to the bone structure, a cutting surface is generated. A properties mapping is performed on each node of the surface, using the affected zone constants that were calculated experimentally, and the cutting and thrust forces are then calculated for each position along the toolpath.

Once the properties mapping stage is finished, it allows to obtain the local values of shear strength and friction coefficient along the toolpath as function of position in the cutting surface, i.e. $\tau = \tau(x, y)$, $\mu = \mu(x, y)$. Thus, this enables the calculation of the cutting forces along the toolpath (see Stage 4 in Fig. 5.6). Employing the assumption of plane-strain conditions and that only shear and shear-crack cutting modes are

present, the cutting (F_c) and thrust (F_t) forces for a specific position *(x,y)* in the cutting surface can be calculated as (Liao and Axinte, 2016a):

$$F_c(x,y) = \tau(x,y)\frac{w}{N_y}h\csc\phi(x,y)\cos(\lambda(x,y)-\alpha)\sec[\phi(x,y)+\lambda(x,y)-\alpha] \quad \text{Eq. 5.4}$$

$$F_t(x,y) = \tau(x,y)\frac{w}{N_y}h\csc\phi(x,y)\sin(\lambda(x,y)-\alpha)\sec[\phi(x,y)+\lambda(x,y)-\alpha] \quad \text{Eq. 5.5}$$

where h is the depth of cut, α the rake angle, λ the friction angle (where $\lambda(x,y) = \arctan\mu(x,y)$) and, due to the plane-strain conditions, the Ernst-Merchant relationship, $\phi(x,y) = \frac{1}{4}(\pi - 2\lambda(x,y) + 2\alpha)$ (Shaw, 2005), can be assumed. Additionally, w/N_y represents the size of the discrete element in the *Y* direction. This way, for a specific position along the tool path (i.e. for any given *x*), the total cutting forces can be calculated as the summation of all the elemental forces along *y*.

5.2.2 Proof that internal irrigation has an influence in the cutting mechanism of ex-vivo bone

Experimental trials were conducted to study the effect of internal irrigation and validate the previously explained mathematical model. Following the standard sample preparation techniques from sections 3.1.1 and 3.1.2 , final bone shapes of 35 x 4 x 4 mm^3 were obtained. Subsequently, an orthogonal cutting section on their top of surface of 12 x 1.25 x 1.25 mm^3 was fabricated with conventional milling under abundant saline solution. All machining trials were conducted in a CNC milling machine (110 PCNC Tormach) with the experimental setup shown in Fig. 5.2.

A solid carbide cutting edge with rake angle of 8º and clearance angle of 8º was used in this investigation, conducing the orthogonal cutting process at depths of cut of 10, 30 and 50 µm to ensure that the bone is not under fracture cutting regime (Liao and Axinte, 2016a), using a constant cutting speed of 3 m/min. Additionally, cutting was conducted along the three principal cutting directions (i.e. parallel, across, transverse) relative to the osteons' main orientation (see Table 5.1). Both internal irrigation (using

sodium chloride 0.9% as the fluid to mimic interstitial fluid) and dry conditions were employed, with the first being used for the model validation, and the second for comparisons of chip formation mechanism and damage assessment.

Table 5.1. Selected orthogonal cutting conditions for the model validation.

Fluid condition	DOC, h, (μm)	Feed direction	Cutting speed, V_c, (m/min)	Repetitions
Dry (D)	10, 30, 50	Parallel, across, transverse	3	5
Internal irrigation (I)	10, 30, 50	Parallel, across, transverse	3	5

Since the DOC was kept below the threshold for fracture cutting mode, a continuous chip was obtained in all tests and for both fluid conditions. A high-speed camera (IDT Y4-S2 Motion Pro), which enabled chip formation mechanism visualisation confirmed this, where as shown in Fig. 5.7, even at the largest DOC (h = 50 μm), a continuous chip can be identified for both dry (Fig. 5.7a) and irrigated (Fig. 5.7b) conditions.

The example shown in Fig. 5.7 corresponds to cutting along the transverse direction of cortical bone; however, the same behaviour was identified for most of the experiments. In dry conditions, the chip formation mechanism remains similar to what has been reported in previous studies (Bai et al., 2020; Feldmann et al., 2017; Liao and Axinte, 2016a). Especially in the case shown in Fig. 5.7a, the dry chip follows a continuous curling trajectory due to the shear-crack cutting mechanism that takes place at such depth of cut. Nevertheless, when the same machining parameters are used in an internally irrigated bone sample, the chip formation mechanism is altered drastically. The moisturising effect of the fluid upon the chip and in the cutting zone produces a chip that tends to flow parallel to the rake face instead of curling forwards, whereby adherence takes place between the chip and the rake face. While this was the dominant chip formation mechanism and chip flow direction due to internal irrigation of the bone, there were a minority of cutting tests in which the chip curled onwards.

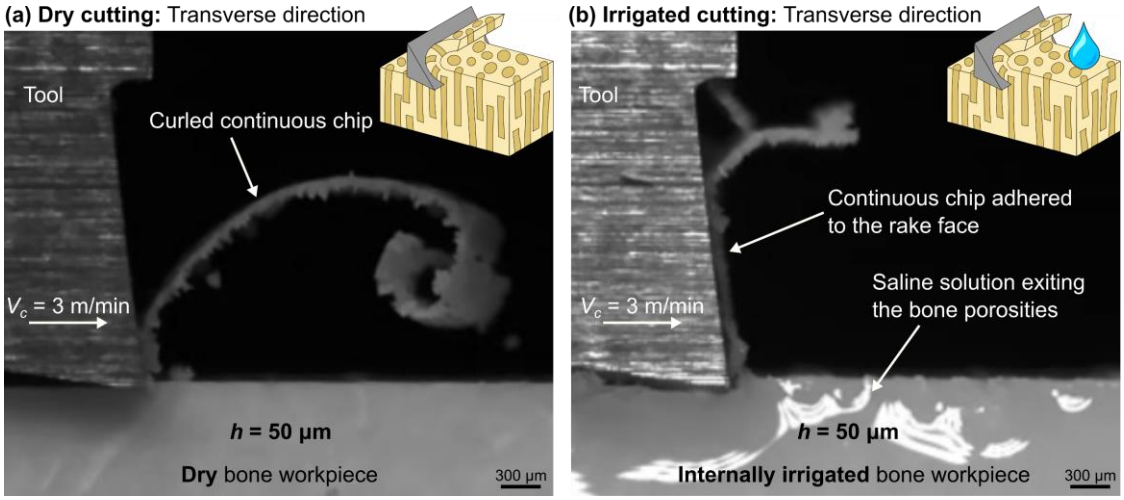

Fig. 5.7. Chip formation mechanism in dry vs. irrigated conditions at 50µm of DOC. (a) Dry cutting depicts the expected shear-crack cutting (SCC) mode, yielding a continuous chip. (b) Due to the internal irrigation of the bone, lubrication is enhanced, thus altering the cutting mechanism and increasing the adherence of the chip onto the rake face of the tool.

However, even though internal irrigation drastically affects the chip formation mechanism, there is still the question of its effect on the cutting forces. To investigate this, the cutting and thrust forces were directly measured with a dynamometer (Kistler 9317C) at a 10 kHz acquisition rate, thereby allowing to calculate the mean values of shear strength and friction coefficient, as depicted in Table 5.2. In all instances, the internal irrigation condition produces lower values of both cutting and thrust forces, which implies that less amount of energy is required to enable the shearing or shear-cracking mechanism in the chip formation process. Inherently, this is since the shear strength and friction coefficient along the tool path are significantly lower in the irrigated condition than in the dry state.

Table 5.2. Mean experimental values of cutting force, thrust force, shear strength and friction coefficient for all cutting directions, depths of cut and irrigation conditions. D = dry, I = internal irrigation; results are shown as avg ± std dev.

Cutting direction	DOC, h (µm)	Cutting force, F_c (N)		Thrust force, F_t (N)		Shear strength, τ_s (MPa)		Friction coefficient, μ	
		D	I	D	I	D	I	D	I
Parallel	10	7.9 ± 1.4	6.7 ± 0.4	3.9 ± 0.3	2.3 ± 0.1	197 ± 29	190 ± 15	0.71 ± 0.17	0.51 ± 0.03
	30	14.2 ± 2.6	13.4 ± 1.4	4.5 ± 0.6	3.6 ± 0.3	139 ± 33	137 ± 15	0.49 ± 0.09	0.43 ± 0.02
	50	20.7 ± 5.2	18.0 ± 2.5	5.0 ± 1.1	4.3 ± 0.4	132 ± 30	113 ± 18	0.42 ± 0.13	0.40 ± 0.03
Across	10	6.9 ± 2.1	4.9 ± 1.0	3.1 ± 0.9	1.5 ± 0.5	179 ± 31	147 ± 28	0.83 ± 0.12	0.47 ± 0.07
	30	12.7 ± 3.9	11.6 ± 2.8	4.0 ± 1.1	2.9 ± 0.9	126 ± 27	122 ± 31	0.53 ± 0.18	0.41 ± 0.09
	50	17.0 ± 4.2	15.4 ± 4.8	4.1 ± 1.2	3.5 ± 1.1	111 ± 29	96 ± 36	0.49 ± 0.24	0.37 ± 0.08
Transverse	10	7.5 ± 1.3	6.5 ± 0.6	2.5 ± 0.3	1.6 ± 0.2	217 ± 28	204 ± 21	0.52 ± 0.12	0.40 ± 0.03
	30	18.9 ± 5.0	15.7 ± 2.0	3.4 ± 0.8	2.3 ± 0.4	212 ± 32	181 ± 27	0.36 ± 0.11	0.30 ± 0.04
	50	27.9 ± 6.1	22.8 ± 3.6	3.8 ± 1.1	2.7 ± 0.6	195 ± 34	162 ± 30	0.30 ± 0.07	0.27 ± 0.04

Generally, as shown in Table 5.3, the cutting forces for all DOC and directions were within 6% and 28% lower when cutting in the internally irrigated state. This difference was more drastic in the thrust force, producing a difference between 13% and 52%. The shear strength proved to be 2% to 18% lower, which is not as noticeable as in the friction coefficient, which ranged between 6% and 43% lower.

Table 5.3. Comparison of irrigated (I) and dry (D) conditions, regarding the cutting forces, thrust forces, shear strength and friction coefficient.

Cutting direction	DOC, h (μm)	Reduction of Irrigated (I) condition vs. Dry (D) condition			
		Cutting force, F_c	Thrust force, F_t	Shear strength, τ_s	Friction coefficient, μ
Parallel	10	-15%	-41%	-4%	-28%
	30	-6%	-20%	-2%	-14%
	50	-13%	-13%	-14%	-6%
Across	10	-28%	-52%	-18%	-43%
	30	-9%	-28%	-4%	-23%
	50	-9%	-15%	-14%	-24%
Transverse	10	-14%	-37%	-6%	-23%
	30	-17%	-31%	-15%	-16%
	50	-18%	-30%	-17%	-10%

The internal irrigation condition during cutting has much more impact in the thrust force and in the friction coefficient, whereas less effect is seen on the cutting force and the shear strength. This can be explained by analysing the fluid effect upon the chip flow. The fluid that gets trapped within the chip then gets in contact with the rake face and produces a significantly lower amount of friction (up to 54% lower friction force), which enables a smooth chip flow (as shown in Fig. 5.7b). Additionally, the friction force runs only with an 8° misalignment from the thrust force direction (i.e. runs along the rake face). This, in line with the fact that the normal force on the rake face is less affected (only up to 19% reduction) and has a greater mismatch in orientation with the cutting force direction is the reason why the thrust forces are more significantly affected (in terms of percentage reduction) than the cutting forces. Additionally, this is also a result of the lower friction angle that is obtained due to the fluid presence.

Since there are evident differences between bone cutting in dry and irrigated state, this implies that traditional bone cutting models could be adapted to consider the effect of the fluid-filled porosities. Such a model has been presented in the previous section and an example of the cutting forces compiled with Eq. 5.2 – Eq. 5.5 are compared with the experimental measurements in Fig. 5.8 for the case of internal irrigation condition.

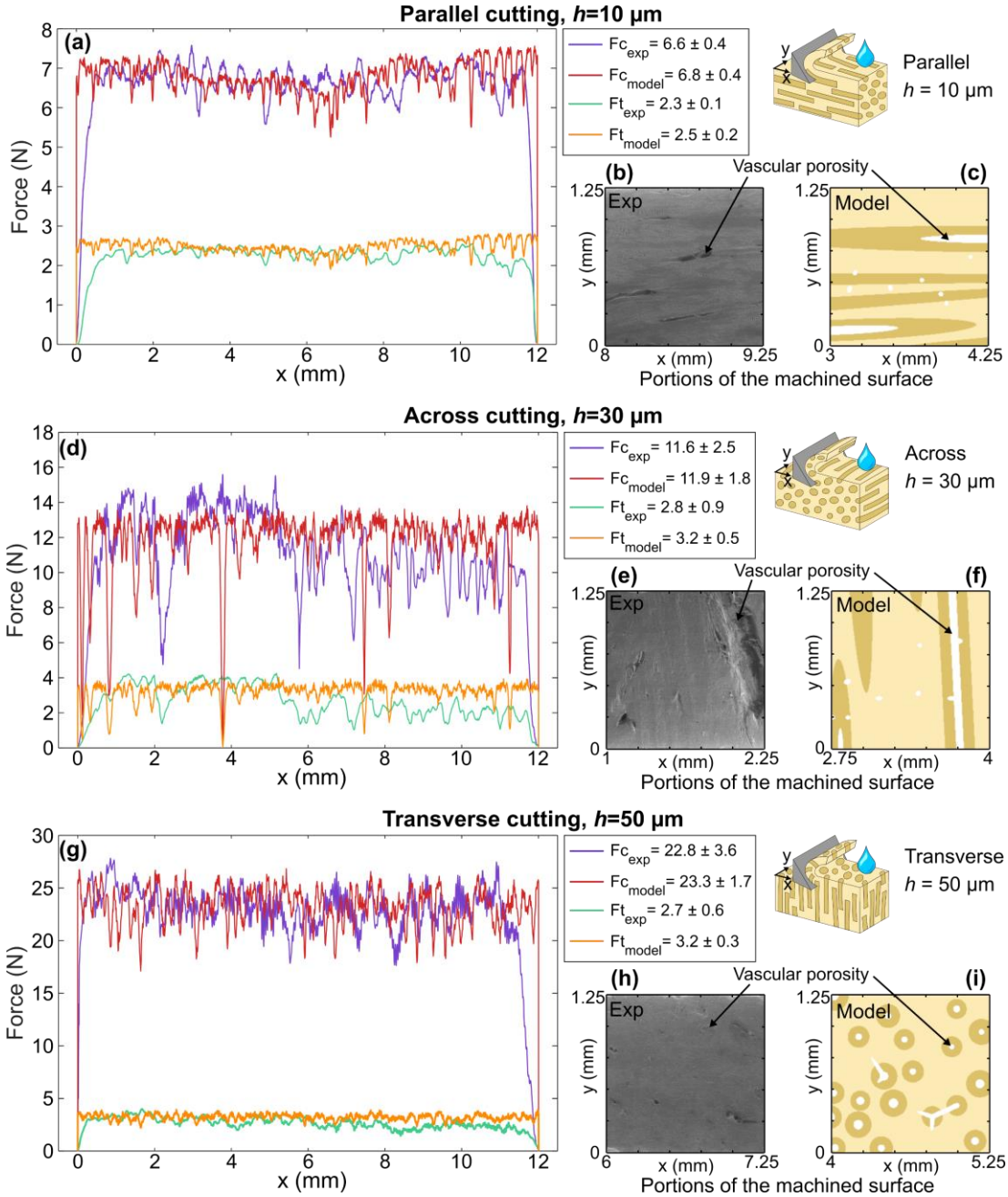

Fig. 5.8. Examples of cutting and thrust forces for the different cutting directions and depths of cut in internally irrigated machining, as obtained experimentally and via the model. (a-c) Parallel cutting direction with a 10 µm DOC. (d-f) Across cutting direction with a 30 µm DOC. (g-i) Transverse cutting direction with a 50 µm DOC.

In general, the model can produce comparable forces to those obtained experimentally (Fig. 5.8a,d,g) not only regarding the mean values of the force, but also in how the forces vary along the toolpath. For all cutting directions and DOC, the cutting forces obtained with the model are less than 3% larger than those from the experimental results. However, the variability of the forces always increases with the DOC, which

is expected to occur due to the larger volume of bone being cut. Nevertheless, the thrust force is less accurate in the model, depicting a difference of up to 18% with experimental results and a minimum of 6%. This might be since for all directions and DOC the cutting forces are positioned in a 22.8 N window while the thrust forces in a 4.3 N window, thereby increasing the sensibility of the thrust force over the cutting force by approximately five times.

In the parallel cutting direction, the osteons are roughly oriented with the feed direction, which implies that longitudinal porosities could be found along the toolpath, as shown in Fig. 5.8b-c; this consequently produces a force variability that is not as important as in the other cutting directions. For the example shown in Fig. 5.8a, the mean cutting and thrust forces are essentially equal, even having similar standard deviation.

In the across cutting direction, the osteons run perpendicular to both the cutting and thrust direction, which implies that the axes of the porosities might, at some point, be roughly coincident with the cutting edge position. This is the reason why when cutting in this direction, the forces depict the largest variation, in some cases going to zero or near-zero values. For instance, the experimental force drops to near-zero values in Fig. 5.8d near the 2 mm mark due to the large porosity that is shown in Fig. 5.8e. However, note how the force starts to drop even before the cutting edge gets in contact with the porosity; this is due to the lubricating effect on the friction coefficient and the softening effect on the shear strength in the regions close to the porosity. The same phenomenon takes place in the forces obtained with the model. In the model forces, the force drops near the 3.75 mm mark, and this is due to the porosity shown in Fig. 5.8f. However, in this case (model) the porosity is significantly smaller than that from Fig. 5.8e (experiment), which is why the affected zone near the porosity is smaller too, thereby producing a narrower force drop width in comparison.

In the transverse cutting direction, the osteons are parallel to the thrust direction, which is why the largest values of shear stress are expected in this direction as opposed to the other two. In this scenario the force variability is mostly dependent on the osteon density (i.e. number of osteons per unit area) and porosity size, which in this case were measured to be 14.5 osteons per mm^2, 38-92 μm Haversian porosity diameter and 31-43 μm Volkmann's porosity diameter; these values are in line with literature values (Predoi-Racila and Crolet, 2008; Yan et al., 2006). This inherently results in a set of forces that is not only similar in mean values, but also in the way in which the variability of the force takes place, which is why the experimental force curves shown in Fig. 5.8g match well with those obtained from the model. Note how the surface shown in Fig. 5.8h has only a little number of porosities that are visible, while many are visible in the model-obtained surface. This is since the fluid also facilitates surface smearing, which could produce porosity clogging, as it will be discussed next.

Post-machining SEM (FEI Quanta 650) analysis was performed on all samples in low vacuum conditions to assess the surface damage related to the cutting conditions. It is well known that the maximum surface damage is expected with the largest DOC, especially if cutting under the fracture regime (Zhang et al., 2022). However, since the fracture mode was avoided in these experiments, the largest damage occurred when cutting with 50 μm of DOC, as shown in Fig. 5.9, where the damage is compared between dry and irrigated conditions.

The surface morphology when cutting in dry state appears more damaged with tissue tearing and material drag, especially in regions close to the porosities. For instance, in Fig. 5.9a, portions of a Haversian porosity and a Volkmann's canal can be properly appreciated, but material in the edges of the porosity exhibits strong signs of material drag. In Fig. 5.8b, the osteon was cut on its upper portion, meaning that only a small portion of the porosity was cut through with the cutting edge; this resulted in a collapsed osteon with breakage in multiple zones near the porosity. In the transverse cutting direction, most of the surface surrounding the Haversian canals depict signs of

material drag and large porosities seem collapsed, which could be explained due to the high forces required in this direction and the ease of collapsing due to the lack of fluid within.

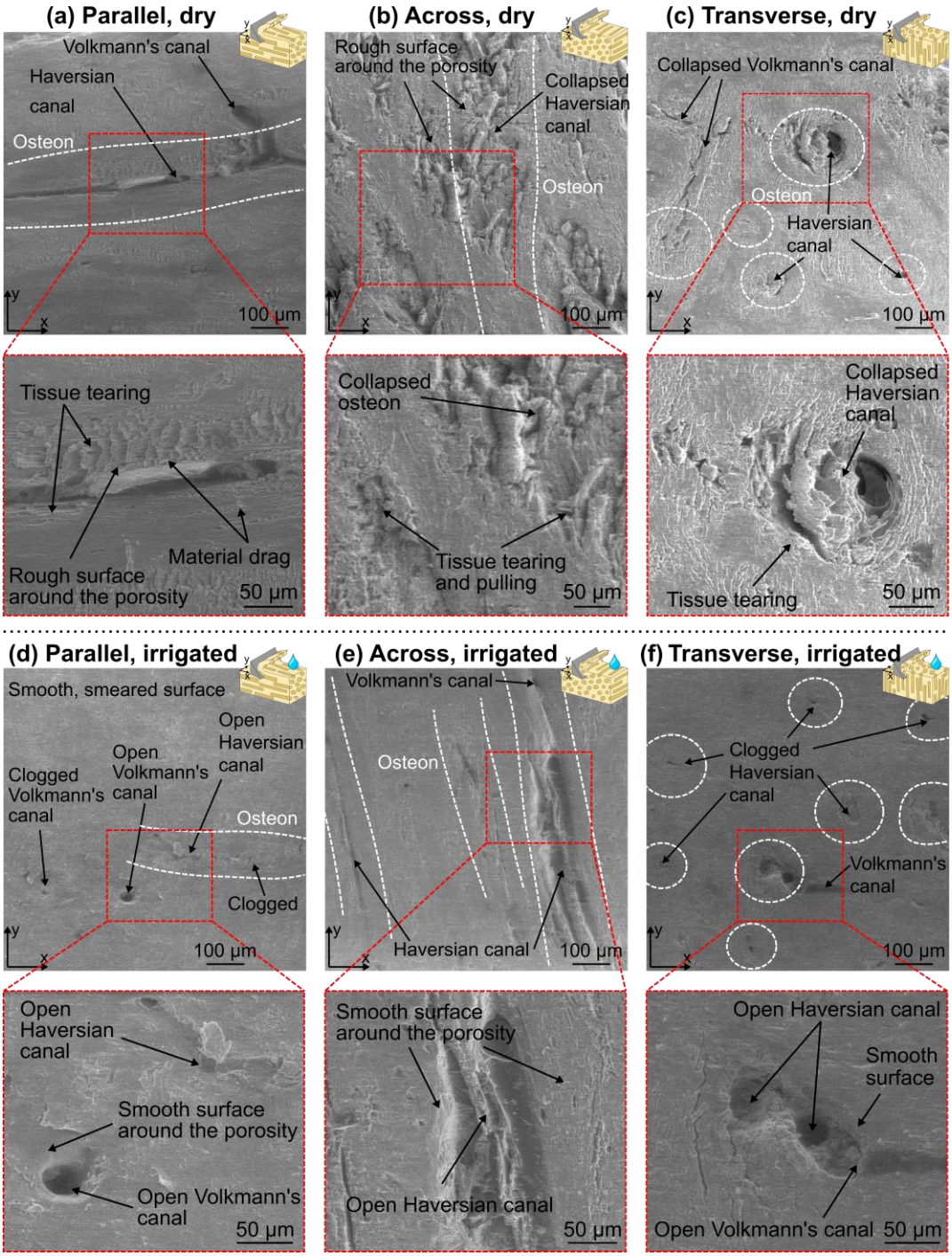

Fig. 5.9. Comparison of post-machining surface damage with *h* = 50 µm via SEM inspection. (a-c) Machined surfaces produced with dry cutting; severe damage and tissue tearing is visible. (d-f) Machined surfaces produced with internal irrigation; smooth surfaces and smearing are visible.

When the cutting is produced in the internally irrigated state, the surface morphology changes drastically, appearing smooth and almost defect-free, even for the largest value of DOC (i.e. 50 µm), which is shown in Fig. 5.9d-f. An interesting effect in this case is that the fluid response on the material can be appreciated not only in terms of lower forces, as it has been shown previously, but also in terms of surface smearing. The fluid from the porosities acts as a lubricant, meaning that the tool-material interaction is less aggressive, and in turn, the machined surface is smooth. For instance, when comparing Fig. 5.9d with Fig. 5.9a, material drag is essentially non-existent; but in lieu of this, the porosities appear to be partially clogged. This might occur due to the possible material smearing or redeposition that is facilitated due to the stickiness of the material in regions near the porosities. However, in the presence of larger porosities (as that in Fig. 5.9e), the lower forces are safe enough to avoid the porosities from collapsing, and the evident material damage near the porosities in dry state (Fig. 5.9b) is difficult to be enabled. Similar signs of minimum damage are shown in Fig. 5.9f in the transverse cutting direction where most of the Haversian canals appear partially clogged due to a superficial layer of smeared material, which was enabled due to the soft material surrounding the fluid-filled porosities.

To produce a more comprehensive analysis of surface damage (in terms of morphology), the surface roughness was assessed. 3D inspection of the machined surfaces was completed using the Bruker Alicona InfiniteFocus G4 and MountainsMap Premium software. This was achieved by non-contact probing by focus variation which allowed for measurements of the surface morphology for all the cutting directions (Fig. 5.10).

Simple comparative inspection of Fig. 5.10 highlights that the roughest surfaces were obtained under dry cutting conditions, especially in the across cutting direction (Fig. 5.10b). It is important to note that the colour scale considers the depth of the vascular porosities, meaning that the deepest portions in each image correspond not to a

machining-induced defect, but to the natural porosity that is located there. In the case of dry machining (Fig. 5.10a-c), regions surrounding the porosities exhibit the largest values of roughness and while this is still true in internally irrigated machining (e.g. Fig. 5.10d,f), it is not the exclusive case, since very smooth near-porosity surfaces can also be obtained, as shown in Fig. 5.10e when cutting in the across direction.

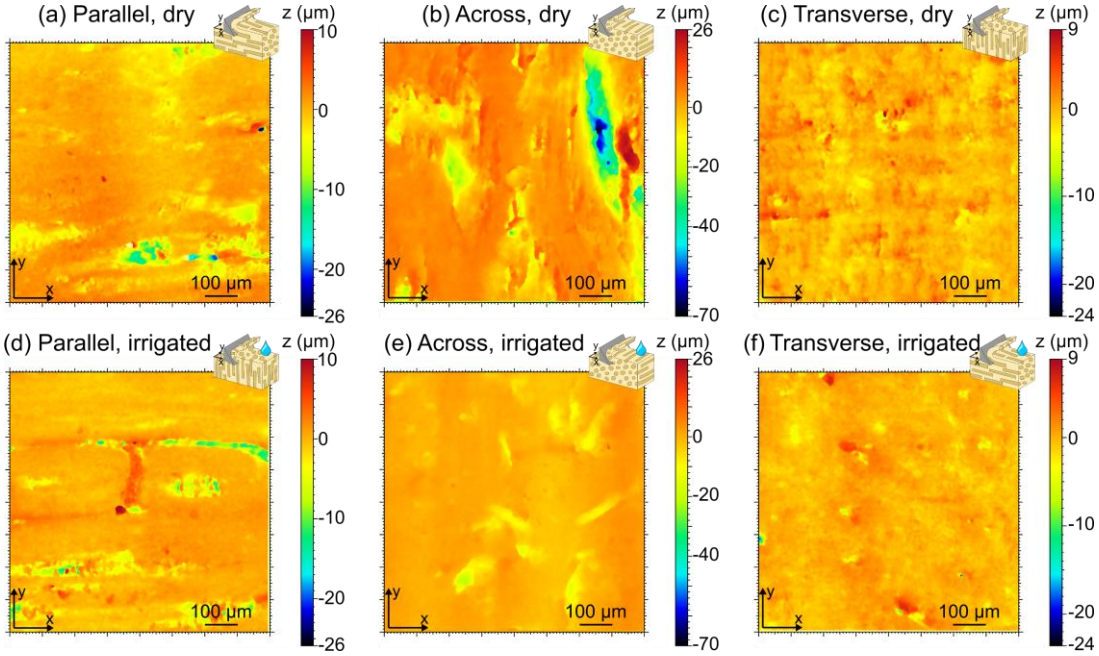

Fig. 5.10. Comparison of post-machining surface scans with *h* = 50 µm DOC. (a-c) Machined surfaces produced with dry cutting. (d-f) Machined surfaces produced with internal irrigation. Note how the roughness values are largely affected by the porosities in the surface.

The mean values of the area surface roughness (*Sa*) corresponding to the surfaces shown in Fig. 5.10 are listed below in Table 5.4. However, making an objective comparison based solely on Fig. 5.10 or on the *Sa* values is largely misleading, as these consider the porosity voids as a change in the roughness. To tackle this, three linear measurements of surface roughness (*Ra*) were averaged for each sample along the cutting direction in positions where no porosities could be encountered, as so to get a roughness value that would correspond only to the real *machined* surface, thereby removing the uncertainty caused by the contribution of the porosity voids into the area surface roughness (*Sa*). In the parallel cutting direction, the surface roughness (*Ra*) decreases from 0.241 µm to 0.199 µm (-17%) when shifting from dry to internally

irrigated machining. Similarly, in the across and transverse directions the roughness are 34% and 19% lower, respectively. This proves that the internal irrigation in the bone produces significant changes in the surface morphology and roughness post-machining.

Table 5.4. Post-machining surface roughness with h = 50 µm. Due to porosities of the bone microstructure, the area surface roughness (*Sa*) depicts larger values than what the machined surface realistically is. Therefore, linear measurements of surface roughness (Ra) were taken in non-porous locations too. D = dry, I = internal irrigation.

Direction	Fluid condition	*Sa* (µm)	*Ra* (µm)
Parallel	D	1.38	0.241
	I	1.12	0.199
Across	D	6.39	0.365
	I	2.01	0.240
Transverse	D	0.894	0.348
	I	0.705	0.282

An interesting result, however, is that the across cutting direction produced the roughest surface (Table 5.4) amongst the three directions. This is not expected as usually the transverse direction exhibits more signs of damage and roughness (Zhang et al., 2022). The reason for this might be traced back to the experimental results of cutting and thrust forces shown in Table 5.2, where even when largest values of shear stress and cutting forces were obtained for the transverse direction, the friction coefficient in the across direction was measured to be larger than in the transverse direction. Thus, the larger signs of damage that were found in the across direction could be due to the increased friction that facilitates material drag or tearing.

Up to now, it has been shown that the internal irrigation condition in the vascular porosities of the bone produces a drastic change in cutting forces, chip formation and surface damage. However, the reason for this is not trivial. Indeed, the simple use of

a lubricant will inherently produce these changes in a general machining environment with any material, but the main difference here is that the lubricant is applied internally and through the natural porosities of the bone; somehow resembling what bone machining would be in a more realistic scenario (i.e. surgery). Interestingly, the fluid affects the bone not only in places where the fluid is contained, but it seems that the fluid has a "reach" capacity that results in lower friction coefficient and lower shear strength, locally, in regions of the bone (i.e. osteon, interstitial lamella) that are within a threshold distance of the vascular porosity. However, the possible explanation for this softening or moisturising effect near the porosities relies on the porosity systems that exist in the bone and their permeability capacities.

While the overall porosity of bone is usually attributed to the vascular porosity (VP) system (i.e. Haversian and Volkmann's canals) due to its large diameter range (40 – 90 μm), there are also two additional porosity systems at the nanometric scale: lacunar-canalicular porosity (LCP), with a diameter range of 50 – 200 nm; and (2) collagen-hydroxyapatite porosity (CAP) with approximately 10 nm in diameter (Cowin and Cardoso, 2015). These porosity systems are interconnected and enable the permeability of the bone from the main VP in the transcortical and intracortical directions via the LCP and CAP (Cardoso et al., 2013). While the LCP and CAP are important for explaining the permeability of bone, the ratio of VP to LCP permeability is in the order of 10^8 and the VP to LCP pore diameter ratio is approximately 167. Nevertheless, due to the low fluid pressure in the VP and the high pressure in the LCP, the latter plays a more significant role in the mechanical behaviour of the tissue (Cowin and Cardoso, 2015). The permeability is able to produce poroelastic changes in the behaviour of bone, meaning that the local dry/irrigated state will exhibit different mechanical properties (Cowin, 1999). Consequently, this justifies why the localised fluid effect can be regarded as it has been previously explained up to now.

In this orthogonal cutting study it has been proven, for the first time, that internal irrigation is of large importance when it comes to modelling of the cutting forces

involved in the process and it has been demonstrated that the solution for this relies on considering a porosity-size-dependent affected region in the bone in which the friction coefficient and the shear strength are decremental due to the permeability of the bone that is enabled from the vascular porosity into the tissue via the LCP and the CAP systems. While it has also been shown that surface morphology and chip formation is drastically affected because of the fluid presence.

5.3 Non-orthogonal cutting of bone considering the influence of internal irrigation and external cooling

While the previous subchapter focused on studying the internal fluid presence effect upon the cutting forces, chip formation mechanism and surface damage, an open question here is if the internal irrigation effect is still significant when applying flood cooling, which is normal practice in surgical conditions. Since the objective of this study is to understand the bone as a material in a "close-to-surgical environment", flood cooling must also be considered. In a surgical scenario, flood cooling is employed with the primary intention of minimising temperature rise and minimising tissue necrosis. As such, to study the effects of internal irrigation and flood coolant, these same aspects (i.e. temperature and necrosis) are here compared.

Due to the small contact time in orthogonal cutting, heat generation is not easily enabled. Therefore, to assess the effects of the interstitial fluid on heat propagation during machining, fly cutting trials were performed. To, this end, a single straight tooth milling tool (HSS) was employed in the milling machine tool (see Fig. 5.11) and since the objective of these tests was to assess the effect of temperature, two different machining conditions were used, to allow a high (HT) and a low (LT) temperature during the cutting process (Table 5.5). The samples were prepared equally as for the orthogonal cutting trials to obtain overall bone samples of 35 x 4 x 4 mm^3 with a cutting section on their top of surface of 12 x 1.25 x 1.25 mm^3.

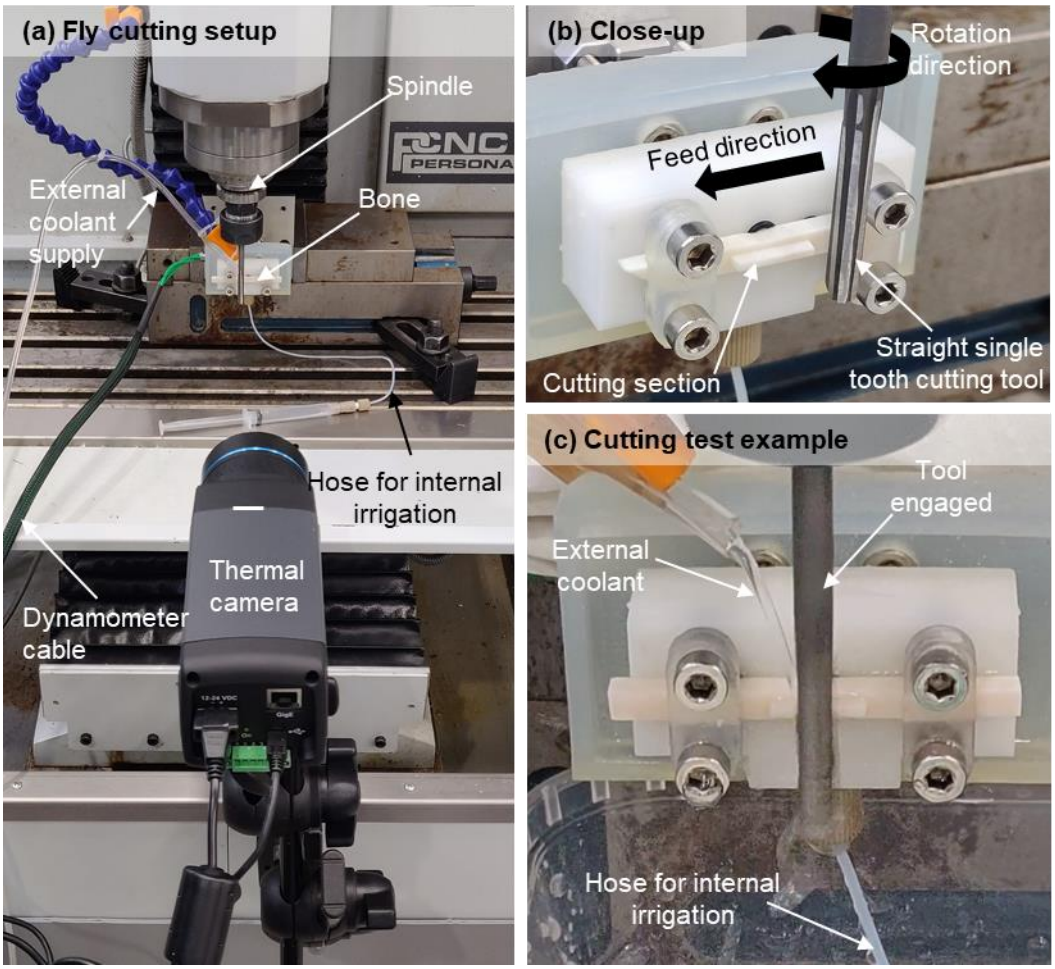

Fig. 5.11. Experimental setup for the fly cutting trials. (a) Overview of the experimental setup, consisting of a similar setup as in the orthogonal cutting trials but with the addition of an external coolant supply system. (b) Close-up view of the sample and the tool. (c) Example of a fly cutting test, where both the internal irrigation and the external coolant supply systems are enabled.

Table 5.5. Selected fly cutting conditions for assessing necrotic damage. A low (LT) and high (HT) temperature set of machining conditions were employed in bone in dry (D), internally irrigated (I), dry with external coolant (DE) and internally irrigated with external coolant (IE) fluid states.

Temperature condition	Fluid condition	Radial DOC (µm)	Cutting speed, V_c, (m/min)	Feed per tooth, h (µm)	Repetitions
LT	D, I, DE, IE	750	25	30	2
HT	D, I, DE, IE	750	100	10	2

It is well known that thermal measurements in bone machining is challenging (Zhang et al., 2022)., but infrared (IR) thermography is capable of providing reliable relative measurements for a given set of machining conditions (Shu et al., 2020b). As such, temperature measurements were completed by IR thermography using a FLIR A655SC Long Wavelength IR camera and data was recorded at 50 Hz, as shown in Fig. 5.12. To record the bone temperature with the IR camera, the emissivity of the bone was set to 0.96 (Feldmann and Zysset, 2016) for all experiments, while locating the camera at approximately 500 mm away from the cutting zone. The data was processed using the ResearchIR Max software by FLIR and MATLAB to calculate the maximum temperatures (T_{max}) for all tests. This was done by averaging the maximum temperature of each frame within the region of interest (i.e. the bone cutting section shown in Fig. 5.11b and Fig. 5.12b), for all the machining conditions (see Table 5.6).

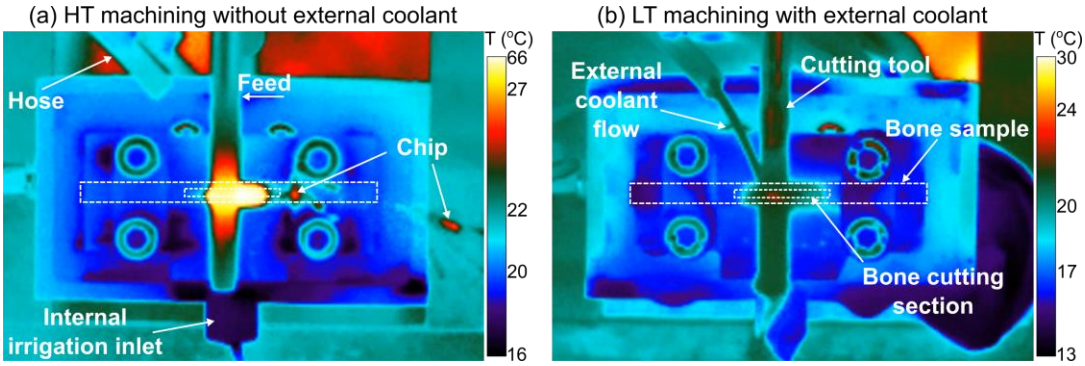

Fig. 5.12. Infrared thermography measurements examples for the maximum and minimum temperature scenarios obtained throughout all the experiments. (a) High temperature (HT) machining without external coolant and in dry (D) state. (b) Low temperature (LT) machining with internal irrigation and external coolant delivery (IE).

To assess the thermal damage related to the measured temperatures, a necrotic assessment was performed via histological analysis to all the fly cutting samples. Since more intense thermal fields are expected near the end of the cut, histological analysis was performed at the 9 mm mark of the 12 mm cutting length. The methodology for the necrosis assessment has been documented in section 3.4.6 . A total of 9 slices per sample were inspected, making at least 5 distance measurements on each of them.

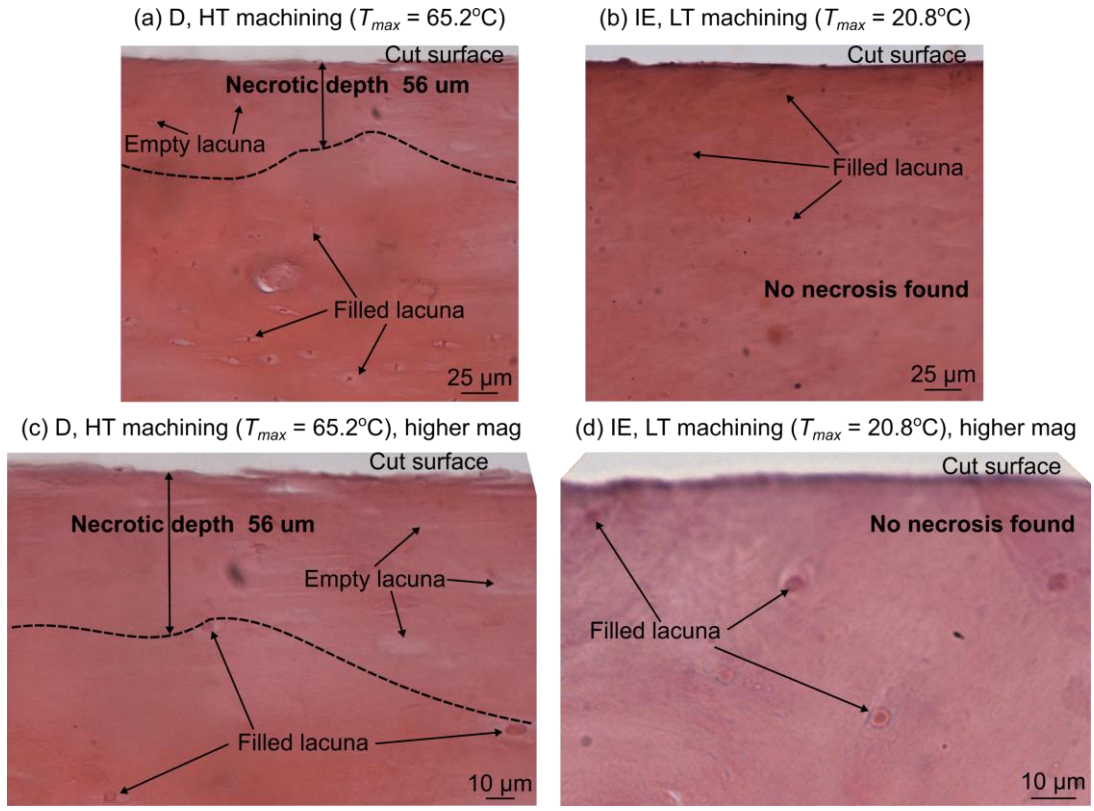

Fig. 5.13. Necrosis assessment with histological analysis on the bone subsurface following fly cutting. (a,c) High temperature (HT) machining in dry (D) conditions, where the maximum temperature and necrosis were measured as 65.2 °C and 56 ± 5.7 µm (n = 55), respectively. (b,d) Low temperature (LT) machining in internally irrigated and external coolant (IE) conditions, where no necrosis was found.

These experimental conditions confirmed that larger temperatures usually produce deeper necrotic depths, but that internal irrigation plays a determining role in terms of heat dissipation and necrotic damage (see Table 5.6). For instance, when cutting under high temperature (HT) conditions in a fully dry (D) bone state (i.e. without internal irrigation and without external coolant) the maximum temperature was measured to be 65.2 °C, which, in terms of necrosis was translated to be 56 ± 5.7 µm (n = 55). It is important to note that these were the maximum values of both temperature and necrosis of all experiments, as it was expected. With internally irrigated (I) bone, the same set of machining parameters (HT) produced a temperature of 57.9 °C with a 37 ± 4.2 µm (n = 49) necrotic depth, which proves that interstitial fluid within the vascular porosities of the bone has the capability of heat dissipation, thereby producing lower levels of thermal fields and necrosis. This might be explained by analysing the

mediums of heat transfer in dry and irrigated conditions. In dry machining, the porosities could be regarded as air-filled spaces that act as poor thermal conductors since air has a very low thermal conductivity (0.026 W/mK (Stephan and Laesecke, 1985) at room temperature and atmospheric pressure), thereby hindering heat propagation into the bone and facilitating heat concentration in the tool-chip interface, which in parallel with bone's low thermal diffusivity (Feldmann et al., 2018) is why it is expected to have heat concentration in the tool-chip interface in bone cutting (Feldmann et al., 2017). However, in internally irrigated machining, the porosities are filled with interstitial fluid, which in this case has been mimicked by employing saline solution, fluid that possesses superior conductivity (0.594 W/mK (Ozbek and Phillips, 1980)) over air and therefore could be expected to conduct heat at a faster rate away from the cutting zone, which is translated into lower temperatures and, therefore, less necrotic damage.

In low temperature (LT) machining of bone in dry (D) state, the maximum temperature was measured to be 47.6 °C, which is 17 °C lower than that achieved with high temperature (HT) machining parameters. In this case (LT, D), the temperature produced a 40.2 ± 3.4 μm (n = 63) necrotic depth, which is significantly lower than the 56 μm measured on its HT-machined counterpart (HT, D). However, it is interesting to note that even if a larger temperature (57.9 °C) was measured for the internally irrigated sample (HT, I) over the LT, D sample (47.6 °C), it displayed slightly less necrotic damage (37 μm vs. 40.2 μm, respectively). The reason for this is related to the employed machining parameters. Cutting with HT machining parameters, while producing larger thermal fields, also reduces the cutting time to 75%, as opposed to the LT parameters that yield lower thermal fields but with an increased time window for the cutting process to take place. This inherently creates a compromise of the time-temperature relation that affects the response of the cells to thermal damage (Augustin et al., 2008) by increasing the time in which lower temperatures are being held within the tissue.

The use of external coolant in both HT and LT machining conditions produced no necrotic damage. As expected, this is due to the intense heat dissipation that is provided by the external fluid, but it should be noted that if more aggressive machining conditions (i.e. in terms of heat generation) were employed, necrosis could be present even while using external cooling solutions.

Table 5.6. Necrotic damage as measured with histological analysis for all the fly cutting samples. LT = low temperature drilling, HT = high temperature drilling, D = dry, DE = dry with external cooling, I = internal irrigation, IE = internal irrigation with external cooling.

Temperature condition	Fluid condition	Maximum temperature T_{max} (°C)	Necrotic depth (μm) avg ± std dev
LT	D	47.6	40.2 ± 3.4 (n = 63)
	DE	22.3	0
	I	38.1	18 ± 2.9 (n = 54)
	IE	20.8	0
HT	D	65.2	56 ± 5.7 (n = 55)
	DE	23.1	0
	I	57.9	37 ± 4.2 (n = 49)
	IE	22.2	0

5.4 Concluding remarks

Bone cutting is a complex material for machining analysis since it comprises both a material with an intricate hierarchical microstructure and a living tissue with embedded cells. Typically, bone cutting research is conducted ex-vivo and in a dry state; thereby creating a scenario fully out of the natural environment of bone. This type of studies, while useful, have neglected the effects that blood and interstitial fluid in the vascular porosities may have upon the chip formation mechanism, cutting forces and thermal and mechanical damage. Therefore, in this work, the mechanical

behaviour of cortical bone was studied in conditions closer to a surgical scenario by enabling fluid flow through the vascular channels of the tissue during machining, aspect that has so far been neglected.

With a series of orthogonal cutting trials, it was found that internal irrigation affects the cutting and thrust forces by reducing them by up to 28% and 52%, respectively, which is attributed to the lower apparent values of shear strength and friction coefficient (up to 18% and 43% lower, respectively) that are produced due to the presence of fluid. It was also found that while severe mechanical damage is produced in dry cutting, internal irrigation produces smoother surfaces with less porosity collapse and increased smearing capability.

The localised effect of fluid-filled porosities was studied with orthogonal cutting, and it was found that the bone material surrounding each individual porosity suffers from a softening effect that is size dependent upon the porosity diameter. In the porosity wall, the shear strength is approximately 50% lower than its bulk value, while the friction coefficient is about 8% lower. Nevertheless, these values linearly increase back to their bulk value in an annular zone surrounding the porosity that is confined to 1.6 times the porosity diameter for the case of shear strength, but 2.2 times in the case of friction coefficient.

A mathematical model was developed considering the microstructure's randomness and the gradient of properties (i.e. shear strength, friction coefficient) in near-porosity sites along the toolpath. This enabled the calculation of cutting and thrust forces and it was demonstrated that the model is capable of not only producing significantly similar mean values of force (3-18% error) when compared to experimental data, but also its variability along the cut. Here, it has been demonstrated that both the porosity randomness and the properties gradients near the porosities play a major role in modelling the variability of cutting forces in orthogonal cutting of cortical bone.

The effect of internal irrigation was also assessed in terms of necrotic damage with fly cutting trials that enabled heat generation. It was found that dry cutting exhibited the largest signs of necrosis, and that internal irrigation is capable of increasing heat dissipation significantly, thereby producing lower levels of necrosis of up to 55% lower than dry cutting. It was also confirmed that the use of external coolant released the tissue of any necrotic damage, thereby proving the importance of always employing external coolant in surgery.

This bone machining study shows, for the first time, that interstitial fluid within the porosities of the bone produces a drastically different machining behaviour in terms of forces, mechanical damage and necrosis, as compared to the traditional state in which bone cutting is studied (i.e. dry condition). This was found to occur due to the reduced friction coefficient and shear strength of the bone, especially in localised portions of the tissue near the porosities. Furthermore, it is believed that this material behaviour should exist under surgical conditions in the absence of external coolant delivery.

While this research is limited to ex-vivo bone and saline solution playing the role of interstitial fluid, it aids to minimise the gap between bone machining research and surgical practice (e.g. orthopaedics, dentistry). For instance, the model here presented can straightforwardly be applied patient-specifically, for example, using computerised tomography (CT) to obtain the microstructural distribution of the patient. This could then be employed to predict the cutting forces (and therefore expected damage) of a fixed set of machining conditions or inversely be modified to calculate the necessary machining parameters to not exceed a threshold force.

Chapter 6 - Conclusions

Bone is a complex material for machining analysis, and its damage mechanisms are little understood in a machining environment. In recent years, the research community has studied the behaviour of cortical bone, thereby enabling smarter tool design for surgical systems and equipment. However, due to the intricacies of the material, straightforward solutions for minimising tissue damage are not easily produced. Throughout this work, it has been shown that the damage inducement process is complex and depends greatly upon the nature of the material removal mechanism (i.e. thermally, thermomechanically or mechanically driven). Additionally, this research has shown evidence that the traditional states of bone used by the research community (i.e. dry with and without external/flood coolant) are much different from what could really be encountered in a living tissue (in-vivo), since internal irrigation (i.e. by interstitial fluid and blood) plays a major role in the local properties of cortical bone in near-porosity sites. Even in the case of machining with flood coolant, there is a clear distinction when internal irrigation is considered.

In this chapter, the key discoveries, novelties and academic contributions are listed and summarised. Following this, areas of opportunity and possible lines of work are outlined as an outcome of this research, regarding the field of bone machining and damage assessment. While some of these rely on the results and observations from this work, others are predictions based on the general impact of the research and the literature that was reviewed. It is expected that the conclusions and future work described here, can shorten the bridge between the medical and the manufacturing communities, towards improved tools and surgical systems that not only improve the cutting mechanisms of cortical bone in surgery, but that also minimise the damage inducement and favour patient recovery.

Research walkthrough and concluding remarks

As discussed in Chapter 1, cortical bone is an important hard tissue in the human body, alongside trabecular bone and teeth (dentin and enamel). However, cortical bone is of vast interest in the scientific community because due to its properties, it is a structure that sustains significant loads and stresses necessary for the daily locomotive functions of the human body. As such, it is also a material that when subjected to machining (e.g. as during a surgery), it can suffer substantial amounts of damage. However, as it has been noted, the mechanisms of damage inducement are not clear, both from a biological (i.e. necrosis, healing capacity) and a mechanical (cracks, properties) perspective following a machining process. To this end, in Chapter 2, a comprehensive review was completed, focusing on the hierarchical structure and properties of cortical bone, its main material removal mechanisms (i.e. orthogonal cutting, drilling, milling, grinding, vibration-assisted machining and laser machining) and the surface integrity of bone post-machining. Understanding the intrinsic hierarchical structure of cortical bone is essential for a machining analysis of cortical bone, given that the combinations of its porosity systems, along with the fact that is possesses interstitial fluid and blood flow within, yields a complex material that is roughly orthotropic and tends to a semi-brittle behaviour. Additionally, the biological functions of bone were reviewed and explained from the fundamentals of the main cell types present in the tissue. Following this, the machining processes were addressed from a fundamental perspective as to understand the nature of each individual material removal process. It was noted that in mechanical material removal methods, the chip formation mechanisms are drastically affected by the machining direction relative to the bone structure and the depth of cut, where at low depths of cut the bone tend to behave ductile (i.e. shear-based material removal), while at increased depth of cut, it transitions to a brittle behaviour (i.e. fracture-based material removal). Additionally, non-conventional machining techniques revealed that other types of material removal (i.e. vibration-

assisted, laser machining) could aid to minimise cutting forces and damage. The surface integrity after the machining process in cortical bone is essential for guaranteeing a proper bone functionality and implant bonding post-surgery, which is why mechanical and thermal damage were reviewed in-depth. Following the literature review, several areas of opportunity and research gaps were noted, being the most important ones the lack of understanding of the damage inducement mechanisms and the lack of consideration of internal irrigation in cortical bone machining studies.

To tackle the research gaps, a thorough research methodology was presented in Chapter 3, where all the conventional and non-conventional machining and tooling equipment was described, as well as all the material and surface characterisation techniques that were employed, ranging from a milling machine tool, to micropillar compression testing, to histological analysis for tissues. All of these were essential for addressing all the challenges of this study.

Chapter 4 focused on the machining-induced damage mechanism in cortical bone from two different material removal process. First, a laser machining study was performed to understand the damage mechanism in a thermally driven material removal process. As such, the surface topography and the necrotic damage were studied. Second, a drilling study was performed to understand the damage mechanism in a thermomechanical material removal process, in which also the surface quality and the necrotic depth were assessed. Both machining techniques were compared and given that drilling offered a much more significant advantage over laser machining (i.e. in terms of processing time and inducing less damage in relation to the material removal rate), it was selected for an in-depth study. In the latter, micromechanical testing was employed in the form of micropillar compression to evaluate the micromechanical properties of the machined subsurface. Analysis of the elastic properties and failure modes at the microscale yielded a complementary assessment for a full damage evaluation of bone post-machining, adding more information than what the traditional histological analysis can provide (i.e. necrotic depth). *In this chapter,*

micromechanical testing is revealed to be a complementary technique for bone damage analysis since mechanical damage could far-exceed necrotic damage.

In chapter 5, the role of internal irrigation was studied under mechanical material removal methods. A setup that enabled bone samples to be internally irrigated was employed to compare dry bone machining against internally irrigated bone. This was done via orthogonal cutting, with the aim of validating a cutting forces model and to study the chip formation mechanism in both dry and irrigated conditions. Additionally, since damage is of great relevance, a set of fly cutting trials were also performed to facilitate heat build-up in the tool-bone interface, thereby permitting a necrotic damage comparative analysis between the two sets of irrigation conditions. *In this chapter, the role of internal irrigation upon the machining behaviour of cortical bone has been reported for the first time.*

In the following sections, the academic contributions that are a result from this work are presented, as well as the future work in this line of research.

6.1 Academic contributions

The academic contributions from this work, in order of importance, are listed and described next. These summarise the main contributions and discoveries from this research.

1. **Micromechanical analysis revealed that machining-induced mechanical damage can be more significant than necrotic damage (the current 'gold-standard' for bone damage assessment), therefore highlighting the importance of employing micromechanical testing as a complementary damage assessment technique.**

   Low (62 °C) and high (110 °C) temperature drilling tests were conducted in cortical bone in dry condition to study the damage inducement with a mild and aggressive machining set of conditions, respectively. Histological analysis

revealed that in high temperature drilling, the necrotic depth reached 419 µm, while in low temperature, only 49 µm were measured. However, micromechanical testing in the high temperature drilling condition provided evidence that the microstructure shifts from a ductile behaviour (i.e. slipping along a single shear plane failure) in the bulk material to a brittle behaviour (i.e. axial crack failure) with weaker mechanical properties (-42% elastic modulus, -41% ultimate strength, -15% yield strength) in the vicinity of the machined surface. However, the surprising aspect is that this brittle and weaker bone layer can extend to at least 1500 µm away from the machined surface, which is more than 3 times the necrotic depth. This inherently implies that more bone volume can be affected micromechanically than biologically. The reason for such a change in the micromechanical behaviour of the tissue requires further studies, but it was theorised that it could be due to a localised dehydration effect surrounding the drill site due to the high temperature.

2. **The role of internal irrigation during bone machining has been reported for the first time. It was found that material surrounding the porosities of the bone are softer than the bulk material, thereby producing a milder material removal process, where the forces and thermal damage are lower than the traditional dry machining studies.**

   While many studies focusing on the machining behaviour of cortical bone have achieved significant advancements, these have so far neglected the role that interstitial fluid or blood flow could have during the cutting process. This aspect was addressed in this work, and it was found that internal irrigation facilitates bone permeability near the porosities and as such, an *affected zone* (i.e. annular region of bone surrounding the porosity) was found to possess a gradient of shear strength (-50% in the porosity wall) and friction coefficient (-8% in the porosity wall). It was revealed that the affected zone is confined to 1.6 times the porosity diameter for the shear strength, but 2.2 for the friction

coefficient. This gradient in properties in the near-porosity sites is traduced to cutting and thrust forces that are significantly smaller (i.e. 28% and 52%, respectively) than in dry bone cutting. It was also confirmed that the role of interstitial fluid is also of major relevance in the surface morphology and the chip formation process, by enabling smoother surfaces with facilitated smearing, and increasing chip adherence to the rake face due to the fluid presence. Additional to this, necrotic damage was found to be 55% lower than in dry cutting, thereby proving that internal irrigation creates a significant change not only in the mechanisms of the material removal process, but also in the induced biological damage that might be incurred.

3. **A mathematical model was developed and validated to predict cutting forces in internally irrigated bone. Contrary to traditional bone cutting models where the properties are considered constant along a single cut, here, significant advancements in the modelling of cortical bone cutting were achieved by considering its porous stochasticity and accounting for the local (i.e. in near-porosity sites) alterations of friction and shear strength that occur due to the internal irrigation and permeability of the tissue.**

   A mechanistic model of cutting forces predictions for orthogonal cutting of cortical bone was developed to account for the microstructure (i.e. randomised porosity structures) and the interstitial fluid within. This was achieved by considering the individual constituents of the bone by generating pseudo-random bone structures that could be used for surface mapping of properties along the toolpath (i.e. nodal values of shear strength and friction coefficient). The mapped surface was set to calculate and assign bulk (i.e. pristine) values of properties in regions away from porosities, and zero values in the porosity zones. However, near-porosity areas (i.e. the affected zone surrounding the porosities) were calculated to account for the gradient of shear strength and

friction coefficient that was described previously. This mapped surface with localised properties was then used for calculation of cutting and thrust forces using a previously established Fracture Mechanics model.

4. **For the first time, real bone samples have been used for machining trials in an internally irrigated manner. This has been done due to the development of a novel rig which enables fluid flow through the natural porosities of a cortical bone sample during a machining test. This allows to replicate more realistic conditions of bone cutting, while still in an ex-vivo environment. Inherently, this is a significant step forward in setup development for mimicking in-vivo conditions of bone in an ex-vivo state.**

   To study the role of interstitial fluid of cortical bone during machining, a setup was engineered to enable a pumping system to be couples with a machining fixture for a small bone sample. The setup consists of three main components, which are additively manufactured, that permit a connection to a fluid input (i.e. syringe, pump tubing or hose). Fluid flow is forced through a small channel in one of the components that is then redirected to flow through the natural porosities on the bone. This is a novel setup that enables the possibility of bone machining closer to an in-vivo condition (i.e. considering interstitial fluid) while still in a laboratory environment.

5. **Alternative methods (e.g. laser machining) for bone material removal can pose certain advantages over conventional techniques (e.g. drilling), but they might not be as competitive in terms of damage inducement or material removal rate, making them challenging to deploy in a surgical environment.**

   To study the machining-induced damage from a thermally driven process, laser machining trials were conducted in cortical bone with various pulse widths (60 ps, 200 ns, continuous wave), and feed speeds (0.25-6.25 mm/s for the 60 ps

laser, 2.50-6.50 mm/s for the 200 ns laser and 5.00-45.00 mm/s for the continuous wave laser). As part of this study, the material removal mechanism was investigated depending on the laser type and it was found that shorter pulse widths create a removal mechanism that is optomechanical (i.e. plasma is generated and then the material is removed by a sequence of micro-explosions caused by the pressure waves that propagate through the surface). However, when longer or continuous pulse widths are used, the mechanisms shift to mostly thermal (i.e. ionisation of material, followed by melting, bubble formation and ejection). The difference in material removal mechanism not only plays an important role in the material removal rate or the inducement of cracks, but also in the way that thermal damage is propagated, as histological analysis revealed. The results obtained from the laser machining trials were compared to those obtained from conventional drilling experiments in terms of necrotic damage and material removal rate and it was revealed that while laser machining can pose some advantages (e.g. increased precision and accuracy of the removed material), it has the main disadvantages of a significantly small material removal rate (i.e. 165 times smaller than drilling) and the ease of necrosis inducement due to the thermal nature of the process. Consequently, by comparison of the experiments of this research, it is concluded that conventional mechanical machining should be the preferred method over laser machining in order to minimise tissue damage and keeping the machining time as short as possible. However, this could also suggest that laser machining could perhaps be employed only for precise cuts that are required to remove only small amounts of material (e.g. finishing process), while keeping the conventional removal methods (e.g. drilling, milling) for roughing passes. In both cases, external coolant should always be employed to minimise temperature rise in the tissue.

6. **Raman spectroscopy was explored to assess its feasibility for evaluating machining-induced bone damage. Since no chemical nor molecular changes are expected to occur at the temperatures developed during cutting (i.e. ≤ 110 °C), this technique, although useful in archaeology, cannot be used for revealing necrotic or micromechanical damage.**

   Since micromechanical damage was measured up to a depth of 1500 µm and necrotic damage up to a depth of 419 µm beneath a mechanically machined bone surface that reached 110 °C during machining, Raman spectroscopy was employed as a possible non-invasive technique that could possibly relatively capture either of these forms of damage. However, it was found that the Raman spectra post-machining near the machined surface displayed no signs of change, meaning that no Raman shift was observed, no amplitude changes were identified and no alterations to the mineralisation, carbonisation and crystallinity of the tissue were observed. This is useful to confirm that Raman spectroscopy is not a suitable technique to capture machining-induced bone damage due to the small temperatures (i.e. Raman spectroscopy is difficultly employed in bones *burned* at temperatures lower than 700 °C) that occurred are not high enough as to generate a change in the molecular structure of the tissue.

6.2 Future work

While this research has brought to light new knowledge in the field of bone machining and its damage assessment techniques, several areas of opportunity remain, and they have potential for in-depth research in the future. Addressing these will minimise the gap between the manufacturing research technologies and the medical field, thereby enabling more hands-on knowledge that could be more easily extrapolated towards a clinical practice.

- Micromechanical testing should be adapted to make it feasible for in-situ and in-vivo testing of bone. In this research, bone was studied micromechanically, but this was done by preparing ex-situ bone samples for micro-testing inside an SEM. However, a solution must be engineered to make of this technique a useful one for use in real surgeries. For instance, a miniaturised system or device should be designed to permit micromechanical testing during surgeries. This would enable to obtain quick results in-situ by surgeons, to have an assessment on the status of bone from a mechanical perspective.

- Using micromechanics along with histology to study the healing process of bone as a function of time (i.e. days, weeks, months). This would provide a better understanding of what would be ideal in a clinical practice. Given that the present work was limited to ex-vivo testing, the bone's healing capacity was non-existent. As such, a scenario in which micromechanics and histology could be employed together to study the healing process over time would be ideal. However, to exploit this idea the main challenge to be addressed is the fact that both histology and micromechanics are invasive techniques and would most likely involve a tissue extraction process form the subject.

- Studies must be carried out to find out the role of local micromechanical properties on functions of bone. It is usually assumed that the bone possesses pristine mechanical properties throughout all its extent; however, as it has been shown in this work, this could not always be the case. As such, it is necessary to understand the implications that having localised variation of properties could affect aspects such as implant bonding strength or healing capacity.

- Further predictive models for bone cutting must be developed. In this study, only the cutting forces were modelled by considering the role of interstitial fluid upon two properties (i.e. shear strength, friction coefficient) of cortical bone in near-porosity sites. However, this should be further expanded towards

predictive models of both necrotic depth and micromechanical damage. In the first, this should be done by accounting for the role that the interstitial fluid could locally have on the thermal properties of the tissue as well as considering the cooling effect of the fluid embedded in the porosities, to enable accurate thermal predictions that could be used for necrotic damage calculations. In the latter, more micromechanical testing post-machining is required for different machining conditions, as to achieve a deeper understanding of the damage propagation at both the micro- and nanoscales.

- While this study focused on cortical bone due to its relevance in a large range of surgeries (e.g. orthopaedics, dentistry, neurosurgery), other in-depth studies should be similarly be conducted for other hard tissues (i.e. trabecular bone, dentin, enamel) towards understanding their biological and micromechanical behaviours in a more in-vivo condition.

- Smarter tool design is imperative in the future. Development of newer and novel tools, including robotic systems, will increase in the following years as a result of all the recent developments on the understanding of tissues as engineering materials. These tools will be tailored to improve the cutting mechanisms and to minimise the damage (thermal, mechanical, biological) induced to the tissue.

- Investigation of the permeability and hydration properties of cortical bone already exist. However, these should be coupled with micromechanical testing to find out the discrete relation between the degree of local permeability (i.e. in terms of local water content) to the micromechanical behaviour in such location. This would further shed light into the findings reported in this work, where first, via drilling experiments, it was explained that micromechanical properties could be reduced due to a local dehydration effect; but then, with the study of internal irrigation, it was found that softer properties can also be

related due to the increased permeability of near-porosity zones were hydration is enhanced.

References

Abouzgia, M.B., James, D.F., 1995. Measurements of shaft speed while drilling through bone. J. Oral Maxillofac. Surg. 53, 1308–1315. https://doi.org/10.1016/0278-2391(95)90590-1

Adharapurapu, R.R., Jiang, F., Vecchio, K.S., 2006. Dynamic fracture of bovine bone. Mater. Sci. Eng. C 26, 1325–1332. https://doi.org/10.1016/j.msec.2005.08.008

Agarwal, R., Jain, V., Gupta, V., Saxena, S., Dwibedi, V., 2020. Effect of surface topography on pull-out strength of cortical screw after ultrasonic bone drilling: an in vitro study. J. Brazilian Soc. Mech. Sci. Eng. 42, 1–13. https://doi.org/10.1007/s40430-020-02449-5

Aghvami, M., Brunski, J.B., Tulu, U.S., Chen, C.H., Helms, J.A., 2018. A Thermal and Biological Analysis of Bone Drilling. J. Biomech. Eng. 140. https://doi.org/10.1115/1.4040312

Akkus, O., Adar, F., Schaffler, M.B., 2004. Age-related changes in physicochemical properties of mineral crystals are related to impaired mechanical function of cortical bone. Bone 34, 443–453. https://doi.org/10.1016/j.bone.2003.11.003

Alam, K., 2015. Experimental measurements of temperatures in drilling cortical bone using thermocouples, Scientia Iranica B.

Alam, K., Mitrofanov, A.V., Silberschmidt, V.V., 2009. Measurements of Surface Roughness in Conventional and Ultrasonically Assisted Bone Drilling. Am. J. Biomed. Sci. 312–320. https://doi.org/10.5099/aj090400312

Alam, K., Mitrofanov, A.V. V., Silberschmidt, V.V. V., 2011. Experimental investigations of forces and torque in conventional and ultrasonically-assisted drilling of cortical bone. Med. Eng. Phys. 33, 234–239. https://doi.org/10.1016/j.medengphy.2010.10.003

Alam, K., Piya, S., Al-Ghaithi, A., Silberschmidth, V., 2020. Experimental investigation on the effect of drill quality on the performance of bone drilling. Biomed. Tech. 65, 113–120. https://doi.org/10.1515/bmt-2018-0184

Altman, K.J., 2009. Microscale machining and mechanical characterization of bone tissue. The Ohio State University.

Amewoui, F., Le Coz, G., Bonnet, A.S., Moufki, A., 2020. An analytical modeling with experimental validation of bone temperature rise in drilling process. Med. Eng. Phys. 84, 151–160. https://doi.org/10.1016/j.medengphy.2020.07.007

Amini-Nik, S., Kraemer, D., Cowan, M.L., Gunaratne, K., Nadesan, P., Alman, B.A., Miller, R.J.D., 2010. Ultrafast Mid-IR Laser Scalpel: Protein Signals of the Fundamental Limits to Minimally Invasive Surgery. PLoS One 5, e13053. https://doi.org/10.1371/journal.pone.0013053

Anderson, T.L., 2017. Fracture Mechanics. Fundamentals and Applications, 4th ed. CRC Press.

Aro, H., Kallioniemi, H., Aho, A.J., Kellokumpu-Lehtinen, P., 1981. Ultrasonic

Device in Bone Cutting: A Histological and Scanning Electron Microscopical Study. Acta Orthop. Scand. 52, 5–10. https://doi.org/10.3109/17453678108991750

Ascenzi, A., Baschieri, P., Benvenuti, A., 1990. The bending properties of single osteons. J. Biomech. 23, 763–771. https://doi.org/10.1016/0021-9290(90)90023-V

Ashby, M.F., Jones, David, R.H., 2012. Engineering Materials 1, 4th ed. Butterworth-Heinemann.

Augustin, G., Davila, S., Mihoci, K., Udiljak, T., Vedrina, D.S., Antabak, A., 2008. Thermal osteonecrosis and bone drilling parameters revisited. Arch. Orthop. Trauma Surg. 128, 71–77. https://doi.org/10.1007/s00402-007-0427-3

Augustin, G., Zigman, T., Davila, S., Udilljak, T., Staroveski, T., Brezak, D., Babic, S., 2012. Cortical bone drilling and thermal osteonecrosis. Clin. Biomech. 27, 313–325. https://doi.org/10.1016/j.clinbiomech.2011.10.010

Axinte, D., Guo, Y., Liao, Z., Shih, A.J., M'Saoubi, R., Sugita, N., 2019a. Machining of biocompatible materials — Recent advances. CIRP Ann. 68, 629–652. https://doi.org/10.1016/j.cirp.2019.05.003

Axinte, D., Guo, Y., Liao, Z., Shih, A.J., M'Saoubi, R., Sugita, N., 2019b. Machining of biocompatible materials — Recent advances. CIRP Ann. - Manuf. Technol. https://doi.org/10.1016/j.cirp.2019.05.003

Babbar, A., Jain, V., Gupta, D., 2019. Thermogenesis mitigation using ultrasonic actuation during bone grinding: a hybrid approach using CEM43°C and Arrhenius model. J. Brazilian Soc. Mech. Sci. Eng. 41, 1–14. https://doi.org/10.1007/s40430-019-1913-6

Bachman, C.H., Ellis, E.H., 1965. Fluorescence of Bone. Nature 206, 1328–1331.

Baek, K. W., Deibel, W., Marinov, D., Griessen, M., Bruno, A., Zeilhofer, H.F., Cattin, P., Juergens, P., 2015. Clinical applicability of robot-guided contact-free laser osteotomy in cranio-maxillo-facial surgery: In-vitro simulation and in-vivo surgery in minipig mandibles. Br. J. Oral Maxillofac. Surg. 53, 976–981. https://doi.org/10.1016/j.bjoms.2015.07.019

Baek, Kyung Won, Deibel, W., Marinov, D., Griessen, M., Dard, M., Bruno, A., Zeilhofer, H.F., Cattin, P., Juergens, P., 2015. A comparative investigation of bone surface after cutting with mechanical tools and Er:YAG laser. Lasers Surg. Med. 47, 426–432. https://doi.org/10.1002/lsm.22352

Bai, W., Pan, P.F., Shu, L.M., Wang, D., Zhang, J.G., Xu, J.F., 2021. Mechanism of chip formation and crack prapagation in ultrasonically assisted cutting of bone tissue. J. Mech. Eng. 57, 69–77.

Bai, W., Shu, L., Sun, R., Xu, J., Silbershmidt, V. V., Sugita, N., 2020. Mechanism of material removal in orthogonal cutting of cortical bone. J. Mech. Behav. Biomed. Mater. in press, 103618. https://doi.org/10.1016/j.jmbbm.2020.103618

Bancroft, J.D., Cook, H.C., 1994. Manual of histological techniques and their diagnostic applications, 1st ed. Churchill Livingstone, London.

Baro, D.K., Deoghare, A.B., 2018. Investigation of cutting force and temperature variation in orthogonal cutting of cortical bone. Mater. Today Proc. 5, 12595–

12608. https://doi.org/10.1016/j.matpr.2018.02.242

Basiaga, M., Paszenda, Z., Szewczenko, J., Kaczmarek, M., 2011. Numerical and experimental analyses of drills used in osteosynthesis. Acta Bioeng. Biomech. 13, 29–36.

Bekker, A., Cloete, T.J., Chinsamy-Turan, A., Nurick, G.N., Kok, S., 2015. Constant strain rate compression of bovine cortical bone on the Split-Hopkinson Pressure Bar. Mater. Sci. Eng. C 46, 443–449. https://doi.org/10.1016/j.msec.2014.10.071

Beltran Bernal, L.M., Schmidt, I.T., Vulin, N., Widmer, J., Snedeker, J.G., Cattin, P.C., Zam, A., Rauter, G., 2018. Optimizing controlled laser cutting of hard tissue (bone). - Autom. 66, 1072–1082. https://doi.org/10.1515/auto-2018-0072

Beltran, L., Abbasi, H., Georg, R., Friederich, N., Cattin, P., Zam, A., 2017. Effect of laser pulse duration on ablation efficiency of hard bone in microseconds regime, in: Martins Costa, M.F.P. (Ed.), Third International Conference on Applications of Optics and Photonics. SPIE, p. 115. https://doi.org/10.1117/12.2272253

Bertollo, N., Gothelf, T.K., Walsh, W.R., 2008. 3-Fluted orthopaedic drills exhibit superior bending stiffness to their 2-fluted rivals: Clinical implications for targeting ability and the incidence of drill-bit failure. Injury 39, 734–741. https://doi.org/10.1016/j.injury.2007.11.286

Bertollo, N., Milne, H.R.M., Ellis, L.P., Stephens, P.C., Gillies, R.M., Walsh, W.R., 2010. A comparison of the thermal properties of 2- and 3-fluted drills and the effects on bone cell viability and screw pull-out strength in an ovine model. Clin. Biomech. 25, 613–617. https://doi.org/10.1016/j.clinbiomech.2010.02.007

Brioschi, V., Cook, J., Arthurs, G.I., 2016. Can a surgeon drill accurately at a specified angle? Vet. Rec. Open 3. https://doi.org/10.1136/vetreco-2016-000172

BSI Standards Publication Metallic materials — Instrumented indentation test of hardness and materials parameters Part 1 : Test method, 2015.

Bushby, A.J., Ferguson, V.L., Boyde, A., 2004. Nanoindentation of bone: Comparison of specimens tested in liquid and embedded in polymethylmethacrylate. J. Mater. Res. 19, 249–259. https://doi.org/10.1557/jmr.2004.19.1.249

Cardoso, L., Fritton, S., Gailani, G., Benalla, M., Cowin, S., 2013. A review of recent advances in the assessment of bone porosity, permeability, and interstitial fluid flow. J. Biomech. 46, 253–265. https://doi.org/10.1016/j.pestbp.2011.02.012.Investigations

Catuna, M.C., 1953. Sonic energy:A possible dental application: Preliminary report of an ultrasonic cutting method. Ann. Dent. 256–260.

Cha, D., Axinte, D., Billingham, J., 2019. Geometrical modelling of pulsed laser ablation of high performance metallic alloys. Int. J. Mach. Tools Manuf. 141, 78–88. https://doi.org/10.1016/j.ijmachtools.2019.04.004

Chen, Q. Sen, Dai, L., Liu, Y., Shi, Q.X., 2020. A cortical bone milling force model based on orthogonal cutting distribution method. Adv. Manuf. 8, 204–215.

https://doi.org/10.1007/s40436-020-00300-7

Chen, Z.H., Zhang, Y., Wang, C.Y., Chen, B., 2021. Understanding the cutting mechanisms of composite structured soft tissues. Int. J. Mach. Tools Manuf. 161, 103685. https://doi.org/10.1016/j.ijmachtools.2020.103685

Childs, T.H.C., Arola, D., 2011. Machining of cortical bone: Simulations of chip formation mechanics using metal machining models. Mach. Sci. Technol. 15, 206–230. https://doi.org/10.1080/10910344.2011.580699

Christen, P., Ito, K., Ellouz, R., Boutroy, S., Sornay-Rendu, E., Chapurlat, R.D., Van Rietbergen, B., 2014. Bone remodelling in humans is load-driven but not lazy. Nat. Commun. 5. https://doi.org/10.1038/ncomms5855

COHEN, J., HARRIS, W.H., 1958. The three-dimensional anatomy of haversian systems. J. Bone Joint Surg. Am. 40 A, 419–434. https://doi.org/10.2106/00004623-195840020-00015

Conward, M., Samuel, J., 2016. Machining characteristics of the haversian and plexiform components of bovine cortical bone. J. Mech. Behav. Biomed. Mater. 60, 525–534. https://doi.org/10.1016/j.jmbbm.2016.03.017

Cowin, S.C., 1999. Bone poroelasticity. J. Biomech. 32, 217–238. https://doi.org/10.1016/S0021-9290(98)00161-4

Cowin, S.C., Cardoso, L., 2015. Blood and interstitial flow in the hierarchical pore space architecture of bone tissue. J. Biomech. 48, 842–854. https://doi.org/10.1016/j.jbiomech.2014.12.013

Croker, S.L., Clement, J.G., Donlon, D., 2009. A comparison of cortical bone thickness in the femoral midshaft of humans and two non-human mammals. HOMO- J. Comp. Hum. Biol. 60, 551–565. https://doi.org/10.1016/j.jchb.2009.07.003

Cseke, A., Heinemann, R., 2018. The effects of cutting parameters on cutting forces and heat generation when drilling animal bone and biomechanical test materials. Med. Eng. Phys. 51, 24–30. https://doi.org/10.1016/j.medengphy.2017.10.009

Currey, J.D., 2002. Bones: Structure and Mechanics, 1st ed. Princeton University Press, New Jersey.

Dahotre, N.B., Joshi, S.S., 2016. Machining of bone and hard tissues, Machining of Bone and Hard Tissues. https://doi.org/10.1007/978-3-319-39158-8

Davidson, S.R.H., James, D.F., 2003. Drilling in Bone: Modeling Heat Generation and Temperature Distribution. J. Biomech. Eng. 125, 305. https://doi.org/10.1115/1.1535190

Davidson, S.R.H., James, D.F., 2000. Measurement of thermal conductivity of bovine cortical bone. Med. Eng. Phys. 22, 741–747. https://doi.org/10.1016/S1350-4533(01)00003-0

Davis, J.M., Saei, M., Mohanty, D.P., Udupa, A., Sugihara, T., Chandrasekar, S., 2020. Cutting of tantalum: Why it is so difficult and what can be done about it. Int. J. Mach. Tools Manuf. 157, 103607. https://doi.org/10.1016/j.ijmachtools.2020.103607

Denis, K., Van Ham, G., Vander Sloten, J., Van Audekercke, R., Van der Perre, G.,

De Schutter, J., Kruth, J.P., Bellemans, J., Fabry, G., 2001. Influence of bone milling parameters on the temperature rise, milling forces and surface flatness in view of robot-assisted total knee arthroplasty. Int. Congr. Ser. 1230, 300–306. https://doi.org/10.1016/S0531-5131(01)00067-X

Dolan, E.B., Haugh, M.G., Tallon, D., Casey, C., McNamara, L.M., 2012. Heat-shock-induced cellular responses to temperature elevations occurring during orthopaedic cutting. J. R. Soc. Interface 9, 3503–3513. https://doi.org/10.1098/rsif.2012.0520

Erikssons, A.R., Albrektsson, T., Albrektsson, B., 1984. Heat caused by drilling cortical bone. Acta Orthop. Scand. 629–631.

Federspil, P.A., Plinkert, B., Plinkert, P.K., 2003. Experimental robotic milling in skull-base surgery. Comput. Aided Surg. 8, 42–48. https://doi.org/10.3109/10929080309146102

Feldmann, A., Anso, J., Bell, B., Williamson, T., Gavaghan, K., Gerber, N., Rohrbach, H., Weber, S., Zysset, P., 2016. Temperature Prediction Model for Bone Drilling Based on Density Distribution and In Vivo Experiments for Minimally Invasive Robotic Cochlear Implantation. Ann. Biomed. Eng. 44, 1576–1586. https://doi.org/10.1007/s10439-015-1450-0

Feldmann, A., Ganser, P., Nolte, L., Zysset, P., 2017. Orthogonal cutting of cortical bone: Temperature elevation and fracture toughness. Int. J. Mach. Tools Manuf. 118–119, 1–11. https://doi.org/10.1016/j.ijmachtools.2017.03.009

Feldmann, A., Wili, P., Maquer, G., Zysset, P., 2018. The thermal conductivity of cortical and cancellous bone. Eur. Cells Mater. 35, 25–33. https://doi.org/10.22203/eCM.v035a03

Feldmann, A., Zysset, P., 2016. Experimental determination of the emissivity of bone. Med. Eng. Phys. 38, 1136–1138. https://doi.org/10.1016/j.medengphy.2016.06.019

Field, J.R., Sumner-Smith, G., 2002. Bone blood flow response to surgical trauma. Injury 33, 447–451. https://doi.org/10.1016/S0020-1383(02)00014-1

Franssen, B.B.G.M., Diest, P.J., Schuurman, A.H., Kon, M., 2008. Drilling k-wires, what about the osteocytes? An experimental study in rabbits. Arch. Orthop. Trauma Surg. 128, 83–87. https://doi.org/10.1007/s00402-007-0382-z

Frentzen, M., Götz, W., Ivanenko, M., Afilal, S., Werner, M., Hering, P., 2003. Osteotomy with 80-µs CO2 laser pulses - Histological results. Lasers Med. Sci. 18, 119–124. https://doi.org/10.1007/s10103-003-0264-8

Garcia Luna, G., Axinte, D., Novovic, D., 2020. Influence of grit geometry and fibre orientation on the abrasive material removal mechanisms of SiC/SiC Ceramic Matrix Composites (CMCs). Int. J. Mach. Tools Manuf. 157, 103580. https://doi.org/10.1016/j.ijmachtools.2020.103580

Gavalda Diaz, O., Garcia Luna, G., Liao, Z., Axinte, D., 2019. The new challenges of machining Ceramic Matrix Composites (CMCs): Review of surface integrity. Int. J. Mach. Tools Manuf. 139, 24–36. https://doi.org/10.1016/j.ijmachtools.2019.01.003

Gerberich, W.W., Michler, J., Mook, W.M., Ghisleni, R., Östlund, F., Stauffer, D.D.,

Ballarini, R., 2009. Scale effects for strength, ductility, and toughness in “brittle” materials. J. Mater. Res. 24, 898–906. https://doi.org/10.1557/jmr.2009.0143

Goh, J.C.H., Ang, E.J., Bose, K., 1989. Effect of preservation medium on the mechanical properties of cat bones. Acta Orthop. 60, 465–467. https://doi.org/10.3109/17453678909149321

Granke, M., Does, M.D., Nyman, J.S., 2015. The Role of Water Compartments in the Material Properties of Cortical Bone. Calcif. Tissue Int. 97, 292–307. https://doi.org/10.1007/s00223-015-9977-5

Greenwood, C., Clement, J.G., Dicken, A.J., Evans, J.P.O., Lyburn, I.D., Martin, R.M., Rogers, K.D., Stone, N., Adams, G., Zioupos, P., 2015. The micro-architecture of human cancellous bone from fracture neck of femur patients in relation to the structural integrity and fracture toughness of the tissue. Bone Reports 3, 67–75. https://doi.org/10.1016/j.bonr.2015.10.001

Gu, G.X., Chen, C.T., Richmond, D.J., Buehler, M.J., 2018. Bioinspired hierarchical composite design using machine learning: Simulation, additive manufacturing, and experiment. Mater. Horizons 5, 939–945. https://doi.org/10.1039/c8mh00653a

Gupta, V., Pandey, P.M., Gupta, R.K., Mridha, A.R., 2017a. Rotary ultrasonic drilling on bone: A novel technique to put an end to thermal injury to bone. Proc. Inst. Mech. Eng. Part H J. Eng. Med. 231, 189–196. https://doi.org/10.1177/0954411916688500

Gupta, V., Pandey, P.M., Mridha, A.R., Gupta, R.K., 2017b. Effect of Various Parameters on the Temperature Distribution in Conventional and Diamond Coated Hollow Tool Bone Drilling: A Comparative Study. Procedia Eng. 184, 90–98. https://doi.org/10.1016/j.proeng.2017.04.074

Gupta, V., Pandey, P.M., Silberschmidt, V. V., 2017c. Rotary ultrasonic bone drilling: Improved pullout strength and reduced damage. Med. Eng. Phys. 41, 1–8. https://doi.org/10.1016/j.medengphy.2016.11.004

Hage, I.S., Hamade, R.F., 2013. Micro-FEM orthogonal cutting model for bone using microscope images enhanced via artificial intelligence. Procedia CIRP 8, 385–390. https://doi.org/10.1016/j.procir.2013.06.121

Hancox, N.M., 1972. Biology of Bone, 1st ed. Cambridge University Press, Cambridge.

Heřt, J., Fiala, P., Petrtýl, M., 1994. Osteon orientation of the diaphysis of the long bones in man. Bone 15, 269–277. https://doi.org/10.1016/8756-3282(94)90288-7

Hillery, M.T., Shuaib, I., 1999. Temperature effects in the drilling of human and bovine bone. J. Mater. Process. Technol. 92–93, 302–308. https://doi.org/10.1016/S0924-0136(99)00155-7

Hou, J.P., Petrinic, N., Ruiz, C., Hallett, S.R., 2000. Prediction of impact damage in composite plates. Compos. Sci. Technol. 60, 273–281. https://doi.org/10.1016/S0266-3538(99)00126-8

Idkaidek, A., Koric, S., Jasiuk, I., 2018. Fracture analysis of multi-osteon cortical

bone using XFEM. Comput. Mech. 62, 171–184. https://doi.org/10.1007/s00466-017-1491-3

Iwaniec, U.T., Wronski, T.J., Turner, R.T., 2008. Histological Analysis of Bone, in: Walker, John, Walker, Jan (Eds.), Methods in Molecular Biology. Springer, pp. 325–341. https://doi.org/10.1007/978-1-59745-242-7_21

Jacobs, C., Pope, M., Berry, J., Hoaglund, F., 1974. A Study of the Bone Machining Process - Orthogonal Cutting. J. Biomech. 7, 131–140.

James, T.P., Chang, G., Micucci, S., Sagar, A., Smith, E.L., Cassidy, C., 2014. Effect of applied force and blade speed on histopathology of bone during resection by sagittal saw. Med. Eng. Phys. 36, 364–370. https://doi.org/10.1016/j.medengphy.2013.12.002

Jindal, R., 2016. Experimental Investigations To Study Cutting temperature and force during cortical bone. THAPAR UNIVERSITY.

Kanaya, H., Enokida, M., Uehara, K., Ueki, M., Nagashima, H., 2019. Thermal damage of osteocytes during pig bone drilling: an in vivo comparative study of currently available and modified drills. Arch. Orthop. Trauma Surg. 139, 1599–1605. https://doi.org/10.1007/s00402-019-03239-y

Karaca, F., Aksakal, B., Kom, M., 2011. Influence of orthopaedic drilling parameters on temperature and histopathology of bovine tibia: An in vitro study. Med. Eng. Phys. 33, 1221–1227. https://doi.org/10.1016/j.medengphy.2011.05.013

Karmani, S., 2006. The thermal properties of bone and the effects of surgical intervention. Curr. Orthop. 20, 52–58. https://doi.org/10.1016/j.cuor.2005.09.011

Kate, M., Palaskar, S., Kapoor, P., 2016. Implant failure: A dentist's nightmare. J. Dent. Implant. 6, 51. https://doi.org/10.4103/0974-6781.202154

Koester, K.J., Ager, J.W., Ritchie, R.O., 2008. The true toughness of human cortical bone measured with realistically short cracks. Nat. Mater. 7, 672–677. https://doi.org/10.1038/nmat2221

Koluaçik, S., Can, M., Bahçe, E., 2020. Experimental investigation of delamination formed by bone drilling. Teh. Vjesn. 27, 711–717. https://doi.org/10.17559/TV-20181228185947

Kong, D., Lin, G., Shi, Y., Gu, Z., Gao, Y., Feng, Y., 2020. Performance of heterotopic bone elicited with bone morphogenic protein-2 microspheres as a bone repair material. Mater. Des. 191, 108657. https://doi.org/10.1016/j.matdes.2020.108657

Krause, L.S., Cobb, C.M., Rapley, J.W., Killoy, W.J., Spencer, P., 1997. Laser Irradiation of Bone. I. An In Vitro Study Concerning the Effects of the CO2 Laser on Oral Mucosa and Subjacent Bone. J. Periodontol. 68, 872–880. https://doi.org/10.1902/jop.1997.68.9.872

Krause, W.R., 1987. Orthogonal bone cutting: saw design and operating characteristics. J. Biomech. Eng. 109, 263–71.

Kuhn, J.L., Goldstein, S.A., Choi, R., London, M., Feldkamp, L.A., Matthews, L.S., 1989. Comparison of the trabecular and cortical tissue moduli from human iliac crests. J. Orthop. Res. 7, 876–884. https://doi.org/10.1002/jor.1100070614

Kurin, D.S., 2013. Trepanation in South-Central Peru during the early late intermediate period (ca. AD 1000-1250). Am. J. Phys. Anthropol. 152, 484–494. https://doi.org/10.1002/ajpa.22383

la Monaca, A., Murray, J.W., Liao, Z., Speidel, A., Robles-Linares, J.A., Axinte, D.A., Hardy, M.C., Clare, A.T., 2021. Surface integrity in metal machining - Part II: Functional performance. Int. J. Mach. Tools Manuf. 164, 103718. https://doi.org/10.1016/j.ijmachtools.2021.103718

Laroche, M., 2002. Intraosseous circulation from physiology to disease. Jt. Bone Spine 69, 262–269. https://doi.org/10.1016/S1297-319X(02)00391-3

Lee, J.E., Gozen, B.A., Ozdoganlar, O.B., 2012a. Modeling and experimentation of bone drilling forces. J. Biomech. 45, 1076–1083. https://doi.org/10.1016/j.jbiomech.2011.12.012

Lee, J.E., Ozdoganlar, O.B., Rabin, Y., 2012b. An experimental investigation on thermal exposure during bone drilling. Med. Eng. Phys. 34, 1510–1520. https://doi.org/10.1016/j.medengphy.2012.03.002

Lee, J.E., Rabin, Y., Ozdoganlar, O.B., 2011. A new thermal model for bone drilling with applications to orthopaedic surgery. Med. Eng. Phys. 33, 1234–1244. https://doi.org/10.1016/j.medengphy.2011.05.014

Li, L., Liang, M., Yu, B., Yang, S., 2014. Analysis of thermal conductivity in living biological tissue with vascular network and convection. Int. J. Therm. Sci. 86, 219–226. https://doi.org/10.1016/j.ijthermalsci.2014.07.006

Li, S., Shu, L., Kizaki, T., Bai, W., Terashima, M., Sugita, N., 2021. Cortical bone drilling: a time series experimental analysis of thermal characteristics. J. Manuf. Process. 64, 606–619. https://doi.org/10.1016/j.jmapro.2021.01.046

Li, Z., Yang, D., Hao, W., Wu, S., Ye, Y., Chen, Z., Li, X., 2017. Ultrasonic vibration-assisted micro-hole forming on skull. Proc. Inst. Mech. Eng. Part B J. Eng. Manuf. 231, 2447–2457. https://doi.org/10.1177/0954405415611363

Li, Z., Yang, D.G., Hao, W.D., Wu, T.C., Wu, S., Li, X.P., 2016. A novel technique for micro-hole forming on skull with the assistance of ultrasonic vibration. J. Mech. Behav. Biomed. Mater. 57, 1–13. https://doi.org/10.1016/j.jmbbm.2015.11.016

Liao, Z., Axinte, D., Gao, D., 2019. On modelling of cutting force and temperature in bone milling. J. Mater. Process. Technol. 266, 627–638. https://doi.org/10.1016/j.jmatprotec.2018.11.039

Liao, Z., Axinte, D.A., 2016a. On chip formation mechanism in orthogonal cutting of bone. Int. J. Mach. Tools Manuf. 102, 41–55. https://doi.org/10.1016/j.ijmachtools.2015.12.004

Liao, Z., Axinte, D.A., 2016b. On monitoring chip formation, penetration depth and cutting malfunctions in bone micro-drilling via acoustic emission. J. Mater. Process. Technol. 229, 82–93. https://doi.org/10.1016/j.jmatprotec.2015.09.016

Liao, Z., Axinte, D.A., Gao, D., 2017. A novel cutting tool design to avoid surface damage in bone machining. Int. J. Mach. Tools Manuf. 116, 52–59. https://doi.org/10.1016/j.ijmachtools.2017.01.003

Liao, Z., la Monaca, A., Murray, J., Speidel, A., Ushmaev, D., Clare, A., Axinte, D.,

M'Saoubi, R., 2021. Surface integrity in metal machining - Part I: Fundamentals of surface characteristics and formation mechanisms. Int. J. Mach. Tools Manuf. 162, 103687. https://doi.org/10.1016/j.ijmachtools.2020.103687

Liebschner, M.A.K., 2004. Biomechanical considerations of animal models used in tissue engineering of bone. Biomaterials 25, 1697–1714. https://doi.org/10.1016/S0142-9612(03)00515-5

Liu, Y., Luo, D., Wang, T., 2016. Hierarchical Structures of Bone and Bioinspired Bone Tissue Engineering. Small 12, 4611–4632. https://doi.org/10.1002/smll.201600626

Lloyd, A.A., Gludovatz, B., Riedel, C., Luengo, E.A., Saiyed, R., Marty, E., Lorich, D.G., Lane, J.M., Ritchie, R.O., Busse, B., Donnelly, E., 2017. Atypical fracture with long-term bisphosphonate therapy is associated with altered cortical composition and reduced fracture resistance. Proc. Natl. Acad. Sci. U. S. A. 114, 8722–8727. https://doi.org/10.1073/pnas.1704460114

Lundskog, J., 1972. Heat and bone tissue. An experimental investigation of the thermal properties of bone and threshold levels for thermal injury. Scand. J. Plast. Reconstr. Surg. 9, 1—80.

Ma, J.X., He, W.W., Zhao, J., Kuang, M.J., Bai, H.H., Sun, L., Lu, B., Tian, A.X., Wang, Ying, Dong, B.C., Wang, Yan, Ma, X.L., 2017. Bone microarchitecture and biomechanics of the necrotic femoral head. Sci. Rep. 7, 1–10. https://doi.org/10.1038/s41598-017-13643-2

Maani, N., Farhang, K., Hodaei, M., 2014. A model for the prediction of thermal response of bone in surgical drilling. J. Therm. Sci. Eng. Appl. 6. https://doi.org/10.1115/1.4026625

Maghsoudi-Ganjeh, M., Wang, X., Zeng, X., 2020. Computational investigation of the effect of water on the nanomechanical behavior of bone. J. Mech. Behav. Biomed. Mater. 101, 103454. https://doi.org/10.1016/j.jmbbm.2019.103454

Mamede, A.P., Vassalo, A.R., Piga, G., Cunha, E., Parker, S.F., Marques, M.P.M., Batista De Carvalho, L.A.E., Gonçalves, D., 2018. Potential of Bioapatite Hydroxyls for Research on Archeological Burned Bone. Anal. Chem. 90, 11556–11563. https://doi.org/10.1021/acs.analchem.8b02868

Marco, M., Rodríguez-Millán, M., Santiuste, C., Giner, E., Miguélez, M.H., 2015. A review on recent advances in numerical modelling of bone cutting. J. Mech. Behav. Biomed. Mater. 44, 179–201. https://doi.org/10.1016/j.jmbbm.2014.12.006

Mediouni, M., Kucklick, T., Poncet, S., Madiouni, R., Abouaomar, A., Madry, H., Cucchiarini, M., Chopko, B., Vaughan, N., Arora, M., Gökkuş, K., Lozoya Lara, M., Paiva Cedeño, L., Volosnikov, A., Hesmati, M., Ho, K., 2019. An overview of thermal necrosis: present and future. Curr. Med. Res. Opin. 35, 1555–1562. https://doi.org/10.1080/03007995.2019.1603671

Mitsuishi, M., Warisawa, S., Sugita, N., 2004. Determination of the machining characteristics of a biomaterial using a machine tool designed for total knee arthroplasty. CIRP Ann. - Manuf. Technol. 53, 107–112. https://doi.org/10.1016/S0007-8506(07)60656-8

Mohsin, S., O'Brien, F.J., Lee, T.C., 2006. Osteonal crack barriers in ovine compact bone. J. Anat. 208, 81–89. https://doi.org/10.1111/j.1469-7580.2006.00509.x

Morris, M.D., Mandair, G.S., 2011. Raman assessment of bone quality. Clin. Orthop. Relat. Res. 469, 2160–2169. https://doi.org/10.1007/s11999-010-1692-y

Nguendon Kenhagho, H., Canbaz, F., Gomez Alvarez-Arenas, T.E., Guzman, R., Cattin, P., Zam, A., 2021. Machine Learning-Based Optoacoustic Tissue Classification Method for Laser Osteotomes Using an Air-Coupled Transducer. Lasers Surg. Med. 53, 377–389. https://doi.org/10.1002/lsm.23290

Noble, B., Alini, M., Richards, R.G., 2003. Bone microdamage and cell apoptosis. Eur. Cells Mater. 6, 46–55. https://doi.org/10.22203/eCM.v006a05

Noble, B.S., 2008. The osteocyte lineage. Arch. Biochem. Biophys. 473, 106–111. https://doi.org/10.1016/j.abb.2008.04.009

Noorazizi, M.S., Izamshah, R., Kasim, M.S., 2017. Effects of Drill Geometry and Penetration Angle on Temperature and Holes Surfaces for Cortical Bovine Bone: An in Vitro Study. Procedia Eng. 184, 70–77. https://doi.org/10.1016/j.proeng.2017.04.072

Notingher, I., Jones, J.R., Verrier, S., Bisson, I., Embanga, P., Edwards, P., Polak, J.M., Hench, L.L., 2003. Application of FTIR and Raman Spectroscopy to Characterisation of Bioactive Materials and Living Cells. Spectroscopy 17, 275–288. https://doi.org/10.1155/2003/893584

O'Brien, F.J., Taylor, D., Lee, T.C., 2005. The effect of bone microstructure on the initiation and growth of microcracks. J. Orthop. Res. 23, 475–480. https://doi.org/10.1016/j.orthres.2004.08.005

Ohashi, H., Therin, M., Meunier, A., Christel, P., 1994. The effect of drilling parameters on bone. J. Mater. Sci. Mater. Med. 5, 225–231. https://doi.org/10.1007/bf00121093

Oliver, W.C., Pharr, G.M., 1992. An improved technique for determining hardness and elastic modulus using load and displacement sensing indentation experiments. J. Mater. Res. 7, 1564–1583. https://doi.org/10.1557/JMR.1992.1564

Östlund, F., Howie, P.R., Ghisleni, R., Korte, S., Leifer, K., Clegg, W.J., Michler, J., 2011. Ductile-brittle transition in micropillar compression of GaAs at room temperature. Philos. Mag. 91, 1190–1199. https://doi.org/10.1080/14786435.2010.509286

Östlund, F., Rzepiejewska-Malyska, K., Leifer, K., Hale, L.M., Tang, Y., Ballarini, R., Gerberich, W.W., Michler, J., 2009. Brittle-to-ductile transition in uniaxial compression of silicon pillars at room temperature. Adv. Funct. Mater. 19, 2439–2444. https://doi.org/10.1002/adfm.200900418

Ozbek, H., Phillips, S.L., 1980. Thermal Conductivity of Aqueous Sodium Chloride Solutions from 20 to 330 °C. J. Chem. Eng. Data 25, 263–267. https://doi.org/10.1021/je60086a001

Pandey, R.K., Panda, S.S., 2015. Evaluation of delamination in drilling of bone. Med. Eng. Phys. 37, 657–664. https://doi.org/10.1016/j.medengphy.2015.04.008

Pandey, R.K., Panda, S.S., 2013. Drilling of bone: A comprehensive review. J. Clin. Orthop. Trauma 4, 15–30. https://doi.org/10.1016/j.jcot.2013.01.002

Pandurić, D.G., Bago, I., Katanec, D., Žabkar, J., Miletić, I., Anić, I., 2012. Comparison of Er:YAG Laser and surgical drill for osteotomy in oral surgery: An experimental study. J. Oral Maxillofac. Surg. 70, 2515–2521. https://doi.org/10.1016/j.joms.2012.06.192

Pang, X.L., Zhang, Y., Wang, C.Y., Chen, Z.H., Tang, N., Chen, B., 2020. Effect of cutting parameters on cutting force and surface quality in cutting of articular cartilage. Procedia CIRP 89, 116–121. https://doi.org/10.1016/j.procir.2020.05.127

Pantawane, M. V., Chipper, R.T., Robertson, W.B., Khan, R.J.K., Fick, D.P., Dahotre, N.B., 2020. Evolution of surface morphology of Er:YAG laser-machined human bone. Lasers Med. Sci. 35, 1477–1485. https://doi.org/10.1007/s10103-019-02927-w

Payne, J.T., Peavy, G.M., Reinisch, L., Van Sickle, D.C., 2001. Cortical bone healing following laser osteotomy using 6.1 μm wavelength. Lasers Surg. Med. 29, 38–43. https://doi.org/10.1002/lsm.1084

Pearce, A.I., Richards, R.G., Milz, S., Schneider, E., Pearce, S.G., 2007. Animal models for implant biomaterial research in bone: A review. Eur. Cells Mater. 13, 1–10. https://doi.org/10.22203/eCM.v013a01

Peterlik, H., Roschger, P., Klaushofer, K., Fratzl, P., 2006. From brittle to ductile fracture of bone. Nat. Mater. 5, 52–55. https://doi.org/10.1038/nmat1545

Poundarik, A.A., Diab, T., Sroga, G.E., Ural, A., Boskey, A.L., Gundberg, C.M., Vashishth, D., 2012. Dilatational band formation in bone. Proc. Natl. Acad. Sci. U. S. A. 109, 19178–19183. https://doi.org/10.1073/pnas.1201513109

Pourgiv, S., n.d. Ultrasonic-Assisted Drilling of Cortical and Cancellous Bone in a Comparative Point of View. https://doi.org/10.21203/rs.3.rs-368773/v1

Predoi-Racila, M., Crolet, J.M., 2008. Human cortical bone: The SiNuPrOs model: Part I-description and elastic macroscopic results. Comput. Methods Biomech. Biomed. Engin. 11, 169–187. https://doi.org/10.1080/10255840701695140

Rajitha Gunaratne, G.D., Khan, R., Fick, D., Robertson, B., Dahotre, N., Ironside, C., 2017. A review of the physiological and histological effects of laser osteotomy. J. Med. Eng. Technol. 41, 1–12. https://doi.org/10.1080/03091902.2016.1199743

Rayan, G.M., Stanfield, D.T., Cahill, S., Kosanke, S.D., Kopta, J.A., 1992. Effects of rapid pulsed CO2 laser beam on cortical bone in vivo. Lasers Surg. Med. 12, 615–620. https://doi.org/10.1002/lsm.1900120608

Reingewirtz, Y., Szmukler-moncler, S., Senger, B., 1997. Influence of different parameters on bone heating and drilling time in implantology. Clin. Oral Implants Res. 8, 189–197. https://doi.org/10.1034/j.1600-0501.1997.080305.x

Renders, G.A.P., Mulder, L., Ruijven, L.J. Van, Eijden, T.M.G.J. Van, 2007. Porosity of human mandibular condylar bone 239–248. https://doi.org/10.1111/j.1469-7580.2007.00693.x

Rho, J.Y., Ashman, R.B., Turner, C.H., 1993. Young's modulus of trabecular and

cortical bone material: Ultrasonic and microtensile measurements. J. Biomech. 26, 111–119. https://doi.org/10.1016/0021-9290(93)90042-D

Rho, J.Y., Tsui, T.Y., Pharr, G.M., 1997. Elastic properties of human cortical and trabecular lamellar bone measured by nanoindentation. Biomaterials 18, 1325–1330. https://doi.org/10.1016/S0142-9612(97)00073-2

Ritchie, R.O., Buehler, M.J., Hansma, P., 2009. Plasticity and toughness in bone. Phys. Today 62, 41–47. https://doi.org/10.1063/1.3156332

Ritchie, R.O., Kinney, J.H., Kruzic, J.J., Nalla, R.K., 2005. A fracture mechanics and mechanistic approach to the failure of cortical bone. Fatigue Fract. Eng. Mater. Struct. https://doi.org/10.1111/j.1460-2695.2005.00878.x

Robles-Linares, J., Ramírez-Cedillo, E., Siller, H., Rodríguez, C., Martínez-López, J., 2019. Parametric Modeling of Biomimetic Cortical Bone Microstructure for Additive Manufacturing. Materials (Basel). 12, 913. https://doi.org/10.3390/ma12060913

Saha, S., Pal, S., Albright, J.A., 1982. Surgical Drilling: Design and Performance of an Improved Drill. J. Biomech. Eng. 104, 245–252. https://doi.org/10.1115/1.3138356

Samuel, J., Park, J.S., Almer, J., Wang, X., 2016. Effect of water on nanomechanics of bone is different between tension and compression. J. Mech. Behav. Biomed. Mater. 57, 128–138. https://doi.org/10.1016/j.jmbbm.2015.12.001

Santiuste, C., Rodríguez-Millán, M., Giner, E., Miguélez, H., 2014. The influence of anisotropy in numerical modeling of orthogonal cutting of cortical bone. Compos. Struct. 116, 423–431. https://doi.org/10.1016/j.compstruct.2014.05.031

Schwiedrzik, J., Raghavan, R., Bürki, A., Lenader, V., Wolfram, U., Michler, J., Zysset, P., 2014a. SUPP INFO - In situ micropillar compression reveals superior strength and ductility but an absence of damage in lamellar bone. Nat. Mater. 13, 740–747. https://doi.org/10.1038/nmat3959

Schwiedrzik, J., Raghavan, R., Bürki, A., LeNader, V., Wolfram, U., Michler, J., Zysset, P., 2014b. In situ micropillar compression reveals superior strength and ductility but an absence of damage in lamellar bone. Nat. Mater. 13, 740–747. https://doi.org/10.1038/nmat3959

Schwiedrzik, J., Taylor, A., Casari, D., Wolfram, U., Zysset, P., Michler, J., 2017. Nanoscale deformation mechanisms and yield properties of hydrated bone extracellular matrix. Acta Biomater. 60, 302–314. https://doi.org/10.1016/j.actbio.2017.07.030

Sezek, S., Aksakal, B., Karaca, F., 2012. Influence of drill parameters on bone temperature and necrosis: A FEM modelling and in vitro experiments. Comput. Mater. Sci. 60, 13–18. https://doi.org/10.1016/j.commatsci.2012.03.012

Shakouri, E., Ghorbani, M., 2020. An in vitro study of bone drilling : infrared thermography and evaluation of thermal changes of bone and drill bit. Phys. Eng. Sci. Med. https://doi.org/10.1007/s13246-020-00842-x

Shakouri, E., Mirfallah, P., 2019. Infrared thermography of high-speed grinding of bone in skull base neurosurgery. Proc. Inst. Mech. Eng. Part H J. Eng. Med.

233, 648–656. https://doi.org/10.1177/0954411919845730

Shaw, M.C., 2005. Metal Cutting Principles, 2nd ed. Oxford University Press, New York.

Sheng, G.T., 2016. The Effect of Using Coolant during Bone Drilling for Surgery Application. Universiti Teknologi PETRONAS.

Shih, A.J., Tai, B.L., Li, R., 2019. Metal and Bone Drilling - The Thermal Aspects, Metal and Bone Drilling - The Thermal Aspects. https://doi.org/10.1007/978-3-030-26047-7

Shih, A.J., Tai, B.L., Zhang, L., Sullivan, S., Malkin, S., 2012. Prediction of bone grinding temperature in skull base neurosurgery. CIRP Ann. - Manuf. Technol. 61, 307–310. https://doi.org/10.1016/j.cirp.2012.03.078

Shin, H.C., Yoon, Y.S., 2006. Bone temperature estimation during orthopaedic round bur milling operations. J. Biomech. 39, 33–39. https://doi.org/10.1016/j.jbiomech.2004.11.004

Shu, L., Bai, W., Shimada, T., Ying, Z., Li, S., Sugita, N., 2020a. Thermographic assessment of heat-induced cellular damage during orthopedic surgery. Med. Eng. Phys. 83, 100–105. https://doi.org/10.1016/j.medengphy.2020.05.014

Shu, L., Li, S., Terashima, M., Bai, W., Hanami, T., Hasegawa, R., Sugita, N., 2020b. A novel self-centring drill bit design for low-trauma bone drilling. Int. J. Mach. Tools Manuf. 154, 103568. https://doi.org/10.1016/j.ijmachtools.2020.103568

Shu, L., Sugita, N., 2020. Analysis of fracture, force, and temperature in orthogonal elliptical vibration-assisted bone cutting. J. Mech. Behav. Biomed. Mater. 103, 103599. https://doi.org/10.1016/j.jmbbm.2019.103599

Singh, G., Babbar, A., Jain, V., Gupta, D., 2021. Comparative statement for diametric delamination in drilling of cortical bone with conventional and ultrasonic assisted drilling techniques. J. Orthop. 25, 53–58. https://doi.org/10.1016/j.jor.2021.03.017

Singh, G., Gahi, A., Jain, V., Gupta, D., 2016a. An investigation on thermal necrosis during bone drilling. Int. J. Mach. Mach. Mater. 18, 341–349. https://doi.org/10.1504/IJMMM.2016.077708

Singh, G., Jain, V., Gupta, D., 2015. Comparative study for surface topography of bone drilling using conventional drilling and loose abrasive machining. Proc. Inst. Mech. Eng. Part H J. Eng. Med. 229, 225–231. https://doi.org/10.1177/0954411915576945

Singh, G., Jain, V., Gupta, D., Ghai, A., 2016b. Optimization of process parameters for drilled hole quality characteristics during cortical bone drilling using Taguchi method. J. Mech. Behav. Biomed. Mater. 62, 355–365. https://doi.org/10.1016/j.jmbbm.2016.05.015

Singh, G., Jain, V., Gupta, D., Sharma, A., 2018. Parametric effect of vibrational drilling on osteonecrosis and comparative histopathology study with conventional drilling of cortical bone. Proc. Inst. Mech. Eng. Part H J. Eng. Med. 232, 975–986. https://doi.org/10.1177/0954411918794983

Singh, R.P., Gupta, V., Pandey, P.M., Mridha, A.R., 2021. Effect of Drilling

Techniques on Microcracks and Pull-Out Strength of Cortical Screw Fixed in Human Tibia: An In-Vitro Study. Ann. Biomed. Eng. 49, 382–393. https://doi.org/10.1007/s10439-020-02565-2

Sneddon, I.N., 1965. The relation between load and penetration in the axisymmetric boussinesq problem for a punch of arbitrary profile. Int. J. Eng. Sci. 3, 47–57. https://doi.org/10.1016/0020-7225(65)90019-4

Sotsuka, Y., Nishimoto, S., Tsumano, T., Kawai, K., Ishise, H., Kakibuchi, M., Shimokita, R., Yamauchi, T., Okihara, S.I., 2014. The dawn of computer-assisted robotic osteotomy with ytterbium-doped fiber laser. Lasers Med. Sci. 29, 1125–1129. https://doi.org/10.1007/s10103-013-1487-y

Stephan, K., Laesecke, A., 1985. The Thermal Conductivity of Fluid Air. J. Phys. Chem. Ref. Data 14, 227–234. https://doi.org/10.1063/1.555749

Sugita, N., Ishii, K., Sui, J., Terashima, M., 2014. Multi-grooved cutting tool to reduce cutting force and temperature during bone machining. CIRP Ann. - Manuf. Technol. 63, 101–104. https://doi.org/10.1016/j.cirp.2014.03.069

Sugita, N., Mitsuishi, M., 2009. Specifications for machining the bovine cortical bone in relation to its microstructure. J. Biomech. 42, 2826–2829. https://doi.org/10.1016/j.jbiomech.2009.08.017

Sugita, N., Osa, T., Aoki, R., Mitsuishi, M., 2009a. A new cutting method for bone based on its crack propagation characteristics. CIRP Ann. - Manuf. Technol. 58, 113–118. https://doi.org/10.1016/j.cirp.2009.03.057

Sugita, N., Osa, T., Mitsuishi, M., 2009b. Analysis and estimation of cutting-temperature distribution during end milling in relation to orthopedic surgery. Med. Eng. Phys. 31, 101–107. https://doi.org/10.1016/j.medengphy.2008.05.001

Sui, J., Sugita, N., Ishii, K., Harada, K., Mitsuishi, M., 2014. Mechanistic modeling of bone-drilling process with experimental validation. J. Mater. Process. Technol. 214, 1018–1026. https://doi.org/10.1016/j.jmatprotec.2013.11.001

Sui, J., Sugita, N., Ishii, K., Harada, K., Mitsuishi, M., 2013. Force analysis of orthogonal cutting of bovine cortical bone. Mach. Sci. Technol. 17, 637–649. https://doi.org/10.1080/10910344.2013.837355

Sui, J., Sugita, N., Mitsuishi, M., 2015. Thermal Modeling of Temperature Rise for Bone Drilling With Experimental Validation. J. Manuf. Sci. Eng. 137, 061008. https://doi.org/10.1115/1.4030880

Sui, J., Wang, C., Sugita, N., 2020. Experimental study of temperature rise during bone drilling process. Med. Eng. Phys. 78, 64–73. https://doi.org/10.1016/j.medengphy.2020.01.007

Tahmasbi, V., Ghoreishi, M., Zolfaghari, M., 2017. Investigation, sensitivity analysis, and multi-objective optimization of effective parameters on temperature and force in robotic drilling cortical bone. Proc. Inst. Mech. Eng. Part H J. Eng. Med. 231, 1012–1024. https://doi.org/10.1177/0954411917726098

Tai, B.L., Zhang, L., Wang, A., Sullivan, S., Shih, A.J., 2013a. Neurosurgical bone grinding temperature monitoring. Procedia CIRP 5, 226–230.

https://doi.org/10.1016/j.procir.2013.01.045

Tai, B.L., Zhang, L., Wang, A.C., Sullivan, S., Wang, G., Shih, A.J., 2013b. Temperature prediction in high speed bone grinding using motor PWM signal. Med. Eng. Phys. 35, 1545–1549. https://doi.org/10.1016/j.medengphy.2013.05.011

Tajdari, M., Tai, B.L., 2016. Modeling of brittle and ductile materials drilling using smoothed-particle hydrodynamics. ASME 2016 11th Int. Manuf. Sci. Eng. Conf. MSEC 2016 2, 1–7. https://doi.org/10.1115/MSEC2016-8801

Takabi, B., Tai, B.L., 2017. A review of cutting mechanics and modeling techniques for biological materials. Med. Eng. Phys. 45, 1–14. https://doi.org/10.1016/j.medengphy.2017.04.004

Tan, C., Zou, J., Li, S., Jamshidi, P., Abena, A., Forsey, A., Moat, R.J., Essa, K., Wang, M., Zhou, K., Attallah, M.M., 2021. Additive manufacturing of bio-inspired multi-scale hierarchically strengthened lattice structures. Int. J. Mach. Tools Manuf. 167, 103764. https://doi.org/10.1016/j.ijmachtools.2021.103764

Tang, T., Ebacher, V., Cripton, P., Guy, P., McKay, H., Wang, R., 2015. Shear deformation and fracture of human cortical bone. Bone 71, 25–35. https://doi.org/10.1016/j.bone.2014.10.001

Taylor, D., Lee, T.C., 2003. Microdamage and mechanical behaviour: predicting failure and remodelling in compact bone. J. Anat. 203, 203–211. https://doi.org/10.1046/j.1469-7580.2003.00194.x

Tertuliano, O.A., Greer, J.R., 2016. The nanocomposite nature of bone drives its strength and damage resistance. Nat. Mater. 15, 1195–1202. https://doi.org/10.1038/nmat4719

Timon, C., Keady, C., 2019. Thermal osteonecrosis caused by bone drilling in orthopedic surgery: A literature review. Cureus. https://doi.org/10.7759/cureus.5226

Tomar, V., 2009. Insights into the effects of tensile and compressive loadings on microstructure dependent fracture of trabecular bone. Eng. Fract. Mech. 76, 884–897. https://doi.org/10.1016/j.engfracmech.2008.12.013

Tomlinson, R.E., Silva, M.J., 2014. Skeletal Blood Flow in Bone Repair and Maintenance. Bone Res. 1, 311–322. https://doi.org/10.4248/br201304002

Torres, A.M., Trikanad, A.A., Aubin, C.A., Lambers, F.M., Luna, M., Rimnac, C.M., Zavattieri, P., Hernandez, C.J., 2019. Bone-inspired microarchitectures achieve enhanced fatigue life. Proc. Natl. Acad. Sci. U. S. A. 116, 24457–24462. https://doi.org/10.1073/pnas.1905814116

Tu, Y.K., Chen, L.W., Ciou, J.S., Hsiao, C.K., Chen, Y.C., 2013. Finite element simulations of bone temperature rise during bone drilling based on a bone analog. J. Med. Biol. Eng. 33, 269–274. https://doi.org/10.5405/jmbe.1366

Tu, Y.K., Tsai, H.H., Chen, L.W., Huang, C.C., Chen, Y.C., Lin, L.C., 2008. Finite element simulation of drill bit and bone thermal contact during drilling. 2nd Int. Conf. Bioinforma. Biomed. Eng. iCBBE 2008 1268–1271. https://doi.org/10.1109/ICBBE.2008.645

Ueda, T., Wada, A., Hasegawa, K.I., Endo, Y., Takikawa, Y., Hasegawa, T., Hara,

T., 2010. The Effect of Drill Design Elements on Drilling Characteristics when Drilling Bone. J. Biomech. Sci. Eng. 5, 399–407. https://doi.org/10.1299/jbse.5.399

Varvani-Farahani, A., Najmi, H., 2010. A damage assessment model for cadaveric cortical bone subjected to fatigue cycles. Int. J. Fatigue 32, 420–427. https://doi.org/10.1016/j.ijfatigue.2009.08.002

Ventura, R.D., Padalhin, A.R., Lee, B.T., 2020. Functionalization of extracellular matrix (ECM) on multichannel biphasic calcium phosphate (BCP) granules for improved bone regeneration. Mater. Des. 192, 108653. https://doi.org/10.1016/j.matdes.2020.108653

Villerius, V., Kooiker, H., Post, J., Pei, Y.T., 2019. Ultrashort pulsed laser ablation of stainless steels. Int. J. Mach. Tools Manuf. 138, 27–35. https://doi.org/10.1016/j.ijmachtools.2018.11.003

Vogel, A., Venugopalan, V., 2003. Mechanisms of Pulsed laser ablation of soft biological tissues. Chem. Rev. 103, 577–644. https://doi.org/10.1007/978-90-481-8831-4_14

Volkov, M. V, Shepeleva, I.S., 1974. The use of ultrasonic instrumentation for the transection and uniting of bone tissue in orthopaedic surgery. Reconstr. Surg. Traumatol. 14, 147–152.

Vollmer, A., Saravi, B., Lang, G., Adolphs, N., Hazard, D., Giers, V., Stoll, P., 2020. Factors influencing primary and secondary implant stability—a retrospective cohort study with 582 implants in 272 patients. Appl. Sci. 10, 1–14. https://doi.org/10.3390/app10228084

Wang, B., Liu, Z.Q., Cai, Y.K., Luo, X.C., Ma, H.F., Song, Q.H., Xiong, Z.H., 2021. Advancements in material removal mechanism and surface integrity of high speed metal cutting: A review. Int. J. Mach. Tools Manuf. 166, 103744. https://doi.org/10.1016/j.ijmachtools.2021.103744

Wang, C.Y., Chen, Z.H., Chen, H.Y., Song, Q.H., Reng, Y.H., Sui, J.B., Shu, L.M., Chen, B., Zheng, L.J., 2021. A review on cutting mechanism for bone material. J. Mech. Eng. 57, 2–32.

Wang, G., Zhang, L., Wang, X., Tai, B.L., 2016. An inverse method to reconstruct the heat flux produced by bone grinding tools. Int. J. Therm. Sci. 101, 85–92. https://doi.org/10.1016/j.ijthermalsci.2015.10.021

Wang, Y., Cao, M., Zhao, X., Zhu, G., McClean, C., Zhao, Y., Fan, Y., 2014. Experimental investigations and finite element simulation of cutting heat in vibrational and conventional drilling of cortical bone. Med. Eng. Phys. 36, 1408–1415. https://doi.org/10.1016/j.medengphy.2014.04.007

Wang, Y., Cao, M., Zhao, Y., Zhou, G., Liu, W., Li, D., 2013. Experimental Investigations on Microcracks in Vibrational and Conventional Drilling of Cortical Bone. J. Nanomater. 2013, 845205. https://doi.org/10.1155/2013/845205

Wiggins, K., Malkin, S., 1978. Orthogonal Machining of Bone. J. Biomech. Eng. 100, 122. https://doi.org/10.1115/1.3426202

Wiggins, K.L., Malkin, S., 1976. Drilling of bone. J. Biomech. 9, 553–559.

https://doi.org/10.1016/0021-9290(76)90095-6

Xu, L., Wang, C., Jiang, M., He, H., Song, Y., Chen, H., Shen, J., Zhang, J., 2014. Drilling force and temperature of bone under dry and physiological drilling conditions. Chinese J. Mech. Eng. (English Ed. 27, 1240–1248. https://doi.org/10.3901/CJME.2014.0912.151

Yacker, M.J., Klein, M., 1997. The effect of irrigation on osteotomy depth and bur diameter. Int. J. Oral Maxillofac. Implants 11, 634–8.

Yan, J., Clifton, K.B., Mecholsky, J.J., Gower, L.A., 2007. Effect of temperature on the fracture toughness of compact bone. J. Biomech. 40, 1641–1645. https://doi.org/10.1016/j.jbiomech.2006.07.011

Yan, J., Clifton, K.B., Mecholsky, J.J., Reep, R.L., 2006. Fracture toughness of manatee rib and bovine femur using a chevron-notched beam test. J. Biomech. 39, 1066–1074. https://doi.org/10.1016/j.jbiomech.2005.02.016

Yang, M., Li, C., Zhang, Y., Jia, D., Zhang, X., Hou, Y., Shen, B., Li, R., 2018. Microscale bone grinding temperature by dynamic heat flux in nanoparticle jet mist cooling with different particle sizes. Mater. Manuf. Process. 33, 58–68. https://doi.org/10.1080/10426914.2016.1244846

Yang, M., Li, C., Zhang, Y., Wang, Y., Li, B., Jia, D., Hou, Y., Li, R., 2017. Research on microscale skull grinding temperature field under different cooling conditions. Appl. Therm. Eng. 126, 525–537. https://doi.org/10.1016/j.applthermaleng.2017.07.183

Yang, Y., Wang, C., Qin, Z., Xu, L., Song, Y., Chen, H., 2010. Drilling force and temperature of bone by surgical drill. Adv. Mater. Res. 126–128, 779–784. https://doi.org/10.4028/www.scientific.net/AMR.126-128.779

Yang, Z., Zhu, L., Zhang, G., Ni, C., Lin, B., 2020. Review of ultrasonic vibration-assisted machining in advanced materials. Int. J. Mach. Tools Manuf. 156, 103594. https://doi.org/10.1016/j.ijmachtools.2020.103594

Yeager, C., Nazari, A., Arola, D., 2008. Machining of cortical bone: Surface texture, surface integrity and cutting forces. Mach. Sci. Technol. 12, 100–118. https://doi.org/10.1080/10910340801890961

Yeni, Y.N., Brown, C.U., Wang, Z., Norman, T.L., 1997. The influence of bone morphology on fracture toughness of the human femur and tibia. Bone 21, 453–459. https://doi.org/10.1016/S8756-3282(97)00173-7

Yerramshetty, J.S., Lind, C., Akkus, O., 2006. The compositional and physicochemical homogeneity of male femoral cortex increases after the sixth decade. Bone 39, 1236–1243. https://doi.org/10.1016/j.bone.2006.06.002

Yin, J.F., Bai, Q., Zhang, B., 2018. Methods for detection of subsurface damage: A review. Chinese J. Mech. Eng. (English Ed. 31. https://doi.org/10.1186/s10033-018-0229-2

Ying, Z., Shu, L., Sugita, N., 2020. Experimental and Finite Element Analysis of Force and Temperature in Ultrasonic Vibration Assisted Bone Cutting. Ann. Biomed. Eng. 48, 1281–1290. https://doi.org/10.1007/s10439-020-02452-w

Zhang, G., Deng, X., Guan, F., Bai, Z., Cao, L., Mao, H., 2018. The effect of storage time in saline solution on the material properties of cortical bone tissue. Clin.

Biomech. 57, 56–66. https://doi.org/10.1016/j.clinbiomech.2018.06.003

Zhang, H., Schuster, B.E., Wei, Q., Ramesh, K.T., 2006. The design of accurate micro-compression experiments. Scr. Mater. 54, 181–186. https://doi.org/10.1016/j.scriptamat.2005.06.043

Zhang, L., Tai, B.L., Wang, A.C., Shih, A.J., 2013a. Mist cooling in neurosurgical bone grinding. CIRP Ann. - Manuf. Technol. 62, 367–370. https://doi.org/10.1016/j.cirp.2013.03.125

Zhang, L., Tai, B.L., Wang, G., Zhang, K., Sullivan, S., Shih, A.J., 2013b. Thermal model to investigate the temperature in bone grinding for skull base neurosurgery. Med. Eng. Phys. 35, 1391–1398. https://doi.org/10.1016/j.medengphy.2013.03.023

Zhang, S., Zhang, J., Zhu, B., Niu, S., Han, Z., Ren, L., 2020. Progress in Bio-inspired Anti-solid Particle Erosion Materials: Learning from Nature but Going beyond Nature. Chinese J. Mech. Eng. (English Ed. 33. https://doi.org/10.1186/s10033-020-00458-y

Zhang, Y., Robles-Linares, J.A., Chen, L., Liao, Z., Shih, A.J., Wang, C., 2022. Advances in machining of hard tissues – From material removal mechanisms to tooling solutions. Int. J. Mach. Tools Manuf. 172, 103838. https://doi.org/10.1016/j.ijmachtools.2021.103838

Zhang, Y., Wang, C.Y., Zhou, S.B., Jiang, W.T., Liu, Z.H., Xu, L.L., 2017. A comparison review on orthopedic surgery using piezosurgery and conventional tools, in: Procedia CIRP. Elsevier B.V., pp. 99–104. https://doi.org/10.1016/j.procir.2017.04.024

Zhang, Y., Xu, L., Wang, C., Chen, Z., Han, S., Chen, B., Chen, J., 2019. Mechanical and thermal damage in cortical bone drilling in vivo. Proc. Inst. Mech. Eng. Part H J. Eng. Med. 233, 621–635. https://doi.org/10.1177/0954411919840194

Zhu, W.L., Beaucamp, A., 2020. Compliant grinding and polishing: A review. Int. J. Mach. Tools Manuf. 158, 103634. https://doi.org/10.1016/j.ijmachtools.2020.103634

Zimmermann, E.A., Gludovatz, B., Schaible, E., Busse, B., Ritchie, R.O., 2014. Fracture resistance of human cortical bone across multiple length-scales at physiological strain rates. Biomaterials 35, 5472–5481. https://doi.org/10.1016/j.biomaterials.2014.03.066

Zimmermann, E.A., Launey, M.E., Ritchie, R.O., 2010. The significance of crack-resistance curves to the mixed-mode fracture toughness of human cortical bone. Biomaterials 31, 5297–5305. https://doi.org/10.1016/j.biomaterials.2010.03.056

Zimmermann, E.A., Schaible, E., Bale, H., Barth, H.D., Tang, S.Y., Reichert, P., Busse, B., Alliston, T., Ager, J.W., Ritchie, R.O., 2011. Age-related changes in the plasticity and toughness of human cortical bone at multiple length scales. Proc. Natl. Acad. Sci. U. S. A. 108, 14416–14421. https://doi.org/10.1073/pnas.1107966108